

Universität der Bundeswehr München
Fakultät für Luft- und Raumfahrttechnik
Institut für Thermodynamik

Experimental and numerical investigations and optimisation of Tesla-radial turbines

Constantin Schosser, M.Sc.

Vollständiger Abdruck der bei der
Fakultät für Luft- und Raumfahrttechnik
der Universität der Bundeswehr München
zur Erlangung des akademischen Grades eines

Doktor-Ingenieurs (Dr.-Ing.)

genehmigten Dissertation.

Vorsitzender: Univ.-Prof. Dr.-Ing. habil. Markus Klein
1. Berichterstatter: Univ.-Prof. Dr. rer. nat. Michael Pfitzner
2. Berichterstatter: Univ.-Prof. Dr. rer. nat. habil. Christian J. Kähler
3. Berichterstatter: Prof. Dr.-Ing. Stefan Lecheler

Diese Dissertation wurde am 09.06.2016 bei der Universität der Bundeswehr München,
85577 Neubiberg eingereicht und durch die Fakultät für Luft- und Raumfahrttech-
nik am 17.11.2016 angenommen.

Tag der Prüfung: 09.12.2016

In loving memory of Karl Czech (1924-2015)

Abstract

In the beginning of the 20th century, Nikola Tesla invented, built and patented the Tesla turbine. Driven by a pressure difference, the kinetic energy of fluids or gases is converted to mechanical shaft power due to wall friction in the gap of one or more co-rotating, parallel disks. While friction turbines do not attract much attention in technical applications up to now, their simple and low-cost design might be an economical alternative to conventional turbomachinery in small power scales at appropriate efficiencies in the near future. These turbines are very well suited for the energy conversion of existing and so far untapped energy resources.

Theoretical investigations, numerical simulations and blackbox performance map measurements of Tesla turbines are the current state of the art in this field of research. Up to now, useful experiments for the validation of rotor flows are lacking, due to the small gap widths for competitive turbines. The scope of this thesis is the investigation of the the velocity distribution between the disks of a Tesla rotor. This is done by theoretical, numerical and experimental means.

A simplified model for the incompressible, laminar and stationary rotor flow is presented and extensively evaluated here. Under the assumption of a parabolic velocity distribution between the rotating disks, fully analytical solutions of the radial and tangential momentum equations are introduced. A suitable analysis of shaft power, pressure difference and efficiency in a dimensionless form reveals the limitations and opportunities of Tesla turbines. An extended model establishes compressibility effects and their influence on turbine performance. Furthermore, a method for the deduction of the mathematical character of fully-developed, laminar velocity profiles is introduced and compared to a laminar CFD solution.

The test rig is designed by means of analytical flow modelling, laminar CFD, FEM, modal and harmonic response analyses of the rotor. The test facility is monitored and feedback-controlled by a software developed using NI LabVIEW real-time on a cRIO and FPGA system.

This thesis focuses on highly resolved optical PIV experiments of the radial and the tangential velocity distribution in the small gap between the co-rotating disks of a Tesla rotor at various operating conditions. Applying this measurement method in turbomachinery is unusual and denotes a particular highlight. However, regular calibration methods are not applicable, because of the limited spatial access to the measurement volume. A fully automated non-intrusive calibration technique using reflections on the rotor walls of a traversable constant wave laser is developed to overcome this issue.

Zusammenfassung

Nikola Tesla hat Anfang des 20. Jahrhunderts die radiale Tesla Turbine erfunden, gebaut und patentieren lassen. Dabei wird kinetische Energie von druckbeaufschlagten Flüssigkeiten oder Gasen mittels Wandreibung im Spalt von rotierenden, parallelen Scheiben in mechanische Energie gewandelt. Obwohl Reibungsturbinen bisher in der Technik wenig Beachtung fanden, könnten sie heute jedoch aufgrund ihres einfachen und kostengünstigen Aufbaus bei kleinen Leistungsklassen und akzeptablen Wirkungsgraden eine rein wirtschaftliche Alternative darstellen. Vor allem eignen sich diese Turbine um vorhandene und bisher ungenutzte Energie in elektrischen Strom zu wandeln.

Theoretische Untersuchungen, numerische Simulationen und Kennfeldmessungen sind der aktuelle Stand der Untersuchungen an Reibungsturbinen. Sinnvolle Experimente zur Validierung der Rotorströmung fehlen allerdings bisher. Die vorliegende Arbeit zielt daher auf Untersuchungen der Spaltströmung mit Hilfe von theoretischen, numerischen und experimentellen Methoden ab.

Ein vereinfachtes Modell für die inkompressible, laminare und stationäre Rotorströmung liefert, unter der Annahme eines parabolischen Geschwindigkeitsprofils, sowohl die vollständig analytische Lösung der Impulsgleichung in Umfangsrichtung, als auch die der radialen Impulsgleichung. Die geeignete, analytische Auswertung von Leistung, Druck und Wirkungsgrad, anhand dimensionsloser Größen zeigt die Grenzen der Teslaturbine auf. Das erweiterte, numerisch gelöste Modell bildet Kompressibilitätseinflüsse der laminaren Strömung ab. Des Weiteren lässt sich das reale, laminare Geschwindigkeitsprofil theoretisch herleiten und mit laminarer CFD validieren.

Die Auslegung des Prüfstands erfolgt mit Hilfe von analytischer Strömungsberechnung, laminarer CFD, Festigkeitsberechnungen, FEM, Modal- und Frequenzganganalyse. Die Software für Messtechnik, Überwachung, Steuerung und Regelung von Strömung und Rotordrehzahl erfolgt mit NI LabVIEW real-time cRIO und FPGA.

Im Fokus der Arbeit stehen die hochpräzisen optische PIV-Messungen der radialen und der umfangsgerichteten Geschwindigkeitsverteilungen der stationären Rotorströmung für verschiedene Betriebspunkte. Der Einsatz dieser Methode im Bereich der Turbomaschinen ist ungewöhnlich und stellt deshalb eine Besonderheit dar. Da der räumliche Zugang zum Messvolumen deutlich eingeschränkt ist, wurde eine berührungslose Methode entwickelt, die Reflektionen eines traversierbaren Lasers an den Rotorwänden nutzt, um die Kameras zu kalibrieren.

Acknowledgements

This doctoral dissertation is the outcome of the theoretical, experimental, and numerical investigations, carried out at the Institute of Thermodynamics, the Institute of Fluid Mechanics and Aerodynamics (Faculty of Aviation and Aerospace Engineering), and the Department of Technical Thermodynamics (Faculty of Mechanical Engineering) of the Bundeswehr University Munich between 2010 and 2015.

First of all, I want to express my gratefulness to Prof. Dr.-Ing. Stefan Lecheler. His enthusiasm for Tesla turbines, his expertise in numerical flow simulations, and his efforts in smoothly providing the budget for financing the project, enabled me to carry out scientific work. I thank Univ.-Prof. Dr. rer. nat. Michael Pfitzner for supporting me constantly during the last years. His expertise and contribution to the project helped to improve this work significantly. I thank Univ.-Prof. Dr. rer. nat. habil. Christian J. Kähler for his participation in this multi-institute collaboration. He provided great expertise in fluid experiments, encouragements for further extensions of research, additional manpower, and the latest optical measurement equipment. I thank Dr.-Ing. Rainer Hain for being a good friend and supporting my fluid experiments. His dedication to fluid mechanics and optical measurements helped to substantially improve the outcome of this thesis.

I thank all my colleagues and especially my former office-mate Dipl.-Ing. Bettina Deixler-Thier for the good and harmonious working atmosphere. Furthermore, I thank Dipl.-Ing. Thomas Fuchs for being a good friend, his patience, and his expertise in particle tracking post-processing development.

Last but not least, special thanks to all the people who encouraged me throughout these years: my parents, my grandparents, my close friends, and of course all those who guided me on my way. I thank all of them for their persistence and devotion shown during all these years.

Munich, April 2016

Contents

Abstract	vi
Zusammenfassung	viii
Acknowledgements	x
Table of contents	xi
List of Figures	xv
List of Tables	xxiii
List of Symbols	xxv
List of Abbreviations	xxxii
1 Introduction	1
1.1 Motivation	1
1.2 The Tesla turbine principle	3
1.3 Previous investigations about the Tesla turbine	4
1.3.1 Theoretical rotor flow models	5
1.3.2 Experimental investigations	15
1.3.3 CFD investigations	22
1.3.4 Summary of earlier investigations	26
2 Theoretical investigations	27
2.1 Energy conversion in Tesla turbines	27
2.2 Performance maps of Tesla turbines	28
2.3 Starting process and operating points of Tesla turbines	28
2.4 Definitions of Reynolds numbers	29
2.5 Navier-Stokes-Equations in cylindrical coordinates	30
2.6 Simplified incompressible flow model	31

2.6.1	Dimensional governing equations	31
2.6.2	Non-dimensional governing equations	33
2.6.3	Performance map calculations	36
2.6.4	Similarity and scaling laws	38
2.6.5	Streamline visualisation	38
2.7	Performance optimisation of Tesla turbines	41
2.7.1	Influences of the friction parameter	41
2.7.2	Influences of the inlet angle	46
2.7.3	Influences of the radius ratio	51
2.7.4	Optimisation criteria	53
2.8	Simplified compressible flow model	55
2.8.1	Dimensional governing equations	55
2.8.2	Non-dimensional governing equations	56
2.8.3	Compressibility effects and model validation	57
2.9	Approximate analytical solution of the velocity profiles	59
2.9.1	Radial and tangential momentum equations in boundary layer approximation	59
2.9.2	Analytical solution for tangential and radial velocity profiles in the viscous limit	61
2.9.3	Approximate solution of non-linear tangential momentum equation	64
3	Numerical investigations	68
3.1	Numerical approach	68
3.2	Computational flow domain with boundary conditions	69
3.2.1	Domain for the validation of the theoretical flow model and the experimental results	69
3.2.2	Domain for the optimisation of rig components	70
3.3	Computational grid	72
3.3.1	Mesh for the validation of the theoretical flow model and the experimental results	72
3.3.2	Mesh for the optimisation of rig components	74
4	Test rig	75

4.1	Working medium	75
4.2	Feasibility study of the measurement task	76
4.3	Requirements	79
4.4	The Tesla rotor	80
4.4.1	Design process	80
4.4.2	Mechanical constraints	81
4.4.3	Rotor design concepts	82
4.4.4	Final rotor design	86
4.4.5	Stress and deformation analysis	89
4.4.6	Modal and harmonic response analysis	91
4.4.7	Rotor balancing	92
4.5	Test rig design	93
4.6	CFD optimisation of test rig components	96
4.7	Measurement techniques and control software	99
5	PTV Set-up	102
5.1	Experimental Set-up	102
5.2	Stereoscopic 3D-PTV	104
5.3	Calibration and particle location determination	106
5.4	Calibration Set-up	107
5.5	Non-intrusive calibration technique	107
5.6	Automation of the calibration scheme	111
5.7	Post-processing of calibration data	111
5.8	Quantification of the calibration error	112
6	Theoretical, numerical, and experimental results	114
6.1	Comparison of incompressible, laminar theory with CFD	114
6.1.1	Validation of the incompressible, laminar flow model	114
6.1.2	Influences of the inlet profiles on turbine performance	118
6.2	Error propagation of particle image measurement data	121
6.2.1	Systematic error	121
6.2.2	Residual error	124

6.3	Experimental, numerical, and theoretical results	126
6.3.1	Laminar flow	126
6.3.2	Turbulent flow	128
6.3.3	Flow oscillations	131
6.3.4	Classification of flow regimes	133
6.3.5	Transition to turbulence	134
6.3.6	Velocity profile shape	138
6.3.7	Velocity magnitude	140
6.3.8	Conservation of mass in Tesla turbines	142
7	Conclusions and future research	144
A	Appendix	146
A.1	Theoretical investigations	146
A.2	Test rig	147
A.3	PTV measurement data	153
A.4	Two-dimensional transient CFD	176
A.5	Post processing of measurement data	177
A.6	CFD investigations	178
	Bibliography	179

List of Figures

1.1	The Tesla turbine principle [11]	3
1.2	Original disk turbine designed by Nikola Tesla [2]	4
1.3	Technical illustration of Beans' test rig of a Tesla turbine [45]	17
2.1	Performance map of a Tesla turbine	28
2.2	Torque curves of turbine and load with operating point	29
2.3	Cylindrical coordinate system in a Tesla rotor	30
2.4	Semi-infinitesimal control volume	32
2.5	Tangential, relative velocity distribution between disks	34
2.6	$\Omega = 0.4, V_1 = 0.1, \beta = 1$	39
2.7	$\Omega = 0.8, V_1 = 0.3, \beta = 100$	39
2.8	Position of streamline plane in the rotor	40
2.9	Streamline at $Z = \pm\sqrt{1/3}$ and of bulk flow are identical ($\beta=5$)	41
2.10	Streamlines at different axial positions ($\beta=5, \Omega=1, V_1=0.3$)	41
2.11	Dimensionless torque map C_M for $R=0.8$	42
2.12	Dimensionless performance map C_P for $R=0.8, V_1=0.3$	42
2.13	Efficiency map η_{is} for $R=0.8, V_1=0.05$	43
2.14	Pressure drop ΔP across the radius for $V_1=0.2, \Omega=0.6$	43
2.15	Tangential velocity distribution across the radius for $\Omega=1.0$	44
2.16	$\Omega=0.6, V_1=0.2, \beta=1$	45
2.17	$\Omega=0.6, V_1=0.2, \beta=100$	45
2.18	Centre streamline plots for high and low β values ($\Omega=0.6, V_1=0.2$)	45
2.19	Low- β streamline study in dependency of the axial inter-disk position Z ($\beta=1, \Omega=0.6, V_1=0.1$)	45
2.20	Parameter β as a function of disk spacing σ and Reynolds number Re_v	46
2.21	Performance mapping for $R=0.2$ with different inlet angles	47
2.22	Efficiency mapping for $R=0.2$ with different inlet angles	47
2.23	Pressure drops at radius $R=0.2$ as a function of β and Ω	47
2.24	Bulk flow streamlines for $R=0.2, \beta=10, \Omega=0.8$ and different V_1	48

2.25	Shaft power for different inlet angles and $\beta=15$, $R=0.2$	48
2.26	Isentropic efficiency for different inlet angles and $\beta=15$, $R=0.2$	49
2.27	Pressure drop for different inlet angles ($\beta=15$, $\Omega=0.75$)	49
2.28	Performance map for different inlet angles V_1	50
2.29	Dimensionless torque map C_M for small and large radius ratios R	51
2.30	Performance map for different radius ratios R	51
2.31	Efficiency map for different radius ratios R	52
2.32	Pressure drop ΔP across the radius	52
2.33	Development of total torque M along the radius ratios R	53
2.34	Power map comparison	58
2.35	Radial Mach number Ma_r across the radius	58
2.36	Radial profile $G(Z)$ in dependency of N	63
2.37	Tangential profile $F_F(Z)/N^2$ in dependency of N	63
2.38	Differences between $F_F(Z)$ and numerical solution of Eq. 2.117 $F(Z)$	64
2.39	Numerical solution for a_0/N^2 (lower surface) with approximation of function $F(Z)$ from Eq. 2.133	66
2.40	Dependence of $F(0)$ in Fourier approximation for $0 \leq N \leq 2$, $0 \leq B \leq 5$	67
3.1	Boundary conditions of the rotor model with ideal inlet and outlet	70
3.2	Boundary conditions of the guide vane model	71
3.3	Detailed view of the guide vanes' trailing edge in Fig. 3.2	71
3.4	Boundary conditions of the real test rig rotor	72
3.5	Mesh of the rotor	73
3.6	Detailed view of inter-disk distribution of cells marked in Fig. 3.5	73
3.7	Mesh of guide vanes	74
3.8	Mesh of test rig rotor with modelled disk spacers	74
4.1	Achievable values of β [134]	76
4.2	Measuring section for first tomographic PIV tests	77
4.3	Calibration target	77
4.4	Stereo PIV set-up for calibration	77
4.5	Measurement results obtained from particle tracking in tomographically reconstructed volumes (evaluation of ten double-frame volumes)	78

4.6	Process of rotor design [134]	80
4.7	Centrally drilled disk under constant rotation [11]	81
4.8	Bearing concept A	82
4.9	Bearing concept B	82
4.10	Illumination A	83
4.11	Illumination B	83
4.12	Design A	83
4.13	Design B	83
4.14	Design C	83
4.15	Disk A	84
4.16	Disk B	84
4.17	Disk C	84
4.18	Spacing A	84
4.19	Spacing B	84
4.20	Carbon floating radial seal ring	85
4.21	Labyrinth radial seal ring	85
4.22	PTFE radial shaft seal ring	85
4.23	Final concept in detail	86
4.24	Mechanical design of the rotor	87
4.25	Outer disk with profiled disk spacer	88
4.26	Inner disk with profiled disk spacer	88
4.27	Assembled rotor with laser beam and deflecting mirror	89
4.28	FEM simulation of von-Mises equivalent tensile stress ($n=12\,000\text{ min}^{-1}$)	90
4.29	FEM simulation of total deformation ($n=6000\text{ min}^{-1}$) [134]	91
4.30	Harmonic response analysis, mode of motion at 34 Hz [134]	91
4.31	Drawing for balancing the rotor	93
4.32	Test rig opened and closed view	94
4.33	Intersected test rig with main components	95
4.34	System layout of the test facility	96
4.35	$n = 1000\text{ min}^{-1}$, $V_1 = 0.34$	97
4.36	$n = 4000\text{ min}^{-1}$, $V_1 = 0.33$	97
4.37	$n = 7000\text{ min}^{-1}$, $V_1 = 0.32$	97

4.38	$n = 10000 \text{ min}^{-1}$, $V_1 = 0.29$	97
4.39	Relative streamline plot at the rotor outlet	98
4.40	Measuring point of mass flow regulator	99
4.41	Test rig with measuring points part 1	99
4.42	Test rig with measuring points part 2	100
4.43	Sequence applied in the measurement and control software [134] . . .	101
5.1	Turbine test rig with stereoscopic PTV set-up and calibration unit . .	102
5.2	Optical access to the rotor	103
5.3	Trajectory of laser beam for the illumination of the measuring volume	104
5.4	Triangulation principle	105
5.5	Sensor search area	105
5.6	Calibration principle [147]	108
5.7	Traversable laser beam creating a non-intrusive calibration target [147]	109
5.8	Greyscale image of light reflections of a single camera [147]	109
5.9	Intensity distribution of a reflection on a glass surface [147]	110
5.10	PTV set-up with non-intrusive calibration unit	110
5.11	Automated calibration process	111
5.12	Residuals of calibration function of sensor #1 (left side: $z = 0.0 \text{ mm}$, right side: $z = 0.5 \text{ mm}$) [147]	113
6.1	Comparison of analytical (solid lines) and numerical (dots) power maps	115
6.2	Comparison of analytical (solid lines) and numerical (dots) torque curves	115
6.3	Comparison of analytical (solid lines) and numerical (dots) efficiency curves	116
6.4	Development of tangential, relative CFD velocity profiles $F_{C,n}(R, Z)$ for $\Omega = 0.92$, $V_1 = 0.27$, $\beta = 11$, $Re_u = 630$ in comparison with the fully-developed analytical parabolic and $F_F(Z)$ the approximate pro- file for $A = 1.98$, $N = 1.48$	117
6.5	Development of radial CFD velocity profiles $G_C(R, Z)$ for $\Omega = 0.92$, $V_1 = 0.27$, $\beta = 11$, $Re_v = 170$ in comparison with the fully-developed analytical parabolic and $G(Z)$ the approximate profile for $A = 1.98$, $N = 1.48$	117
6.6	Comparison of numerical and analytical power maps	118

6.7	Comparison of numerical and analytical efficiency maps	119
6.8	Development of torque across the radius	119
6.9	Tangential, absolute bulk velocity comparison	120
6.10	Deformation of the gap width between the disks at the outer radius .	122
6.11	Particle displacement $\overline{\Delta z}$ averaged for each operational point as a function of the rotational speed n	123
6.12	Tangential, laminar velocity profile at the outer radius	126
6.13	Radial, laminar velocity profile at the outer radius	127
6.14	Tangential, laminar velocity profile at the inner radius	127
6.15	Radial, laminar velocity profile at the inner radius	128
6.16	Tangential, turbulent velocity profile at the outer radius	129
6.17	Radial, turbulent velocity profile at the outer radius	129
6.18	Tangential, turbulent velocity profile at the inner radius	130
6.19	Radial, turbulent velocity profile at the inner radius	130
6.20	Transient, laminar flow through the non-aligned, 2D, simplified stator- rotor domain at the time step $\Delta t = 0.001$ s ($2s=0.5$ mm; $\bar{u}_1=20$ m/s; $\bar{p}_2=1$ bar)	132
6.21	Radial velocity profile under rotation ($n = 1000 \text{ min}^{-1}$)	132
6.22	Radial velocity profile without rotation ($n = 0 \text{ min}^{-1}$)	132
6.23	Standard deviation $\sigma_{\Delta z}$ of the particle displacement Δz in z -direction along the inter-disk spacing at the outer radius (laminar flow)	133
6.24	Standard deviation $\sigma_{\Delta z}$ of the particle displacement Δz in z -direction along the inter-disk spacing at the inner radius (turbulent flow) . . .	134
6.25	Tangential, laminar velocity profile at the outer radius	135
6.26	Radial, laminar velocity profile at the outer radius	135
6.27	Standard deviation $\sigma_{\Delta z}$ of the particle displacement Δz in z -direction along the inter-disk spacing at the outer radius	136
6.28	Transitional, tangential velocity profile at the inner radius	136
6.29	Transitional, radial velocity profile at the inner radius	137
6.30	Standard deviation $\sigma_{\Delta z}$ of the particle displacement Δz in z -direction along the inter-disk spacing at the inner radius	137
6.31	Tangential, relative velocity profile at $n = 1000 \text{ min}^{-1}$	141
6.32	Tangential, relative velocity profile at $n = 5000 \text{ min}^{-1}$	141
6.33	Radial, velocity profile at $n = 1000 \text{ min}^{-1}$	141

6.34	Radial, velocity profile at $n = 5000 \text{ min}^{-1}$	141
6.35	Laminar, radial velocity profiles with second and fourth-order polynomial curve fits at different radial positions for one operational point	142
A.1	Concept 1	148
A.2	Concept 2	148
A.3	Concept 3	148
A.4	Concept 4	148
A.5	Concept 5	148
A.6	Concept 6	148
A.7	Concept 7	148
A.8	Concept 8	148
A.9	Image of the test rig	149
A.10	Top view of the test rig	150
A.11	Optical access to the measurement volume	151
A.12	Rotor and guide vanes	151
A.13	PIV laser in operation	152
A.14	LabVIEW front panel	152
A.15	Laminar, tangential velocity profile without rotation at the outer radius	158
A.16	Laminar, radial velocity profile without rotation at the outer radius .	158
A.17	Standard deviation $\sigma_{\Delta z}$ of the particle displacement Δz in z -direction along the inter-disk spacing without rotation at the outer radius . . .	158
A.18	Transitional, tangential velocity profile without rotation at the outer radius	159
A.19	Transitional, radial velocity profile without rotation at the outer radius	159
A.20	Standard deviation $\sigma_{\Delta z}$ of the particle displacement Δz in z -direction along the inter-disk spacing without rotation at the outer radius . . .	159
A.21	Laminar, tangential velocity profile at the outer radius	160
A.22	Laminar, radial velocity profile at the outer radius	160
A.23	Standard deviation $\sigma_{\Delta z}$ of the particle displacement Δz in z -direction along the inter-disk spacing at the outer radius	160
A.24	Laminar, tangential velocity profile at the outer radius	161
A.25	Laminar, radial velocity profile at the outer radius	161

A.26 Standard deviation $\sigma_{\Delta z}$ of the particle displacement Δz in z -direction along the inter-disk spacing at the outer radius	161
A.27 Laminar, tangential velocity profile at the outer radius	162
A.28 Laminar, radial velocity profile at the outer radius	162
A.29 Standard deviation $\sigma_{\Delta z}$ of the particle displacement Δz in z -direction along the inter-disk spacing at the outer radius	162
A.30 Transitional, tangential velocity profile at the inner radius	163
A.31 Transitional, radial velocity profile at the inner radius	163
A.32 Standard deviation $\sigma_{\Delta z}$ of the particle displacement Δz in z -direction along the inter-disk spacing at the inner radius	163
A.33 Laminar, tangential velocity profile at the outer radius	164
A.34 Laminar, radial velocity profile at the outer radius	164
A.35 Standard deviation $\sigma_{\Delta z}$ of the particle displacement Δz in z -direction along the inter-disk spacing at the outer radius	164
A.36 Transitional, tangential velocity profile at the inner radius	165
A.37 Transitional, radial velocity profile at the inner radius	165
A.38 Standard deviation $\sigma_{\Delta z}$ of the particle displacement Δz in z -direction along the inter-disk spacing at the inner radius	165
A.39 Transitional, tangential velocity profile at the outer radius	166
A.40 Transitional, radial velocity profile at the outer radius	166
A.41 Standard deviation $\sigma_{\Delta z}$ of the particle displacement Δz in z -direction along the inter-disk spacing at the outer radius	166
A.42 Transitional, tangential velocity profile at the inner radius	167
A.43 Transitional, radial velocity profile at the inner radius	167
A.44 Standard deviation $\sigma_{\Delta z}$ of the particle displacement Δz in z -direction along the inter-disk spacing at the inner radius	167
A.45 Turbulent, tangential velocity profile at the outer radius	168
A.46 Turbulent, radial velocity profile at the outer radius	168
A.47 Standard deviation $\sigma_{\Delta z}$ of the particle displacement Δz in z -direction along the inter-disk spacing at the outer radius	168
A.48 Turbulent, tangential velocity profile at the inner radius	169
A.49 Turbulent, radial velocity profile at the inner radius	169
A.50 Standard deviation $\sigma_{\Delta z}$ of the particle displacement Δz in z -direction along the inter-disk spacing at the inner radius	169

A.51 Turbulent, tangential velocity profile at the outer radius	170
A.52 Turbulent, radial velocity profile at the outer radius	170
A.53 Standard deviation $\sigma_{\Delta z}$ of the particle displacement Δz in z -direction along the inter-disk spacing at the outer radius	170
A.54 Turbulent, tangential velocity profile at the inner radius	171
A.55 Turbulent, radial velocity profile at the inner radius	171
A.56 Standard deviation $\sigma_{\Delta z}$ of the particle displacement Δz in z -direction along the inter-disk spacing at the inner radius	171
A.57 Turbulent, tangential velocity profile at the outer radius	172
A.58 Turbulent, radial velocity profile at the outer radius	172
A.59 Standard deviation $\sigma_{\Delta z}$ of the particle displacement Δz in z -direction along the inter-disk spacing at the outer radius	172
A.60 Turbulent, tangential velocity profile at the inner radius	173
A.61 Turbulent, radial velocity profile at the inner radius	173
A.62 Standard deviation $\sigma_{\Delta z}$ of the particle displacement Δz in z -direction along the inter-disk spacing at the inner radius	173
A.63 Turbulent, tangential velocity profile at the outer radius	174
A.64 Turbulent, radial velocity profile at the outer radius	174
A.65 Standard deviation $\sigma_{\Delta z}$ of the particle displacement Δz in z -direction along the inter-disk spacing at the outer radius	174
A.66 Turbulent, tangential velocity profile at the inner radius	175
A.67 Turbulent, radial velocity profile at the inner radius	175
A.68 Standard deviation $\sigma_{\Delta z}$ of the particle displacement Δz in z -direction along the inter-disk spacing at the inner radius	175
A.69 Transient, laminar flow through a simplified 2D domain; stator and rotor axially aligned ($\Delta t = 0.001$ s; $2s = 0.5$ mm; $\bar{u}_1 = 20$ m/s; $\bar{p}_2 = 1$ bar)	176
A.70 Transient, laminar flow through a simplified 2D domain; stator and rotor with 20% axial offset ($\Delta t = 0.001$ s; $2s = 0.5$ mm; $\bar{u}_1 = 20$ m/s; $\bar{p}_2 = 1$ bar)	176
A.71 Coordinate transformation from Cartesian into cylindrical coordinates	177

List of Tables

2.1	Coefficients of Eq. 2.135	66
4.1	Gap width blockage error [134]	90
5.1	Average absolute residuals in sensor planes	112
5.2	Average absolute spatial residuals	112
A.1	Rotor configurations for compressible, laminar flow validations using CFD (see chapter 2.8.3 for details)	146
A.2	Morphological box for subtasks and partial solutions	147
A.3	Concept assessment of possible mechanical designs	148
A.4	Additional information about PTV measurements part 1	153
A.5	Additional information about PTV measurements part 2	153
A.6	Additional information about PTV measurements part 3	154
A.7	Additional information about PTV measurements part 4	155
A.8	Additional information about PTV measurements part 5	156
A.9	Additional information about PTV measurements part 6	157
A.10	Physical quantities used for normalisation of laminar CFD	178

List of Symbols

notation	description	unit
Latin		
a_i	Fourier coefficients	—
b_i	Fourier coefficients	—
c	tangential, relative velocity component	m/s
c_p	specific heat capacity	J/kgK
d	disk diameter	mm
d_h	hydraulic diameter	m
$d_{\tau X,Y}$	Gaussian peak width in camera sensor coordinates	pixel
ΔXY	particle image displacement in camera sensor coordinates	pixel
Δz	particle displacement in axial direction in physical space	μm
e	gap blockage error	%
e_{bias}	bias measurement error (vector field)	%
e_{field}	total measurement error of a displacement vector field	%
e_{res}	residual measurement error of a single displacement vector	%
e_{rms}	measurement uncertainty (vector field)	%
e_{sys}	systematic measurement error of a single displacement vector	%
e_{vec}	total measurement error of a single displacement vector	%
$f_{\#}$	f-number (aperture)	—
f	focal length of lenses	mm
$g_{r,\varphi,z}$	body forces (gravitation)	m/s^2
h	enthalpy	J/kg
k	turbulent kinetic energy	m^2/s^2
\dot{m}	mass flow	kg/s
m	rotor mass	kg
n	revolutional speed	min^{-1}
p	pressure	Pa
r	disk radius, radial direction	mm/rad
s	half of the inter-disk spacing	mm
$2s$	inter-disk spacing	mm
s_f	mechanical safety factor	—
Δt	time step	s

notation	description	unit
t	time	s
u	tangential, absolute velocity component	m/s
v	radial velocity component	m/s
w	axial velocity component	m/s
x	Cartesian coordinate	m
y	Cartesian coordinate	m
y^+	dimensionless wall distance	—
z	Cartesian or cylindrical coordinate	m
A_1	lateral surface between the disks at rotor inlet	m ²
A	dimensionless coefficient for approximate solution of velocity profile F and G	—
B	dimensionless coefficient for approximate solution of velocity profile F and G	—
C	dimensionless, tangential, relative velocity	—
C_0	Sutherland constant	K
C_M	dimensionless torque coefficient	—
C_P	dimensionless power coefficient	—
C_{po}	dimensionless power coefficient, normalised by the shaft power maximum	—
$C_{P,t}$	dimensionless power coefficient normalised by total pressure difference	—
$C(R)$	radial component of factorised solution of tangential, relative velocity profile	—
$C_{\tau,r}$	dimensionless, radial velocity	—
$C_{\tau,\varphi}$	dimensionless, circumferential or tangential, relative velocity	—
C_{to}	dimensionless torque coefficient	—
$D(R)$	radial component of factorised solution of tangential, relative velocity profile	—
D_s	dynamic similarity number	—
E	sum of potential and kinetic energy	J
E_k	Ekman number	—
$F(R, Z)$	tangential, relative velocity profile from product approach	—
$F(Z)$	axial component of factorised solution of tangential, relative velocity profile	—
$F_F(Z)$	approximate solution of tangential, relative velocity profile (linear term of $F(Z)$)	—
$F_H(Z)$	non-linear term of tangential, relative velocity profile $F(Z)$	—
$F_C(R, Z)$	tangential, relative velocity profile (CFD)	—
$F_{C,n}(R, Z)$	normalised tangential, relative velocity profile (CFD)	—

notation	description	unit
$F_{C,n}(Z)$	normalised fully-developed tangential, relative velocity profile (CFD)	—
F	fundamental matrix	—
$G(R, Z)$	radial velocity profile from product approach	—
$G(Z)$	axial component of factorised solution of radial velocity profile	—
$G_C(R, Z)$	radial velocity profile (CFD)	—
$G_C(Z)$	fully-developed radial velocity profile (CFD)	—
H	non-dimensional enthalpy	—
I	permitted residual imbalance	g mm
I_0	intensity at peak height	—
$I(X, Y)$	2D Gaussian intensity distribution	—
M_μ	non-dimensional dynamic viscosity coefficient	—
M	torque	Nm
M	magnification	—
Ma_r	radial Mach number	—
M_b	breakdown torque of an asynchronous machine	Nm
M_{\max}	maximum occurring torque in a certain investigation	Nm
N	dimensionless coefficient for approximate solution of velocity profile F and G	—
$O()$	higher order terms	—
P	geometric point	—
P_ρ	non-dimensional density coefficient	—
P	dimensionless pressure	—
$P_{1,2}$	Camera matrices of sensor 1 and 2	—
P_o	Poiseuille number	—
P_{Ph}	Pohlhausen parameter	—
Q	quality class of residual rotor imbalance	mm/s
\dot{Q}	Heat flow	W
R	dimensionless radius, radius ratio	—
Re	Reynolds number	—
$R_{\Delta x, y, z}$	absolute spatial residuals in physical space	μm
$R_{\Delta X, Y}$	absolute residuals in sensor planes	pixel
Re_ω	Reynolds number normalised with $2s \cdot \omega$	—
Re_u	tangential Reynolds number	—
Re_v	radial Reynolds number	—
R_{air}	specific gas constant	J/kgK
T	temperature	K
T_0	reference temperature of Sutherland formula	K
Ta	Taylor number	—
T^*	non-dimensional temperature	—

notation	description	unit
U	dimensionless, tangential, absolute velocity	—
V	dimensionless, radial velocity	—
V_1	inlet angle or inlet velocity ratio	—
\dot{W}	mechanical power	W
X	non-dimensional, Cartesian, or sensor coordinate	—/pixel
Y	non-dimensional, Cartesian coordinate	—/pixel
Z	non-dimensional, Cartesian, or cylindrical coordinate	—
Greek		
α	inlet angle	°
α_ν	visco-geometric number	—
β	dimensionless friction coefficient	—
δ	boundary layer thickness	mm
η_{is}	isentropic efficiency	—
$\eta_{\text{is,t}}$	isentropic efficiency based on total enthalpy	—
κ	isentropic coefficient	—
μ	dynamic viscosity	Pa·s
μ_0	reference viscosity of Sutherland formula	Pa·s
ν	kinematic viscosity	m ² /s
ν_p	Poisson's ratio	—
ω	angular velocity	rad/s
ρ	density of fluid	—
σ	dimensionless disk spacing ratio	—
σ_i	standard deviation of a physical quantity	—
σ_{max}	maximum mechanical, tangential stress	MPa
σ_v	von-Mises equivalent tensile stress	MPa
σ_y	yield strength of a material	MPa
τ	wall shear stress	Pa
φ_B	Breiter's flow rate coefficient	—
φ	tangential, cylindrical coordinate	rad
Ω	non-dimensional angular velocity coefficient	—
Scripts		
1	physical quantity at rotor inlet	—
2	physical quantity at rotor outlet	—
a	ambient	—
crit	critical	—
dyn	dynamic	—
i	inner position	—
lin	linear	—
max	maximum	—

notation	description	unit
min	minimum	—
o	outer position	—
pl	plenum	—
r	radial direction	rad
rad	radial	—
rel	relative	—
shaft	(turbine) shaft	—
total	total	—
tan	tangential or circumferential	—
φ	tangential or circumferential direction	rad
$\vec{()}$	vectorial physical quantity	—
$\overline{()}$	area-averaged physical quantity	—
$\tilde{()}$	median of physical quantity	—
$()'$	turbulent fluctuation of velocity component	—

List of Abbreviations

2D

Two-Dimensional

3D

Three-Dimensional

AFP

Analytical (tangential) *F*-Profile

AGP

Analytical (radial) *G*-Profile

ANSYS

ANalysis SYStem (Software producer)

CAD

Computer Aided Design

CCD

Charge-Coupled Device

CFD

Computational Fluid Dynamics

CFL

Courant-Friedrichs-Lewy number

CFX

Commercial CFD code by ANSYS

CNC

Computerised Numerical Control

compact RIO

Compact Reconfigurable In-/Output real-time system

DC

Direct Current

DEHS

Di-Ethyl-Hexyl-Sebacat (tracer particles)

FE

Finite Element

FEM

Finite Element Method

FPGA

Field Programmable Gate Array

GGI

General Grid Interface

HeNe

Helium-Neon

ICEM

Integrated Computer Engineering and Manufacturing (grid generation)

LAN

Local Area Network

LASER

Light Amplification by Stimulated Emission of Radiation

LDV

Laser Doppler Velocimetry

LES

Large Eddy Simulation

MAX

Maximum

Nd:YAG

Neodymium-doped Yttrium Aluminium Garnet

NI

National Instruments

NSE

Navier-Stokes-Equations

ODE

Ordinary Differential Equation

ORC

Organic Rankine Cycle

PDE

Partial Differential Equation

PID

Proportional Integral Derivative controller

PIV

Particle Image Velocimetry

PTFE

Poly-Tetra-Fluoro-Ethylene

PTV

Particle Tracking Velocimetry

RANS

Reynolds-Averaged-Navier-Stokes simulation

RMS

Root Mean Square

RS232

Standard for serial communication transmission of data

sCMOS

Scientific Complementary Metal-Oxide-Semiconductor

SST

Shear Stress Transport turbulence model

TKE

Turbulent Kinetic Energy

TTL

Transistor-Transistor Logic

UAV

Uninhabited Aerial Vehicle

1 Introduction

1.1 Motivation

Since the beginning of the industrialisation, human's lifestyle is characterised by an increase of energy consumption without comparison. This ongoing trend is driven by globalisation, the progress being made by developing nations, and also by the exponential increase of the world population. It is therefore very likely to continue over the next centuries. To meet mankind's technological revolutions and the continuously growing level of prosperity, the energy production also has to rise with the demands of the consumers. All these facts are leading the world to a serious and global energy problem with an increase in environmental pollution. Conventional resources like fossil fuels such as oil, gas, coal, and wood are mainly used for heating, transportation, and electrical power generation. Coal and natural gas are still dominating the worldwide production of electricity [1].

The demand of electrical power is also increasing rapidly, which could be compensated by renewable energy resources. In general, the world's rise in energy consumption leads to higher emissions of greenhouse gases like carbon-dioxide, thus accelerates climate change. International climate conferences and political decisions in boosting renewables, like in Germany, show that climate change is taken seriously. On- and offshore wind farms, photovoltaics, solar-thermal, and hydro power plants are well known regenerative energy technologies from kilowatt to megawatt scale. These technologies will probably be the majority in the share of renewables of electrical power generation in mankind's future. But there are still untapped small-scale energy sources which can optimise this share. These sources can be found in industry, in private households, in public sector, and even in nature. There is waste and unused energy from industrial gas flows, where low pressures are involved, which just needs to be harvested. Reliable, low-cost devices with particularly low maintenance, easily scalable shaft power, which are independent of the operating fluid are needed for these applications. This device might be the so-called Tesla turbine - invented and patented by the famous scientist Nikola Tesla [2] in 1913.

Diverse applications of Tesla turbines have been proposed in the past:

- process heat recovery [3]
- heat to electricity in general [3]
- heat recovery from exhaust gases of bio-gas operated combustion engines [3]
- geothermal applications [3–7]
- biomass heat recovery applications [3]

- solar-thermal applications [7]
- hydro power applications in irrigation channels [7]
- unused heat from fuel cell generators [7]
- waste heat from thermal power plants [6, 7]
- additional power generation in hybrid vehicles [7]
- micro Tesla turbine applications at home [7, 8]
- expander for ORC-processes [3]
- mobile power applications [6, 8]
- power generation in unmanned aircraft UAV [6, 8]
- expansion of highly-viscous fluids in chemical process engineering [9]
- use in the field of micro turbines [10].

There are plenty of possibilities to utilise Tesla turbines. The military could independently produce electricity of wasted heat from fuel powered machines or mobile solar-thermal devices in operational areas with high level of incident solar radiation. Another application might be the use of waste heat from bio-gas plants. Furthermore, it is conceivable that Tesla turbines in combination with Tesla pumps could be used as turbochargers at least for small combustion engines to reduce manufacturing costs. These kind of turbines definitively have the possibility to find their entitlement to exist wherever heat or energy is an unused side product.

Scientists and hobbyists have investigated Tesla's turbine since the time of the invention. Tesla turbine researchers have reported various and sometimes contradictory results in the last century. Present scientific investigations are mainly of numerical nature, lacking experimental validation of the rotor flow. Few publications with attempts to validate theoretical or numerical solutions are available. They mainly compare performance maps from black box experiments to theoretical solutions or computational fluid dynamics (CFD). The character of the real flow field remains unrevealed.

This thesis attempts to understand and prove the mechanisms inside a Tesla turbine and does not investigate Tesla turbomachinery for any specific application. This is done by comparing theoretical solutions of the rotor flow, with the help of numerical simulations and optical flow measurements of the velocity distribution between the disks in a comprehensive investigation using Particle Tracking Velocimetry (PTV). Engineers can use this knowledge to precisely predict shaft power and efficiency in order to decide, whether a custom-tailored Tesla turbine might be an unconventional alternative to expensive radial turbines in specific cases.

1.2 The Tesla turbine principle

In well-known conventional turbines, energy conversion is established by fluid flowing around curved rotating blades, which creates a pressure difference between the suction and the pressure side. The pressure difference acting on the blades results in an aerodynamic force. Unlike conventional turbomachinery, the frictional interaction between rotating disks and fluid converts kinetic energy to mechanical shaft power in a Tesla turbine. Tesla turbines are also called boundary layer, blade-less, drag-type, shear-force, viscous flow, disk or friction turbines. They are characterised by their particularly simple, blade-less rotor design. They consist of two or more circular, parallel, flat disks with an outlet passage at the centre of rotation. All disks are equally spaced with narrow gaps. A swirling flow driven by a comparatively low pressure difference enters the rotor at its outer disk diameter via a nozzle or guide vanes. It follows a spiral path to the rotor outlet at the inner rotor diameter. The circumferential shear stress induces torque. Depending on the rotational speed, shaft power is delivered. Furthermore, Tesla rotors are able to work efficiently, depending on the choice of the operating fluid, the flow parameters, and the rotor geometry [6, 11].

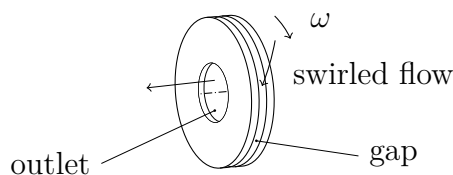


Figure 1.1: The Tesla turbine principle [11]

The main advantages of Tesla friction turbines in contrast to conventional turbomachinery are: Low-cost design, easy balancing, low maintenance costs, an excellent scalability of shaft power, the competitiveness in small scale turbomachinery, robustness, capability regarding operating fluids (viscous or non-Newtonian fluids), the strong belief in the possibility to handle droplets, and eventually even abrasive particles [12–14], the self-cleaning nature due to centrifugal forces [15–21]. There is also considerable evidence that Tesla turbomachinery can be quieter in operation, while producing nearly white noise sound signature, compared to conventional turbomachinery [12, 14]. Another advantage might be the competitive efficiency in comparison with miniaturised, conventional turbines, which usually provide very low efficiencies at small shaft power scales [10, 22].

However, Tesla turbomachinery will never meet conventional turbines as equals in large power scales, due to the design-related disadvantages of the energy conversion process. Despite these limitations, the Tesla turbine has the ability to find its existence in small-scale turbomachinery applications [11].

1.3 Previous investigations about the Tesla turbine

The Serbian inventor, engineer, and physicist Nikola Tesla (1856-1943) is best known for his outstanding contributions in experiments with alternating currents and the transmission of electrical power [23]. In addition to that, he is the inventor of the Tesla pump [24] and the Tesla turbine [2] (cf. Fig. 1.2). He designed, built, and extensively tested the so-called friction, blade-less or Tesla turbine in the beginning of the 20th century. Due to technical issues and small efficiencies, he was not able to get his product ready for the market.

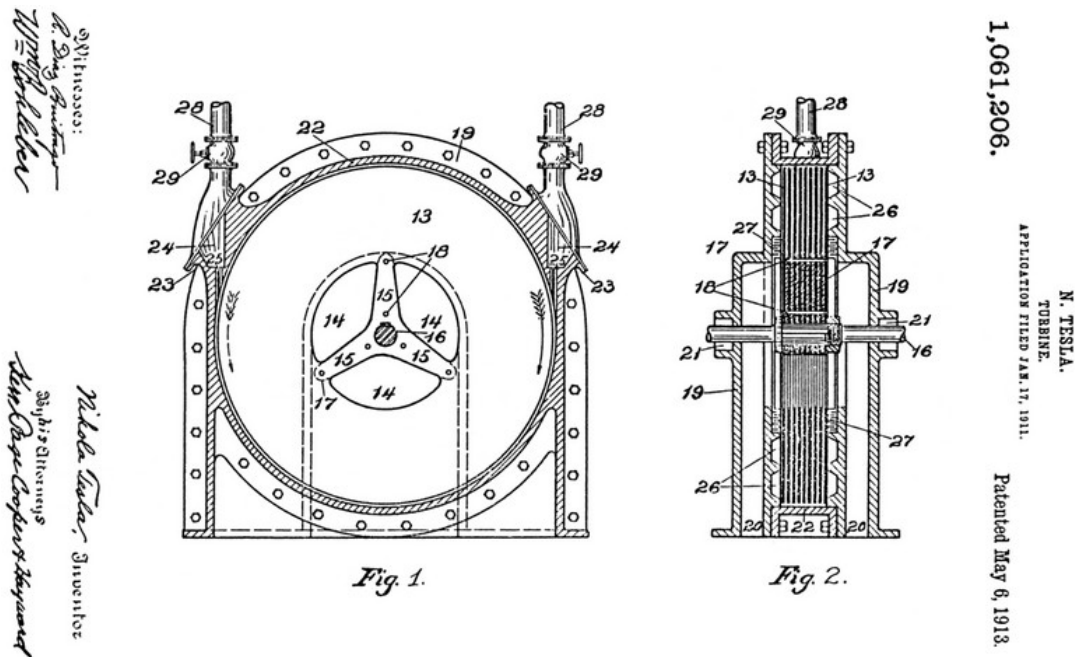


Figure 1.2: Original disk turbine designed by Nikola Tesla [2]

Rice [12, 14] summarised most of Tesla turbomachinery activities from the invention until 1991. Furthermore, Ladino [25] expanded Rice's review in 2004. Research is still ongoing. Therefore, and in the interest of completeness, these summaries are reported and updated in this chapter.

According to Rice [12, 14], the invention was first discussed in the semi-technical press [26–31]. There was only little activity in research until the 1950s, when the Tesla turbine revival started. From that time on, research covers a wide spectrum from theoretical modelling, experimental investigations to recently modern CFD methods.

In general, a distinction of the investigations may be drawn between the three main parts of a friction turbine itself:

- nozzle flow and delivery
- rotor throughflow

- rotor outflow.

Few publications about nozzle design and efficiency are available. Most of the theoretical investigations are focusing on the isolated rotor flow. Experiments mainly cover investigations about the entire turbine concerning performance and efficiency. In the 1960s and 1970s, experimental studies about the rotor flow were carried out. Furthermore, they were conducted using measurement techniques with limited capabilities for that specific problem. Moreover, unsuitable rotor geometries for turbine applications with large inter-disk spacings were studied by researcher, such as Nendl [32]. Few CFD investigations regard the entire turbine, consisting of the flow through the nozzles, the rotor flow, and the rotor outflow, such as in [33, 34]. Other publications, like [10, 35, 36] only consider parts of the turbine. In particular, the rotor outflow is not yet fully investigated. However, only steady state CFD calculations were performed up to now.

It is difficult to categorise all previous investigations about Tesla turbomachinery, as analytical approaches, CFD methods, and experiments are collectively used to compare the results of the different approaches. However, for the sake of clarity, previous investigations are divided into these three major categories depending on where the individual focus is set. They are summarised and listed in a chronological manner as much as possible. Important and specific topics are described in separate chapters.

1.3.1 Theoretical rotor flow models

In general, theoretical flow modelling provides the operating characteristics (torque, shaft power, efficiency) of Tesla turbines. Highest isentropic rotor efficiencies are achieved, if the flow rate is approaching zero, as analysed in [12, 14].

Theoretical flow studies on the following topics of radial, blade-less turbines are available:

- incompressible, laminar, and turbulent rotor flows
- compressible, laminar, and turbulent rotor flows
- influences of disk roughness
- multi-phase rotor flows
- heat transfer in rotor
- stability analyses of the flow field.

Incompressible and compressible rotor flow

There are several attempts in analytical rotor flow modelling. Amongst all of the existing mathematical procedures, the most important ones are:

- bulk parameter analysis
- finite difference solutions
- integral methods
- truncated series substitution methods.

Beginning in the 1950s, the investigations mainly considered theoretical rotor flow modelling in comparison with simple performance measurements, as highlighted in [12, 14]. The references [37–48] are representative for Tesla turbine investigations during that time [12, 14].

First attempts of mathematical flow modelling was the bulk-parameter analysis using an empirical friction factor for each turbine and operational point which represents the wall shear stress. This concept is applied in [31, 38, 39, 44, 46, 48]. Regardless of whether the flow is laminar or turbulent, this concept leads to ordinary differential equations and an initial value problem. This can be solved numerically with correct boundary conditions. According to [12, 14], the usability of this method is limited by the inadequacy of the friction factor concept. Furthermore, it is pointed out that the mathematical flow modelling can be improved for laminar and mainly incompressible flows by simplifying partial differential equations to a pseudo-parabolic form. The equations are solvable with appropriate boundary and inlet conditions using truncated series substitution with accuracy limitations, reported in [49–52]. The finite-differences method can also be applied to obtain a solution, as reported in [53, 54].

In the 1960s, the velocity distribution of the inter-disk spacing of a Tesla pump for radial outward flow was calculated [53]. The Navier-Stokes-Equations (NSE) for incompressible, laminar flow were simplified and linearised to obtain a closed solution. Furthermore, it was shown that the shape of the velocity profiles only depend on the so-called Pohlhausen parameter

$$P_{\text{Ph}} = s \cdot \sqrt{\frac{\omega}{\nu}}. \quad (1.1)$$

It describes the ratio of inter-disk spacing to the laminar boundary layer thickness δ of a single, rotating disk. The boundary layer thickness δ is independent of the radius.

$$\delta \sim \sqrt{\frac{\nu}{\omega}} \quad (1.2)$$

Optimum efficiency was found for $P_{\text{Ph}} = \pi/2$. The profiles showed deflections at values of $P_{\text{Ph}} > 2$, where the flow in the centre of the disks is beginning not to

participate the pumping process any more. However, these investigations focus on Tesla pumps and provide guidelines for an optimum inter-disk spacing. A theoretical Tesla pump design and an experimental validation of the theoretical study [53] was performed by [55]. In the discussion of the publication [46], it is stated that the basic approach of their Tesla pump analysis should equally be suitable for the turbine case.

A theoretical model for the incompressible, laminar, steady rotor flow of Tesla turbines is outlined in [45, 47]. The differential form of the momentum equations was applied. Compared to the full set of Navier-Stokes-Equations, the momentum equations neglect gravitational and inertial forces, the axial velocity, and all derivatives of the tangential coordinate φ . He found a partial closed-form solution for the incompressible, laminar, tangential momentum equation of the bulk flow. In order to calculate performance data from that, parabolic velocity profiles were assumed and scaled with the bulk velocities for the laminar flow field. Results for turbulent flow were achieved by changing the velocity distribution.

Laminar and incompressible flow between parallel, co-rotating disks was modelled in [56]. However, in [57] it is mentioned that all inertia terms are neglected in [56]. An approximate solution with partial consideration of inertial forces for the same problem is presented in [58]. In order to retain all inertia terms in the equations of motion, the Slezkin-Targ method [59], which uses an integral approach, is applied in [57]. This method leads to an analytical solution of pressure and velocity distributions of a simplified set of the Navier-Stokes-Equations in a cylindrical coordinate system. In a first approximation, the radial velocity profile between the disks was assumed to be parabolic. Nevertheless, the solution was not compared to experimental results and remains unvalidated.

The incompressible flow between two co-rotating disks was investigated and reported in [60]. As a result, an approximate solution to the problem was applied, using iterative methods. The usability of the results in terms of Tesla turbines is limited, due to the consideration of radial outward flow.

For turbulent flow calculations, the momentum integral equation methods were applied in [61]. These ordinary differential equations are based on assumptions of velocity distribution across the gap. The quality of the results relies fundamentally on that hypothesis, which is not yet validated.

A solution for the potential flow of an incompressible fluid between two circular disks is outlined in [62]. The radial and tangential bulk velocity across the rotor radius and the streamlines for different cases were published. The authors suggested that the solution applies for rotating disks, because of the lack of momentum exchange between fluid and walls for potential flow. The need for a potential flow solution in terms of friction turbines may be doubted.

An integral method for the incompressible, laminar flow between two co-rotating disks is presented in [63], which was also used by previous researchers. A reduced computation time enabled the calculation of a large number of flow cases. They were validated by theoretical results from earlier investigations provided in [53, 54] and

by experimental results reported in [64]. In [65], the method was further improved to obtain a lower computation time and the capability to handle uniform inlet profiles.

A few years later, the turbine calculation program, published in [63], was adapted in [66, 67] to use the Reynolds number, the tangential, and the radial bulk velocity (modified to a volume flow rate) as an input parameters. The resulting performance maps showed the quantitative dependency of shaft power, efficiency and total pressure on turbine geometry, revolution speed, nozzle inlet angle, pressure drop, and fluid properties for a huge number of dimensionless exit radii. Hence, data for the design and performance of a Tesla turbine was provided. Rotor losses were not considered in this investigation, but summarised for the first time. According to [66, 67], shaft power is lowered by the nozzle efficiency, the nozzle-rotor interference, the rotor-to-housing disk-friction (cf. [68]), the bearing, and the seal friction, as well as the exhaust passage pressure change.

In the mid 1970s and early 1980s laminar, compressible rotor flows in friction turbine rotors were theoretically studied in [69–72].

The solution of the three-dimensional, compressible, laminar flow between two co-rotating disks for full peripheral admission was computed, giving an integral solution for the flow field, as outlined in [69]. The continuity equation and the momentum equations were simplified and normalised. The method described in [63] was used to solve the equations. The numerical solution scheme started with the Runge-Kutta method. After an adequate number of initial values, the Adam-Bashforth predictor-corrector method continued, due to stability reasons. The technique contained an eighth-order polynomial fit of the velocity distribution in radial direction at each incremental step, satisfying the boundary conditions. It is noticed in [73] that compressibility effects generally improve some of the performance parameters, but to the disadvantage of rotor efficiency. These insights are confirmed in [70].

In the early 1980s, the solutions published in [52] were expressed as a power series of one dimensionless parameter only. This is reported in [74]. The single parameter is proportional to the radial velocity at a given radius, averaged over the axial gap. Compared to the solutions, which are presented in [52], this approach is useful for the analysis of the flow under a wider range of parameters. In [74], the calculated velocity components in the centre of the disks are compared to those, which were experimentally determined in [75]. The author claimed that the results show excellent agreement. Due to the unavailability of the publication [75] and the fact that neither the measurement method, nor the gap width, which was used in [75] is reported in [74], no further assessment is possible. Measurements of the wall pressure distribution along the radius were introduced in [64]. The rotor diameters were 203.2 mm and 25.4 mm. The gap width was 1.524 mm. Towards the outlet of the rotor, the calculated pressure distributions, reported in [74], deviate more and more from the experimental data set, used in [64].

The steady, incompressible, laminar Navier-Stokes-Equation, and the continuity equation of the radial inward flow in the slot of two co-rotating disks are solved

in [76] by applying the pressure correction method, as outlined in [77]. This method saved computation time and was therefore advantageous during that time.

In 1989, the laminar flow in a Tesla rotor was studied, as it is outlined in [78]. A method comparable to the investigations reported in [53] was used. In order to handle the governing equations, several simplifications were made. The assumptions were: Incompressibility, parabolic velocity profiles, zero axial flow velocity, neglected gravitation effects. Coriolis, centrifugal, and viscous effects were considered. The analysis was accomplished by solving the differential equations simultaneously with a 5th order Runge-Kutta method. Geometry, angular velocity, and mass flow were used as input parameters. For the determination of the boundary conditions, the relative tangential velocity at the outlet was set to zero. Starting at the inner radius, the equations were solved and the computed velocities were used as boundary conditions for the actual calculation. It was reported that efficiencies above 80 % are possible. However, it is difficult to gain general knowledge about Tesla turbines, because he only examined a few cases. In [79], the author pointed out that while this approach generates solutions, the indicated parametric variations of performance can be difficult to interpret, because of the backward integration scheme. Unfortunately, a validation of the theoretical results is missing, as no experimental results are given.

In 2006, a simplified technique to estimate the total number of required disks for certain flow conditions was introduced. The investigations are outlined in [80]. The method was based on the calculation of the boundary layer thickness of laminar and turbulent flow regimes. The use of the results is limited, due to the large simplifications. Furthermore, no experimental or numerical verifications are performed.

In 2008, Deam et al. [16] analysed the flow through a Tesla rotor from an incompressible one-dimensional model. The aim of that examination was to predict the maximum theoretical efficiency. They considered rotors with diameters of less than 7 mm. A maximum efficiency of about 40 % was concluded. Romanin [6] emphasised that the results rely on the assumption that the inlet and outlet velocities of the model are equal. If the overall exit velocity was lower compared to the inlet, a higher theoretical efficiency limit might have been possible. In addition to that, it is not clear, if a linear one-dimensional model represents rotating and squeezing flows sufficiently accurate.

A so-called one-dimensional model for the incompressible, laminar flow in a Tesla rotor was proposed in [81]. The flow model is a slightly modified version of the one described in [46]. To be more accurate, it differs in the derivation of the system of equations and in how the frictional forces are modelled. The equations are averaged over the disk spacing. Thereby, coefficients were introduced, which allow the calibration of the governing equations by three-dimensional CFD calculations using ANSYS CFX. This procedure generally improves the accuracy of the flow model. It was assumed that analytical solutions are possible with the inter-disk averaging approach. Despite accuracy improvements, by calibrating theoretical model constants using laminar CFD, no validation of the results are given.

A quasi-one-dimensional, incompressible, laminar flow model with an analytical treatment including closed-form solutions was presented in [79]. Although the flow was taken to be two-dimensional, he neglected viscous transport in radial and axial directions. The viscous drag in tangential direction, which is responsible for torque generation, was modelled as a body force using a friction factor approach. Radial pressure gradients were fully neglected, because for choked flow almost the entire pressure drop occurs in the nozzle, as outlined by [46]. The model predictions agree well with the experimental results reported in [46], although the tangential inlet velocity from the experiment was unknown. Finally, it was concluded that efficiencies above 75 % were possible, if the rotor design and the operating conditions are optimised.

The idealised one- and two-dimensional theoretical models, described in [17, 79], were further examined in [82]. According to the author, the theoretical model results agreed well with Rice's measurements, outlined in [46]. Furthermore, it allows the parametric exploration of performance and efficiency. Finally, a CFD approach was suggested, which would give more complex insights of details like the three-dimensional inlet and outlet effects or the influences of housing and rotor.

The flow model, reported in [79] was extended to simulate a higher surface disk roughness, as outlined in [17]. An integral solution for the incompressible, laminar, and rotating flow between the disks was developed. This led to a perturbation series solution that includes momentum and viscous effects. The resulting lowest order terms were solved analytically. Higher order terms were determined numerically. The governing equations were simplified and integrated across the gap width, assuming a parabolic velocity profile. Furthermore, surface roughness increases shear stress and shaft power. It was modelled by changing the shape of the velocity profile across the gap according to the Poiseuille number Po . An enhancement number was introduced, which quantified the resulting shear stress. The analysis was based on the assumption that enhancement of rotor drag generally enhances efficiency. Body forces, entrance, and exit effects were neglected. It is worth mentioning that the nozzle flow was assumed to be compressible in contrast to the incompressible rotor flow. Unfortunately, the model was only verified for a low efficiency range, due to the limited experimental data set. Nevertheless, the model offers the exploration of parametric trends of the machine parameters.

Despite the fact that the friction factor concept is inadequate [12, 14], a preliminary design study of Tesla turbines applying this approach was published. It is described in [83]. A turbine design was proposed, which was based on the governing equations introduced in [46]. A MATLAB code solved the ordinary differential equations (ODEs). The dimensionless tangential velocity and the pressure drop across the rotor was computed for an assumed radius ratio. Several combinations of turbine parameters were solved and an optimum was defined [46]. The remaining dimensional parameters from geometry and flow conditions were computed by the selection of the outer diameter and the rotational speed. Shaft power, torque, and efficiency were determined by the choice of the friction factor. Efficiencies showed values close to

80%. Additionally, it was discovered that Tesla turbines require high levels of inlet pressure. As mentioned in [12, 14], the usefulness of such techniques is restricted, due to the insufficiency of the friction factor method.

A mathematical theory for the rotor flow field of a blade-less radial turbine is outlined in [15]. However, it is similar to the investigations of [17, 79, 82]. The flow model predicts torque, shaft power, and efficiency. Also, closed-form analytical relations were obtained. Navier-Stokes-Equations in cylindrical coordinates were simplified by a systematic order of magnitude analysis. The partial differential equations (PDEs) were converted to ODEs under the following key assumptions: Newtonian fluid, steady, incompressible, laminar, and axis-symmetric flow, fully-developed, parabolic velocity profiles, axial velocity, and body forces negligible. The governing equations rewritten into a dimensionless form were integrated simultaneously by numerical means. Ideal performance and also losses were computed by a linear function suggested in [33]. However, it was not fully revealed, how the authors determined the constant in detail. The theoretical results were compared to experimental data measured in [33]. Considering the noticeable uncertainty of the experimental results in combination with the modelled loss mechanism, the theoretical results were reasonable, as summarised in [15]. In addition to that, in [15] it was proposed to artificially change the surface roughness to enhance the disk drag and shaft power in future applications. However, this was first modelled and partially, experimentally validated in [17].

In [84], a simple mathematical theory for the description of the three-dimensional, laminar, and incompressible flow field within a friction turbine was described. The calculations were based on the parabolic velocity profile assumption in radial and tangential direction. Torque and shaft power was computed, analytical solutions were formulated, and the influences of centrifugal, Coriolis, inertial, and viscous forces were derived. The flow model applied a correlation for the overall losses given in [33], which was determined experimentally. Furthermore, fluid path lines were determined through numerical solutions.

Scaling properties and loss mechanisms of Tesla turbines were addressed in [20]. This investigation provides design guidelines for hydro micro Tesla turbines with rotor diameters below 60 mm. The rotor model was based on the integral perturbation model proposed in [17]. The lowered turbine performance was calculated by adding loss models. Nozzle path and disk friction were the prevailing losses for laminar flows. The impact of volume losses, exit kinetic energy losses, and bearing losses magnify at high flow speeds and high revolution speeds. The following turbine losses were considered in the loss models:

- head loss (function of mass flow)
 - frictional losses in the nozzle
 - rotor losses
 - pressure drop across the rotor (depending on velocity profiles)

- losses due to turbulence near rotor outlet
- kinetic energy losses at the outlet
- volume leakage
 - leakage losses
 - bearing losses
- shaft power loss contributors
 - disk friction losses between
 - enclosure and end disk
 - cylindrical enclosure walls and rotor tips
- impact losses at rotor inlet edge.

According to [20], the turbine losses are strongly depending on the performance parameters: Outer rotor radius, radius ratio, disk spacing, disk thickness, number of disks, tip clearance, clearance between rotor and housing, and nozzle geometry (width and height). Therefore, different optimum operating ranges were derived for micro and macro turbines. The efficiency prediction agreed well with experimental results provided in [18, 19]. It was concluded that efficiencies can be approaching 40 % for small-scale rotors.

In the study, reported in [10] the flow model from [79] was improved by the consideration of the pressure drop across the rotor radius. It was found that isentropic efficiency is a function of the rotor tip Mach number, the dimensionless tangential velocity difference, the Reynolds number, the radius ratio, the specific heat ratio, and the pressure ratio across the rotor. Numerical simulations (CFD) were in good agreement with the model.

The fluid dynamics of work transfer in the gap of a Tesla turbine was theoretically and computationally analysed in [36]. The integral work transfer and the spatial development of the work transfer was investigated. The Reynolds transport theorem was applied. Furthermore, it was demonstrated that mass flow-averaged tangential velocities were needed to determine the change of angular momentum correctly. The work equivalence principle of a Tesla turbine (net torque produced by shear stress of disk surfaces equals the change in angular momentum) in a rotating reference frame was presented. An analytical method without assuming specific velocity distributions demonstrated the principle of work transfer. A computational approach revealed that torque is created by the shear forces acting on the disk and the Coriolis force in the relative frame of reference. The non-dimensional quantity named torque potential fraction was introduced. It describes the converted fraction of the inlet torque potential at the rotor outlet at a certain operating point. In general, it was found that the torque potential fraction is increasing with decreasing inter-disk spacing.

More recently, similarity and scaling laws were derived in [21]. A systematic dimensional analysis of the governing equations for laminar, incompressible flow through a Tesla rotor was achieved by applying the Buckingham Pi theorem. The following non-dimensional numbers were obtained: Radius ratio, aspect ratio, tangential inlet speed ratio, inlet angle, power coefficient, pressure drop coefficient, and dynamic similarity number. Thereby, geometric, kinematic, and dynamic similarity were established. The principle of similarity and scaling of Tesla turbines was verified by the use of CFD. Furthermore, the conservation equations were simplified to obtain closed-form analytical solutions for the flow field. However, the “dynamic similarity number” β was first mentioned in 1961 in a slightly different form. In [45, 47] the dimensionless coefficient β was derived. It is basically the inverse of the dynamic similarity number D_s . Equation 1.3 makes this statement more clear

$$\beta = 6 \cdot \frac{r_1 \cdot \nu}{\bar{v}_1 \cdot (2s)^2} = \frac{6}{D_s}. \quad (1.3)$$

Further details about the non-dimensional variable β can be found in the chapters 2.6.2, 2.6.4, 2.6.5, and 2.7.

Multi-phase flows

The 1970s provided also scientific results about multi-phase flow models. The laminar flow of varying quality steam through a Tesla rotor, which would arise in geothermal applications for power generation was examined and reported in [5]. The model includes the mass and momentum conservation equations for vapour and droplet fields. In addition to that, it contains the mass, the momentum, and the energy equation for single droplets, as well as for droplet interaction. The equations were simplified to a system of algebraic equations, which were solved directly. Numerical solutions of the radial outward flow were obtained. For radial inward flow, the solutions only exist for small droplets.

In general, friction turbines are also considered to operate with unfiltered gases containing (abrasive) particles. Therefore, the laminar, compressible, and incompressible flow in such turbines providing solid particles was analysed by [71]. The researchers concluded that particles exceeding the diameter of approximately $4 \mu\text{m}$ do not pass the disks, due to the influence of the centrifugal forces. Beginning at a particle size of $3 \mu\text{m}$, particle trajectories depart clearly from the streamlines of the bulk flow. As discussed in [5, 85], multi-phase solutions for the radial inward flow only exist for a limited range of inlet conditions.

Rotor flows and heat transfer

Early investigations, accomplished by [40, 86] did not offer insights into the thermal relations of heat transfer in Tesla rotors, as remarked in [72]. Around 1980, the

heat transfer in Tesla turbines was theoretically examined in [87, 88]. The mathematical formulation of the heat transfer was given in [89, 90]. Later, the influences of the frictional heat as a consequence the changes of viscosity in the flow on the radial pressure distribution, on the operating characteristics, and on the efficiency were determined in [88]. The incompressible Navier-Stokes-Equations, the continuity equation, and the energy equation were applied together with an empirical law for the dynamic viscosity. The resulting non-linear, partial differential equations were solved using an implicit, numerical solution of the finite difference equations. The numerical solutions yielded the result that the operating conditions for a thermo-viscous connection between flow and temperature field show only small changes compared to a case with constant viscosity [88].

In [90], the concept of utilising the blade-less turbine as a heat exchanger was discussed. The idea was picked up in [87]. It was theoretically investigated, how far the dissipation, caused by the energy conversion process of the incompressible, laminar, viscous flow inside the rotor, influences the increase of temperature. Three cases of heat transfer between the disks were inspected: One rotor wall adiabatic the other one diathermic, both rotor walls adiabatic and both rotor walls diathermic. The continuity equation, the Navier-Stokes-Equations, and the energy equation were simplified under the assumptions of constant density, dynamic viscosity, specific heat capacity, and thermal conductivity. The results were based on an implicit finite difference method and an integral method. The heat transfer through the disks works best for low Reynolds and Prandtl numbers. In highly viscous fluids the temperature may increase dramatically and could completely change the flow field, as well as the turbine efficiency.

Flow stability analyses

The hydrodynamic stability of the rapidly rotating interplate flow between the plates of a separator for emulsions was investigated in [56]. A stability criterion was suggested. Although often cited, the geometrical configuration, as well as the flow direction differs clearly from the Tesla turbine set-up.

The linear stability problem for the steady shear flow between two parallel, co-rotating planes, driven by a pressure difference, were studied in [91–93]. Ideal, unperturbed inflow conditions were assumed in all of these investigations. The energy stability limit of these flows were computed in [94].

It was found in [91] that the critical Reynolds number depends on the Taylor number, which describes the ratio between Coriolis and viscous forces. It is defined as

$$Ta = \frac{\omega \cdot (2s)^2}{4\nu}. \quad (1.4)$$

Furthermore, it was concluded that the instability mechanism for very small Taylor numbers is the same as the one for the plane Poiseuille flow. A critical Reynolds number, which depends on the Taylor number Ta was suggested. An asymptotic

estimate of the critical Reynolds number Re_{crit} as a function of the Taylor number for large values of Ta was also presented. The instability mechanism arises from the Coriolis forces.

The influence of the Taylor number Ta on the critical Reynolds number Re_{crit} for the parameter range $0 \leq Ta \leq 1$ was studied in [92]. Direct numerical procedures were used to solve the stability problem. For values of $0 < Ta < 0.4$ the most unstable mode is called type I. This viscosity driven instability mode vanishes at $Ta \approx 0.35$. Another instability mode was detected for Taylor numbers $Ta \rightarrow 0$. The so-called type II. instability mode is a result of the Coriolis effect onto the flow. The type II. instability reveals the critical Reynolds numbers depending on Taylor numbers between 0.06 and 1.

The outcome of the work of [91, 92] was extended into the parameter range $1 < Ta < 100$ by [93]. The instability mode type II. discovered in [92] was confirmed. The theoretical results agree qualitatively well with experimental results presented in [95–97] for values of $1.75 < Ta < 3$. The disagreement between theory and experiment for Taylor numbers below 1.75 was attributed to inlet effects of the experimental test facilities.

The motion of a pressure driven flow through the gap of two co-rotating disks with constant angular velocity was theoretically analysed by [98]. The investigation was an attempt to clarify the influence of small periodic pressure changes of the inflow conditions on the rotor flow field. Therefore, the equations of unsteady motion of an incompressible, viscous flow were solved. It was noticed that the resulting velocity field is a superposition of damped oscillations with a frequency equal to twice of the angular velocity of the disks and forced oscillations with a frequency equal to the frequency of the oscillations of the pressure field [98]. Even for small, harmonic pressure oscillations, the fluctuation of the radial velocity component reaches values of the same order of magnitude as the average velocity of the bulk flow.

1.3.2 Experimental investigations

Since Tesla's invention, various Tesla turbine experiments were performed concerning:

- performance and efficiency tests
 - incompressible and laminar or turbulent rotor flows
 - compressible and laminar or turbulent rotor flows
- influence of disk roughness
- nozzle flow delivery
- rotor flow field investigations.

Performance and efficiency measurements

Most of the investigations in literature focused on black box performance map experiments of the entire turbine comparing the results to those from theoretical models of the rotor flow. The following references contain published information concerning experimental data in blade-less turbines [4, 26–30, 37–39, 41, 44, 46, 48, 99, 100]. However, the most important investigations are described in this chapter.

Six different air driven turbines were built and extensively tested, as outlined in [46]. The results were compared to the friction factor model for incompressible flows. The first turbine was designed from the descriptions of Nikola Tesla. The outer rotor diameter was 228.6 mm with a gap width of 1.59 mm. The rotor consisted of nine disks and was further modified by decreasing the gap width. The flow model revealed that design and flow conditions of the two turbines were not even close to the optimum performance or efficiency. Therefore, four other turbines were designed. The best turbine consisted of 24 disks with an outer rotor diameter of 203.2 mm and a gap width of 0.51 mm. The nozzle angle was about 20° from the tangent. The efficiency decreased with rising flow rate in all cases. Tesla turbine losses were addressed. They are: Nozzle losses, energy dissipation at the inlet edges and at the two outer disks, exhaust losses due to uncontrolled diffusion, bearing and sealing losses, and losses due to partial admission. It was stated that the performance of the turbines can be predicted approximately, if the losses were estimated by methods available in the engineering literature. A detailed description of the measurement method is missing. However, recordings of pressures and temperatures at the inlet and outlet of the turbine were reported. In the discussion of [46], Hasinger and Kehrt commented the theoretical and experimental results. They pointed out that their Tesla pump investigations, outlined in [55] clearly indicate that a closer disk spacing is required.

A test rig for the performance measurements of a Tesla turbine using compressed air as the working fluid was built and tested, as outlined in [45, 47]. For shaft power measurements, the rotor was directly coupled to a dynamometer. Different disk spacings from 0.66 mm to 12.7 mm and different inlet pressures from 1.70 bar to 3.77 bar exhausting to the atmosphere were tested. Compared with his theoretical predictions, the qualitative agreement was acceptable, the quantitative agreement instead was less than satisfactory [45, 47]. However, disk vibration and significant losses in the rotor sealing were reported. The rotor, which was used for the measurements is illustrated in Fig. 1.3.

An experimental and also numerical study to determine the performance characteristic of Tesla turbines was carried out and summarised in [33]. The load on the turbine was applied by an eddy current dynamometer, which was placed in the plenum chamber. Torque and shaft power without bearing losses were measured by a strain gauge and a rev counter. The rig was designed such that the entire mechanical power (from the dynamometer) including the losses from the bearings dissipate into the flow at the inlet of the turbine. The measurements were recorded and aver-

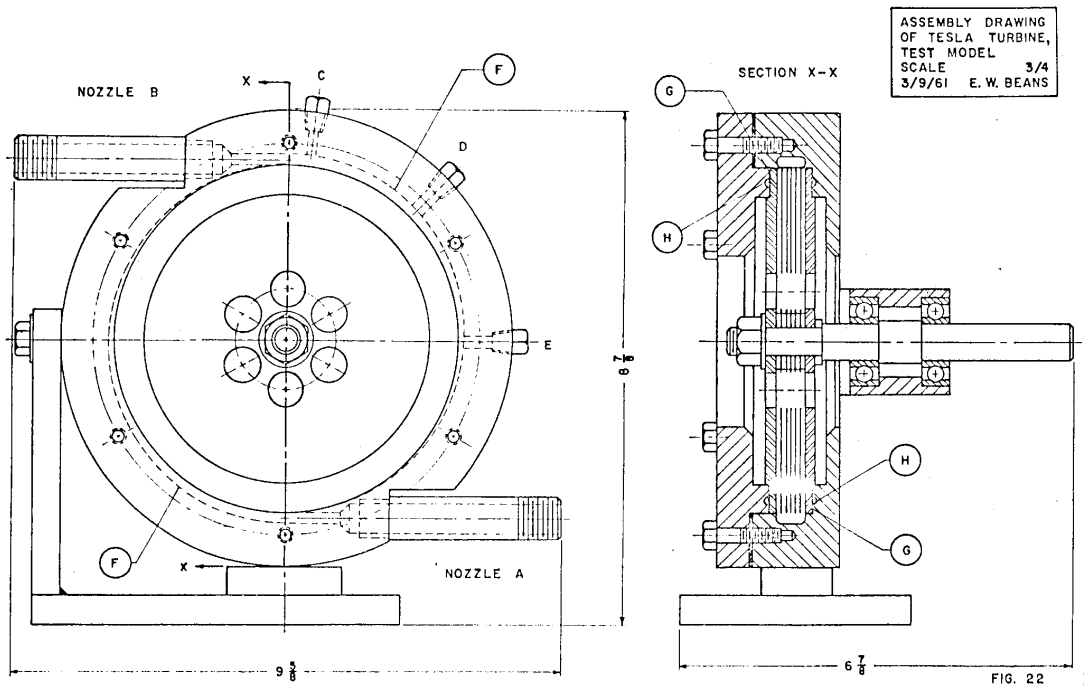


Figure 1.3: Technical illustration of Beans' test rig of a Tesla turbine [45]

aged over ten minutes, after a steady state was reached. The enthalpy drop across the turbine and therefore the total power with consideration of bearing losses was calculated from temperature measurements at the inlet and outlet of the turbine. The difference between those two power measurements is the power loss created by the bearings. Low turbine efficiency as reported by previous investigators were experimentally confirmed. Furthermore, the main loss mechanisms were identified. Bearing friction, viscous losses at the rotor end walls, and dissipative losses in the plenum chamber lowered the theoretical peak efficiency significantly. The results indicated that the losses were about 90 % of the measured load. Oscillations of torque, flow rate, rev speed, and pressure drops were reported for higher pressure drops. The reason for that remained unknown, but were assumed to be originated by flow instabilities.

Results from the experiments in a test rig for systematic performance and efficiency studies are outlined in [101]. Measurements of temperatures, static, and total pressures were carried out at various locations, such as nozzle, inlet, housing, and outlet. A simple method for measuring the torque and the shaft power was presented. The angular acceleration method for torque measurements under unsteady states overcame the problems of straightforward measurements. Additionally, different types of nozzles were tested. The results are in qualitative agreement with those, reported in [14]. However, they indicated that the losses in the nozzle are large and would therefore improve the overall turbine efficiency, if reduced. The exhaust flow was deemed to be complex and lead to problems in the determination of total pressure and temperature at that location.

Parametric trends on turbine efficiency were studied in [102] using the theoretical flow model proposed by [79] in combination with performance testing. A purchased air-driven Tesla turbine with an outer diameter of 73 mm and an inter-disk spacing of 1.2 mm consisting of ten disks was tested. It was equipped with a flow meter, a tachometer, and several temperature and pressure sensors at the inlet, between nozzle and rotor and at the outlet. The turbine shaft was connected to a three-phase generator with three resistors in a delta configuration. Delivered power was determined by measuring the voltage drop across the resistors. The resistance was adjustable to vary the load. Losses were measured by analysing the deceleration rate of the rotor without through-flow. The agreement between theory and experiment was good. However, the model predicted a decrease in efficiency with increasing flow rate, while the tests showed opposite trends. Additionally, an optimised rotor with 0.4 mm gap width and 18 disks was built and tested. Efficiency increased, but not as much as the model predicted. However, incompressible model predictions covered a much wider range of rotor tip Mach numbers compared to the experimental data.

A micro Tesla turbine was designed, built and tested, as reported in [18]. Modern rapid prototype methods were used for manufacturing. Stainless steel rotors with diameters of 10 mm and 20 mm were fabricated. Different versions with variations in the rotor outlet region were designed. Rotors with different numbers of disks, gap widths, and radius ratios were built. However, it was nearly impossible to hit stable operating points, because the small turbines were mechanically unloaded. Therefore, torque was computed from video data containing the acceleration and deceleration of the rotor under perfusion. Efficiency varied around 20 % using a single nozzle. Increasing the number of nozzles in order to create a more homogeneous circumferential mass flow distribution was not improving the efficiency. Maximum efficiency was achieved at lower flow rates. Smaller outlet radii, as well as higher gap widths lowered efficiency. Highest shaft power was obtained for tangential nozzle exit angle. Despite typical and well-known influences of turbine parameters, it was unclear if a tangential nozzle exit angle really leads to a maximum in shaft power. The resulting inflow angle at the outer radius was crucial for maximum performance. However, the measurements remain unvalidated.

A comparison of theoretical, numerical, and experimental results of a sub-watt scale micro Tesla turbine was presented in [19]. Water was used as a working fluid. The experimental data was obtained, as outlined in [18]. The theoretical efficiency equation derived in [17] was modified for incompressible rotor flows in this investigation. Results from steady, laminar CFD using ANSYS Fluent 13 exposed difficulties in predicting the inlet velocity. Two approaches for solving this problem were discussed. Several nozzles and rotor configurations for different flow rates were analysed. The overall experimental uncertainty was estimated to be about 12 %. The results showed that several predicted performance trends matched the experimental results. Despite certain differences and the fact that loss mechanisms were not considered, the agreement between theory, CFD, and experiments were deemed to be satisfactory. However, performance measurements were very difficult to obtain correctly in such small scales.

The experimental results from a flexible test rig for the performance and efficiency analysis was presented in [103]. Water was used as the working fluid. Torque measurements were performed using a Prony break. The experimental results showed a significant dependency of surface roughness and disk spacing on performance and efficiency. It showed typical and well known effects of geometrical influences on turbine performance. The examinations on disk roughness showed an increase of about 5 % in efficiency. The study confirmed the theoretical predictions presented in [17]. Nevertheless, it is still desirable to establish a more systematic and more comprehensive experimental analysis about the effects of disk roughness.

The well-known Tesla rotor geometry was changed during the investigations in [104]. The idea behind the modification was the use of the combination of boundary layer effect and blades at the outer radius - similar to an impulse turbine. The new rotor was built, tested, and experimentally proven to create more power compared to a conventional rotor design. However, blades at the outer radius required space. Therefore, the clearance between rotor and nozzles increased. However, this should generally be avoided, as impact losses occur, when the flow entered the gap. This was also reported in [20]. The jet of nozzles further decayed with increasing clearance. As the rotor inlet velocity is a sensitive parameter on turbine performance, the results should be investigated more accurately. On the other hand, if the effect of the blades is dominating the frictional rotor forces without increasing costs too dramatically, a pure impulse turbine could be an alternative to a Tesla turbine.

The performance of rainwater and air driven Tesla turbines were lately investigated in a parametric analysis, outlined in [105]. Disk diameter, number of disks, flow rates, and gap widths were varied and examined regarding turbine performance. CFD methods were used in order to gain insight into the rotor aerodynamics. The turbine was connected to a DC motor, which produced electrical power. The load of the turbine was set by adjusting a resistor. Performance tests were conducted by closed-loop (with load resistor) and also by open-loop (without load resistor) voltage measurements. It was found that the turbine worked more efficiently with water than with air, due to the increase of the kinematic viscosity.

Recently, a single stage ORC system consisting of evaporator, Tesla turbine, condenser, feed water pump, and an three-phase generator was developed. The approach and the results are summarised in [3]. Saturated water steam was used as the working fluid. Mass flow rate, temperatures, pressures, and revolution speed were recorded. Unfortunately, there was no detailed description about the measurements available. A modified and a typical Tesla rotor were examined. The modifications included blade deflection profiles, a conical outlet, and a profiled shaft. The authors observed an increase of shaft power and efficiency compared to the conventional blade-less rotor. Moreover, CFD investigations were conducted.

Nozzle flows

In [14], it is stated that rotor efficiency of friction turbines can be very high. Unfortunately, it was difficult to design efficient nozzles. The nozzle flows of Tesla turbines was studied in [106]. It was shown that the nozzle delivery and the inlet of the co-rotating disks were responsible for the large losses in Tesla turbines. They introduced a plenum chamber inlet, which significantly reduced the nozzle losses and considerably improved the uniformity of the jet. This was investigated by Pitot tube experiments in comparison with CFD. Differences between theoretical rotor flow investigations and performance map experiments of Tesla turbines with traditional and therefore inefficient nozzle designs might be partially answered here.

Flow field investigations

Moreover, flow field investigations were performed to determine the flow regime. A precise performance map can only be established, if the wall shear stress is determined correctly.

The velocity profiles in the gap between a single rotating and a stationary disk with radial outward flow were determined first by [68]. A modified Pitot tube was used for that purpose. In [50, 107], hot-wire and radial pressure distribution measurements were accomplished in a similar configuration. In [108] a single gap Tesla pump was built for the measurement of the velocity distribution between the disks by means of hot-wire anemometry. Furthermore, an experimental validation of the theoretical pump analysis, outlined in [53], was given in [109]. The radial velocity profiles in the flow passage of a Tesla rotor for radial inward flow with zero angular velocity were measured and reported in [110].

The velocity profiles between parallel and co-rotating disks with radial outward flow applying two-channel hot-wire probes were analysed in [111]. Unfortunately, no criterion for the laminar-turbulent transition was deduced. The disk spacing was examined between 5.1 mm and 7.6 mm. This is untypically wide for Tesla turbine applications and would produce lowest efficiencies only.

The radial, static pressure distribution of a real Tesla turbine rotor configuration with 69 pressure taps and telemetry were measured and outlined in [64]. In order to create a constant tangential velocity distribution, the flow was delivered by a nozzle ring with 30 discrete nozzles. The experimental results from the radial pressure difference agreed well with the predictions from the laminar flow model.

In [97], Rice's radial pressure distribution experiments were modified and repeated. They were combined with the flow visualisation by means of injected dye over a wide range of parameters. The outer diameter of the rotor was 406.4 mm and the inter-disk spacing was 1.5 mm. The upper disk was transparent and made of Lexan polycarbonate. It was mounted on a massive steel cross bracing. The operating fluid was a water-ethylene glycol mixture for adjusting the kinematic viscosity. More de-

tails about this test facility can be found in [64, 95, 96]. Laminar and turbulent flow conditions were determined from the qualitative visual inspection of the streamlines in the mid-plane of the flow. In order to assist in such an interpretation, the experiments of Osborne Reynolds applying the same visualisation technique, were conducted and presented in [97]. Both cases were compared. According to [97], the results from the theoretical modelling of the laminar flow agreed excellently with the experimental investigations of [64, 95]. However, these experiments are lacking the determination of the laminar and turbulent velocity profiles.

Hot-wire measurements for the determination of the velocity distribution between the disks in a 7 mm gap of a Tesla turbine were performed and mentioned in [32, 112]. The spatial resolution in axial direction was about 0.35 mm. Independently from each other, Nendl [32, 112–114] and Fiebig [115] proposed the visco-geometric number α_ν to characterise the flow regime in a friction turbine.

In [53], the dimensionless rotational speed is expressed in the form of a Reynolds number, which is the so-called Pohlhausen parameter

$$P_{\text{Ph}} = s \cdot \sqrt{\frac{\omega}{\nu}}. \quad (1.5)$$

With the flow rate coefficient φ_B

$$\varphi_B = \frac{v}{\omega \cdot r}, \quad (1.6)$$

the visco-geometric number α_ν was obtained

$$\alpha_\nu \sim P_{\text{Ph}}^2 \cdot \varphi_B \quad \text{or} \quad \alpha_\nu = \frac{v \cdot (2s)^2}{\nu \cdot r}. \quad (1.7)$$

The values of α_ν for the different flow regimes were:

- laminar for $\alpha_\nu < 10$
- in transition for $10 \leq \alpha_\nu < 20$
- turbulent for $\alpha_\nu \geq 20$.

From the rotor flow experiments, it was concluded that the laminar velocity profiles are similar and independent of the dimensionless revolution speed [32]. These observations were confirmed in [11], where laminar CFD simulations were performed. According to [32], the velocity profiles only depend on the visco-geometric number α_ν . In contrast to this information, it is shown in [53, 116] that the shape of the velocity profiles depend on the magnitude of the rotational speed. The results, presented in [112] did not confirm these existing findings. The measurement results reported in [95, 117] on the other hand, definitively did confirm the results shown in [112]. However, the gap was untypically wide for a Tesla turbine. Such a configuration would not produce competitive shaft power. Hence, precise and highly resolved measurements in a small gap configuration are desirable.

A sophisticated experimental analysis was published in 1985. [118] investigated the radial outward flow pattern between two parallel and co-rotating disks. The outer diameter of the rotor was 800 mm. The investigations featured an inter-disk spacing of 5 mm to 15 mm. Air and water was used to investigate the influence of viscosity. In water, flow-visualisation methods of dye injection, hydrogen-bubble generation, and paraffin mist were applied. A camera combined with a deflection mirror enabled a closer look into the gap. The airflow was examined by means of hot-wire anemometry. The results were limited for the development of Tesla turbines, because of the radial outward flow direction. Nevertheless, the description of the experimental approach is still very useful for the development of test rigs for future flow field investigations.

Flow field investigations using more modern measurement techniques, such as PIV were performed by [119] in the 1990s. The laminar flow field within an enclosed cylindrical chamber with one rotating disks was investigated by applying PIV measurements in comparison with CFD. The rotating disk had a diameter of 80 mm. The test rig was adjusted to the geometric configurations and the Reynolds numbers of the previous investigations, reported in [68, 120]. The air flow containing olive oil seeding was illuminated by a laser sheet with a thickness of 0.2 mm. The light sheet was parallel to the disk and was traversable in height. The camera was attached perpendicularly to the disks. A close agreement between PIV and CFD was found. The outcome of the investigation was valuable in terms of the design of the outer rotor disks.

In 2005, the flow between two co-rotating disks was examined by means of PIV [121]. The experimental rig was basically a simplified model of hard-disk drives with acrylic disks. Therefore, relatively wide gap widths from 18.4 mm to 30.6 mm were examined. The use of this analysis is limited for Tesla turbines. Nevertheless, the experimental apparatus is helpful for the development of test rigs for future flow field investigations of Tesla rotors.

LDV and PIV measurements of the unobstructed flow between two co-rotating disks were carried out and reported in [122]. The gap width of the disks in this test rig is 16.9 mm. The typical flow velocities occurring in this experiment were about 1.5 m/s. Flow conditions and also the rotor geometry were far away from typical Tesla turbine configurations. However, it is still worth mentioning that periodic velocity oscillations were reported and examined.

1.3.3 CFD investigations

Around the turn of the millennium, modern CFD methods became more and more commonly used in Tesla turbine investigations. CFD calculations were performed by [3, 19, 21, 36, 81, 105, 106, 119]. Some of these papers were already mentioned in previous chapters, because their focus was on theoretical flow modelling or experiments.

The inter-disk flow through a Tesla turbine using numerical approaches are out-

lined in [123, 124]. In these investigations, the flow was treated as laminar and incompressible. Two radial regions were mentioned, where the shape of the velocity profiles differed from each other. The boundary layer built-up region after the inlet and the (asymptotic) Ekman-Couette region were considered. The Ekman number E_k is defined as the ratio of half of the inter-disk spacing and the boundary layer thickness

$$E_k = \frac{s}{\delta} = \frac{s}{\sqrt{\frac{\nu}{\omega}}}. \quad (1.8)$$

Highest efficiencies were achieved for an Ekman number of 1. Rotor efficiencies of up to 80 % were obtained for small rotor diameters. However, the approach was basically identical with the investigations of [53]. Furthermore, the Pohlhausen parameter P_{Ph} equals the Ekman number E_k (cf. Equations 1.5, 1.8).

Two rotors from literature, where experimental data were available are modelled and analysed in [125]. The first one had an outer diameter of 125 mm, just like the turbine in [37]. The second model was inspired from [126], applying an outer diameter of 254 mm. The examined gap width range was between 0.5 mm and 2.0 mm. One and two nozzles configurations were explored. The algebraic Baldwin Lomax turbulence model was applied. An exhaust pipe was placed at the outlet of the disks. Typical Tesla turbine behaviour was observed. Furthermore, windage losses (rotor partially creates negative torque), kinetic energy losses at the exhaust and interaction between streamlines and fresh nozzle flow were detected from flow visualisation. An optimum gap width of 1 mm was the best compromise between the losses. It was found that more nozzles increased the performance of the turbine.

An extensive literature review, which is mainly based on [12] is summarised in [25, 127]. CFD simulations of the geometry used in the experiments reported in [46] were performed. Some of these cases very slightly modified. Fluent was used to simulate incompressible, laminar, and turbulent flows. The k - ϵ turbulence model with wall treatment was applied in the turbulent cases. As the flow regime was mainly transitional, the results from CFD did not represent the exact flow physics accurate enough. As observed in previous investigations, the simulations showed typical Tesla turbine behaviour. Velocity profiles, efficiencies, pressures, and streamline plots were presented. Ladino observed that the efficiency was strongly effected by the inlet angle and the number of nozzles. In contrast to [12, 14], the losses in the nozzle were not dominant. In summary it can be stated that the results were mainly in good approximation with those of previous investigators. There was no experimental validation available for the results. The author concluded that measurements of velocity profiles were impossible, due to the small gap width needed in Tesla turbine applications.

In [73], published, theoretical performance data was compared with CFD results, using ANSYS CFX. To improve performance, he slightly modified the disks. However, the focus was on the radial outward flow case.

A CFD design analysis for Tesla turbines and the application of low-boiling mediums for ORC purposes is outlined in [22]. Several turbine configurations for a certain

range of design parameters were investigated. The RANS equations in combination with the $k-\omega$ SST turbulence model were solved in Fluent. The nozzle and the rotor flow was modelled. The computational domain was modelled stationary with rotating disk walls. One, two, and four nozzle set-ups were studied. From streamline plots, it was observed that the flow made three to four rotations until it left the rotor. However, the inlet angles were nearly tangential in most of the cases. Furthermore, it is concluded that this type of turbine operates more like a reaction turbine with large pressure drops in the rotor. The computed isentropic efficiencies reached values of up to 50%. Power and efficiency were rising with the number of nozzles. There was neither a theoretical, nor an experimental validation given in this examination.

The previous numerical investigations about ORC Tesla turbines using low-boiling mediums, introduced in [22], were extended and presented in [35]. Simplified and full geometry models were studied. A specific flow rate and a constant pressure drop of 12.9 bar was set. The simpler models consisted of one gap only with four, six or eight nozzles along the circumference. Inlet angles of 10° and 15° were modelled. Ideal outflow was assumed. The disk diameters were 100 mm and 300 mm. A gap width of 0.25 mm was used in all cases. The efficiency was slightly higher for the 10° inlet angle. Maximum efficiency was obtained with the four nozzle case. A higher efficiency was observed for higher rotational speeds. Maximum efficiency was about 50%, showing the longest path lines. A larger disk diameter did not improve efficiency significantly. The full geometry model with a rotor diameter of 100 mm consisted of 12 flow channels. The flow left the rotor through four openings near the axis of rotation. The efficiency was about 16% and hence lower than in the simplified cases. Path lines were shorter and eddies at the outlet disturbed the flow in that region. Nevertheless, CFD can only cover specific cases and does not derive general influences of performance parameters. However, the investigations are lacking an experimental validation.

A CFD optimisation of a Tesla turbine to exploit potential energy from household water supplies with smallest head losses was performed and outlined in [128]. With simple equations derived in [53, 55], which describe the Tesla pump, a rotor design was suggested. CFD helped to optimise the number of disks, the gap width, and the disk size. The whole turbine was modelled from the single nozzle to the seven drillings near the centre of rotation, where the flow usually leaves the rotor. It consisted of thirteen disks with a gap width of 0.32 mm and an outer diameter of 70 mm. The pressure drop was about 0.03 bar. The efficiency improved from 6.8% to 10.7%, the head loss decreased to about 1/10 of the first turbine design. Despite general difficulties in measuring small torques, the results from the test turbine agreed very well with the simulation. CFD is a helpful tool for the optimisations of certain flow problems. However, it does not derive universal design parameters. Moreover it is not clear, if the efficiency could be further improved.

A Tesla turbine with an outer diameter of 100 mm and a gap width of 0.5 mm was analysed by numerical means and presented in [10]. Different nozzle numbers, rotational speeds, and pressure ratios were calculated. The outlet was assumed to be

the lateral surface consisting of inter-disk spacing and inner radius. Air was used as the working medium. The ANSYS CFX solver was chosen in this computation. The flow was treated as laminar and incompressible. Highest isentropic efficiencies were achieved with lowest nozzle numbers (cf. [35]), highest rotational speeds and lowest pressure ratios across the turbine. Shaft power rose with increasing rotational speed and increasing nozzle number. As a consequence, two or four nozzles were suggested. It is not clear, if this is universal and can be applied for all Tesla turbines.

In [34], the entire Tesla-disk turbine was studied, focusing the inlet and outlet design by numerical means. The commercial CFD code Fluent was chosen to solve the laminar, compressible governing equations. The model had an outer diameter of 80 mm and an inter-disk spacing of 0.25 mm. Uniform inflow and outflow was assumed in the first case. It was considered that the radial velocity profile showed inflections at the centre of the disks. Efficiency was high for small flow coefficients. The flow coefficient and therefore the relative velocity between disks and flow was directly related to the viscous dissipation rate. It was responsible for the lowered efficiency. In the second case, different numbers and outlet areas of nozzles were modelled. Compared to the uniform inflow, the viscous dissipation rate increased at low radius ratios. However, it was concluded that nozzle inlets are meaningful in Tesla turbine applications. Furthermore, a practical and optimised rotor outlet was suggested in order to reduce the recirculating flow of previous design philosophies. There was no experimental validation given in this study.

The experiments, reported in [12] were investigated by numerical means in [129]. Fluent was used to solve the incompressible, laminar, and turbulent RANS equations. The $k-\epsilon$ model with near wall treatment was applied in the turbulent cases. At low radius ratios, the laminar radial velocity profile showed inflections, which vanish for turbulent flow conditions. However, the authors concluded that it was difficult to obtain appropriate results, due to the transitional flow regime. Furthermore, the authors had the strong belief that velocity profiles cannot be determined in experiments, because of the small disk spacing required in turbine applications.

In [130], a CFD study is presented, using the geometry, the flow, and the operating conditions similar to the turbine design described in [35]. A rotor with an outer diameter of 100 mm and inter-disk spacings from 0.25 mm to 1 mm were examined. One, two, and four nozzle inlets were compared. Exactly like in [35], maximum efficiency and shaft power was obtained with the four nozzle model. The results were not directly compared to experimental data.

The CFD approach is used in [21, 36], in order to verify the theoretical investigations about the similitude, the scaling laws, and the work transfer in Tesla turbines. The studies are described in chapter 1.3.1.

Recently, a preliminary CFD study for the basic understanding of Tesla turbines with a rotor diameter of 254 mm and a relatively large disk spacing of 2.54 mm was presented in [131]. The residual RMS target convergence was $1 \cdot 10^{-4}$ and is therefore no longer acceptable nowadays. However, this study is still worth mentioning,

because at least the rotor outlet is modelled. The shape of the outlet was similar to the configuration of Nikola Tesla's original turbine.

Further references for additional information about Tesla turbines and pumps can be found in [132].

1.3.4 Summary of earlier investigations

Theoretical investigations offered numerical and analytical solutions to the rotor flow in Tesla turbines. Nevertheless, optimisation criteria and influences of significant performance parameters were not presented yet. Moreover, the validation of theoretical results was generally achieved by comparing experimental to theoretical turbine performance data so far. Flow field measurements inside Tesla rotors were performed using hot-wire anemometry. However, this required large inter-disk spacings, which are unsuitable for efficient power generation. Furthermore, the spatial resolution was relatively low compared to the state-of-the-art measuring technology. Nevertheless, if a rotor would be up-scaled to a gap width providing enough space for hot-wire probes, the outer radius would be too large, as the disk spacing is usually infinite compared to the rotor radius. If this rotor would resist the mechanical stress under the load of rotation, one could at least keep the Reynolds number constant, but not the Mach number, which is desired to study compressibility effects experimentally. Although the velocity profiles are crucial for energy conversion, academic literature still lacks accurate flow field measurements in the gap of application-oriented Tesla turbines. Despite the absence of experimental validations, CFD methods provide insights into the rotor flow field. However, it is not clear if turbulence models with standard model constants are valid in those pressure driven, squeezed, and rotating flows.

The scope of this work is to study and determine the velocity distribution between the disks of a Tesla rotor by theoretical, numerical, and experimental means. Measurements of the tangential and radial velocity distribution across the inter-disk spacing of Tesla turbines using the particle imaging approach are in focus. This leads to the experimental validation of theoretical and numerical modelling of the flow field. Furthermore, universal optimisation criteria for Tesla turbines are derived from theoretical solutions.

2 Theoretical investigations

Two different concepts to describe the rotor flow of Tesla turbines are introduced in this chapter. The first approach is a simple mathematical model for the physical processes to estimate power, torque, and efficiency of blade-less turbines. It is based on the investigations reported in [45, 47] and leads to a fully analytical solution of the incompressible, laminar rotor bulk flow. Turbine performance is computed by assuming a parabolic velocity distribution in both directions between the disks. Furthermore, the method provides a smart evaluation, which finally leads to more general remarks about the characteristics and optimisation of Tesla turbines. Laminar, incompressible, and compressible cases are considered. If the turbulent velocity profiles were exactly known, the flow model could be adapted to compute turbulent turbine performance. Losses are not considered. The second approach is an approximate-analytical solution of the incompressible, laminar Navier-Stokes-Equations. The momentum equations are approximated using assumptions similar to the ones used in standard boundary layer theory. This leads to a semi-analytical determination of the velocity profiles in radial and tangential direction, in order to assess the assumptions made in the simplified model. All calculations are carried out using Wolfram Mathematica.

2.1 Energy conversion in Tesla turbines

Before the mathematical rotor flow models are described in detail, the flow physics through a rotor of a Tesla turbine have to be understood. The flow enters the gap under a certain angle of attack. It is driven by a pressure difference from the inlet slot at the outer radius to the outlet slot at inner radius. The kinetic energy of the flow is converted into torque and shaft power in the inter-disk spacing of a pair of co-rotating disks. The basic principle of energy conversion in Tesla turbines is the momentum exchange of the viscous drag force between fluid and both walls of each gap. The velocity profile is usually split up into a radial and a tangential velocity component using cylindrical coordinates. Only the shear stress of the relative, tangential velocity component produces torque. Power is induced under rotation. Furthermore, torque is only delivered, if the tangential, relative velocity component of the flow is higher than the circumferential speed of the disks at a certain radial position. However, torque can locally be negative, if the circumferential speed of the disks is higher compared to the tangential, relative velocity component of the flow. It has to be pointed out that the conversion of kinetic into mechanical energy does not happen constantly across the radius. The power, which is delivered at a stationary operational point of a blade-less turbine is the integral of the torque along the radius times the rotational speed of the disks. The radial velocity component determines the flow rate. Depending on the Reynolds number, the flow can either be laminar or turbulent.

2.2 Performance maps of Tesla turbines

An example of a typical performance map of a Tesla turbine is given in Fig. 2.1. The dimensionless torque and power coefficients are defined in Eqs. 2.52 and 2.54. The flow rate and therefore the absolute velocity at the rotor inlet is constant for all rotational speeds. In general, the highest torque can be found for zero rotation.

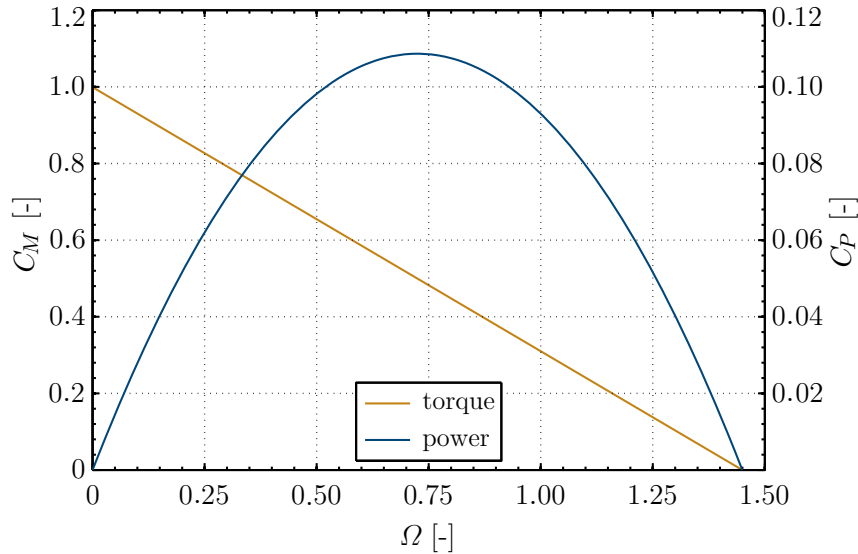


Figure 2.1: Performance map of a Tesla turbine

It decreases linearly with the rotational speed, if the inflow conditions are kept constant and are stable. The shaft power, which is delivered by this type of turbine, shows a parabolic shape.

2.3 Starting process and operating points of Tesla turbines

In the following, the starting procedure of an unloaded Tesla turbine is described. At first, the mass flow rate is set to a constant value. Therefore, the absolute velocity delivered by the guide vanes or nozzles is constant, too. The rotor will start to spin when the fluid-wall friction exceeds the value of the adhesive frictional forces of bearing and sealing. The rotational speed will then climb up the performance map to a value in which the torque is in balance with the sliding frictional forces of bearing and sealing, as well as the ventilation losses between housing and rotor. Therefore, a steady state occurs. If there were no frictional losses during energy conversion inside the rotor in a theoretical case, the turbine would increase its rotational speed until no torque is produced any more. This would happen exactly at the rotational speed where the linear torque curve intersects the abscissa. In reality, the addressed losses would slightly lower the maximum rotational speed near the zero torque point. The resulting balance between delivered torque and the torque originated by losses is a

stationary operating point. However, a Tesla turbine with a mechanical load applied on the rotor shaft would rather be accelerated to a point, where torque of load and turbine are equal. In many applications, this would probably be a resistive torque from a generator, where its magnitude strongly depends on the rotational speed. Furthermore, a gear unit would most likely be used to link an electrical generator, due to the low-torque and high-rev speed nature of these devices. Figure 2.2 gives one possible example how Tesla turbines could be utilised for power generation in the public electricity grid. It illustrates a Tesla turbine with an asynchronous machine at an operating point. Nevertheless, in this case, the turbine will have to be accelerated to the operating point, to overcome the breakdown torque M_b .

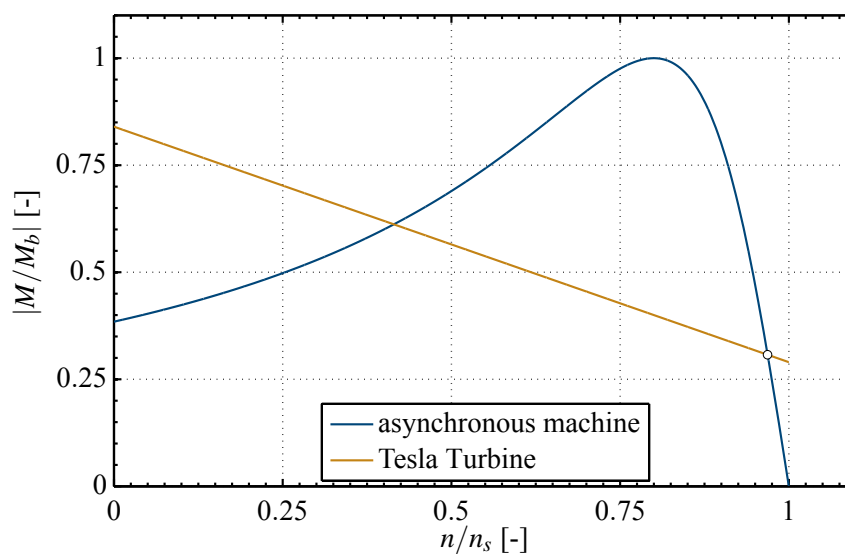


Figure 2.2: Torque curves of turbine and load with operating point

2.4 Definitions of Reynolds numbers

Throughout the years of research about the Tesla turbine, scientists used different forms of the Reynolds number. There is apparently no common understanding of the most useful from in literature. In [87] the angular velocity ω multiplied by the gap width $2s$ was used as the reference velocity. The inter-disk spacing is defined as the characteristic length in the Reynolds number in Eq. 2.1

$$Re_{\omega} = \frac{(2s)^2 \cdot \omega}{\nu}. \quad (2.1)$$

In [79] the relative velocity c at the disks' inlet and the hydraulic diameter d_h was used for the definition of the Reynolds number

$$Re_{\text{rel}} = \frac{c_1 \cdot d_h}{\nu}. \quad (2.2)$$

In [45, 47] a radial

$$Re_{\text{rad}} = \frac{v_1 \cdot r_1}{\nu} \quad (2.3)$$

and a tangential Reynolds number

$$Re_{\text{tan}} = \frac{u_1 \cdot s}{\nu} \quad (2.4)$$

was defined. Several other combinations of available characteristic lengths and velocities are possible. In this thesis, it is suitable and consistent to define the radial and the tangential Reynolds number

$$Re_v = \frac{v_1 \cdot s}{\nu} \quad \text{and} \quad Re_u = \frac{u_1 \cdot s}{\nu}. \quad (2.5)$$

The resulting Reynolds number is

$$Re = \frac{\sqrt{v_1^2 + u_1^2} \cdot s}{\nu}. \quad (2.6)$$

2.5 Navier-Stokes-Equations in cylindrical coordinates

The working principle in a Tesla turbine is the same as in any other turbomachine. The torque applied on the rotor shaft equals the change of angular momentum of the flow through the rotor without consideration of the energy conversion process itself [55].

The cylindrical coordinate system, used for the mathematical modelling of the flow, is illustrated in Fig. 2.3. In the following, the Navier-Stokes-Equations, derived in

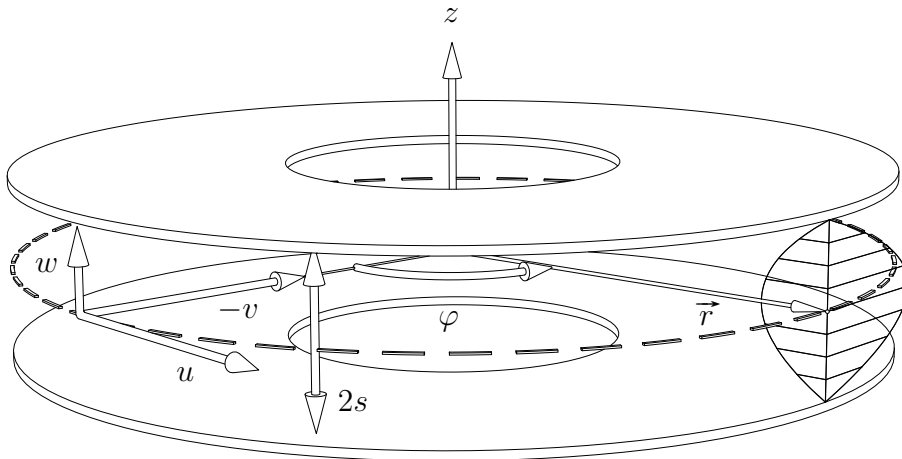


Figure 2.3: Cylindrical coordinate system in a Tesla rotor

[133], are presented. The continuity equation yields

$$\frac{\partial \rho}{\partial t} + \frac{1}{r} \cdot \frac{\partial(\rho \cdot r \cdot v)}{\partial r} + \frac{1}{r} \cdot \frac{\partial(\rho \cdot u)}{\partial \phi} + \frac{\partial(\rho \cdot w)}{\partial z} = 0. \quad (2.7)$$

The momentum equation in r -direction is

$$\begin{aligned} \rho \cdot \left[\frac{\partial v}{\partial t} + v \cdot \frac{\partial v}{\partial r} + \frac{u}{r} \cdot \frac{\partial v}{\partial \varphi} + w \cdot \frac{\partial v}{\partial z} - \frac{u^2}{r} \right] = \\ - \frac{\partial p}{\partial r} + \mu \cdot \left[\frac{\partial^2 v}{\partial r^2} + \frac{1}{r} \cdot \frac{\partial v}{\partial r} + \frac{1}{r^2} \cdot \frac{\partial^2 v}{\partial \varphi^2} + \frac{\partial^2 v}{\partial z^2} - \frac{v}{r^2} - \frac{2}{r^2} \cdot \frac{\partial u}{\partial \varphi} \right] + \rho \cdot g_r. \end{aligned} \quad (2.8)$$

The momentum equation in φ -direction is

$$\begin{aligned} \rho \cdot \left[\frac{\partial u}{\partial t} + v \cdot \frac{\partial u}{\partial r} + \frac{u}{r} \cdot \frac{\partial u}{\partial \varphi} + w \cdot \frac{\partial u}{\partial z} + \frac{u \cdot v}{r} \right] = \\ - \frac{1}{r} \cdot \frac{\partial p}{\partial \varphi} + \mu \cdot \left[\frac{\partial^2 u}{\partial r^2} + \frac{1}{r} \cdot \frac{\partial u}{\partial r} + \frac{1}{r^2} \cdot \frac{\partial^2 u}{\partial \varphi^2} + \frac{\partial^2 u}{\partial z^2} - \frac{u}{r^2} + \frac{2}{r^2} \cdot \frac{\partial v}{\partial \varphi} \right] + \rho \cdot g_\varphi. \end{aligned} \quad (2.9)$$

The momentum equation in z -direction is

$$\begin{aligned} \rho \cdot \left[\frac{\partial w}{\partial t} + v \cdot \frac{\partial w}{\partial r} + \frac{u}{r} \cdot \frac{\partial w}{\partial \varphi} + w \cdot \frac{\partial w}{\partial z} \right] = \\ - \frac{\partial p}{\partial z} + \mu \cdot \left[\frac{\partial^2 w}{\partial r^2} + \frac{1}{r} \cdot \frac{\partial w}{\partial r} + \frac{1}{r^2} \cdot \frac{\partial^2 w}{\partial \varphi^2} + \frac{\partial^2 w}{\partial z^2} \right] + \rho \cdot g_z. \end{aligned} \quad (2.10)$$

The Navier-Stokes-Equations, which describe the flow physics inside a Tesla rotor are only solvable under certain assumptions. These simplifications are introduced in chapters 2.6 and 2.9.

2.6 Simplified incompressible flow model

Beans [45, 47] introduced a simplified, analytical model for the incompressible, laminar flow between the disks. He assumed parabolic velocity distributions in radial and tangential direction and provided a semi-analytical solution. Some of the terms in his solution were only resolvable by numerical means during that time. A purely analytical solution of the velocity distributions and for the pressure drop using this approach was presented in [134]. A more detailed description of the incompressible model is presented in this chapter.

2.6.1 Dimensional governing equations

Following Beans [45, 47] and assuming parabolic velocity distributions in radial and tangential directions across the inter-disk spacing and integrating over half of the gap width s , the steady-state continuity equation yields

$$\frac{d(\rho \cdot r \cdot v)}{dr} = 0. \quad (2.11)$$

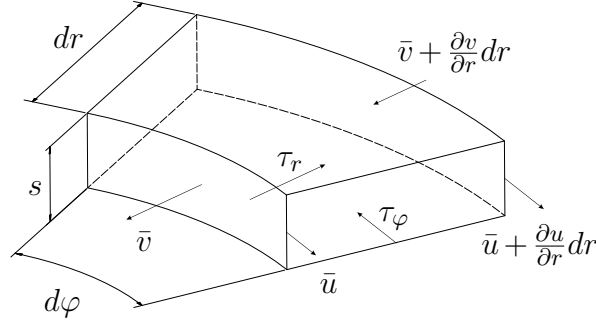


Figure 2.4: Semi-infinitesimal control volume

The radial and tangential momentum equations from [47] can be derived from Fig. 2.4, as generally described in [135]. They are defined as

$$\rho \cdot \left[v(r) \cdot \frac{dv}{dr} - \frac{u(r)^2}{r} \right] + \frac{dp}{dr} = \frac{\tau_r}{s}, \quad (2.12)$$

$$\rho \cdot \left[v(r) \cdot \frac{du}{dr} + \frac{u(r) \cdot v(r)}{r} \right] = \frac{\tau_\varphi}{s}. \quad (2.13)$$

Furthermore, the absolute velocity is calculated using

$$u(r) = c(r) + \omega \cdot r. \quad (2.14)$$

Assuming a parabolic velocity distribution, the radial velocity profile is given by

$$v(r, z) = \frac{3}{2} \cdot v(r) \cdot \left(1 - \left(\frac{z}{s} \right)^2 \right). \quad (2.15)$$

The mathematical expression of the tangential, absolute velocity profile is

$$u(r, z) = c(r, z) + \omega \cdot r = \frac{3}{2} \cdot c(r) \cdot \left(1 - \left(\frac{z}{s} \right)^2 \right) + \omega \cdot r. \quad (2.16)$$

The wall shear stress in radial and tangential direction can be expressed as

$$\tau_r = \mu \cdot \left. \frac{dv}{dz} \right|_{\text{wall}} \quad (2.17)$$

and

$$\tau_\varphi = \mu \cdot \left. \frac{dc}{dz} \right|_{\text{wall}}. \quad (2.18)$$

Together with Eqs. 2.15 and 2.16 the wall shear stresses are functions of the bulk velocities \bar{v} and \bar{c}

$$\tau_r(z = \pm s) = \mu \cdot \left| \frac{3 \cdot z}{s^2} \cdot v(r) \right|, \quad (2.19)$$

$$\tau_\varphi(z = \pm s) = \mu \cdot \left| \frac{3 \cdot z}{s^2} \cdot c(r) \right|. \quad (2.20)$$

2.6.2 Non-dimensional governing equations

Rotor geometry is made dimensionless with appropriate length scales. The radius ratio R is defined to be

$$R = \frac{r}{r_1}. \quad (2.21)$$

The dimensionless inter-disk spacing is normalised with half of the gap width

$$Z = \frac{z}{s}. \quad (2.22)$$

Furthermore, the geometrical similarity is achieved with the ratio

$$\sigma = \frac{s}{r_1}. \quad (2.23)$$

The governing equations are normalised by the velocities

$$V(R) = \frac{v(r)}{u_1}, \quad C(R) = \frac{c(r)}{u_1}, \quad U(R) = \frac{u(r)}{u_1}, \quad \Omega = \frac{r_1 \cdot \omega}{u_1}, \quad (2.24)$$

and their derivatives

$$\frac{dU}{dR} = \frac{du}{dr} \cdot \frac{r_1}{u_1} \quad \text{and} \quad \frac{dV}{dR} = \frac{dv}{dr} \cdot \frac{r_1}{u_1}. \quad (2.25)$$

The inlet bulk velocity in the absolute frame (or inlet angle) is

$$V_1 = \frac{v_1}{u_1} \quad \text{or} \quad \alpha = \arctan\left(\frac{v_1}{u_1}\right). \quad (2.26)$$

All velocities are non-dimensionalised with the tangential, absolute velocity u_1 at the rotor inlet. The dimensionless pressure is normalised with twice the dynamic pressure p_{dyn} in tangential direction at the rotor inlet. It is given by

$$P(R) = \frac{p(r)}{\rho_1 u_1^2}. \quad (2.27)$$

Its derivative is defined to be

$$\frac{dP}{dR} = \frac{dp}{dr} \cdot \frac{r_1}{\rho_1 u_1^2}. \quad (2.28)$$

Absolute and relative velocities are transformed by

$$U(R, Z) = C(R, Z) + \Omega \cdot R. \quad (2.29)$$

The non-dimensional, radial velocity distribution is

$$V(R, Z) = \frac{3}{2} \cdot V(R) \cdot (1 - Z^2). \quad (2.30)$$

The non-dimensional, tangential, relative velocity distribution is given by

$$C(R, Z) = \frac{3}{2} \cdot C(R) \cdot (1 - Z^2), \quad (2.31)$$

where the absolute velocity distribution is

$$U(R, Z) = C(R, Z) + \Omega \cdot R = \frac{3}{2} \cdot C(R) \cdot (1 - Z^2) + \Omega \cdot R. \quad (2.32)$$

The dimensionless wall shear stress in radial direction is defined as

$$C_{\tau,r} = \frac{\tau_r}{\frac{1}{2}\rho u_1^2} = \frac{2 \cdot \nu}{s \cdot u_1} \cdot V_1 \left| \frac{dV}{dZ} \right|_{\text{wall}}. \quad (2.33)$$

In tangential direction, it is

$$C_{\tau,\varphi} = \frac{\tau_\varphi}{\frac{1}{2}\rho u_1^2} = \frac{2 \cdot \nu}{s \cdot u_1} \cdot V_1 \left| \frac{dC}{dZ} \right|_{\text{wall}}. \quad (2.34)$$

With the derivatives of the solutions of Eqs. 2.30 and 2.31 at the wall, the non-dimensional wall shear stresses can also be written in the following forms

$$C_{\tau,r}(Z = \pm 1) = \frac{2 \cdot \nu}{s \cdot u_1} \cdot V_1 |3 \cdot Z \cdot V(R)|, \quad (2.35)$$

$$C_{\tau,\varphi}(Z = \pm 1) = \frac{2 \cdot \nu}{s \cdot u_1} \cdot V_1 |3 \cdot Z \cdot C(R)|. \quad (2.36)$$

In this simplified model, a parabolic velocity distribution across the gap between the co-rotating disks is assumed in radial and tangential direction. The tangential velocity profile and the velocity gradient at one wall is illustrated in Fig. 2.5.

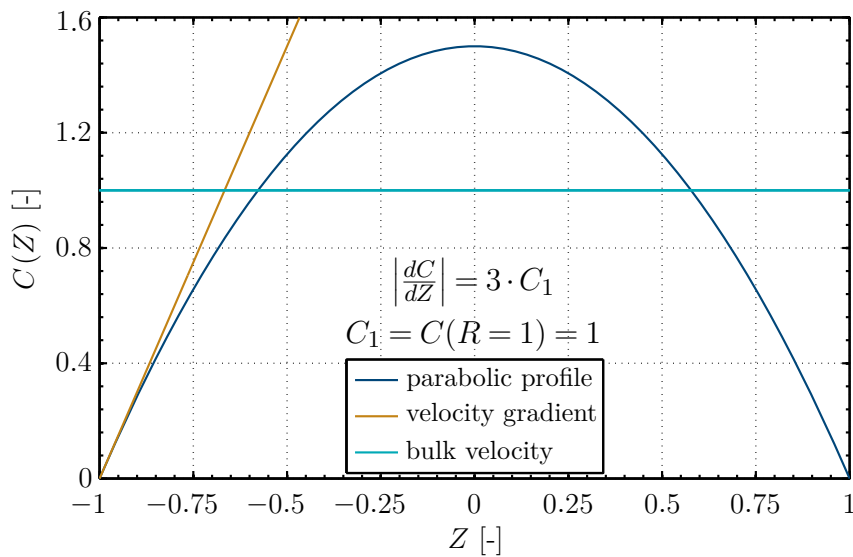


Figure 2.5: Tangential, relative velocity distribution between disks

Shaft power and efficiency is strongly influenced by the dimensionless machine parameters β , V_1 , R , and Ω , which are used in Eqs. 2.38, 2.39, and 2.40. Probably the most important parameter, derived in [45, 47] is

$$\beta = \frac{3}{2} \cdot \underbrace{\frac{r_1}{s}}_{\frac{1}{\sigma}} \cdot \underbrace{\frac{\nu}{v_1 \cdot s}}_{\frac{1}{Re_v}} = \frac{3}{2} \cdot \underbrace{\left(\frac{r_1}{s}\right)^2}_{\frac{1}{\sigma^2}} \cdot \underbrace{\frac{\mu}{\rho v_1 r_1}}_{\frac{1}{Re_{rad}}} = \frac{6\pi \cdot r_1 \mu}{2\pi r_1 (2s) v_1 \rho \cdot \sigma}. \quad (2.37)$$

The friction parameter β is a geometrical factor divided by the Reynolds number. It is mainly dependent on inter-disk spacing. The geometry parameter in β is in fact proportional to the reciprocal of the squared geometrical similitude coefficient σ . In addition to that there is also the mass flow hidden in Eq. 2.37.

The dimensional momentum equations (Eqs. 2.12 and 2.13) are normalised with Eqs. 2.21 to 2.28, and 2.37. The non-dimensional radial momentum equation is defined as follows

$$\frac{dP}{dR} - V_1^2 \cdot \left(\frac{1}{R^3} + \frac{2\beta}{R} \right) - \frac{U(R)^2}{R} = 0. \quad (2.38)$$

The dimensionless momentum equation in tangential direction is

$$\frac{dU(R)}{dR} + \left(\frac{1}{R} - 2\beta R \right) \cdot U(R) + 2\beta \Omega R^2 = 0. \quad (2.39)$$

The analytical solution of the flow field is obtained by solving the differential equation (Eq. 2.39) in the absolute frame with the boundary condition $U(1) = 1$. Solutions equal to those from Eq. 2.39 can also be obtained by solving the Eq. 2.40 in the relative frame with the boundary condition $C(1) = 1 - \Omega$

$$\frac{dC(R)}{dR} + \left(\frac{1}{R} - 2\beta R \right) C(R) + 2 \cdot \Omega = 0. \quad (2.40)$$

The analytical solution for the pressure is obtained from the integration of Eq. 2.38

$$\begin{aligned} P(R) = \frac{e^{-2\beta}}{2\beta^2} \left[\frac{1}{R^2} \left(2e^{\beta(1+R^2)} \Omega (\beta(\Omega - 1) + \Omega) - e^{2\beta R^2} \right. \right. \\ \cdot (\beta(\Omega - 1) + \Omega)^2 + e^{2\beta} \left(\Omega^2 (\beta^2 R^4 - 1) - 2\beta^2 \Omega R^2 \right. \\ \left. \left. + \beta^2 (R^2 + V_1^2 (R^2 - 1)) \right) \right) + 4\beta e^\beta \Omega (\beta(\Omega - 1) + \Omega) \\ \cdot \left(\text{Ei}(\beta) - \text{Ei}(\beta R^2) \right) - 2\beta (\beta(\Omega - 1) + \Omega)^2 \left(\text{Ei}(2\beta) \right. \\ \left. \left. - \text{Ei}(2\beta R^2) \right) + 4\beta e^{2\beta} \left(\Omega^2 + \beta^2 V_1^2 \right) \log(R) \right]. \end{aligned} \quad (2.41)$$

The equation for the radial bulk velocity distribution averaged over the inter-disk spacing is

$$V(R) = \frac{V_1}{R}. \quad (2.42)$$

As a result of the integration of the tangential momentum equation (Eq. 2.40) in the relative frame, the analytical solution yields

$$C(R) = e^{-\beta} \cdot \frac{\beta e^{\beta R^2} + e^{\beta} \Omega - e^{\beta R^2} \Omega - \beta e^{\beta R^2} \Omega}{\beta \cdot R}. \quad (2.43)$$

Integrating Eq. 2.39 in analogy with Eq. 2.40 yields the analytical solution of the tangential bulk velocity in the absolute frame

$$U(R) = e^{-\beta} \cdot \frac{(e^{\beta} - e^{\beta R^2}) \Omega + \beta (-e^{\beta R^2} (\Omega - 1) + e^{\beta} \Omega R^2)}{\beta \cdot R}. \quad (2.44)$$

With the help of

$$U(R) = C(R) + \Omega \cdot R, \quad (2.45)$$

the Eqs. 2.43 and 2.44 can easily be transformed into each other. This leads to a slightly different form of the non-dimensional absolute velocity in tangential direction

$$U(R) = e^{-\beta} \cdot \frac{\beta e^{\beta R^2} + e^{\beta} \Omega - e^{\beta R^2} \Omega - \beta e^{\beta R^2} \Omega}{\beta \cdot R} + \Omega \cdot R. \quad (2.46)$$

2.6.3 Performance map calculations

The mass flow \dot{m} is computed from

$$\dot{m} = A_1 \cdot v_1 \cdot \rho_1 = 2\pi r_1 (2s) \cdot v_1 \cdot \rho_1. \quad (2.47)$$

The torque per gap is further defined as

$$M = \int_0^{2\pi} \int_{r_1}^{r_2} \tau_{\varphi} \cdot r^2 dr d\varphi = \dot{m} (u_1 r_1 - u_2 r_2). \quad (2.48)$$

Absolute power per gap can be written as

$$\dot{W}_{\text{shaft}} = \int_0^{2\pi} \int_{r_1}^{r_2} \tau_{\varphi} \cdot r^2 dr d\varphi \cdot \omega = \underbrace{\dot{m} (u_1 r_1 - u_2 r_2)}_{\text{torque } M} \cdot \omega. \quad (2.49)$$

The isentropic efficiency for incompressible rotor flows is defined as

$$\eta_{\text{is,t}} = \frac{\dot{W}_{\text{shaft}}}{\dot{m} \cdot \underbrace{\left[\left(\frac{p_2}{\rho_1} + \frac{u_2^2}{2} + \frac{v_2^2}{2} \right) - \left(\frac{p_1}{\rho_1} + \frac{u_1^2}{2} + \frac{v_1^2}{2} \right) \right]}_{\text{total enthalpy difference}}}. \quad (2.50)$$

Tesla turbines may have considerable outlet velocities. Therefore, it is physically more suitable to use the total enthalpy difference without neglecting the inlet and

outlet velocities, which is usually assumed in conventional turbomachinery. For small outlet velocities, it is also valid to write

$$\eta_{\text{is}} = \frac{\dot{W}_{\text{shaft}}}{\frac{\dot{m}}{\rho_1} \cdot (p_2 - p_1)}. \quad (2.51)$$

On the one hand, the torque of a Tesla turbine can in general be expressed with

$$C_M = \frac{M}{u_1 \cdot r_1 \cdot \dot{m}} = 1 - U(R) \cdot R. \quad (2.52)$$

For a better comparison of CFD results systematically varying different design parameters, it can also be normalised with the maximum occurring torque in a certain investigation

$$C_{\text{to}} = \frac{A_1 v_1 \rho_1 \cdot (u_1 r_1 - u_2 r_2)}{M_{\text{max}}} \quad (2.53)$$

on the other hand. The non-dimensionalised shaft power is given by

$$C_P = \frac{\dot{W}_{\text{shaft}}}{A_1 \cdot \rho_1 \cdot u_1^3} = \Omega \cdot V_1 \cdot (1 - U(R) \cdot R). \quad (2.54)$$

However, for the determination of the inlet angle that corresponds to the performance maximum for a constant absolute value of the radial and the tangential Reynolds number, it is favourable to normalise shaft power using the local peak value, yielding

$$C_{\text{po}} = \frac{\dot{W}_{\text{shaft}}}{\dot{W}_{\text{max}}}. \quad (2.55)$$

The power coefficient C_P represents physically correct results, but does not indicate performance maxima. Instead, the power coefficient C_{po} is a good indicator for shaft power peaks. A first measure for rotor efficiency was the coefficient $C_{P,t}$, described in [134]. Shaft power C_P is made dimensionless by the total, dynamic pressure difference from the inlet to the outlet of the rotor and yields

$$C_{P,t} = \frac{M \cdot \Omega \cdot \sqrt{\rho_1}}{A_1 \cdot (p_{1,t} - p_2)^{\frac{3}{2}}}. \quad (2.56)$$

The coefficient for the performance optimisation delivers the correct inlet angle for maximum performance. However, it is not the best indicator for efficiency. Therefore, the isentropic efficiency is expressed in terms of non-dimensional variables

$$\eta_{\text{is,t}} = \frac{2 \cdot \Omega \cdot (1 - U(R) \cdot R)}{2 \cdot (P_2 - P_1) + (U_2^2 - 1) + (V_2^2 - V_1^2)}. \quad (2.57)$$

If the differences between the inlet and outlet velocities in radial and tangential direction are negligible, Eq. 2.57 can be simplified to the expression

$$\eta_{\text{is}} = \frac{\Omega \cdot (1 - U(R) \cdot R)}{(P_2 - P_1)}. \quad (2.58)$$

2.6.4 Similarity and scaling laws

Similarity and scaling laws can be derived from the theoretical and incompressible solution of the flow field between co-rotating disks. A non-dimensional analysis and additionally CFD studies were performed by [21]. Although their evaluation of the characteristics and performance optimisation of Tesla turbines could be presented more useful regarding the generality, criteria for scaling laws are introduced. The results complement the theoretical analyses, carried out in this thesis most helpfully. Therefore, the outcome of this valuable work is presented and expressed in form of the non-dimensional variables, established in chapter 2.6. According to [21], the geometric, and the kinematic similarity, as well as the identical dynamic similarity number between two turbines of different sizes, are required for proper scaling. The dimensionless quantities, obtained in this thesis, are similar to those used in [21]. The geometric similarity is achieved, if the dimensionless disk spacing σ and the radius ratio R are equal. The kinematic similarity is found for equal inlet angles V_1 and equal tangential speed ratios $1/\Omega$ at the rotor inlet, which denotes the ratio between the tangential, absolute velocity and the circumferential disk velocity at the rotor inlet. With the exception of a numerical constant, which comes from a different method of normalising, the dynamic similarity number is the reciprocal of Beans' friction factor (cf. [45, 47]). The algebraic transformation of β into D_s is already demonstrated in Eq. 1.3 in chapter 1.3.1. However, as β is actually a certain form of Reynolds number, it was expectable that Tesla turbines scale with this value.

As result of the study of [21], it is possible to state in summary that scaling of Tesla turbines is achieved, if the following non-dimensional physical quantities are equal:

$$R = \frac{r}{r_1} \quad \text{and} \quad \sigma = \frac{s}{r_1}, \quad (2.59)$$

$$V_1 = \frac{v_1}{u_1} \quad \text{and} \quad \Omega = \frac{r_1 \cdot \omega}{u_1}, \quad (2.60)$$

$$\beta = \frac{3 \cdot r_1 \cdot \nu_1}{2 \cdot s^2 \cdot v_1}. \quad (2.61)$$

2.6.5 Streamline visualisation

Streamlines of the bulk flow

This chapter describes how analytical streamline functions through a Tesla rotor can be retrieved. In first approximation, the streamlines of the bulk flow in the absolute frame are derived. The radial velocity

$$\frac{dR}{dt} = V(R) = -\frac{V_1}{R} \quad (2.62)$$

and the tangential absolute velocity

$$\frac{d(R \cdot \varphi)}{dt} = U(R) = R \cdot \frac{d\varphi}{dt} + \varphi \cdot \frac{dR}{dt} \quad (2.63)$$

are known. Inserting Eq. 2.62 into Eq. 2.63, leads to the analytical streamline function, which is analytically solvable for the boundary condition $\varphi(1) = 0$

$$\frac{d\varphi}{dR} = \frac{U(R) - V(R) \cdot \varphi}{-V(R) \cdot R} = -\frac{U(R)}{V_1} - \frac{\varphi}{R}. \quad (2.64)$$

The streamline function is the analytical solution of the ordinary differential equation of first order (Eq. 2.64) and yields

$$\varphi(R) = \frac{\Omega \cdot (R-1) \cdot (3 + \beta + \beta R + \beta R^2)}{3\beta R V_1} - \frac{e^{-\beta} \cdot \sqrt{\pi} \cdot (\beta\Omega + \Omega - \beta) \cdot (\operatorname{Erfi}(\sqrt{\beta}) - \operatorname{Erfi}(\sqrt{\beta}R))}{2\beta^{3/2} R V_1}. \quad (2.65)$$

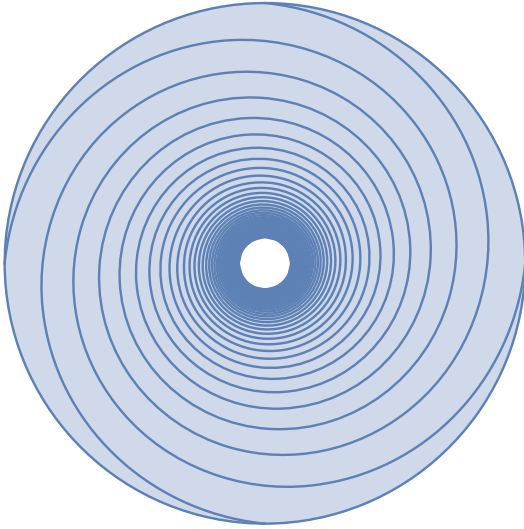


Figure 2.6: $\Omega = 0.4$, $V_1 = 0.1$, $\beta = 1$

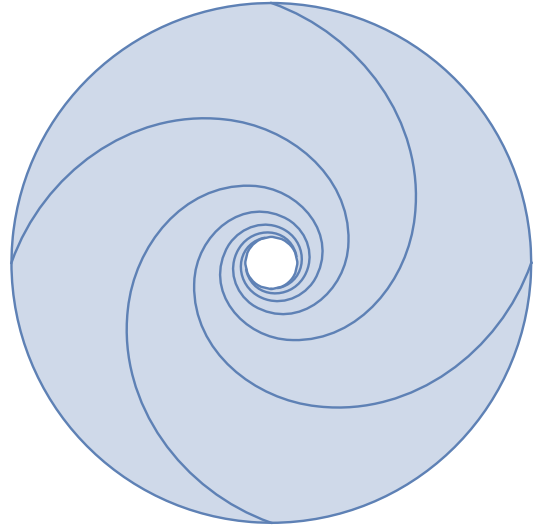


Figure 2.7: $\Omega = 0.8$, $V_1 = 0.3$, $\beta = 100$

By way of example, the streamlines through a rotor of a Tesla turbine are plotted in Figs. 2.6 and 2.7. Choosing certain values of the dimensionless machine parameters R , β , V_1 , and Ω , leads to various flow fields. This offers a great opportunity to investigate rotor flows. A detailed analysis of the fluid dynamic processes in Tesla rotors and their influences on turbine performance is provided in chapter 2.7.

Inter-disk streamlines

More information about the flow field can be obtained, if streamlines are accessible in different axial planes of the gap, as shown in Fig. 2.8.

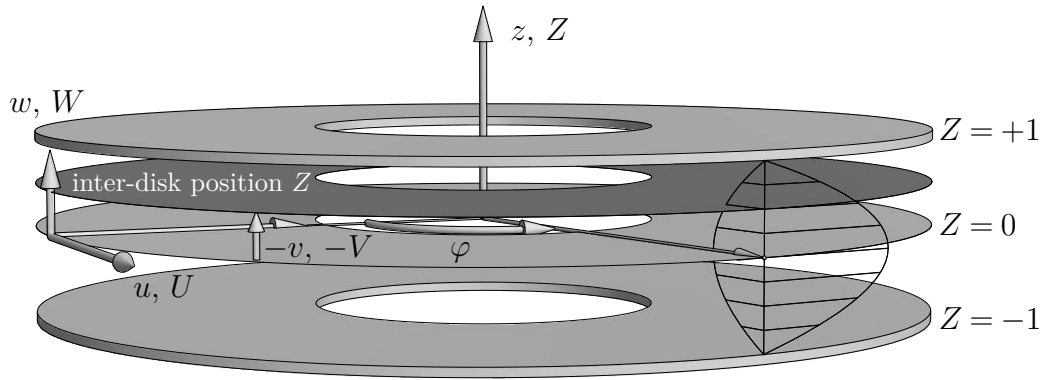


Figure 2.8: Position of streamline plane in the rotor

A pure parabolic velocity distribution across the gap is assumed for laminar flows. The tangential, absolute velocity can be expressed as a function of the radius R and the axial inter-disk position Z . It is given by

$$U(R, Z) = \frac{3}{2} \cdot U(R) \cdot (1 - Z^2). \quad (2.66)$$

Inserting Eq. 2.64 into Eq. 2.66 leads to the analytical streamline equation for a variable inter-disk position. The centre plane is accessible for $Z = 0$, the dimensionless wall position is at $Z = \pm 1$

$$\frac{d\varphi}{dR} = -\frac{3 \cdot U(R) \cdot (1 - Z^2)}{2 \cdot V_1} - \frac{\varphi}{R}. \quad (2.67)$$

Equation 2.67 is solved for $\varphi(1) = 0$. The analytical function for the inter-disk streamline is given by

$$\begin{aligned} \varphi(R, Z) = & \frac{\Omega \cdot (R - 1) \cdot (3 + \beta + \beta R + \beta R^2) \cdot (Z^2 - 1)}{2\beta R V_1} \\ & + \frac{3 \cdot e^{-\beta} \cdot \sqrt{\pi} \cdot (\beta \Omega + \Omega - \beta) \cdot (Z^2 - 1) \cdot (\operatorname{Erfi}(\sqrt{\beta}) - \operatorname{Erfi}(\sqrt{\beta} R))}{4\beta^{3/2} R V_1}. \end{aligned} \quad (2.68)$$

Figure 2.9 gives evidence that the streamlines of the bulk flow equal the streamlines at the inter-disk position $Z = \pm\sqrt{1/3}$ for a parabolic velocity distribution in radial and tangential directions. Figures 2.9 and 2.10 show the rotor streamlines in the absolute frame of reference.

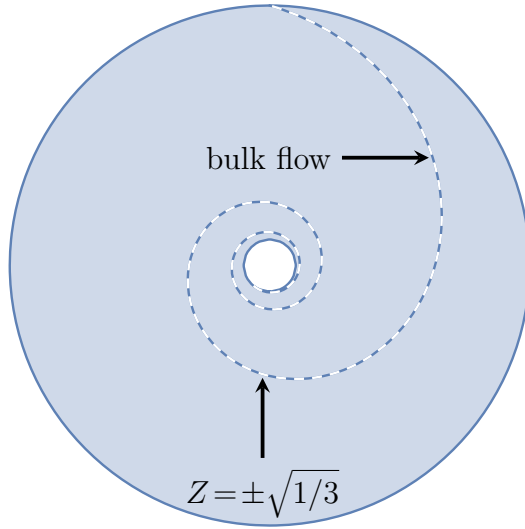


Figure 2.9: Streamline at $Z = \pm\sqrt{1/3}$ and of bulk flow are identical ($\beta=5$)

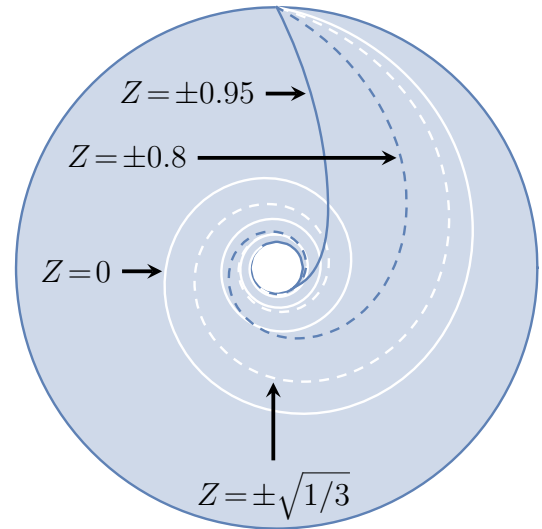


Figure 2.10: Streamlines at different axial positions ($\beta=5$, $\Omega=1$, $V_1=0.3$)

Figure 2.10 shows the variation of the streamlines from the bulk flow for $\beta = 5$, $\Omega = 1$, and $V_1 = 0.3$ at different axial inter-gap positions. The centre streamline has the longest path. Compared to the bulk flow, the fluid makes less revolutions closer to the wall. The strong variation of the streamline lengths in axial direction generally indicates high shear forces in the rotor.

2.7 Performance optimisation of Tesla turbines

Although there are many sophisticated attempts to describe the rotor flow of Tesla turbines in literature, one cannot find a comprehensive evaluation of a flow model that reveals all design criteria. The incompressible, analytical solution described in chapter 2.6 enables the parametric exploration of the Tesla turbine in terms of all non-dimensional variables. The desired operating conditions and the geometry of Tesla turbines for maximum performance and efficiency are now derived in general. The characteristics of Tesla turbines offer different optimisation strategies.

2.7.1 Influences of the friction parameter

The performance of Tesla turbines is significantly influenced by the dimensionless parameter β . Figure 2.11 exemplarily shows the qualitative mapping of the torque as a function of the parameter β and the angular velocity ratio Ω for a given radius ratio R and a constant inlet velocity ratio V_1 . Maximum torque is obtained for zero angular velocity, when the integral of the relative velocity is high compared to the surface of the disks. The torque decreases linearly with the angular velocity. Fur-

thermore, it is also dependent on the dimensionless parameter β . Largest torques can be extracted for β values exceeding 10. Above this level, the delivered torque is mainly independent of β itself, which means that the torque is saturated. Same ap-

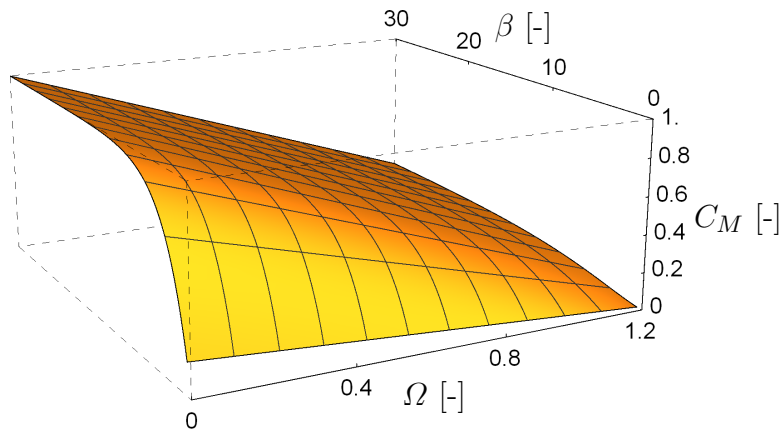


Figure 2.11: Dimensionless torque map C_M for $R=0.8$

plies to shaft power, due to the multiplicative link between both physical quantities (cf. Eq. 2.49). The corresponding performance map is shown in Fig. 2.12. The normalised power shows the typical second order polynomial development as a function of the angular velocity of a Tesla turbine. Nevertheless, the plot also confirms the observations from Fig. 2.11 that the parameter β requires a lower limiting value for maximum performance. It must therefore be considered that the threshold of $\beta \geq 10$ must be exceeded for competitive shaft power. However, a saturation of maximum power occurs with increasing β .

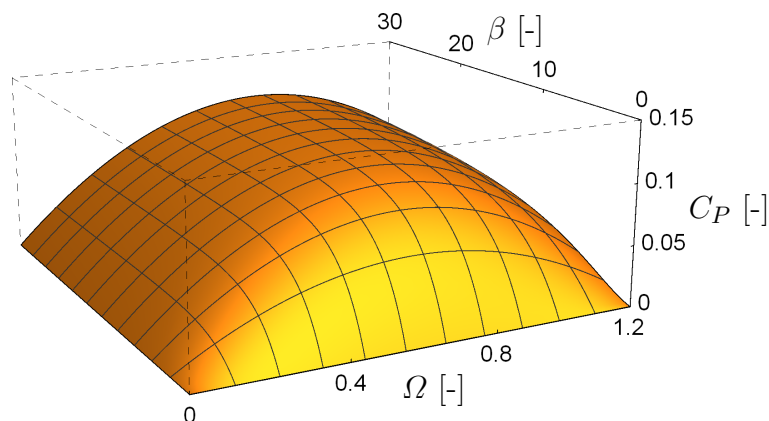


Figure 2.12: Dimensionless performance map C_P for $R=0.8$, $V_1=0.3$

Figure 2.13 shows the qualitative isentropic efficiency map for the radius ratio $R=0.8$ and the inlet velocity ratio $V_1=0.05$. The isentropic efficiency dramatically drops down for small values of β . This also demonstrates how important it is to overcome

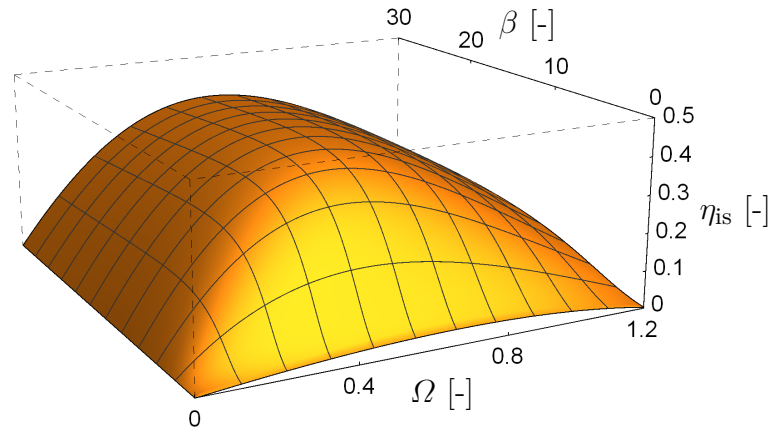


Figure 2.13: Efficiency map η_{is} for $R=0.8$, $V_1=0.05$

the threshold on β greater 10 for a competitive turbine. The efficiency maximum is between $10 \leq \beta \leq 20$, where the curve is relatively flat. Beyond this region, the efficiency slightly falls off. Nevertheless, the value of the angular velocity ratio Ω at the isentropic efficiency maxima does not entirely meet the one for maximum performance. This is due to the fact that the pressure drop across the rotor slightly changes with the angular velocity. However, lowest pressure drops across the radius can be found for $4 \leq \beta \leq 6$, as shown in Fig. 2.14. The pressure drops are huge below $\beta < 4$ and are continuously decreasing for $\beta > 6$. Acceptable pressure drops are achievable below $\beta = 20$. The curve of the isentropic efficiency is basically a superposition of the pressure drop and the power coefficient (cf. Eqs. 2.57, 2.58). The values of the power coefficient C_P fall off for $\beta \leq 10$ and are relatively constant

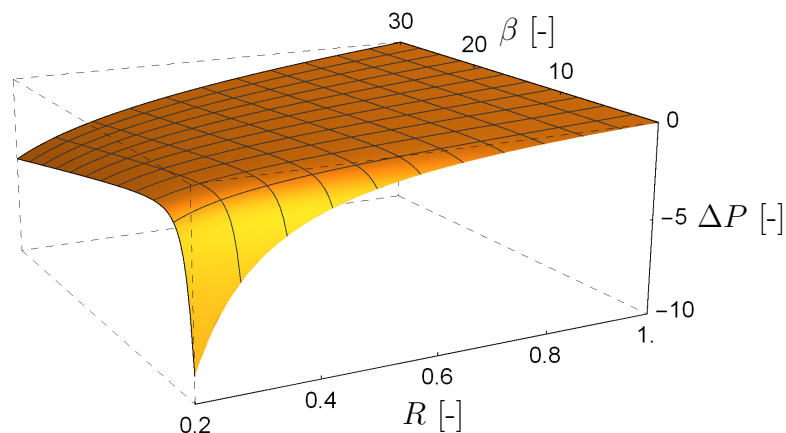


Figure 2.14: Pressure drop ΔP across the radius for $V_1=0.2$, $\Omega=0.6$

for $\beta \geq 10$. The isentropic efficiency optimum is therefore achieved for values of β between ten and twenty.

Increasing β values lead to rotors with highest shaft power. Regarding the tangential velocity distribution across the radius, high β values let the flow behave more and more like a solid body vortex. Relative velocities between flow and disks are small in the marginal case. Figure 2.15 shows minimal differences between the velocities of bulk flow and the disks for $\beta \rightarrow 100$. Low values of β lead to a tangential bulk velocity behaviour along the radius, which is similar to the velocity distribution of a potential vortex. As the bulk velocity increases with the rotor radius, apparently less energy extracted from the flow.

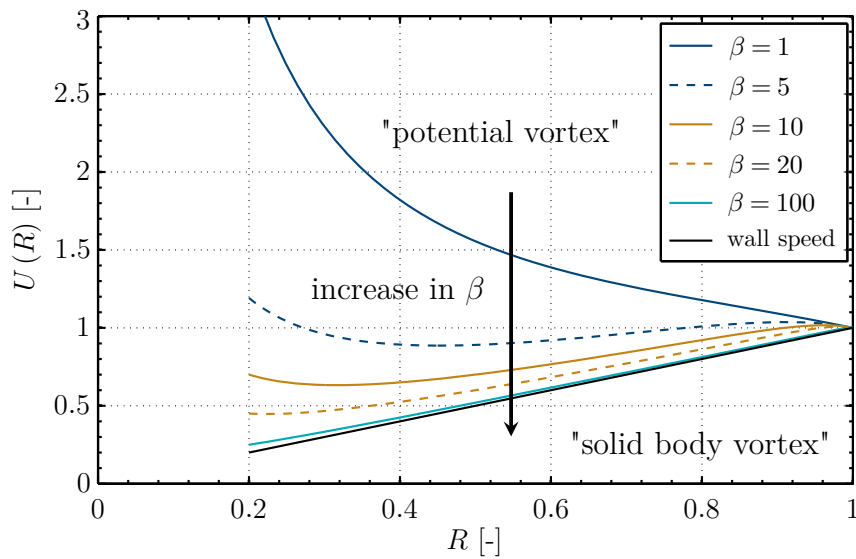
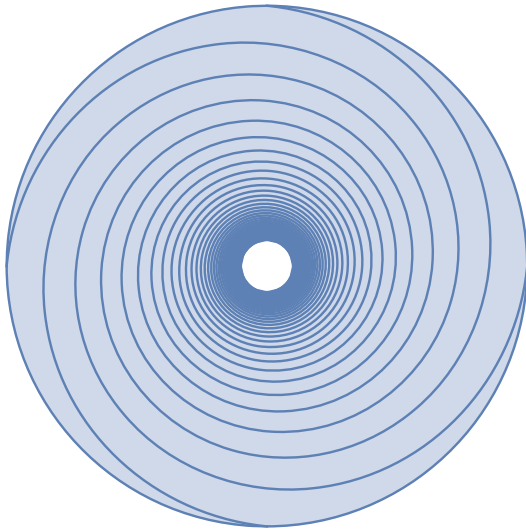
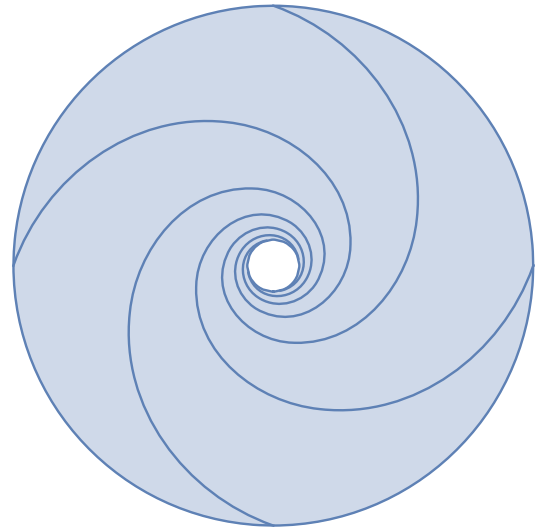
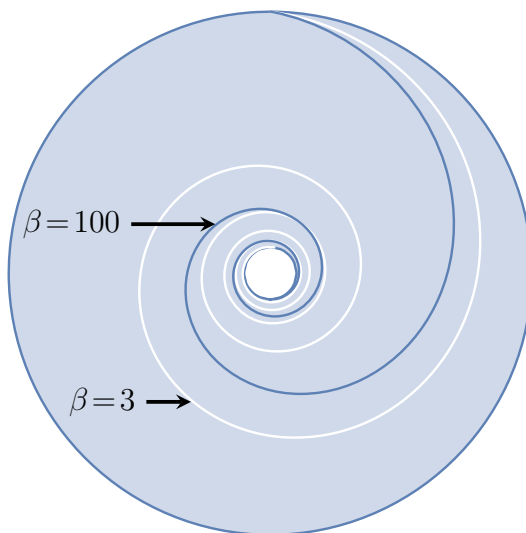
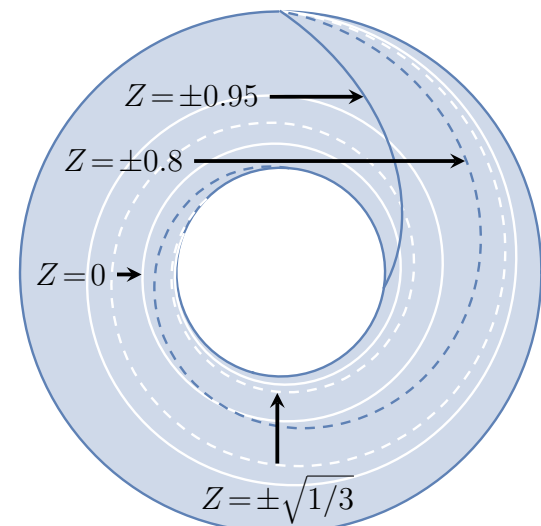


Figure 2.15: Tangential velocity distribution across the radius for $\Omega = 1.0$

The streamlines' path of the bulk flow between the disks for low- and high- β values in the absolute frame of reference is shown in Figs. 2.16 and 2.17. The fluid path of the low- β flow field is longer compared to the high- β case. In contrast to high- β conditions, the streamlines show more revolutions before they leave the rotor at the outlet in the centre of rotation. This indicates that shorter streamlines and therefore higher β values denote higher friction between flow and disk surfaces, because more kinetic energy is extracted from the flow. The tangential absolute velocity is significantly lowered for the high- β cases (cf. Figs. 2.17, 2.18). Figure 2.19 shows local streamlines in different Z -planes for low- β conditions, computed with Eq. 2.68. Closer to the wall, the fluid makes less revolutions compared to the bulk and the centre flow. Streamlines with closer wall distances Z look like those of high- β flows. This is due to the no-slip condition at the walls and therefore a typical boundary layer behaviour. For that reason, shorter streamlines refer to more friction. The strong deviation in streamline lengths across the inter-disk spacing lead to high shear forces inside this rotor.

Figure 2.16: $\Omega=0.6$, $V_1=0.2$, $\beta=1$ Figure 2.17: $\Omega=0.6$, $V_1=0.2$, $\beta=100$ Figure 2.18: Centre streamline plots for high and low β values ($\Omega=0.6$, $V_1=0.2$)Figure 2.19: Low- β streamline study in dependency of the axial inter-disk position Z ($\beta=1$, $\Omega=0.6$, $V_1=0.1$)

In summary we can say that highest turbine performance is found for β greater 10. The parameter β increases with the kinematic viscosity ν . Changing the medium can therefore help to adapt β . However, for most fluids, low disk spacing ratios σ and low radial Reynolds numbers Re_v are needed in order to meet this objective (cf. Eq. 2.37). Figure 2.20 shows the influences of disk spacing and Reynolds number on the friction parameter. Low gap widths $2s$ are simultaneously crucial for low disk spacing ratios σ and low radial Reynolds numbers Re_v , which then leads to high values of β . Besides these facts, the radial Reynolds number Re_v can be decreased by lowering the radial inlet velocity v_1 . This, on the other hand lowers the mass flow

and therefore the power per gap, but could be good for investigations of the flow field. In order to deliver the desired amount of power for a given mass flow \dot{m} , more gaps and therefore more disks are needed. This is certainly undesirable, because it increases the rotating mass and the manufacturing costs. This is the reason why an upper limitation of the parameter β is proposed in [134]. Maximum performance at an appropriate efficiency is obtained for β -values between 10 and 20. However, the upper limit of the parameter β has to be reconsidered during the development of each Tesla turbine, because ultimately it is an economical decision. As Tesla turbines scale with the disk spacing ratio σ , it is of special importance that the manufacturing tolerances of the gap width restrict the smallest possible values.

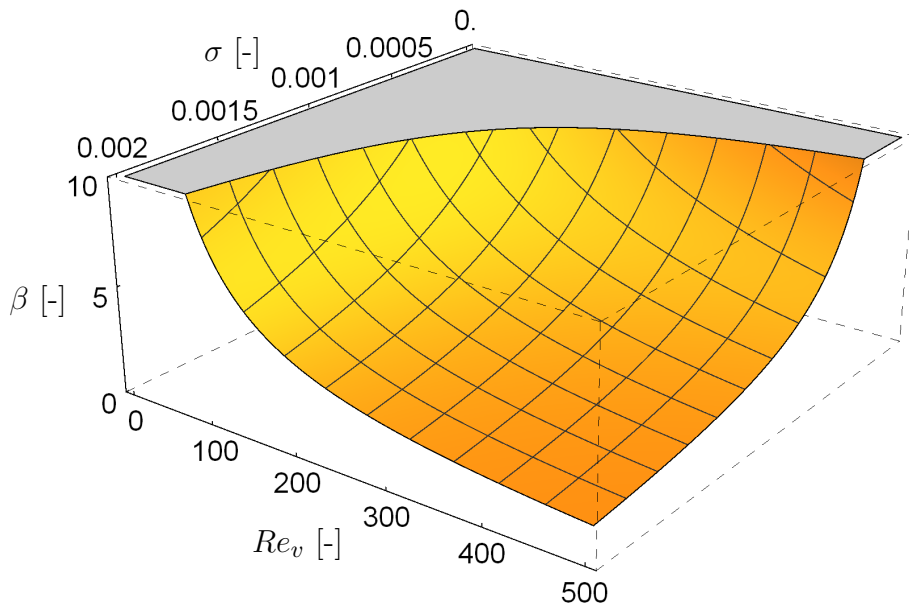


Figure 2.20: Parameter β as a function of disk spacing σ and Reynolds number Re_v

2.7.2 Influences of the inlet angle

The dimensionless parameter V_1 (Eq. 2.26) represents the inlet angle of a Tesla turbine and has major impact on performance and efficiency. Figures 2.21 to 2.24 qualitatively illustrate the influence of different inlet angles on performance, efficiency, pressure drop, and streamline path. The smaller the angle between the bulk flow direction and the tangent at the rotor inlet, the higher is the isentropic efficiency. Unfortunately, this involves lowest shaft power per pair of disks. With increasing inlet angles, more and more power is delivered with a simultaneous decrease in isentropic efficiency. Highest shaft power for the rotor geometry (chapter 4.4.4) with an inter-disk spacing of 0.2 mm and a constant stator outlet velocity between $0.3 \leq V_1 \leq 0.4$ was found in [11]. The power coefficient $C_{P,t}$, defined in Eq. 2.56 and in [134] also indicates that maximum power per gap is achieved for $V_1 \approx 0.3$.

However, maximum performance is slightly increasing with β , as shown in Fig. 2.21. Figure 2.22 indicates that the isentropic efficiency peak increases marginally with β . For small inlet angles, the efficiency maximum is located below $\Omega=1$. In addition to that, maximum efficiency is shifted to higher angular velocities with increasing β for increasing inlet angles beginning at $V_1=0.1$ (Fig. 2.22). The corresponding pressure drops across the rotor, which clearly increase with the inlet angle and the angular velocity are shown in Fig. 2.23. The streamlines of the bulk flow for small and large inlet angles are illustrated in Fig. 2.24. Compared to the streamlines of the rotor

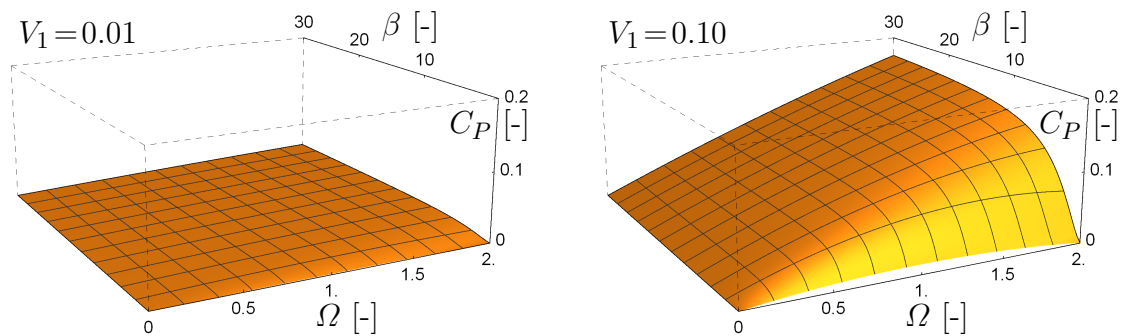


Figure 2.21: Performance mapping for $R=0.2$ with different inlet angles

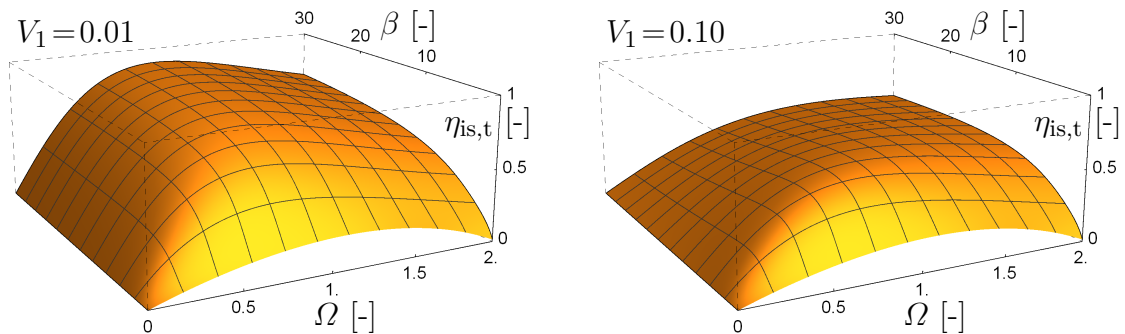


Figure 2.22: Efficiency mapping for $R=0.2$ with different inlet angles

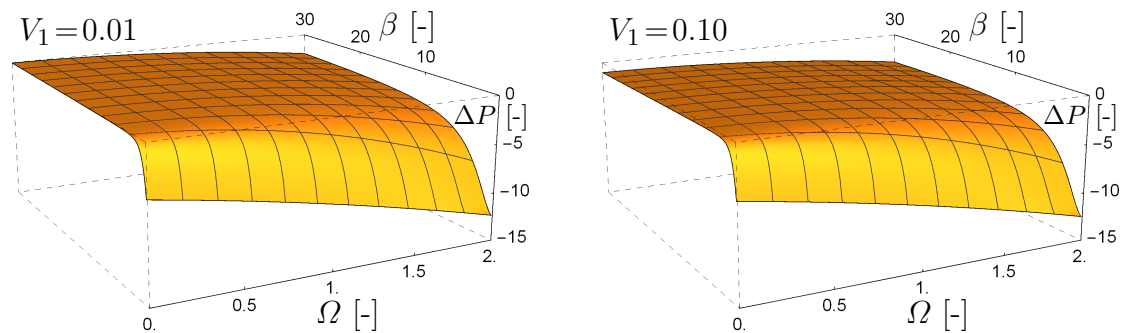


Figure 2.23: Pressure drops at radius $R=0.2$ as a function of β and Ω

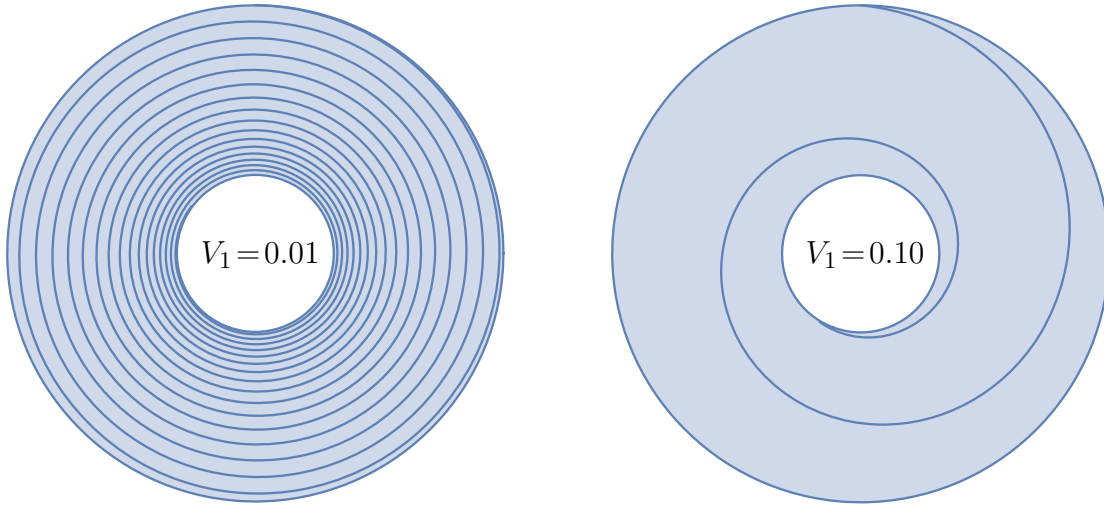


Figure 2.24: Bulk flow streamlines for $R=0.2$, $\beta=10$, $\Omega=0.8$ and different V_1

flow at large inlet angles, small inlet angles lead to streamlines, which are longer providing more revolutions before leaving the rotor. The streamlines of the bulk flow field at small inlet angles look like those from a low- β configuration. The tangential, absolute velocity increases continuously along the radius. The distribution is similar to the one of a potential vortex, as shown in Fig. 2.15. In summary, we can say that lowest inlet angles lead to lowest shaft power, lowest pressure drops, highest isentropic efficiencies, and longest streamline paths with many revolutions.

One major problem of Tesla turbines is the sensitivity of the inlet angle to the turbine performance and efficiency. In order to make a quantitative assessment Figs. 2.25, 2.26, and 2.27 are introduced. Performance, isentropic efficiency, and pressure

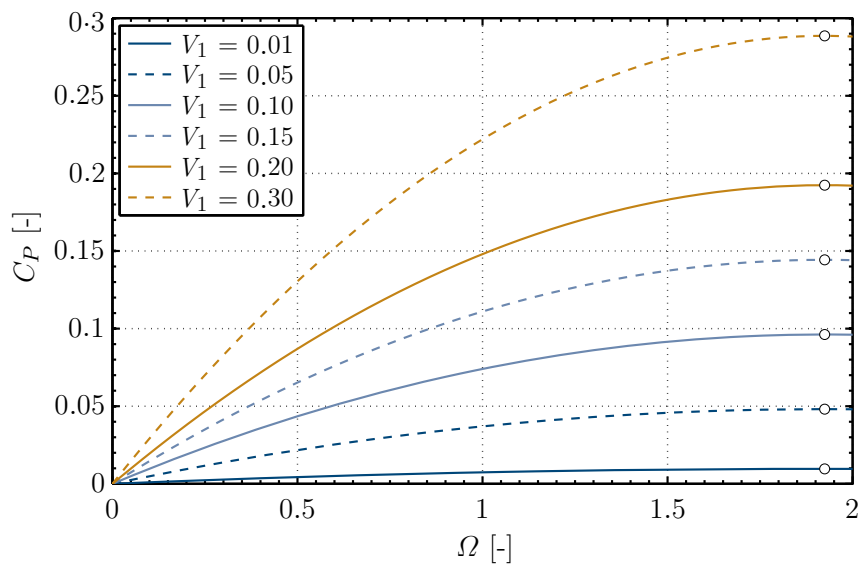


Figure 2.25: Shaft power for different inlet angles and $\beta=15$, $R=0.2$

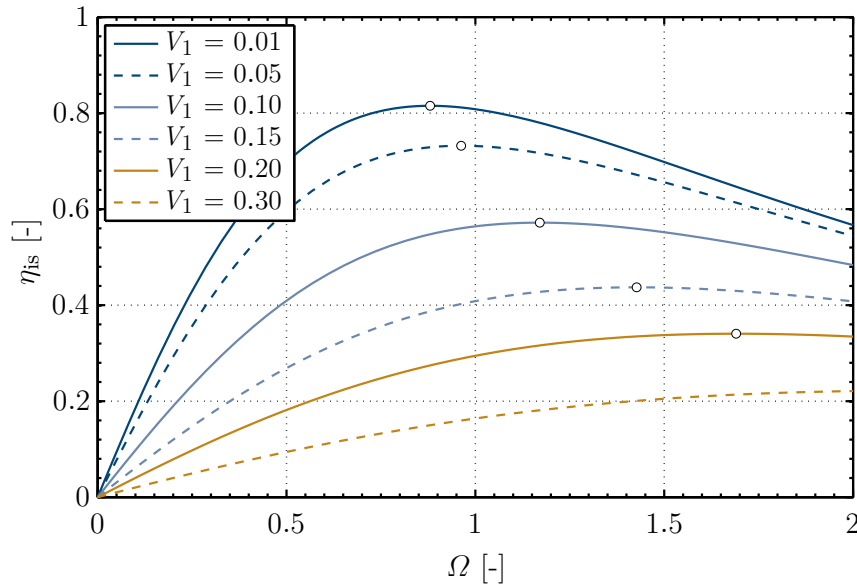


Figure 2.26: Isentropic efficiency for different inlet angles and $\beta=15$, $R=0.2$

drops of a competitive Tesla turbine with parameters of $\beta=15$ and $R=0.2$ are shown. An increase of the inlet angle V_1 from 0.01 to 0.05, which is approximately a change of 3° , results in an increase in performance of about 400% and a simultaneous decrease in isentropic efficiency of roughly 10%. Thereby, the pressure drop increases by about 20%. To give an example, larger inlet angles like configurations with $V_1=0.3$ in Fig. 2.25, create nearly 35 times more power at $\Omega=0.75$. Power per gap is dramatically increased, however with an eightfold increase in pressure drop. This involves a significantly reduced isentropic efficiency to about 20% of the peak efficiency. The above-mentioned numerical values are valid for $\Omega=0.75$, where

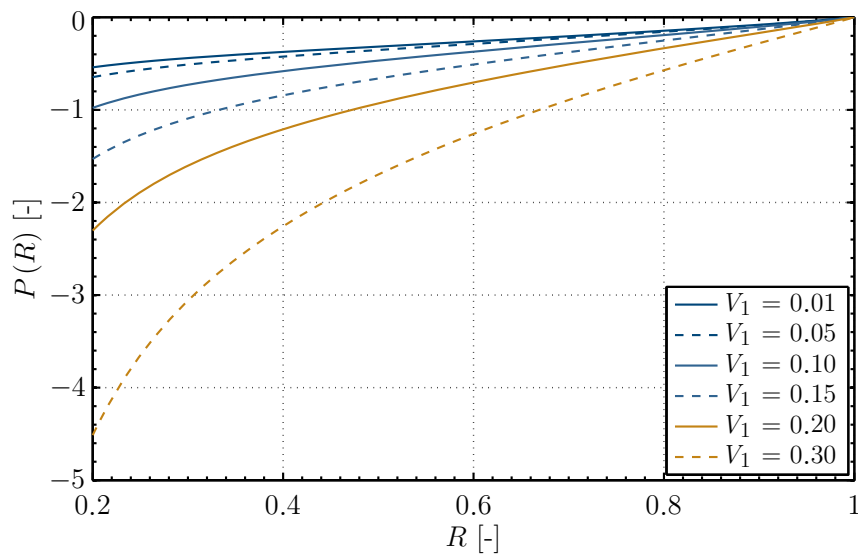


Figure 2.27: Pressure drop for different inlet angles ($\beta=15$, $\Omega=0.75$)

maximum efficiency at small inlet angles can be found. Furthermore, the efficiency peaks are decreasing with rising inlet angle. They are thereby more and more shifted to higher angular velocities.

The power coefficient C_{po} reveals the inlet angle that is corresponding to the performance maximum for a given absolute value of the radial and tangential Reynolds number

$$\sqrt{Re_u^2 + Re_v^2} = \text{const.} \quad (2.69)$$

Figure 2.28 shows the power maps, which are computed for different inlet angles. The calculations are valid for an inter-disk spacing of 0.5 mm and the rotor geometry, described in chapter 4. Shaft power \dot{W}_{shaft} is normalised by the maximum occurring power of 88 W. The angular velocity Ω is non-dimensionalised by the absolute value of the stator outlet velocity 100 m/s. As a consequence, the mass flow, the radial velocity, the tangential, relative and the tangential, absolute velocity, the angular velocity, and the dimensionless parameter β are changing with the inlet angle. However, maximum performance is found for $V_1 \approx 0.4$. Performance and efficiency of Tesla

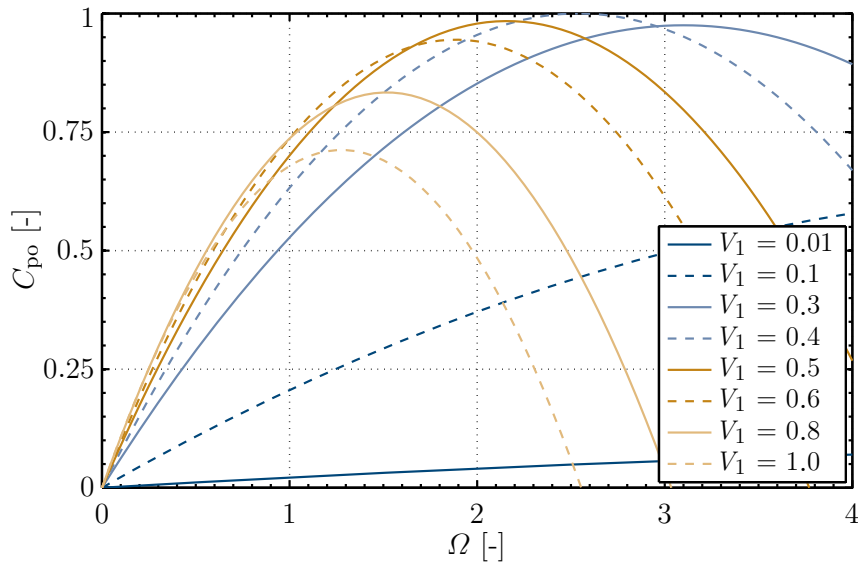


Figure 2.28: Performance map for different inlet angles V_1

turbines are working in opposite directions, as for instance in gas turbines. Therefore, the characteristics offer the possibility for different optimisation strategies. We further distinguish between the approach to optimise for maximum performance disregarding the efficiency and the opportunity to find the highest possible efficiency with acceptable shaft power.

Maximum performance per gap can be found for

$$0.3 \leq V_1 \leq 0.5 \quad (2.70)$$

and highest possible efficiency with acceptable shaft power per gap can be found for

$$0.05 \leq V_1 \leq 0.1. \quad (2.71)$$

2.7.3 Influences of the radius ratio

Large radius ratios leads to steeper sloping torques as a function of Ω compared to those at low radius ratios. Figure 2.29 shows the qualitative course of the dimensionless torque coefficient for different radius ratios. Both torque curves are equal

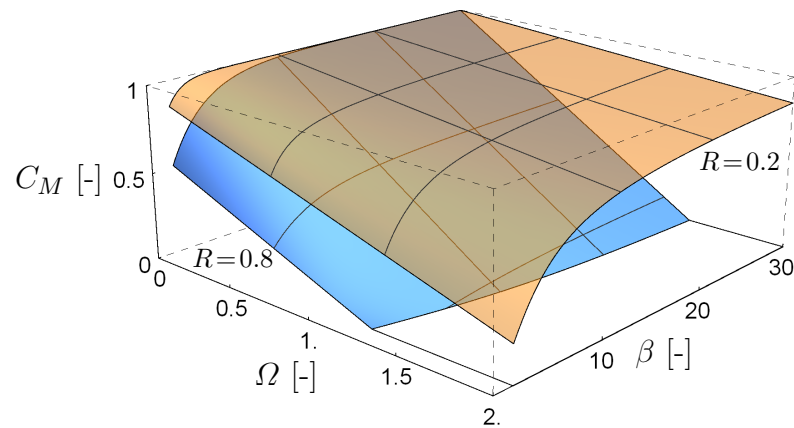


Figure 2.29: Dimensionless torque map C_M for small and large radius ratios R

at zero angular velocity, when levels exceed $\beta \geq 10$. Turbine performance vs. the angular velocity is plotted in Fig. 2.30. It allows quantitative statements about the influence of the radius ratio. Rotors with low radius ratios deliver more power per gap over the whole range of rotational speeds. The performance peaks are shifted to higher angular velocities with decreasing radius ratios. The isentropic efficiency is also increasing with decreasing radius ratio, as shown in Fig. 2.31. The maxima of the isentropic efficiency are also shifted to higher values of the angular velocity.

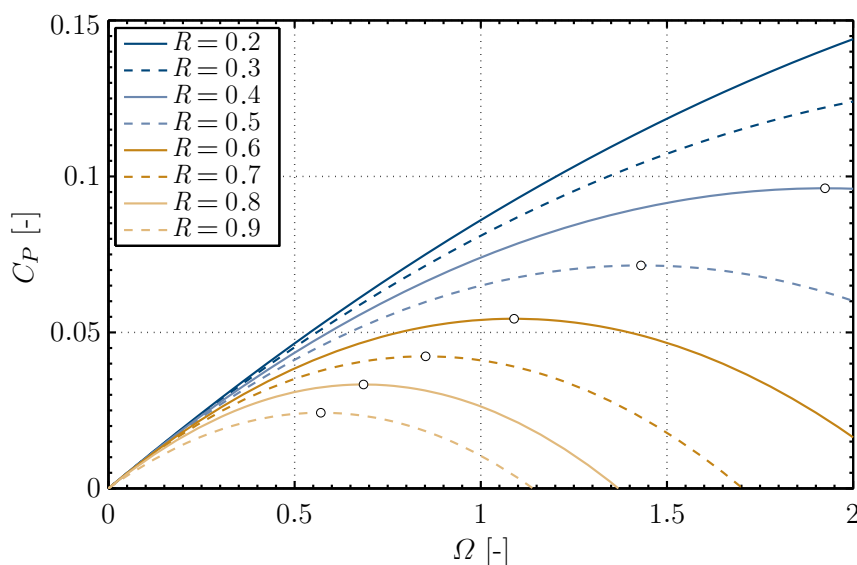


Figure 2.30: Performance map for different radius ratios R

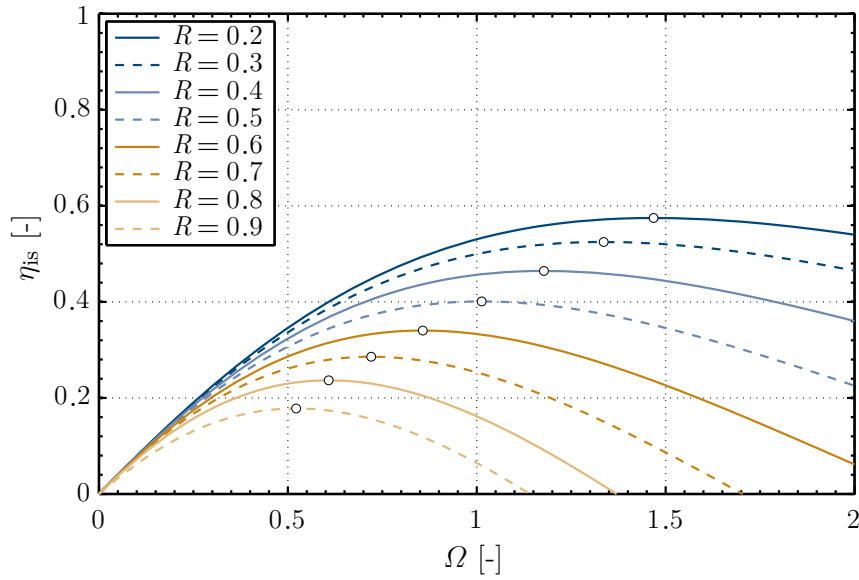


Figure 2.31: Efficiency map for different radius ratios R

However, efficiency does not increase to the extent of turbine performance. This is caused by the fact that the pressure drops are generally increasing with the angular velocity and with decreasing radius ratio, as shown in Fig. 2.32. Moreover, the distribution of the total amount of torque along the radius ratio, illustrated in Fig. 2.33, provides further details about the characteristics of Tesla turbines. The major share of the entire torque delivered at low angular velocities is generated within the first ten percent of the radius. Highest torque is produced with lowest angular velocities. With rising angular velocity, the above-mentioned major share of the torque production is shifted to lower radius ratios. The circumferential velocity of the disks at

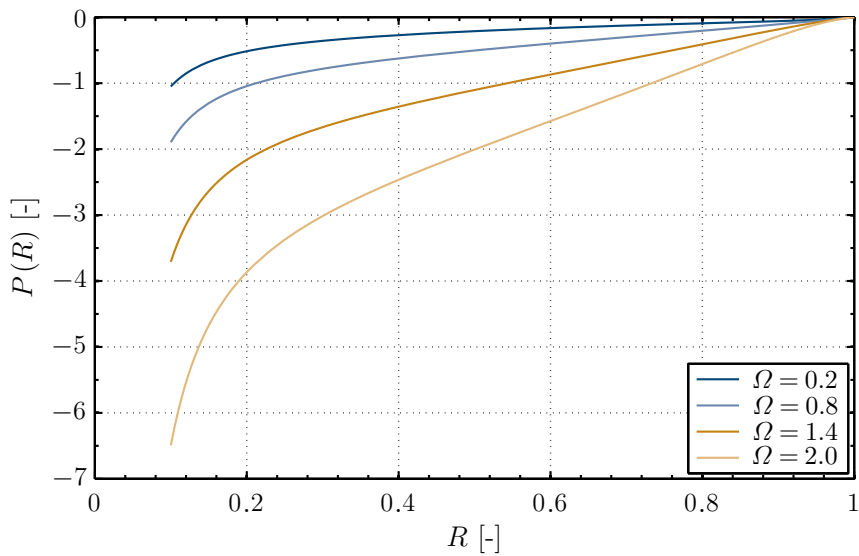


Figure 2.32: Pressure drop ΔP across the radius

the outer radius of the rotor equals the tangential absolute velocity at the rotor inlet at a value of $\Omega = 1.0$. Values of Ω exceeding 1.0 involve a lower tangential, absolute velocity compared to the circumferential speed of the disks at the rotor inlet, which generates a negative torque. In this case, the turbine works as a compressor within the first twenty to forty percent of the radius. Obviously, the tangential, absolute velocity is rising along the rotor radius. Thereby, it overshoots the circumferential disk velocity at a certain radius and is starting to generate positive torques. However, Fig. 2.33 clarifies, why the torque is falling stronger with the angular velocity at high radius ratios.

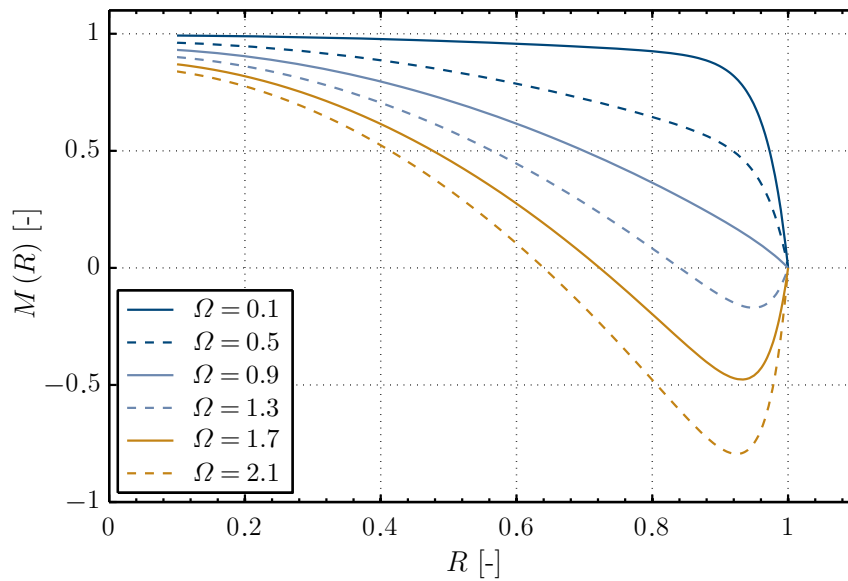


Figure 2.33: Development of total torque M along the radius ratios R

2.7.4 Optimisation criteria

The characteristics and flow physics of Tesla turbines concerning performance and efficiency are generally discussed in this chapter. To summarise, the operation of Tesla turbines for laminar and incompressible flow can be described in terms of the non-dimensional coefficients β , V_1 , R , and Ω . However, obtaining optimum performance and optimum isentropic efficiency at the same time is impossible. The nature of these power devices offers different optimisation strategies. This is caused by the fact that shaft power and efficiency are partially working in opposite direction. Therefore, two different optimisation approaches are suggested. The optimisation for maximum shaft power per gap without consideration of efficiencies and the optimisation for highest possible efficiency with an appropriate performance per gap are conceivable.

However, performance and efficiency increase with rising parameter β and decreasing

radius ratio R . Nevertheless, the coefficient β should generally be in the range of

$$10 \leq \beta \leq 20. \quad (2.72)$$

Higher values of β would still increase the potential of power and efficiency, but then involve small gap widths, which restrict the mass flow and therefore maximum performance for a single gap. Furthermore, small radius ratios R increase power and efficiency. However, they shift the performance maximum to higher rotational speeds. Moreover, too small radius ratios lead to small outlet areas, which might induce choked flow conditions for a rotor with many gaps. The radius ratio can be optimised individually, if the number of disks is known. It can be estimated from the available mass flow, if the gap width and the inlet angle are already defined.

The choice of the inlet angle V_1 is responsible for the optimisation of power or efficiency. On the one hand, maximum performance per gap is obtained for

$$0.3 \leq V_1 \leq 0.5, \quad (2.73)$$

compromising a low isentropic efficiency. On the other, highest efficiency at an appropriate power per gap is achievable for

$$0.05 \leq V_1 \leq 0.1. \quad (2.74)$$

Finally, it is an individual decision, whether gap efficiency or power per gap should compete with other devices. The optimisation for maximum performance per gap is important, if the source of energy cannot be tapped with other turbines. Ultimate efficiencies are only needed, if Tesla turbines enter into competition with other devices. However, micro turbines generally supply power with lower efficiencies, due to their size and the related secondary losses between rotating blades and housing. Isentropic efficiencies of Tesla turbines only have to be comparable for being a challenging competitor, because they are cheaper to manufacture. In this case, highest efficiencies are not needed and the reduced performance per gap would only increase the number of disks, the weight of the rotating mass, and the manufacturing costs.

The decision for an appropriate optimisation strategy of the entire turbine is only useful, if the acquisition and the operating costs – especially the fuel price – are considered. If the price of fuel is huge, the acquisition costs are not in focus. Therefore, the optimisation for maximum efficiency is preferred. In the field of renewables or waste heat recovery for instance, the price for the fluid is rather negligible and the acquisition costs have to be minimised to compete with other devices. Provided that the mass flow is given, this can be done by maximising the power per gap, which leads to less gaps and therefore to a lower rotor weight, as well as to lower manufacturing costs. Maximum power per gap at an optimum utilisation of material can be achieved by optimising the disk radius r_1 and the angular velocity ω for a constant mechanical stress inside the disks. Equation 4.1 indicates that the product $\omega^2 \cdot r_1^2$ dominates the magnitude of the mechanical stress at the critical point of a centrally drilled disk under constant rotation. High radii r_1 and angular velocities ω lead to the maximum of power per gap. However, high radii r_1 also increase the mass of disks and gap, increase the mass flow per gap (Eq. 2.47), decrease the number of gaps, lower the disk spacing ratio (Eq. 2.23), and therefore increase β (Eq. 2.37).

2.8 Simplified compressible flow model

In a second step, the flow model is extended to compressible conditions. The differential equations are coupled solved for given fluid properties and inlet conditions. Wolfram Mathematica enables the possibility to obtain numerical results in a short computation time on state-of-the-art computers.

2.8.1 Dimensional governing equations

The assumption of a parabolic velocity distribution of the inter-disk spacing, as well as the radial and the tangential momentum equation (Eqs. 2.12, 2.13) are applied again. The continuity equation is slightly different from the incompressible case, due to the change of density

$$\rho(r) \cdot r \cdot v = \rho_1 \cdot r_1 \cdot v_1. \quad (2.75)$$

For compressible flow conditions, the radial momentum equation

$$\rho \cdot \left[v(r) \cdot \frac{dv}{dr} - \frac{u(r)^2}{r} \right] + \frac{dp}{dr} = \frac{\tau_r}{s}, \quad (2.76)$$

as well as the tangential momentum equation

$$\rho \cdot \left[v(r) \cdot \frac{du}{dr} + \frac{u(r) \cdot v(r)}{r} \right] = \frac{\tau_\varphi}{s} \quad (2.77)$$

feature the variation of the density across the radius.

The energy equation is implemented, assuming calorically perfect gas for compressible and adiabatic flows. For an open and stationary system, the energy equation is given by

$$\begin{aligned} \frac{\partial E}{\partial t} = & \sum_{\substack{i \\ =0}} \dot{Q}_i + \sum_j \dot{W}_{t,j} + \sum_{\substack{\dot{m}_{in} \\ =\dot{m}}} \left(h_{in} + \underbrace{g \cdot z_{in}}_{=0} + \frac{1}{2} \cdot c_{in}^2 \right) \\ & - \sum_{\substack{\dot{m}_{out} \\ =\dot{m}}} \left(h_{out} + \underbrace{g \cdot z_{out}}_{=0} + \frac{1}{2} \cdot c_{out}^2 \right). \end{aligned} \quad (2.78)$$

With the simplifications mentioned in Eq. 2.78, by splitting up the universal velocity c into its velocity components

$$\vec{c} = |u| \cdot \vec{e}_\varphi + |v| \cdot \vec{e}_r + |w| \cdot \vec{e}_z \quad (2.79)$$

and inserting Eq. 2.48 into Eq. 2.78, leads to the dimensional form of the energy equation

$$\underbrace{\dot{m}(u(r)r - u_1 r_1)}_{\dot{W}_t} \omega + \dot{m} \left[\underbrace{c_p(T(r) - T_1)}_{\Delta h} + \frac{1}{2} \underbrace{\left[(u(r)^2 - u_1^2) + (v(r)^2 - v_1^2) \right]}_{\Delta c^2} \right] = 0. \quad (2.80)$$

Substituting the density of the perfect gas equation

$$\rho(r) = \frac{p(r)}{R_{\text{air}} \cdot T(r)} \quad (2.81)$$

into the continuity equation (Eq. 2.75), yields the algebraic, radial velocity

$$v(r) = \frac{\rho_1 v_1 r_1}{r} \cdot R_{\text{air}} \cdot \frac{T(r)}{p(r)} \quad (2.82)$$

with the specific gas constant

$$R_{\text{air}} = c_p \cdot \left(\frac{\kappa - 1}{\kappa} \right). \quad (2.83)$$

Applying the assumption of the parabolic velocity distribution between the disks for laminar flow conditions, the radial shear stress can be expressed as

$$\tau_r = \mu \left. \frac{dv}{dz} \right|_{\text{wall}} = \frac{3 \cdot \mu}{s} \cdot v(r). \quad (2.84)$$

By analogy to Eq. 2.84, the equation for the tangential shear stress is

$$\tau_\varphi = \mu \left. \frac{dc}{dz} \right|_{\text{wall}} = \frac{3 \cdot \mu}{s} \cdot c(r). \quad (2.85)$$

In order to compute the shear stresses, the dynamic viscosity yields

$$\mu(r, T) = \mu_0 \cdot \frac{T_0 + C_0}{T(r) + C_0} \cdot \left(\frac{T(r)}{T_0} \right)^{\frac{3}{2}}. \quad (2.86)$$

2.8.2 Non-dimensional governing equations

In the following, the transformation of the compressible governing equations into a dimensionless form is conducted. The non-dimensional temperature is defined as

$$T^*(R) = \frac{T(r)}{T_1}. \quad (2.87)$$

The dimensionless enthalpy reads

$$H_1 = \frac{h_1}{u_1^2} = \frac{c_p \cdot T_1}{u_1^2}. \quad (2.88)$$

Using the non-dimensional variables from chapter 2.6.2, defined from Eq. 2.21 to 2.28, together with Eq. 2.37 and inserting them into the compressible continuity equation (Eq. 2.75), leads to the dimensionless density coefficient

$$P_\rho(R) = \frac{\rho(r, T)}{\rho_1} = \frac{r_1 \cdot v_1}{r \cdot v(r)} = \frac{V_1}{R \cdot V(R)}. \quad (2.89)$$

The last step for normalising the governing equations, the non-dimensional dynamic viscosity M_μ often called Sutherland's formula

$$M_\mu(R) = \frac{\mu(r, T)}{\mu_1} = \frac{\mu_0}{\mu_1} \cdot \frac{T_0 + C_0}{T^*(R) \cdot T_1 + C_0} \cdot \left(\frac{T^*(R) \cdot T_1}{T_0} \right)^{\frac{3}{2}} \quad (2.90)$$

is used. The dimensionless, radial momentum equation yields

$$\frac{dP}{dR} - V_1 \cdot \left[\frac{dV}{dR} + \frac{U(R)^2}{V(R)R^2} + 2\beta M_\mu(R) V(R) \right] = 0. \quad (2.91)$$

By analogy with Eq. 2.91, the dimensionless, tangential momentum equation reads

$$\frac{dU}{dR} + R \cdot [U(R) + 2\beta M_\mu(R) \cdot (\Omega - U(R))] = 0. \quad (2.92)$$

The expression for the dimensionless energy equation and therefore the dimensionless temperature $T^*(R)$ in an algebraic formulation is given by

$$T^*(R) = \frac{H_1}{2} \cdot \left[\frac{\Omega}{2} (1 - R \cdot U(R)) - U(R)^2 - V(R)^2 + V_1^2 + 1 \right] + 1. \quad (2.93)$$

The radial velocity from Eq. 2.82 can be transformed in the non-dimensional expression

$$V(R) = \frac{V_1}{R \cdot H_1} \cdot \frac{T^*(R)}{P(R)} \cdot \left(\frac{\kappa - 1}{\kappa} \right), \quad (2.94)$$

using Eqs. 2.21, 2.24, 2.27, 2.83, 2.87, and 2.88.

2.8.3 Compressibility effects and model validation

The influences of compressibility on turbine performance are studied and presented here. Therefore, the numerical solutions of the compressible flow model are compared to the analytical solutions of the incompressible flow description. In order to obtain numerical results, the dimensional, coupled differential momentum equations (Eqs. 2.76, 2.77) can be solved together with the energy equation (Eq. 2.80) for the boundary conditions $u(r_1) = u_1$ and $p(r_1) = p_1$. The dimensionless equivalent to the governing equations (Eqs. 2.91 to 2.93) can be solved for the boundary conditions $U(R_1) = U_1$ and $P(R_1) = P_1$. The computer algebra system Wolfram Mathematica accomplishes this task within a short computational time. Non-dimensional results are predominately presented in this thesis so far. At this point, it is appropriate to provide specific numerical values and to give the reader a feeling for the performance of Tesla turbines. Therefore, the dimensional governing equations are solved for the rotor geometry and the flow conditions, described in Tab. A.1 of Appendix A.1. The performance maps for different mass flows are provided in Fig. 2.34. The results computed from the incompressible and the compressible flow model are compared for different mass flows. Both performance map solutions agree well for low

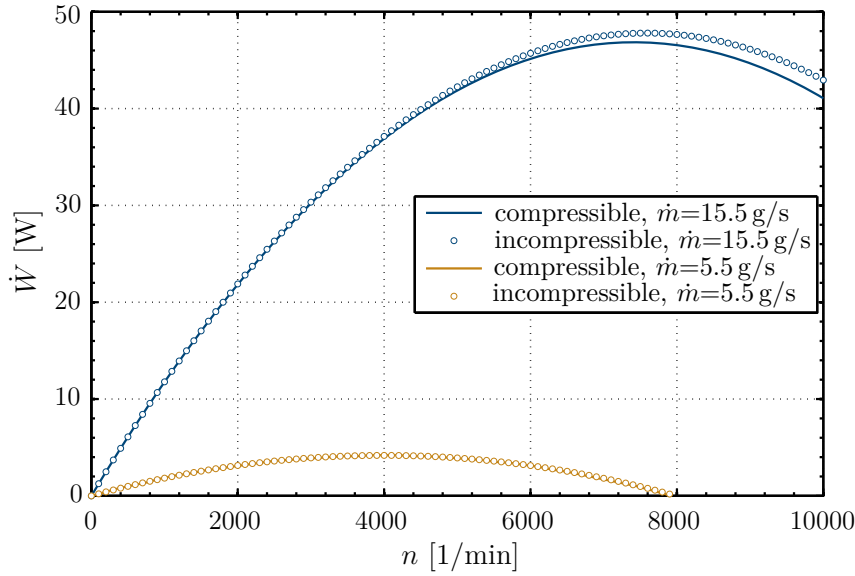
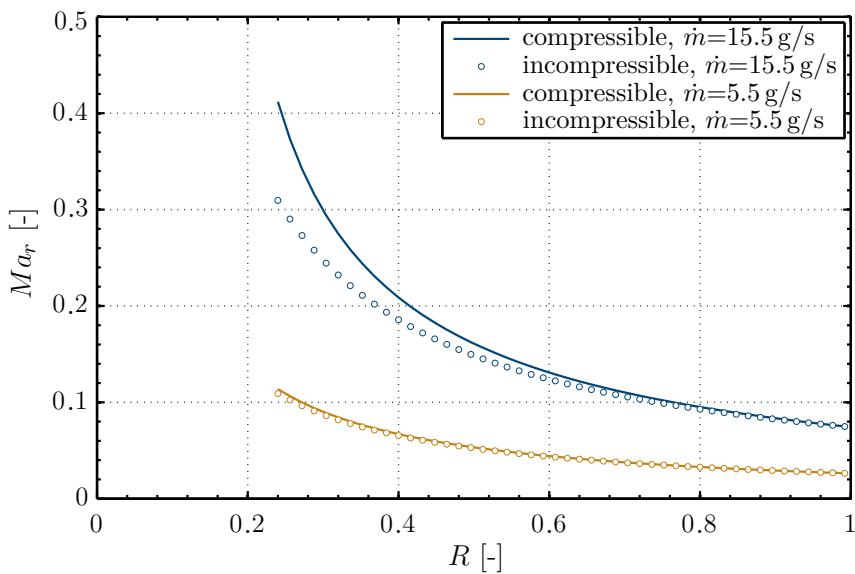


Figure 2.34: Power map comparison

flow rates and therefore low radial Mach numbers. As the rotational speed and the Mach number is rising, the compressible effects become increasingly noticeable. Obviously, shaft power is reduced by the influence of compressibility. Closer examination of the radial Mach number in Fig. 2.35 reveals the effects of compressibility. The torque is decreasing more strongly, compared to the incompressible solution. With increasing radius ratio, the deviation in radial velocity rises more and more. The compressible velocity in radial as well as in tangential direction is always higher compared to the incompressible velocities. The increase in tangential outlet velocity of the compressible case, leads to a lowered performance (cf. Eqs. 2.48, 2.49).

Figure 2.35: Radial Mach number Ma_r across the radius

2.9 Approximate analytical solution of the velocity profiles

The simplified, incompressible, and compressible, laminar flow models assume a parabolic velocity distribution across the axial inter-disk spacing of a Tesla rotor, in order to compute the performance map either analytically or numerically. However, the radial and tangential velocity profiles can directly be derived from boundary layer approximation of the laminar Navier-Stokes-Equations for laminar and incompressible flows.¹ This enables the assessment of the original assumption used in the simplified models.

2.9.1 Radial and tangential momentum equations in boundary layer approximation

In order to describe the flow field in the narrow gap between two co-rotating disks of a Tesla turbine, simplifications of the Navier-Stokes-Equations (Eqs. 2.7 to 2.9, and 2.10) can be made. Assumptions similar to the ones used in standard boundary layer theory are used. Under the assumption of steady-state flow conditions, all derivatives with respect to t vanish

$$\frac{\partial u}{\partial t} = \frac{\partial v}{\partial t} = \frac{\partial w}{\partial t} = \frac{\partial \rho}{\partial t} = 0. \quad (2.95)$$

Furthermore, the gravitational forces

$$g_\varphi = g_r = g_z = 0. \quad (2.96)$$

are neglectable for gases. Under the consideration that the velocities in z -direction are small compared to those in φ - and r -direction, Eq. 2.97 yields

$$w = \frac{\partial w}{\partial r} = \frac{\partial^2 w}{\partial r^2} = \frac{\partial w}{\partial \varphi} = \frac{\partial w}{\partial z} = \frac{\partial^2 w}{\partial z^2} = \frac{\partial p}{\partial z} = 0. \quad (2.97)$$

Further simplifications can be made. As suggested in [134], friction turbines should use guide vanes instead of nozzles for a homogeneous velocity distribution along the circumference. The solution of the flow is assumed to be rotationally symmetrical. Hence, it is permitted to presume that all derivatives with respect to φ vanish

$$\frac{\partial v}{\partial \varphi} = \frac{\partial^2 v}{\partial \varphi^2} = \frac{\partial u}{\partial \varphi} = \frac{\partial^2 u}{\partial \varphi^2} = \frac{\partial p}{\partial \varphi} = 0. \quad (2.98)$$

Laminar and incompressible flow is assumed. Two differential equations for the radial and tangential velocity are obtained.

¹This section was developed in cooperation with Univ.-Prof. Dr. rer. nat. M. Pfitzner and will soon be published in a separate paper.

The momentum equation in radial direction yields

$$\rho \cdot \left(v(r, z) \cdot \frac{dv}{dr} - \frac{u^2(r, z)}{r} \right) + \frac{dp}{dr} = \mu \cdot \left(-\frac{v(r, z)}{r^2} + \frac{d^2v}{dz^2} + \frac{1}{r} \cdot \frac{dv}{dr} + \frac{d^2v}{dr^2} \right). \quad (2.99)$$

The momentum equation in tangential direction can be reduced to

$$\rho \cdot \left(v(r, z) \cdot \frac{du}{d\varphi} + \frac{1}{r} \cdot v(r, z) \cdot u(r, z) \right) = \mu \cdot \left(-\frac{u(r, z)}{r^2} + \frac{d^2u}{dz^2} + \frac{1}{r} \cdot \frac{du}{dr} + \frac{d^2u}{dr^2} \right). \quad (2.100)$$

The Eqs. 2.99 and 2.100 are normalised under consideration of the Eqs. 2.6, 2.21 to 2.24, 2.26, and 2.27. Without loss of generality, the flow profiles $F(R, Z)$ and $G(R, Z)$ in tangential and radial directions are introduced.

$$U(R, Z) = \underbrace{\frac{V_1}{R} \cdot F(R, Z)}_{C(R, Z)} + R \cdot \Omega \quad (2.101)$$

$$V(R, Z) = -\frac{V_1}{R} \cdot G(R, Z) \quad (2.102)$$

Moreover, the continuity equation in radial direction requires

$$\int_{-1}^1 G(R, Z) dZ = 2. \quad (2.103)$$

The zero relative velocity condition at the walls for all radii requires

$$F(R, Z = \pm 1) = G(R, Z = \pm 1) = 0 \quad (2.104)$$

The symmetry of the flow field between the co-rotating disks requires that

$$\frac{\partial}{\partial Z} F(R, Z = 0) = \frac{\partial}{\partial Z} G(R, Z = 0) = 0. \quad (2.105)$$

Following non-dimensionalised differential momentum equations for $F(R, Z)$ in tangential

$$\begin{aligned} & \sigma^2 \cdot \frac{AV_1}{R^2} \cdot \left(\frac{1}{R} \cdot \frac{dG}{dR} - \frac{d^2G}{dR^2} \right) - \frac{AV_1}{R} \cdot \frac{d^2G}{dZ^2} + \frac{V_1^2}{R^3} \cdot F(R, Z)^2 \\ & + \frac{2V_1\Omega}{R} \cdot F(R, Z) - \frac{V_1^2}{R^2} \cdot G(R, Z) \cdot \frac{dG}{dR} + \frac{V_1^2}{R^3} \cdot G(R, Z)^2 - \frac{dP}{dR} + R \cdot \Omega^2 = 0 \end{aligned} \quad (2.106)$$

and for $G(R, Z)$ in radial direction

$$\begin{aligned} & \sigma^2 \left(A \cdot R \cdot \frac{d^2F}{dR^2} - A \cdot \frac{dF}{dR} \right) + A \cdot R \cdot \frac{d^2F}{dZ^2} + V_1 \cdot \frac{dF}{dR} \cdot G(R, Z) \\ & + 2R\Omega \cdot G(R, Z) = 0 \end{aligned} \quad (2.107)$$

are obtained, where

$$A = \frac{1}{Re_u \cdot \sigma}. \quad (2.108)$$

From chapter 2.7 it is known that highly efficient Tesla turbines need a small disk spacings. Therefore, solutions for Eqs. 2.106 and 2.107 with $\sigma \rightarrow 0$ are aspired. Moreover, factorised solutions in tangential

$$F(R, Z) = F(Z) \cdot C(R) \quad (2.109)$$

and radial direction

$$G(R, Z) = G(Z) \cdot D(R), \quad (2.110)$$

are sought. Equation 2.103 additionally requires that

$$D(R) = 1. \quad (2.111)$$

This assumption was also used in [17, 45, 47, 82].

2.9.2 Analytical solution for tangential and radial velocity profiles in the viscous limit

The existence of a solution with

$$C(R) = \text{const.} \quad (2.112)$$

is assumed. This constant can be included into the definition of $F(Z)$. Furthermore, the tangential equation

$$AR \cdot \frac{d^2 F}{dZ^2} + 2R\Omega \cdot G(Z) = 0 \quad (2.113)$$

can be derived. The equation can be solved for any $F(Z)$ by

$$G(Z) = -\frac{A}{2 \cdot \Omega} \cdot \frac{d^2 F}{dZ^2}. \quad (2.114)$$

Now it is possible to use the freedom in the definition of $F_F(Z)$ to find a solution to the radial equation. Inserting Eq. 2.114 into Eq. 2.106 and setting all derivatives of F and G to zero, the simplified radial equation

$$\frac{dP}{dR} = \frac{2V_1\Omega}{N^4R} \cdot \left(4 \cdot \frac{d^4 F}{dZ^2} + N^4 F(Z) \right) + \frac{V_1}{N^4 R^3} \cdot \left(4 \cdot \frac{d^2 F}{dZ^2} + N^4 \cdot F(Z)^2 \right) + R \cdot \Omega^2 \quad (2.115)$$

with

$$N = 2 \cdot \sqrt{\frac{1}{A \cdot \Omega}} \quad (2.116)$$

is obtained. We take the derivative of Eq. 2.115 with respect to Z . This leads to a fifth order ordinary differential equation for $F(Z)$

$$B \cdot \underbrace{\left(F(Z) \cdot \frac{dF}{dZ} + \frac{4}{N^4} \cdot \frac{d^3 F}{dZ^3} \cdot \frac{d^2 F}{dZ^2} \right)}_{\text{non-linear part } F_H(Z)} + \underbrace{\frac{4}{N^4} \cdot \frac{d^5 F}{dZ^5} + \frac{dF}{dZ}}_{\text{linear part } F_F(Z)} = 0, \quad (2.117)$$

where

$$B = \frac{V_1}{R^2 \cdot \Omega}. \quad (2.118)$$

The solution of Eq. 2.117 requires five conditions to be set. Wall boundary and symmetry conditions for $F(Z)$ and $G(Z)$ yield already the four conditions

$$F(\pm 1) = 0, F'(0) = 0, F''(\pm 1) = 0, F'''(0) = 0. \quad (2.119)$$

The fifth condition

$$F'(\pm 1) = \pm \frac{N^2}{2} \quad (2.120)$$

can be derived from the normalisation condition for $G(Z)$ (Eq. 2.103). The solutions of the differential equations depend parametrically on the parameters N and B . Due to the factor $1/R^2$ in Eq. 2.118, it is impossible to find a solution $F(Z)$, which is independent of R . Nevertheless, it is observable that the dependency is only present in the non-linear part of Eq. 2.117. The linear part of the equation however, is fully independent of R . As a first step, the non-linear part is ignored and only the linear part of Eq. 2.117

$$\frac{4}{N^4} \cdot \frac{d^5 F_F}{dZ^5} + \frac{dF_F}{dZ} = 0 \quad (2.121)$$

is solved. The above-mentioned five boundary conditions lead to the analytical solutions of the velocity profiles. The tangential profile yields

$$F_F(Z) = \frac{N \cdot \left(2 \sin\left(\frac{N}{2}\right) \cdot \sinh\left(\frac{N}{2}\right) \cdot \sin\left(\frac{N \cdot Z}{2}\right) \cdot \sinh\left(\frac{N \cdot Z}{2}\right) \right)}{\sin(N) - \sinh(N)} + \frac{N \cdot \left(2 \cos\left(\frac{N}{2}\right) \cdot \cosh\left(\frac{N}{2}\right) \cdot \cos\left(\frac{N \cdot Z}{2}\right) \cdot \cosh\left(\frac{N \cdot Z}{2}\right) + \cos(N) + \cosh(N) \right)}{\sin(N) - \sinh(N)}. \quad (2.122)$$

The shape of the radial profile can be described with the algebraic expression

$$G(Z) = \frac{2N \cdot \cos\left(\frac{N}{2}\right) \cdot \cosh\left(\frac{N}{2}\right) \cdot \sin\left(\frac{N \cdot Z}{2}\right) \cdot \sinh\left(\frac{N \cdot Z}{2}\right)}{\sin(N) - \sinh(N)} - \frac{2N \cdot \sin\left(\frac{N}{2}\right) \cdot \sinh\left(\frac{N}{2}\right) \cdot \cos\left(\frac{N \cdot Z}{2}\right) \cdot \cosh\left(\frac{N \cdot Z}{2}\right)}{\sin(N) - \sinh(N)}. \quad (2.123)$$

In the limit of small N , a series expansion in N^2 of Eqs. 2.122 and 2.123 yields

$$F_F(Z) = \frac{N^2}{16} \cdot (Z^4 - 6 \cdot Z^2 + 5) + O(N^6) \quad (2.124)$$

and

$$G(Z) = -\frac{3}{2} \cdot (Z^2 - 1) + O(N^4). \quad (2.125)$$

The radial velocity profile $G(Z)$ reduces to a parabolic velocity profile in the limit of small N , like it is expected for laminar channel flows. However, the tangential velocity profile is proportional to N^2 . Consequently, the non-linear part scales with N^4 . In the limit of $N \rightarrow 0$ the solution of $F_F(Z)$ from Eq. 2.124 becomes an exact solution of Eq. 2.122. Figures 2.36 and 2.37 show the velocity profiles for $N = 0.1$, $N = 2$ and $N = 5$. The function $F_F(Z)/N^2$ depends only weakly on N itself. It can

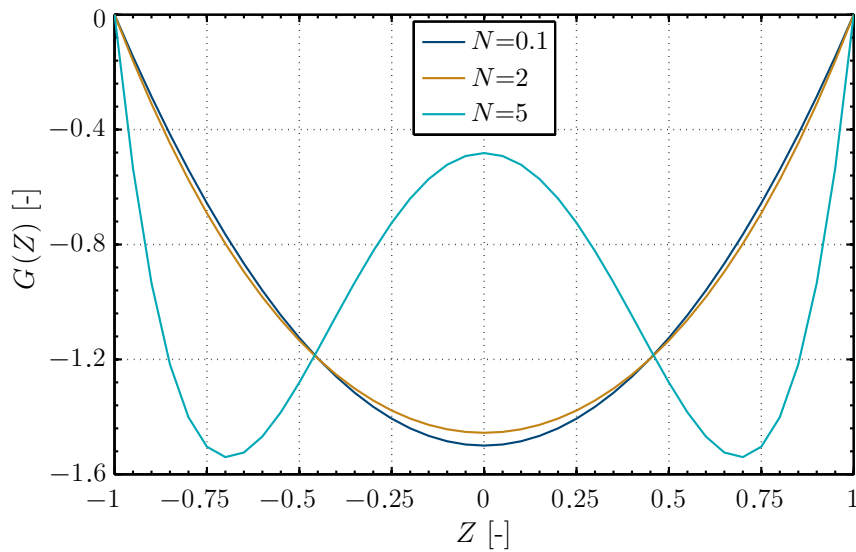


Figure 2.36: Radial profile $G(Z)$ in dependency of N

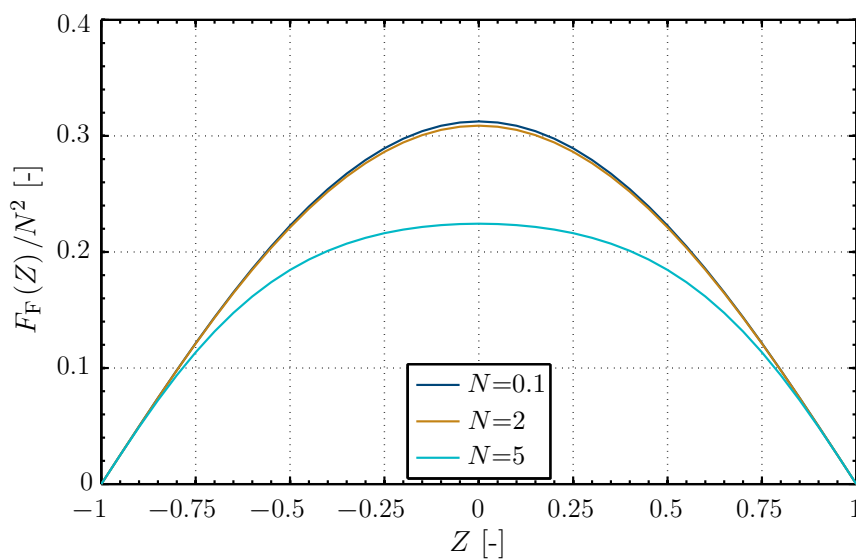


Figure 2.37: Tangential profile $F_F(Z)/N^2$ in dependency of N

be represented in quickly converging Fourier series

$$F_{\text{F}}(Z) = \sum_{n=0}^{\infty} f_n(n, N) \cdot \cos(\pi \cdot Z/2) \quad (2.126)$$

with

$$f_n(n, N) = \frac{8 \cdot N^5 \cdot \left((-1)^n - 1\right) (\cos(N) + \cosh(N))}{\pi n \cdot (4N^4 + \pi^4 \cdot n^4) (\sin(N) + \sinh(N))}. \quad (2.127)$$

Only odd values of n are contributing, because of the wall boundary condition of $F_{\text{F}}(Z)$ at $Z = \pm 1$.

2.9.3 Approximate solution of non-linear tangential momentum equation

The non-linear momentum Eq. 2.117 can not be solved analytically for $F(Z)$. However, it is possible to solve $F(Z)$ numerically for special values of B and N revealing smallest deviations between the functions $F_{\text{F}}(Z)$ and $F(Z)$, as shown in Fig. 2.38. The function $F_{\text{F}}(Z)$ gives a close representation of the real tangential velocity profile

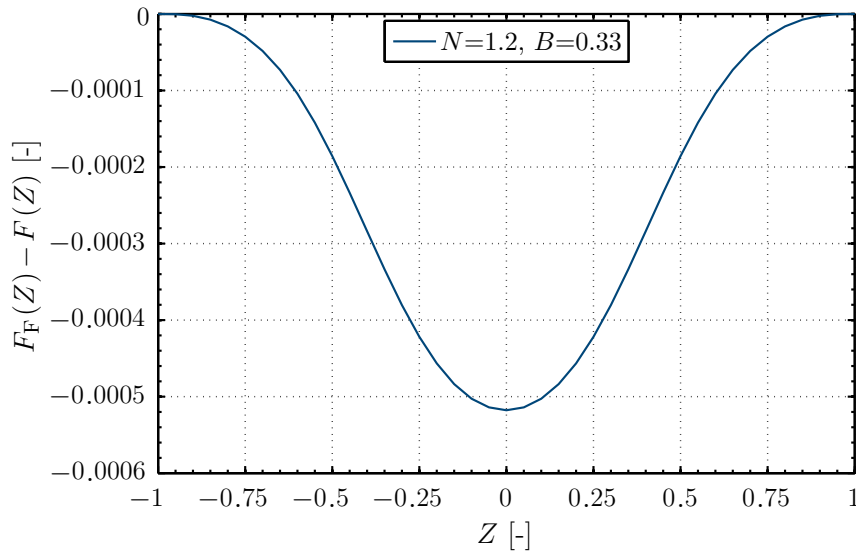


Figure 2.38: Differences between $F_{\text{F}}(Z)$ and numerical solution of Eq. 2.117 $F(Z)$

$F(Z)$ even for realistic Tesla turbines. However, the structure of Eq. 2.117 suggests that the lowest order correction to $F(Z)$ in B to $F_{\text{F}}(Z)$ scale with $B \cdot N^4$, while $F_{\text{F}}(Z)$ scales with N^2 for small N . To clarify this argument, Eq. 2.117 is solved semi-analytically using a truncated Cosinus Fourier series

$$F(Z) = a_0 \cdot \cos\left(\frac{\pi Z}{2}\right) - a_1 \cdot \cos\left(\frac{3\pi Z}{2}\right) + a_2 \cdot \cos\left(\frac{5\pi Z}{2}\right) + b_0 - b_1 \cdot \cos(\pi Z) + b_2 \cdot \cos(2\pi Z) - b_3 \cdot \cos(3\pi Z). \quad (2.128)$$

Due to the required boundary and symmetry conditions, defined in Eq. 2.119

$$F'(0) = 0, F'''(0) = 0 \quad (2.129)$$

and the conditions

$$F(\pm 1) = 0, F'(\pm 1) = \pm N^2/2, F''(\pm 1) = 0, \quad (2.130)$$

the Fourier coefficients are defined as follows

$$a_2 \rightarrow -\frac{\pi a_0 + 3\pi a_1 - N^2}{5\pi}, b_2 \rightarrow \frac{1}{5}(-9b_0 - 8b_1), b_3 \rightarrow \frac{1}{5}(4b_0 + 3b_1). \quad (2.131)$$

The remaining Fourier coefficients a_0, a_1, b_0, b_1 are determined for $F(Z)$ to approximately solve Eq. 2.117. The coefficients can be appraised by inserting the approximation equation (Eq. 2.128) into Eq. 2.117, multiplying successively by $\sin(\frac{\pi}{2}Z)$, $\sin(\pi Z)$, $\sin(3\frac{\pi}{2}Z)$, $\sin(2\pi Z)$, integrating over Z from -1 to 1 , setting all four equations to zero and seeking solutions in $\{a_0, a_1, b_0, b_1\}$.

Applying this procedure only to the linear part of Eq. 2.117, which is defined in Eq. 2.121, the solution in $\{a_0, a_1, b_0, b_1\}$ can be found analytically. The first three terms in a series expansion of the coefficient a_0 in the approximation for $F_F(Z)$ in N yield

$$a_{0,\text{lin}} \approx 0.30543 \cdot N^2 - 0.00051953 \cdot N^6 + 3.8157 \cdot 10^{-7} \cdot N^{10} + O(N^{14}). \quad (2.132)$$

However, Eq. 2.128 also should represent $F(Z)$ accurately over a wide range of values for N . Inserting

$$F(Z) = F_F(Z) + F_H(Z) \quad (2.133)$$

into Eq. 2.117 and linearising in $F_H(Z)$ yields the fifth order ordinary differential equation

$$\begin{aligned} \frac{4}{N^4} \cdot F_H''''''(Z) + \frac{4B}{N^4} \cdot (F_H(Z)''' F_F''(Z) + F_F'''(Z) F_H''(Z) + F_F''''(Z) F_H'(Z) \\ + F_H'(Z) + B \cdot (F_H'(Z) F_F'(Z) + F_H(Z) F_F(Z) + F_F(Z)^2) = 0. \end{aligned} \quad (2.134)$$

Approximating $F_H(Z)$ according to Eq. 2.128 and requiring $F_H(\pm 1) = 0$, $F_H'(\pm 1) = 0$, and $F_H''(\pm 1) = 0$, the coefficients of $F_H(Z)$ can be solved in the same way as described before. A series expansion of the coefficients in N and B reveals that indeed the lowest order contributions in the coefficients of $F_H(Z)$ are proportional to $B \cdot N^4$, $B^2 \cdot N^6$, $B \cdot N^8$, and $B^3 \cdot N^8$.

Since it turns out that the linearisation in $F_H(Z)$ restricts the validity of the solution to $N < 1$ and since the coefficients $\{a_0, a_1, b_0, b_1\}$ are not analytically solvable with Eq. 2.128 inserted in Eq. 2.117 and integrated with the above-mentioned lowest Fourier modes, the information gained from the asymptotic analysis above is used to fit the Fourier coefficients of the full solution of Eq. 2.117 in the approximation Eq. 2.128 to lowest order in B and N .

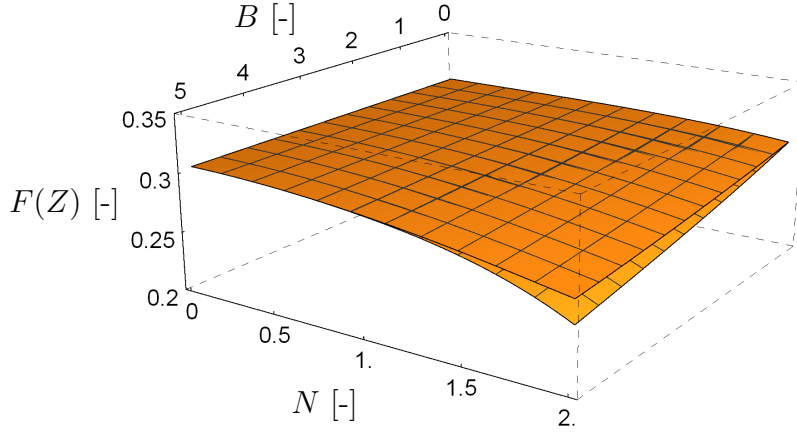


Figure 2.39: Numerical solution for a_0/N^2 (lower surface) with approximation of function $F(Z)$ from Eq. 2.133

Figure 2.39 shows the numerical solution for a_0/N^2 together with the approximation $F_F(Z) + F_H(Z)$. The almost linear dependence on B even for values up to $B = 5$ is a highlight. Using the lowest order terms in N and B ($N^2, B \cdot N^4, N^6, B \cdot N^8$) to fit to the numerical solution of Eq. 2.117 for the coefficients $\{a_0, a_1, b_0, b_1\}$ (Eq. 2.135) in the range of $0 \leq N \leq 2$ and $0 \leq B \leq 5$, we obtain

$$\begin{aligned}
 a_0(N, B) &= (a_{0,1} \cdot N^2 + a_{0,2} \cdot BN^4 + a_{0,3} \cdot N^6 + a_{0,4} \cdot BN^8) \\
 b_0(N, B) &= (b_{0,1} \cdot N^2 + b_{0,2} \cdot BN^4 + b_{0,3} \cdot N^6 + b_{0,4} \cdot BN^8) \\
 a_1(N, B) &= (a_{1,1} \cdot N^2 + a_{1,2} \cdot BN^4 + a_{1,3} \cdot N^6 + a_{1,4} \cdot BN^8) \\
 b_1(N, B) &= (b_{1,1} \cdot N^2 + b_{1,2} \cdot BN^4 + b_{1,3} \cdot N^6 + b_{1,4} \cdot BN^8).
 \end{aligned} \tag{2.135}$$

The coefficients $\{a_{0,i}, a_{1,i}, b_{0,i}, b_{1,i}\}$ of Eq. 2.135 are listed in Tab. 2.1. The theo-

i	1	2	3	4
$a_{0,i}$	0.3053900	-0.00173770	-0.00062097	-0.000033053
$b_{0,i}$	0.0045615	0.00054988	0.00020233	0.000014722
$a_{1,i}$	0.0050248	0.00065492	0.00023939	0.000012765
$b_{1,i}$	-0.0062001	-0.00074454	-0.00027540	-0.000019791

Table 2.1: Coefficients of Eq. 2.135

retical investigations show that the deviation between the numerical solution of Eq. 2.117 and the Fourier approximation above is negligible. Figure 2.40 shows the maximum values of $F(Z)$ for a range of parameters. $F(0)$ is evaluated with this Fourier approximation as function of N and B in the range of $0 \leq N \leq 2$ and $0 \leq B \leq 5$. It proves that the velocity profile changes less than 7% for $B = 5$ due to the non-linear term in Eq. 2.117 at $N = 2$ and less than 2% for $N < 1$. It is thus demonstrated numerically that $F_F(Z)$ is indeed also a very good approximation to the solution of Eq. 2.117 in this range of parameters. Since the boundary condition Eq. 2.120

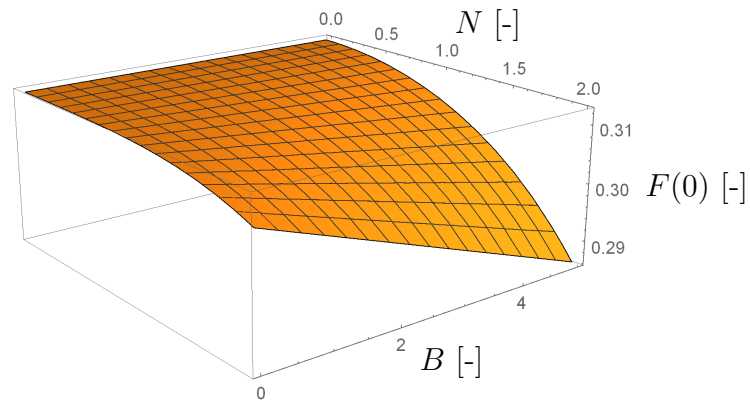


Figure 2.40: Dependence of $F(0)$ in Fourier approximation for $0 \leq N \leq 2$, $0 \leq B \leq 5$

applies to $F(Z)$ as well as to $F_F(Z)$ due to the normalisation condition of the radial velocity component, the wall shear stress of the tangential velocity component is not affected by the non-linear term of Eq. 2.117.

Extensions of the above-described theoretical investigations regarding the solution of the radial pressure equation will be presented in a separate paper.

3 Numerical investigations

The continuously increasing computing performance allows detailed numerical analyses in aerodynamics and turbomachinery. With this development, CFD is becoming a more and more powerful tool for the design of turbomachinery and the prediction of fluid flows in general. The computationally intensive numerical analyses are in competition with experimental approaches that entail substantial costs and effort. However, CFD offers the possibility to gain insights into details of the flow field that are extremely difficult to measure. Nevertheless, measurements are desperately needed to validate numerical results, especially when turbulence models are used to predict the flow regime. The numerical constants of the turbulence models are valid for most of the standard CFD applications. However, it is not clear, if the turbulent flow field of a Tesla turbine is reproduced correctly by numerical means. The velocity distribution between the disks of a Tesla rotor and the resulting wall shear stress is crucial for its performance. Deviations from reality caused by modelling errors have a particularly strong impact on the results.

3.1 Numerical approach

CFD tools are applied for different purposes in this thesis. They are used to validate the incompressible, laminar theory, to optimise rig components, and for the comparison to the experimental results carried out in this thesis. All simulations assume steady flows and are carried out with ANSYS CFX 14.0 and 16.1. Laminar flow calculations are considered to be incompressible. Turbulent flows are computed with Reynolds-Averaged-Navier-Stokes-Equation models (RANS) using the standard SST or the $k-\omega$ turbulence model. Mesh independence studies are performed for all grids used in this thesis.

At first, the laminar, incompressible flow model, which is described in chapter 2.6, is validated by laminar CFD calculations, considering the rotor flow only. Different inlet profiles and their influences on turbine performance are tested. In order to compare the numerical results with those obtained from the incompressible flow model, the outlet is assumed to be ideal. The boundary conditions and the computational domain can be found in chapter 3.2.1. The computational mesh is illustrated and described in chapter 3.3.1. The comparison of the CFD results with those obtained from the incompressible flow model are presented in chapter 6.1.

During the development of the test rig, the entire turbine is simulated. It is used to optimise the rig components guide vanes, the rotor, and the outlet passage. In this specific case, the $k-\omega$ turbulence model is chosen, although the rotor flow might have still be treated as laminar. Guide vanes, stator-rotor interface, rotor, and disk spacers at the outlet are considered. Turbulence is mainly induced by the passage

between stator and rotor and the axial step at the rotor outlet (Figs. 3.4, 4.25). The radial gap between guide vanes and rotating disks is 3 mm. The choice of this gap is conservative in order to avoid contact during operation. However, the complex outlet design is necessary for the flexible adaptation of the inter-disk spacing. The (total) energy equation including the viscous work term is simultaneously solved with the momentum equations. The spatial resolution of the mesh near the walls is refined in order to create a dimensionless wall distance of approximately $y^+ \approx 1$ in case of turbulent flows. The boundary conditions are described in chapter 3.2.2 and the computational grid is introduced in chapter 3.3.2. The results of the rig component optimisation are shown in chapter 4.6.

Numerical simulations are carried out for the validation of the velocity components, which are measured inside the rotor. Only the pure rotor flow is simulated in this case. Depending on the operating conditions, the flow inside the test rig is either laminar or turbulent. The flow is treated as laminar and incompressible, whenever the experimental data indicated that the velocity profiles are laminar. More details about the classification of the flow fields can be found in chapter 6.3.4. The axial velocity distribution at the rotor inlet is modelled using the ANSYS block-profile approximations. The outlet is assumed to be ideal. The standard SST turbulence model is applied for turbulent flows. Furthermore, the dimensionless wall distance of in the computational grid is approximately $y^+ \approx 1$. The flow is simulated under the assumption of compressible flow conditions. Therefore, the (total) energy equation including the viscous work term is additionally solved. The computational domain, as well as the mesh of the rotor are illustrated and described in the chapters 3.2.1 and 3.5. The numerical results are compared to the experimental data introduced in chapter 6.3.

3.2 Computational flow domain with boundary conditions

The flow domains with the boundary conditions, used in this thesis, are shown hereafter. In general, the mass flow rate is used as the parameter at all inlets. Whenever the rotor flow is simulated without guide vanes, the inlet angle α (or V_1) is specified by the direction of the mass flow at the rotor inlet. The outlet area of the flow domain is applied with the ambient pressure.

3.2.1 Domain for the validation of the theoretical flow model and the experimental results

The flow domain introduced in Fig. 3.1 is used for the validation of the laminar, incompressible flow model introduced in chapter 2. Furthermore, it is utilised for the computation of the flow field for the comparison with the experimental data in chapter 6. For lowering the number of cells in order to achieve a shorter computational time, a 90° section of the rotor is modelled. Rotational periodicity using a

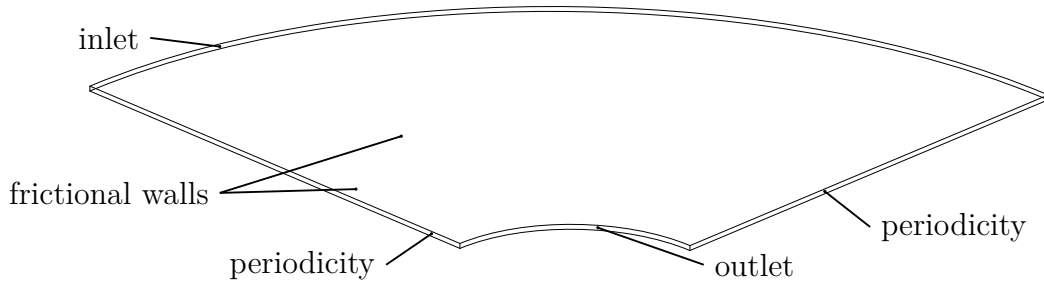


Figure 3.1: Boundary conditions of the rotor model with ideal inlet and outlet

1:1 periodic interface is therefore applied at the boundaries of the computational flow domain. Being aware of the consequences of the simplification, all (frictional) walls are computed with the adiabatic heat transfer option. Figure 3.1 illustrates the boundary conditions, which are applied in both sets of simulations.

In case of the flow model validation, the mass flow rate is imprinted at the inlet of the rotor under different angles of attack. The angles are specified in chapter 6.1.1. Depending on the individual investigation in chapter 6.1.1, either the ANSYS block-profile approximations or the inlet profiles $F_{C,n}(R, Z)$ in tangential and $G_C(R, Z)$ in radial direction are chosen. Atmospheric pressure is assumed at the rotor outlet.

For the validation of the measurement results, the outlet angle of the guide vanes, which are obtained from the CFD results in chapter 4.6, are used at the inlet of the rotor. Furthermore, the ambient pressure is recorded during the measurements and is applied at the outlet in the CFD simulations for each operational point.

3.2.2 Domain for the optimisation of rig components

For the optimisation of the test rig components, the entire turbine consisting of stator and rotor is modelled. The geometry of guide vanes and rotor corresponds exactly to the dimensions of the test rig. The guide vanes are supplied with air by an annular plenum. Their inlet is at the radius of 238 mm and delivers the flow to the rotor at the desired inflow angle and the radius of 128 mm. The outer radius of the rotor is 125 mm and the inner radius is 45 mm. The height of the guide vanes and the rotor is 0.5 mm. However, the domain of the guide vanes is fixed. However, the domain of the rotor is rotating. The computations are carried out using different rotational speeds between 1000 and 10000 min^{-1} and several mass flow rates between 0.2 and 20 g/s. The stage rotor interface is applied to connect the stator to the rotor. In order to overcome the multiple frame of reference problem, this model generates a time-averaged steady-state solution, as described in the ANSYS Theory Guide [136]. Transient effects are neglected at the frame interface. However, the stage modelling approach circumferentially averages the fluxes at the domain interface. Therefore, the GGI option has to be applied, which conserves the fluxes and features non-aligned nodes across the interface, as remarked in the ANSYS Theory Guide

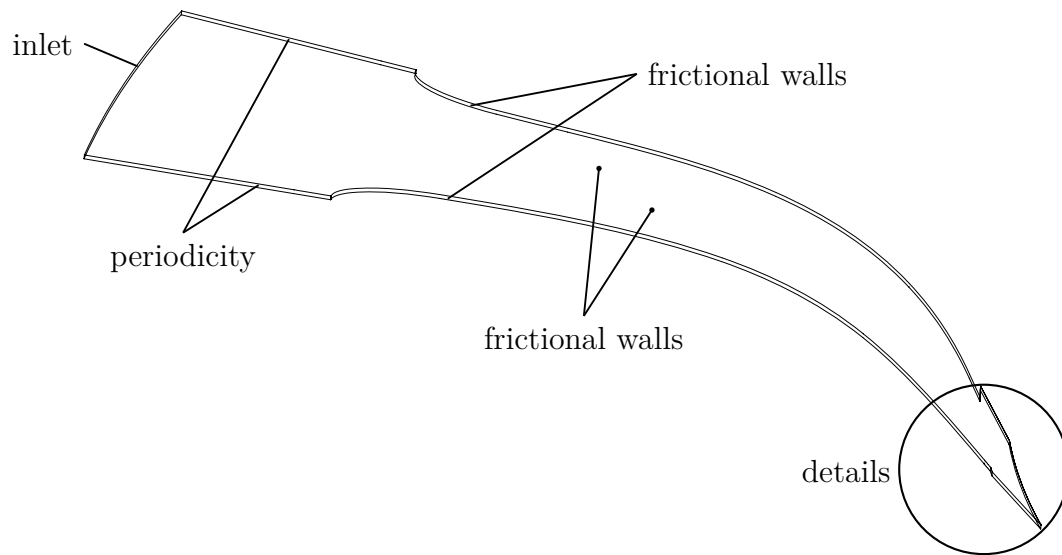


Figure 3.2: Boundary conditions of the guide vane model

[136]. The 36 profiles deliver a swirled inflow for the rotor at the desired inlet angle, described in chapter 2.7.2. To reduce the number of cells, nine 10° sections of a single flow channel of the guide vanes are used. In addition to that one 90° section of the rotor is modelled, because of the symmetry of the four disk spacers near the outlet at the centre of rotation. Rotational 1:1 periodicity is applied at the boundaries. Besides the gap between the disks, the flow domain of the rotor includes the spacers near the outlet at the centre of rotation. The desired mass flow rate normal to the inlet of the guide vanes is specified. Atmospheric pressure is assumed at the rotor outlet. The walls of guide vanes and rotor are no-slip boundaries. The adiabatic heat transfer option is chosen for all walls. Figure 3.2 shows one 10° section of the guide vanes' flow domain. An enlarged view of Fig. 3.2 reveals the details near the

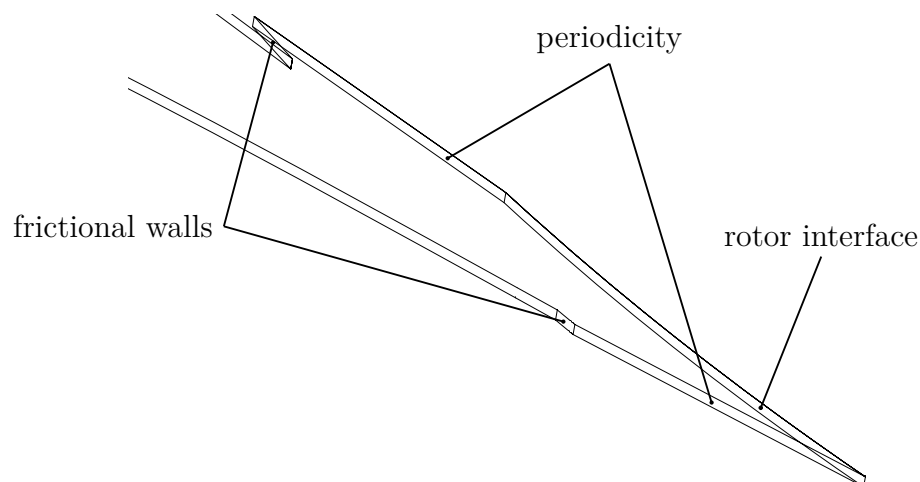


Figure 3.3: Detailed view of the guide vanes' trailing edge in Fig. 3.2

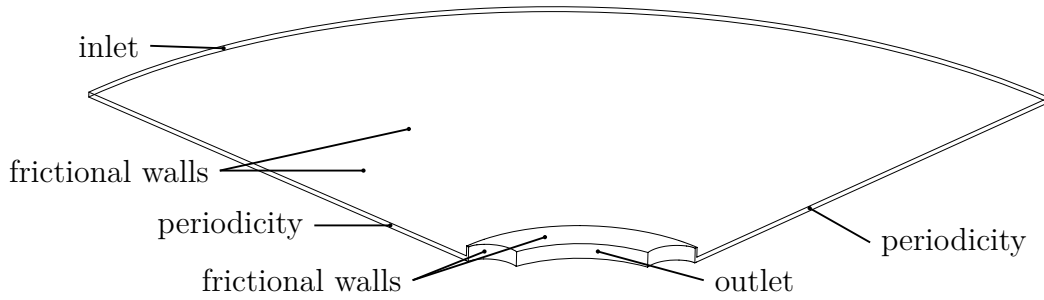


Figure 3.4: Boundary conditions of the real test rig rotor

stator-rotor interface in Fig. 3.3. Moreover, Fig. 3.4 illustrates the flow domain of the rotor. The applied boundary conditions are tagged in the Figs. 3.2, 3.3, and 3.4.

3.3 Computational grid

The generation of computational grids is realised with ANSYS ICEM 14.0 and 16.1. All grids are pure hexahedral meshes. The preparation of hexahedral meshes requires more effort compared to tetrahedral computational grids. Nevertheless, higher resolutions with a lower number of cells are achievable, particularly in boundary layers. This is due to the fact that tetrahedral meshes ideally require isosceles triangles on their sides for best convergence behaviour. The deviation from equal proportions of height to length of hexahedral meshes do not result in a substantial increase of numerical errors. All simulations are performed using double precision accuracy.

3.3.1 Mesh for the validation of the theoretical flow model and the experimental results

The geometry of the computational rotor domain corresponds to the dimensions of the test rig's rotor. The outer radius is 125 mm and the inner radius is 30 mm. The inter-disk spacing is 0.2 mm in case of the theoretical flow modelling, because high- β flows are desired. For the comparison of the measurement results, the rotor mesh has a gap width of 0.5 mm, as it is used in all PTV tests carried out. The mesh of the rotor, which is used in the simulations for the numerical validation of the incompressible theory and of the measurement results consists of approximately 2.2 million hexahedral elements. To find a mesh independent solution for the laminar and the turbulent cases, the grid is refined until the outlet velocities are converged. Figure 3.6 shows a detailed view of the distribution of the computational cells across the inter-disk spacing, which is marked in Fig. 3.5. The residual convergence of the rotor simulations carried out here is $1 \cdot 10^{-7}$ RMS and $1 \cdot 10^{-5}$ MAX.

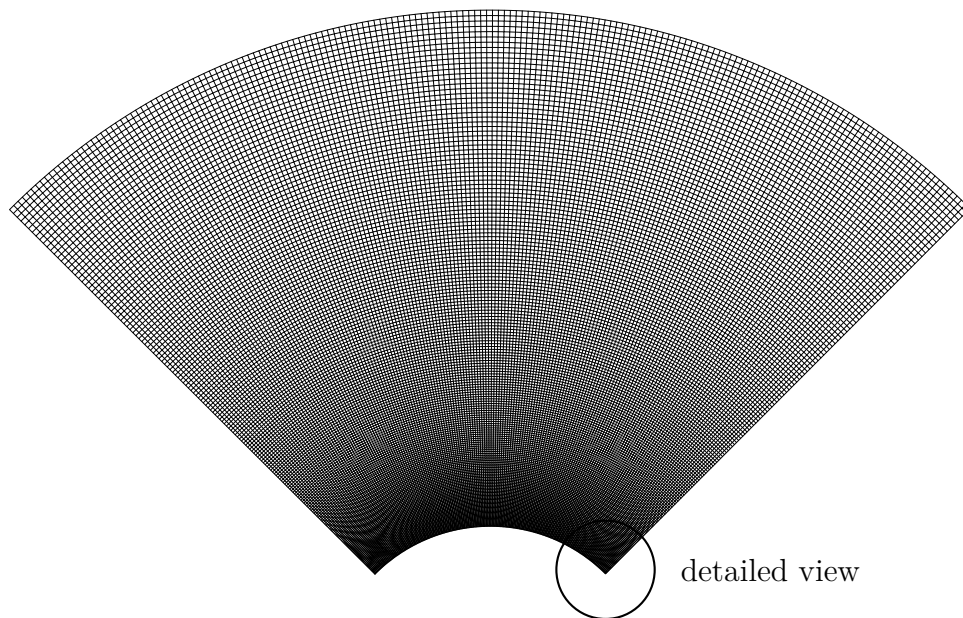


Figure 3.5: Mesh of the rotor

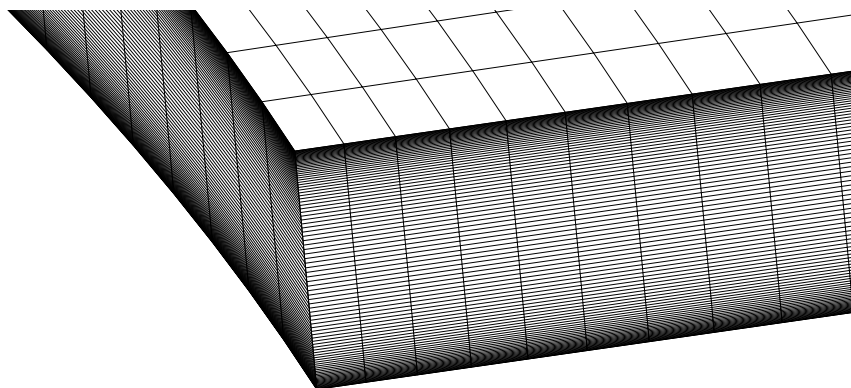


Figure 3.6: Detailed view of inter-disk distribution of cells marked in Fig. 3.5

3.3.2 Mesh for the optimisation of rig components

The generation of the stator mesh with a good resolution of the boundary layer is achieved using the ICEM O-grid blocking strategy around the profiles. It consist of about 450000 hexahedral elements. The ICEM O-grid blocking strategy is used around the disk spacers at the outlet, in order to create a highly resolved rotor mesh in the boundary layer. However, the mesh of the stator and rotor consist of about 3 million hexahedral elements in total. The residual convergence of the entire stator and rotor configuration is $1 \cdot 10^{-5}$ RMS and $1 \cdot 10^{-3}$ MAX. The meshes of guide vanes and rotor are illustrated in Figs. 3.5 and 3.6.

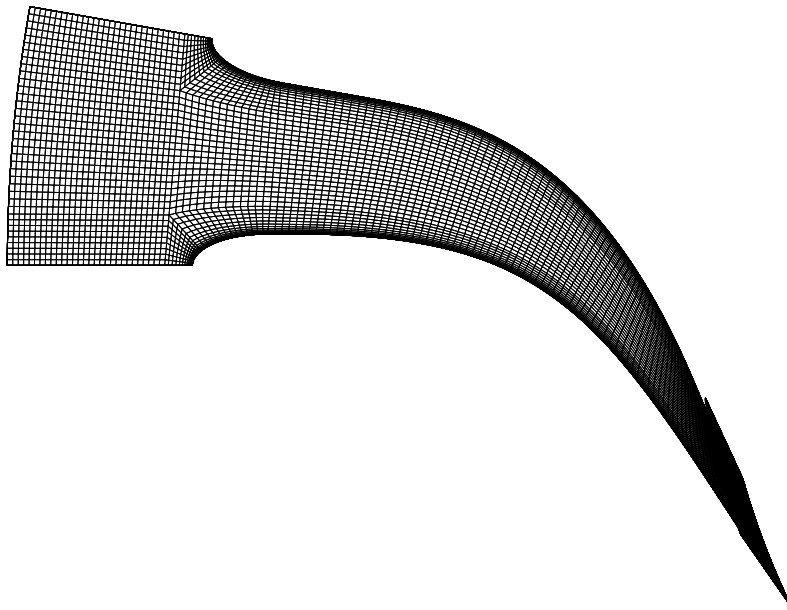


Figure 3.7: Mesh of guide vanes

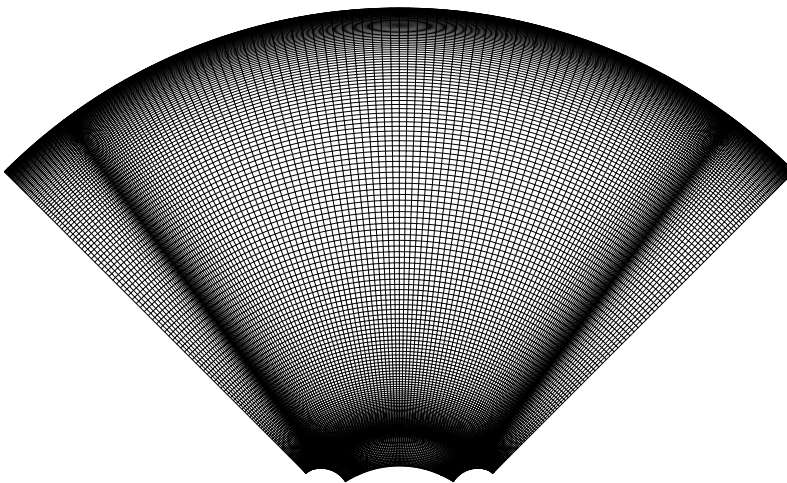


Figure 3.8: Mesh of test rig rotor with modelled disk spacers

4 Test rig

The test rig is developed and designed to measure the radial and tangential velocity distribution across the inter-disk spacing of a Tesla turbine at different radial positions. Earlier investigations, reported in the literature applied measurement techniques like hot-wire anemometry, which require a large inter-disk spacing. The usefulness of those results is limited, due to accuracy limitations caused by blockage of the flow and the unsuitably large gap width. Furthermore, provision is made for measuring performance maps and efficiency curves of future multi-disk rotors. Therefore, the test rig design is flexible and the components are modularly exchangeable. However, the primary goal of this test facility is to determine the velocity profiles non-intrusively with a high spatial resolution in a typical small-gap configuration, as clarified in chapter 1.3.4. Beginning with the definition of the working medium, a feasibility study, and the resulting requirements in regard to the test facility, this chapter leads the reader from the evaluation of different design concepts to the dimensioning procedures and finally to the favourite mechanical rig design. The rotor dimensions are based on the simplified, theoretical models for incompressible, and laminar flow, which are described and extensively evaluated in chapter 2.6 and chapter 2.7. Furthermore, the state-of-the-art measurement technology, which is implemented in the test rig, as well as the developed measurement and control software, is described here. Detailed information about the particle imaging measurement setup is given in chapter 5. Digital images of the test rig can be found in Figs. A.9 to A.13 in Appendix A.1. The manufacturing of the entire test rig was managed by the company consulting engineers Dingeldein from Michelstadt.

4.1 Working medium

Several working fluids are conceivable. Most Tesla turbines operate with water, low-boiling mediums, or air. Water is incompressible and would perfectly fit to the theoretical solution. However, it would be impossible to obtain compressible results and would constitute a restriction of the test rig. Moreover, the spatial access to the measuring volume would be more difficult. Low-boiling mediums like Hydrofluorocarbons are interesting for ORC cycles, but the additional effort for the cycle would have exceeded the budget. It is also challenging to ensure the tightness of the entire system. An existing air compressor, which fills the pressure vessels of a small transonic wind tunnel, delivered enough mass flow for one pair of disks. It is also possible to enhance the available mass flow in the future by connecting additional compressors to the system for multi-gap rotors. Therefore, it was decided to choose air as the operating medium. The compressor constantly delivers about 850 l/s at a flow pressure of 14 bar. The pressure vessels have a total volume of 1.05 m³. The first rotor design calculations revealed that the disk spacing can be less or equal

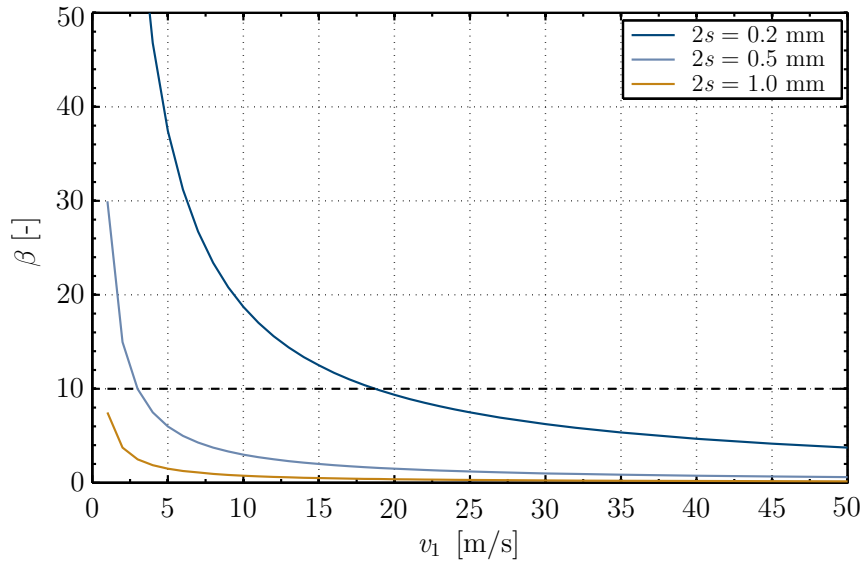


Figure 4.1: Achievable values of β [134]

to 1 mm for air and values of β greater than ten. The test rig should in general be able to handle high and low β values. Figure 4.1 shows the values of β , which are achievable with the intended gap widths and the working medium air. As β should be above a value of ten, low radial inlet velocities are required. Lower disk-spacing leads to higher values of β .

4.2 Feasibility study of the measurement task

The detailed analysis of the incompressible theory, described in chapter 2.6 resulted in a good understanding of the operating conditions of a Tesla turbine. It was possible to determine the size and the geometry of a Tesla rotor for the flow field measurements. During this time, preliminary tests were conducted. For the demonstration of the measurement method and to gain knowledge for the test rig design, the velocity distribution between two parallel, flat glass plates was determined. Measurement tasks in cavity-like volumes require three-dimensional measurement techniques. Planar techniques fail to resolve the strong velocity gradients with dimensions on the order of 1 mm due to the averaging of the particle motion over the light sheet thickness. Therefore, the tests are carried out by means of 3D tomographic reconstruction with PTV techniques, as described in [137].

The measuring section, shown in Fig. 4.2, consists of two parallel and flat glass plates (300 mm \times 75 mm \times 10 mm) with a gap spacing of 1 mm. First PIV tests with acrylic glass failed, because of the low signal-to-noise ratio of the particle images scatter. The test section was directly connected to a seeding generator via a pressure reducing valve. Two LaVision Imager sCMOS cameras with two 2 \times teleconverters and a 100 mm Zeiss macro planar lens were used. An Innolas Spitlight 400 laser was

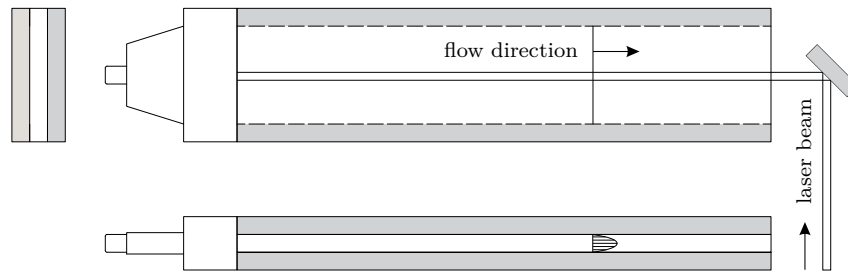


Figure 4.2: Measuring section for first tomographic PIV tests

applied for DEHS tracer particle illumination. In order to create a divergent beam to ensure that the whole gap is illuminated, two adjustable spherical lenses with a focal length of $f=-50$ mm and $f=+50$ mm were used. The standard technique to derive calibration points is to place a calibration target within the measurement volume. For three-dimensional techniques, calibration targets have to be traversed in depth direction. Therefore, the target was mounted on a micrometer screw to take an image at two locations in depth. The calibration target, illustrated in Fig. 4.3, was a printout of a point matrix generated by a \LaTeX code. The diameter of the points is 0.5 mm and the distance between the points was 1.5 mm. It was measured with a sliding caliper to ensure the correct diameters and distances between the calibration points. During calibration, the rear glass plate had to be removed, as shown in Fig. 4.4. The critical Reynolds number for rectangular cross sections with

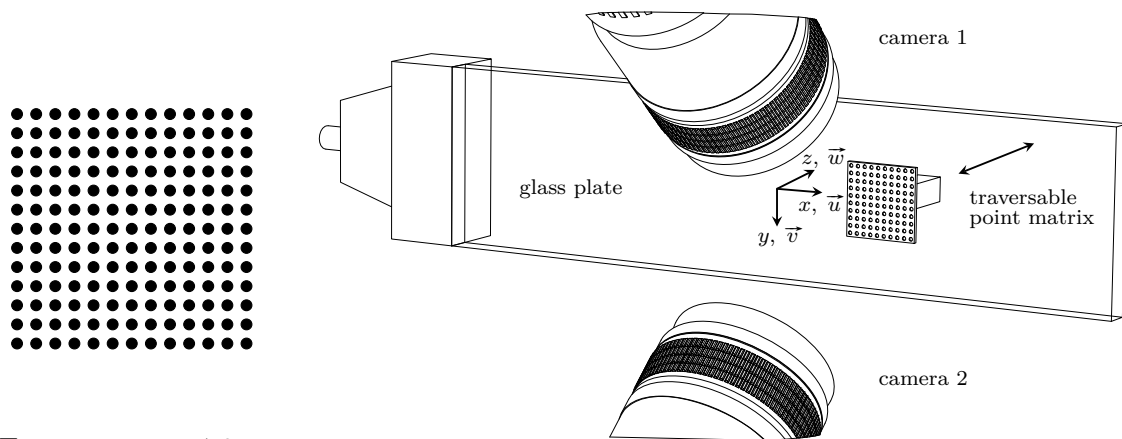


Figure 4.3: Calibration target

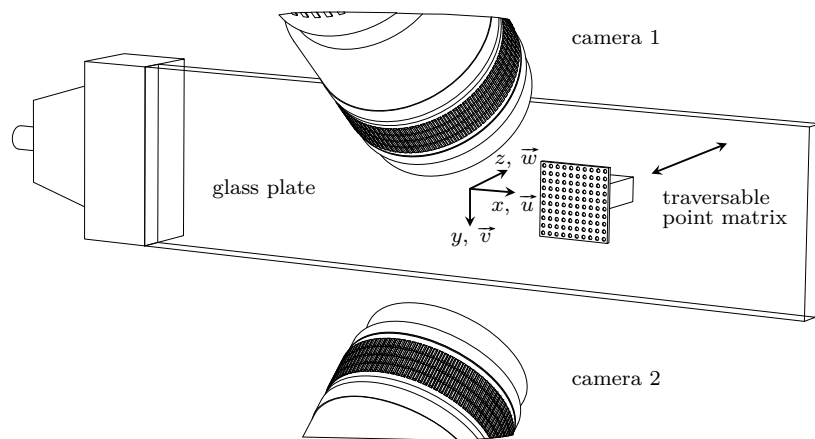


Figure 4.4: Stereo PIV set-up for calibration

high aspect ratios using the hydraulic diameter as the characteristic length was around 2800, as described in [138, 139]. The flow velocity was set to values below 20 m/s in order to fulfil the requirements to achieve laminar flow conditions. The 350 double-frame images ($\Delta t=10$ μ s), which were recorded, were post processed and then used for the tomographical volume reconstruction with the commercial DaVis fast M.A.R.T. algorithm. This comprises stabilising the bouncing images, suppressing the reflections by subtracting averaged images, applying non-linear filters, and setting

the unlit background to a light intensity of zero using a threshold, as outlined in [137]. Due to the relatively low particle image density, two cameras are sufficient for the tomographic reconstruction. A standard tomographic evaluation using a correlation of interrogation volumes requires large interrogation volumes. This finally leads to a low spatial resolution. In order to resolve strong velocity gradients, a particle tracking code described in [140] was applied. The particle positions, which are required for the tracking algorithm, were determined by 1D Gauss fits of the particles' light intensity in the reconstructed volumes in all three directions in space. Figure 4.5 shows the laminar velocity distribution between the stationary glass plates determined using the evaluation method described above. Despite a certain noise

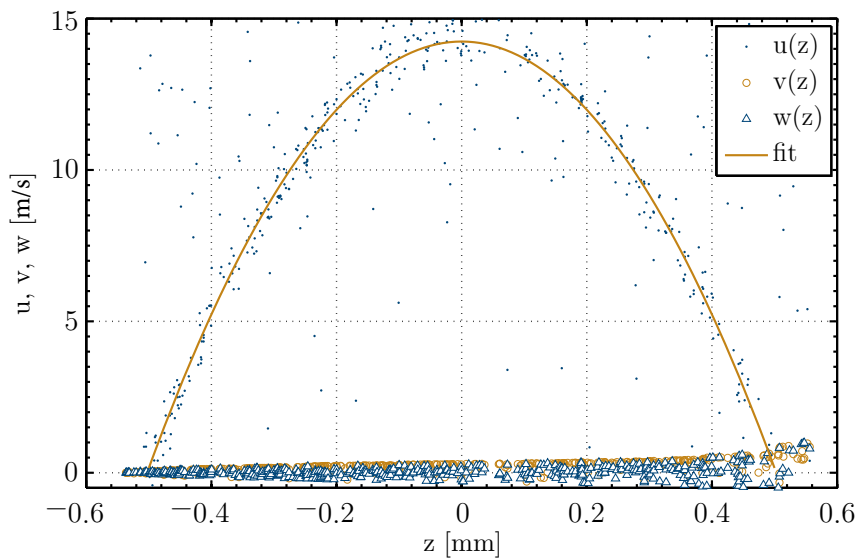


Figure 4.5: Measurement results obtained from particle tracking in tomographically reconstructed volumes (evaluation of ten double-frame volumes)

level (spurious displacements), a curve fit was possible and the velocity distribution is clearly visible. However, the remaining velocity components, which should be zero, show a slight increase across the gap. It is difficult to find a suitable explanation, but the reason for that might be an error in alignment of the glass plates. The wall in positive z -direction is the rear glass plate. During calibration, the rear glass plate had to be removed. The target was perfectly aligned with the front glass plate in the first of two positions in depth. In the second position in depth, the target was not aligned to any walls. As the target was glued to a flexible object slide, possible deformations cannot be excluded. Nevertheless, the problem likely originates from the calibration method and not from physical reasons. The position of both walls can be determined, because of the no-slip condition at the walls. The average gap width was computed from all images yielding a deviation of less than 1% from the theoretical gap. The successful feasibility study provides a deeper understanding of how to illuminate the DEHS particles behind uncoated glass plates. Light sheet illumination was not successful, because of the low signal. Instead, better results were achieved using a

volume illumination. In order to light up the particles across the entire gap, the laser beam had to be adjusted with care. Different settings had to be tested, before getting acceptable results. A divergent beam moderated this effect. It is concluded from the experience of the measurements that the contamination of the glass plates originated from the seeding is not negligible. Therefore, a dismountable rotor is required for cleaning the windows inside the gap after each run. The introduced standard calibration procedure worked well and provides reasonable measurement results. Nevertheless, possible misalignments of the calibration target and limited spatial accessibility to the rotor gap cannot be excluded. Therefore, a non-intrusive calibration method for three-dimensional particle imaging was developed. A detailed description of this method can be found in chapter 5.5. The computation time of post processing was significantly improved and deemed to be acceptable. However, it was still too long for large numbers of measurement data, as parameters are desired to be studied. Therefore, a quicker evaluation method had to be found, while developing the test facility.

4.3 Requirements

The desirable operating conditions of the rotor could be derived from the theoretical knowledge, which was gained from the extensive analyses of the theoretical models (cf. chapter 2). Moreover, the preliminary PTV tests, outlined in chapter 4.2, offered the possibility to extend the know-how by the practical part. Consequently, it was possible to specify the requirements for the design of the test rig. The most important issues are also listed in [134].

- adjustable and decomposable Tesla rotor
- test rig suitable for single gap or multiple-disk rotors
- lowest flow disturbance by additional parts like spacers
- maximum optical accessibility for PTV measurements
- enough space for both sCMOS cameras
- lowest disk deformation under load
- adequate safety coefficient $s_f \leq 2.0$
- low vibration and low residual imbalance
- modular concept for future adaptations
- exchangeable guide vanes or nozzles
- optimum dimensionless parameters: $\beta \leq 20$, $V_1 \approx 0.3$

- adequate working medium with $10 \leq \beta < 20$
- maximum circumferential disk speed at the outer radius should reach velocities, where compressibility effects are expectable
- adjustable level of inlet pressure and/or mass flow
- ambient pressure at rotor outlet
- electric motor powering the rotor (instead of a generator)
- flexible design for a future multi-disk rotor
- revolutional speeds suitable for single- and multi-disk rotors
- no gearbox, if possible.

4.4 The Tesla rotor

The mechanical design of the rotor was developed with the acquired experience from the preliminary tests, the knowledge about the characteristics of Tesla turbines from the theoretical flow models, and the specified criteria for the test rig.

4.4.1 Design process

The process of designing a Tesla turbine is iterative and illustrated in Fig. 4.6. Fluid properties and rotor geometry are used to define the dimensionless parameters β ,

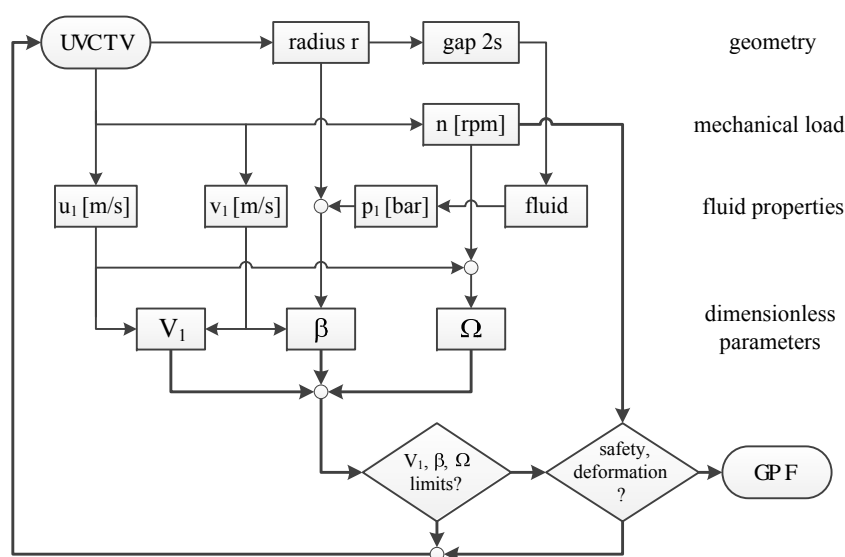


Figure 4.6: Process of rotor design [134]

Ω , and V_1 . Furthermore, the maximum allowable mechanical stress and a minimal deformation of the disks to maintain the inter-disk spacing has to be considered. Rotor geometry, fluid, and operating conditions are chosen for first estimations. The incompressible, laminar flow model is coded in Wolfram Mathematica and yields the solution in dimensionless variables. Furthermore, it predicts the performance characteristics of a single gap rotor. The flow model computations additionally involve the analytical calculation of the mechanical stress for a drilled disk under rotation, which are merely provided as a basic information. A detailed explanation of the mechanical stress calculation is provided in chapter 4.4.2. Besides the mechanical load from the performance prediction, the disk material has to be defined. The disk diameter is iteratively chosen with respect to the manageable mechanical stress and to the optimal dimensionless parameters, which are defined in chapter 2.7. After finding useful solutions of the dimensionless parameters with an adequate mechanical stress and a safety factor for a given geometry, a given fluid, and fluid properties, the first rotor geometry is selected. It has to be ensured that the gap width is technically feasible. Then, the first rotor is designed in CAD. After that, FEM tools compute the mechanical stress and the deformation of the disks. From this point on, each iteration step includes a new detailed mechanical rotor design in CAD with an FEM evaluation of mechanical stress, safety factor, and disk deformation under rotation.

4.4.2 Mechanical constraints

A centrally drilled disk under constant rotation generates tangential and radial mechanical stress. The mechanical stress maximum is at the inner radius r_2 . Only the circumferential mechanical stress is acting on the disk at the inner radius, like it is shown in Fig. 4.7. The analytical Eq. 4.1 obtained from [141] yields the value of the maximum mechanical stress for a certain disk material, a given geometry, and a

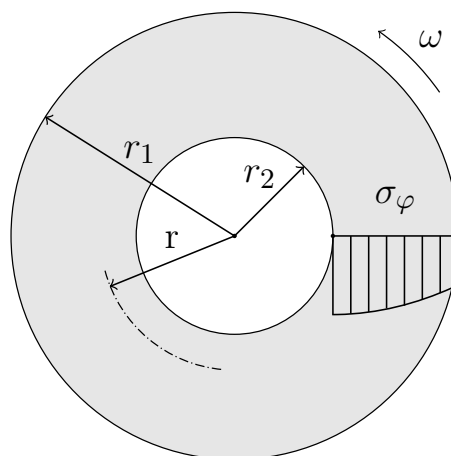


Figure 4.7: Centrally drilled disk under constant rotation [11]

rotational speed. It represents the mechanical limit of a drilled disk under rotation,

$$\sigma_{\varphi}(r) = \frac{3 + \nu_p}{8} \cdot \rho \cdot \omega^2 \cdot r_1^2 \cdot \left[1 + \left(\frac{r_2}{r_1} \right)^2 + \left(\frac{r_1}{r} \right)^2 - \frac{1 + 3 \cdot \nu_p}{3 + \nu_p} \left(\frac{r}{r_1} \right)^2 \right] \quad (4.1)$$

which can be compared to the yield strength of the disk material. Equation 4.2 provides the value for the safety factor. This immediately enables the assessment of

$$s_f = \frac{\sigma_y}{\sigma_{\max}} \quad (4.2)$$

the proposed rotor configuration. Technically unfeasible solutions can be excluded quickly. It is shown in [11] that the radius ratio R limits the maximum angular velocity Ω for a selected material. The higher the radius ratio, the lower is the maximum allowable revolutionary speed. This procedure was used for estimating the rotor dimensions.

4.4.3 Rotor design concepts

The initial step for finding an appropriate rotor design is to define the bearing concept. The most attractive ideas are shown in Figs. 4.8 and 4.9. Bearing concept A has advantages with regard to residual imbalance. However, bearing concept B provides more space and therefore more flexibility during the optical measurements. A vertical rotor axis is less sensitive to vibrations, because there is no deflection. Furthermore, there is definitively no influence of gravity on the flow for denser media.

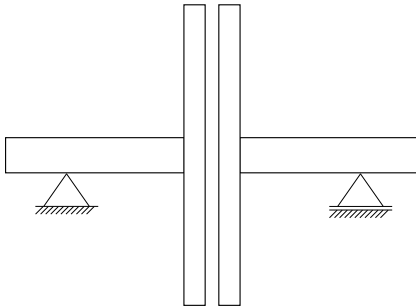


Figure 4.8: Bearing concept A

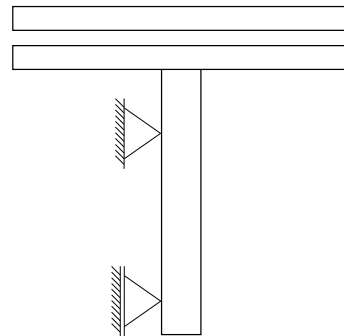


Figure 4.9: Bearing concept B

The optical access for the PTV measurements is briefly discussed in [137]. The preliminary investigations showed that velocity profile measurements with transparent walls are possible, if the contamination of the disks is low. A fundamental finding of the study is that the measurements have to be carried out with a volume illumination of the tracer seeding. Light sheet illumination does not lead to the desired results. The laser beam has to be coupled into the rotor gap. This is either possible with a beam coming from the outer disk radius to the centre of rotation (Fig. 4.10) or the other way around (Fig. 4.11).

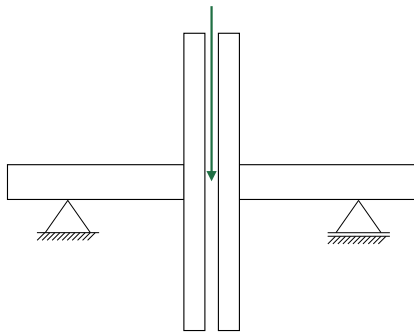


Figure 4.10: Illumination A

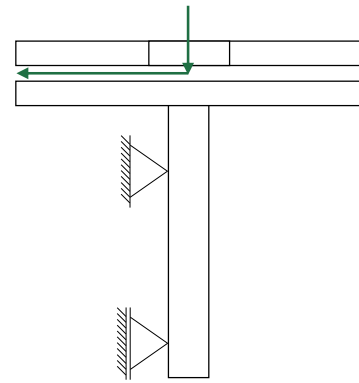


Figure 4.11: Illumination B

Different concepts of partially transparent disks are illustrated in Figs. 4.12 to 4.14. Design A, which is shown in Fig. 4.12, offers the greatest flexibility regarding the optical access. It consists of transparent acrylic glass, which is held together by a metal fixation. Preliminary results from the analytical stress calculation and the

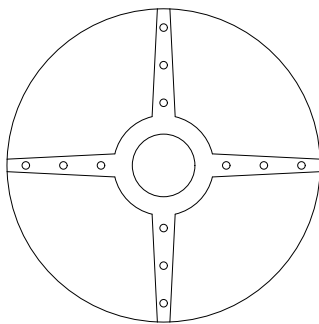


Figure 4.12: Design A

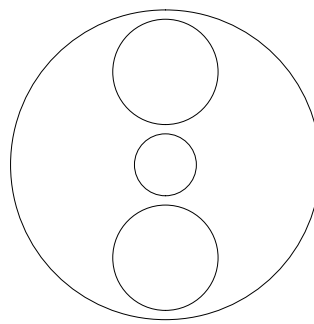


Figure 4.13: Design B

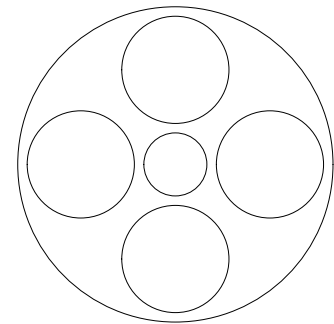


Figure 4.14: Design C

FEM showed that transparent acrylic glass will deform strongly, which limits the maximum rotational speed, due to its mechanical properties. Furthermore, glass is the favourable material and offers the best signal-to-noise ratio during PTV measurements [137]. Unfortunately, glass is anisotropic material. It resists a much higher compressive stress, than a tensile stress. Therefore, the use of bull's eyes made from glass seems to be the best solution (design B, C). The bull's eyes will have to be glued into the rotor in this case. On the one hand, a rotor with four bull's eyes has small advantages in residual imbalance. On the other, it is more expensive compared to a rotor with only two. Design B is therefore favourable.

Numerous disk outlet design solutions are conceivable. Most interesting disk concepts are exemplarily shown in Figs. 4.15 to 4.17. Lowest manufacturing costs are achievable with disk geometry C (Fig. 4.17). Obviously, highest mass flow rates can pass here without generating choked flow conditions in future multi-disk rotors. Furthermore, the mechanical stress acting on the disks, caused by centrifugal forces, can be calculated with an analytical function. This offers a first estimation

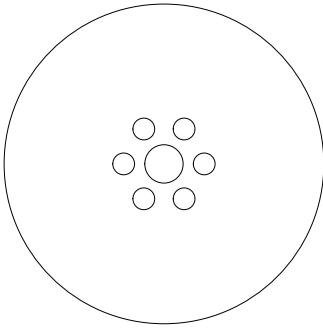


Figure 4.15: Disk A

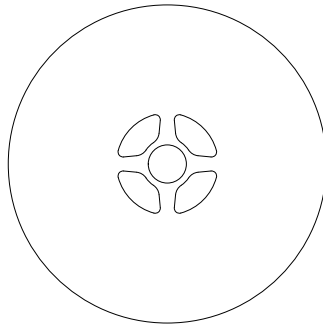


Figure 4.16: Disk B

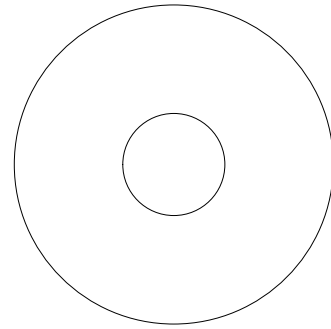


Figure 4.17: Disk C

of the range of disk diameters and rev speeds. In addition to that, it is well known that drillings near the axis of rotation result in an enlarged mechanical stress. They should therefore be avoided as much as possible, because it further limits the maximum revolutionary speed. Depending on the rotor diameter, this can be the key issue for a successful rotor design.

Under rotation, the gap between the disks should remain constant as much as possible. This can be ensured by placing spacers between the disks (Fig. 4.18). They can possibly be circular or even profiled. In this case, the disks will have to be drilled to connect them, which comes along with a structural weakening. Another problem of the well-known spacers is that they would disturb the flow and would influence the measurements. However, PIV measurements require a homogeneous velocity distribution along the circumference. Another possibility to connect the pair of disks is a shaft connection near the centre of rotation (Fig. 4.19). The flow would remain undisturbed, but the disks would then have to be very stiff in order to maintain the inter-disk spacing at the outer radius. Moreover, arbitrary combinations of both introduced possibilities and the position of the disk spacers are conceivable.

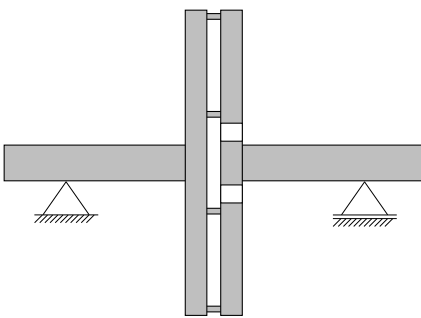


Figure 4.18: Spacing A

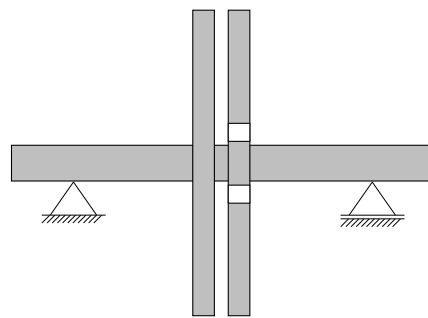


Figure 4.19: Spacing B

Another critical point for a successful Tesla turbine is rotor shaft sealing. The leakage has to be minimised as much as possible. Otherwise the efficiency decreases significantly. It is important to guarantee that the flow leaves the turbine without bypassing the disks' gap. We generally distinguish between radial and axial seals. Radial designs seal on the shaft. However, axial designs seal on the casing side.

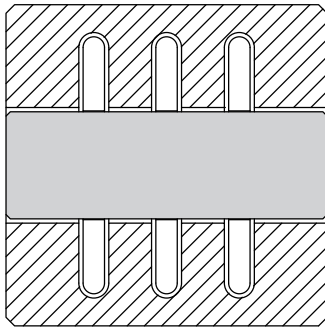


Figure 4.20: Carbon floating radial seal ring

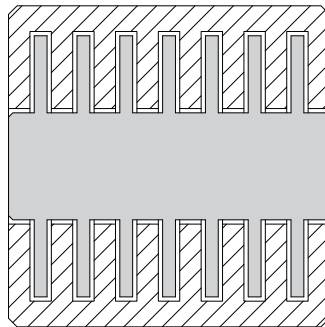


Figure 4.21: Labyrinth radial seal ring

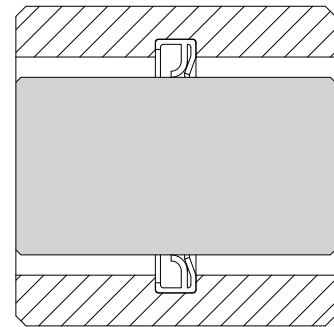


Figure 4.22: PTFE radial shaft seal ring

Some Tesla turbine designs from previous investigators or manufacturers require axial shafts. While these designs offer certain advantages, axial seals usually perform secondary sealing tasks like optimal protection against dirt, dust, and splashing water, described in [142]. In addition to that, radial seals involve less frictional forces, as they are usually located at smaller radii. Therefore, radial seals are generally favourable. Figures 4.20, 4.21, and 4.22 exemplarily show possible solutions for radial seals. The radial solutions for sealing the rotor, presented here, are also available in the axial design and are not explicitly shown. A carbon floating seal ring is often used in screw compressors, because of its good sealing effect. It is running dry and provides lowest friction. However, radial carbon floating seal rings require a lot of space and would therefore limit the spatial and optical accessibility to the measurement volume. However, it is recommended for performance map measurements. Labyrinth seal rings are contact-free shaft seals. The sealing effect is based on the extension of the flow path and the resulting increase of pressure drop of the gap to be sealed. The disadvantage is the required space in axial direction. In addition to that, leakage is higher compared to other solutions. Blocking air can be used to improve this approach, but it would falsify the mass flow measurements, as additional mass flow is added. The PTFE radial shaft seal ring features the most compact design. Furthermore, it is a mass product and is therefore an economical solution. The tightness is brilliant, but it involves an increase in friction. Greasing shaft and seals moderates this effect. Variants for applications requiring reduced friction are commercially available. As the rotor is powered for PIV measurements, friction is not the key issue. In all cases, it is recommended to use smallest diameters in order to create lowest peripheral speeds and to reduce sealing friction.

Different geometrical combinations of disks and shaft are possible. All subtasks and partial solutions, which are needed for a successful test rig design are summarised in Tab. A.2 in Appendix A.2. This table represents the morphological box for systematically finding the best possible mechanical design. Most interesting combinations of the partial solutions are composed to different concepts, which are listed and rated in Tab. A.3 in Appendix A.2. The evaluation takes place according to a rating system. Zero points is the poorest possible rating, ten is the best. The above-mentioned

criteria are all given equal weighting. Up to 70 points are awarded. The morphological box for subtasks, possible partial solutions, and rating can be found in Fig. A.7 in Appendix A.2. All conceivable concepts are illustrated in Figs. A.1 to A.8 in Appendix A.2. The systematic search for the best partial design solutions indicates that concept 7 is the best compromise for all subtasks. Figure 4.23 illustrates the preferred concept in more detail. A laser beam illuminates the measuring volume.

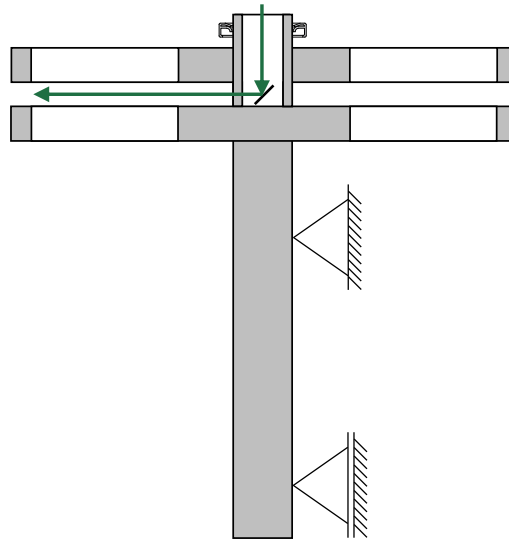


Figure 4.23: Final concept in detail

In an ideal situation, it passes through the axis of rotation and enters the rotor at the hollow shaft. Furthermore, it is deflected by a rotating mirror to illuminate the entire gap from inside out. Two bull's eyes are symmetrically placed in each disk for a lower imbalance. The bull's eyes in the lower disk are required for the non-intrusive calibration method, described in chapter 5.5. A PTFE radial shaft seal ring, featuring lowest leakage, is selected to ensure that as much of the mass flow as possible streams through the gap between the disks.

4.4.4 Final rotor design

Finding an optimal rotor design for the desired measurement task is challenging. It is all about compromising between size, mass, deformation, and eigenfrequencies. The rotor should be as compact as possible with an appropriate mass. Balancing has to be considered during the design process. Mechanical losses, like bearing and sealing losses will probably dominate shaft power with two disks only. Therefore, it is required that the rotor is powered and feedback controls the rotational speed. In addition to that, a rotor with only one inter-disk spacing is needed for the particle image investigations. A multi-disk rotor is not necessary and therefore not desired. Nevertheless, the test rig must also handle multi-disk rotors for future performance map investigations.

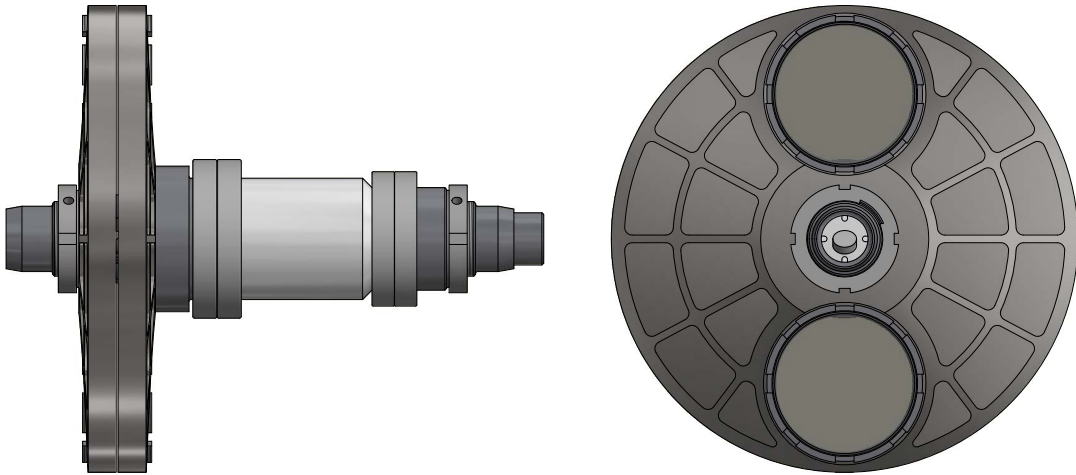


Figure 4.24: Mechanical design of the rotor

The compact rotor is illustrated in Fig. 4.24. Fully assembled, its mass is about 10 kg. A pair of spindle bearings in an O-arrangement is used for the locating and also for the floating bearing. All bearings are encapsulated and lifetime lubricated. A static and dynamic bearing calculation is performed according to [142]. The bearings are clamped together on the rotor shaft by a shaft shoulder, two sleeves, and a shaft nut. Both disks are also clamped together on the hollow shaft by a shaft shoulder, and a shaft nut. The gap width is established by using a spacer near the hollow shaft. Figures 4.25 and 4.26 show the outlet region with the exchangeable and aerodynamically profiled spacers. Three spacers are manufactured in different heights to create the inter-disk spacings of 0.2 mm, 0.5 mm, and 1.0 mm. Smaller, but also higher disk spacings of height up to 4 mm are possible, if new spacers are manufactured. The tightening torque of both shaft nuts is 25 Nm. The nuts are protected from becoming detached by grub screws. To ensure that the air is not bypassing the disks, the rotor is sealed on both shaft ends with PTFE radial shaft seal rings. Therefore, the shell surfaces of the shaft are hardened.

The disks are milled from a whole piece. The outer disk diameter is 125 mm and the outlet region is located at a diameter of 30 mm. The inner disk diameter is implemented using an artificial axial step, which is milled into the outer disk (Fig. 4.25), which remains the same for all possible disk spacings. Near the centre of rotation, the disks are thicker to withstand the highest tensile forces. The milled pockets in the disks are arranged, so that braces are created. Shape and size of the pockets are varied across the radius, in order to create a stiff disk with lowest deformation and to reduce the rotating mass. The optimisation for lowest deformation is described in chapter 4.4.5.

The main task of both disks is to transmit torque to the shaft. The inner disk (Fig. 4.26) is connected to the shaft by two metal pins. The disk spacer uses a positive form locking to transmit torque. The geometrical shape of an ellipse is used here. The junction between the surfaces of disk and spacer is not noticeable by hand. The



Figure 4.25: Outer disk with profiled disk spacer



Figure 4.26: Inner disk with profiled disk spacer

transmission of torque from the outer disk to the spacer is established with four pins, which fit directly into the disk spacer (Figs. 4.25, 4.26).

The glass windows are equipped with a shoulder. Its frame is the counterpart of the window with exactly the same shoulder, to ensure that the transition between glass and frame surfaces is smooth. Glass windows and frames are glued together with a two-component glue for very heavy loads. The frames feature a M85×1.5 thread on their shell surface and are shaped with a crown nut. The frames are screwed into the disks with a counterpart tool. They are levelled in order to create a very smooth transition between disk surface and metal frame. To prevent the frames from loosening themselves, they are fixed with screw lock glue. Crown nuts transmit highest torques with their low wear characteristics, because of their so-called form-locking connection. Therefore, the frames can be removed and exchanged easily, if desired.

Figure 4.27 shows the illumination of the measuring volume by the pulsed laser light. The beam enters the flow domain via a fixed and coated deflecting mirror in the centre of the rotation axis. Further on, it passes radially outwards through the slots of the hollow shaft into the gap between the co-rotating disks. The inner diameter of the hollow shaft is chosen to be as large as possible. In that case, the mirror is not significantly blocking the outflow.

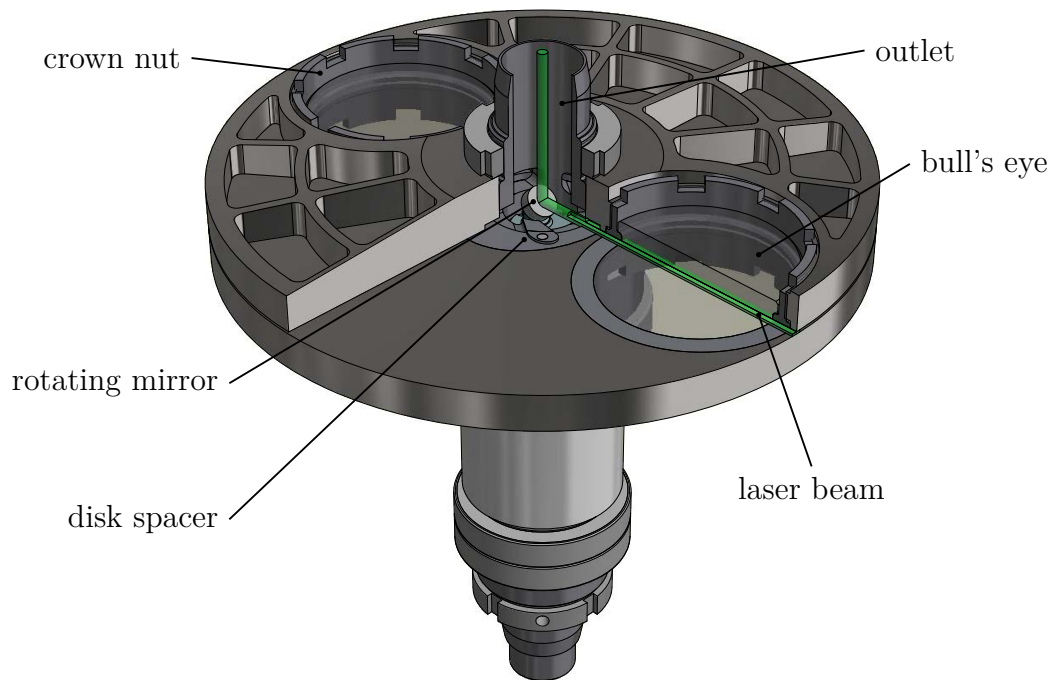


Figure 4.27: Assembled rotor with laser beam and deflecting mirror

4.4.5 Stress and deformation analysis

The rotor design is changed and recalculated iteratively, in order to create the lowest possible disk deformation at an appropriate and safe stress level. The best compromise is found and presented here. The calculations of stress and deformation, caused by rotation are carried out with the FEM tool in Autodesk Inventor 2013. The peak values of axial deformation and von-Mises equivalent tensile stress are converged with the refinement of the FE-grid. The simulations consider the mechanical loads due to rotation and preloaded forces, which are caused by the shaft screw to clamp the disks to the shaft. The design speed of the rotor is 12000 min^{-1} . Due to safety reasons, the maximal revolution speed is approved for 1000 min^{-1} only. The validity of the simulation results are estimated by the mechanical stress calculation using the analytical Eq. 4.1 in chapter 4.4.2. Furthermore, this procedure offers the possibility to immediately assess, whether a design is practical and feasible. The rotor disks consist of the chromium, nickel, and molybdenum alloyed tempering steel 30CrNiMo8 (material number 1.6580). It is a steel for higher requirements on strength and toughness. The maximum yield strength is 700 MPa for diameters up to 250 mm and 1050 MPa for diameters up to 40 mm. The bull's eyes are made of quartz glass with a compressive strength between 700 MPa and 900 MPa. The tensile strength of the material is only a tenth of the compressive strength. However, there are only compressive loads acting on the glass using the proposed mechanical design. The stress maxima of 220 MPa at the outer disk and 240 MPa at the inner disk can be obtained from Fig. 4.28. They are located in the drillings of the disks, as

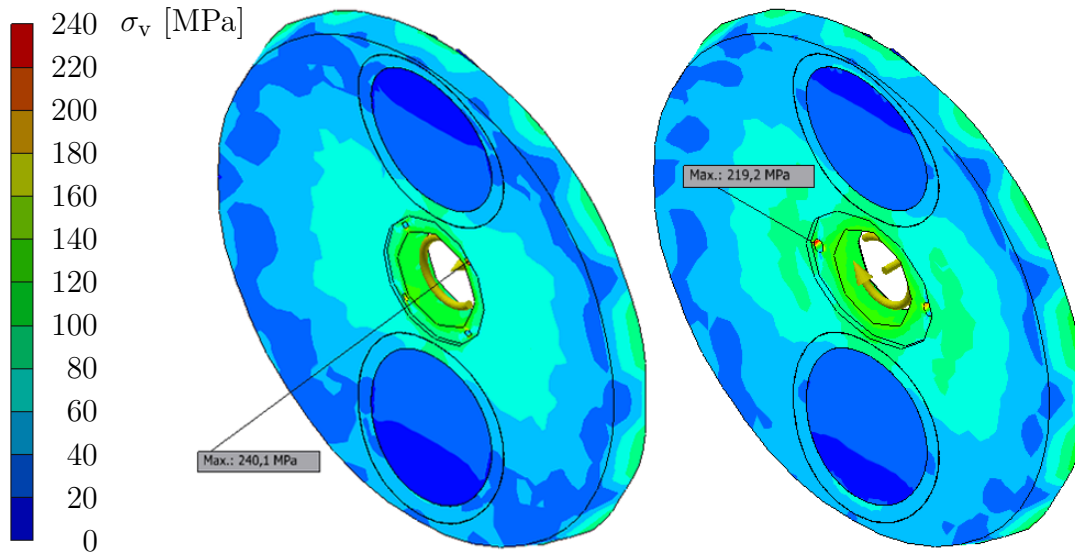


Figure 4.28: FEM simulation of von-Mises equivalent tensile stress ($n=12000 \text{ min}^{-1}$)

it is expected from theory. It is concluded from the results that the rotor withstands the expected loads. The rotor has the tendency to close the gap under rotation and therefore to block the inlet. This blockage error e at the outer disk diameter in dependency of rotational speed can be found in Tab. 4.1.

n	Δe	$e(0.2 \text{ mm})$	$e(0.5 \text{ mm})$	$e(1.0 \text{ mm})$
4000 min^{-1}	0.005 mm	2.5 %	1.0 %	0.5 %
6000 min^{-1}	0.019 mm	9.6 %	3.8 %	1.9 %
8000 min^{-1}	0.041 mm	20.5 %	8.2 %	4.1 %
10000 min^{-1}	0.065 mm	32.5 %	13.0 %	6.5 %

Table 4.1: Gap width blockage error [134]

The blockage error e is moderate for revolution speeds below 8000 min^{-1} . The moderate deformation under rotation is exemplarily illustrated in the FEM simulation results in Fig. 4.29. Highest deformations are found between $R=1.0$ and 0.9 , which denotes the outer rim region. The inner region of the disks, which is located below the radius of $R=0.9$ has a comparatively low deformation. Details can be found in Fig. 4.29 using the colour combinations red, yellow, green, and blue, which denote an increasing level of deformation.

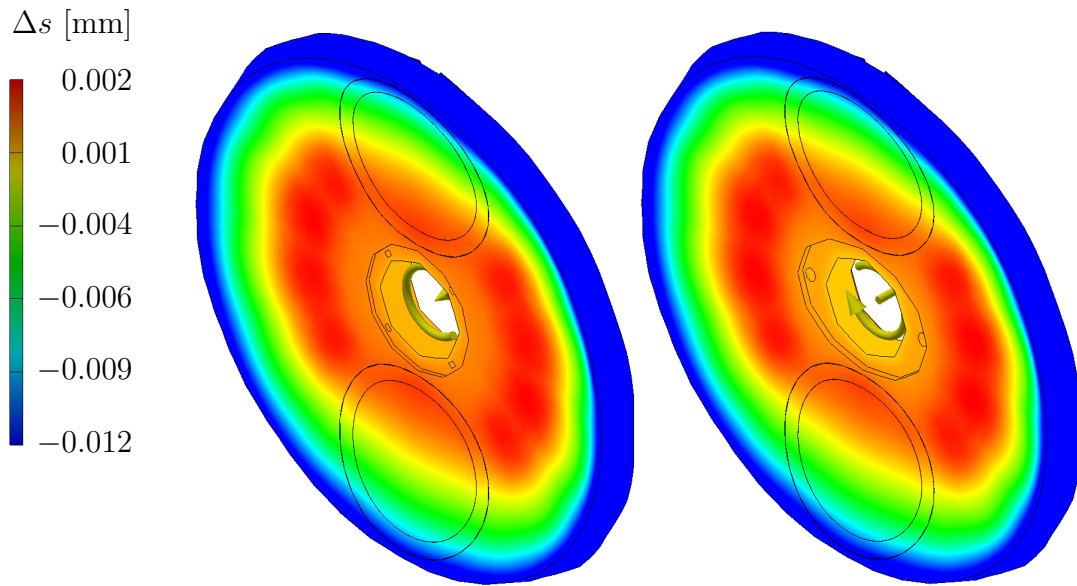


Figure 4.29: FEM simulation of total deformation ($n=6000 \text{ min}^{-1}$) [134]

4.4.6 Modal and harmonic response analysis

If possible, a rotor should be operated below his first eigenfrequency. If this is not the case, a rotor should be passed through all critical revolutionary speeds, as quickly as possible. A good method to predict the eigenfrequencies of a rotor is the modal analysis, which is carried out in ANSYS 14.0. The first eigenfrequency is found at about 760 Hz. In addition to that, a harmonic response analysis is performed. It computes the amplitude response of a selected point P in the geometry of a body, as a result of harmonic excitation. The oscillating load, which is caused by the residual

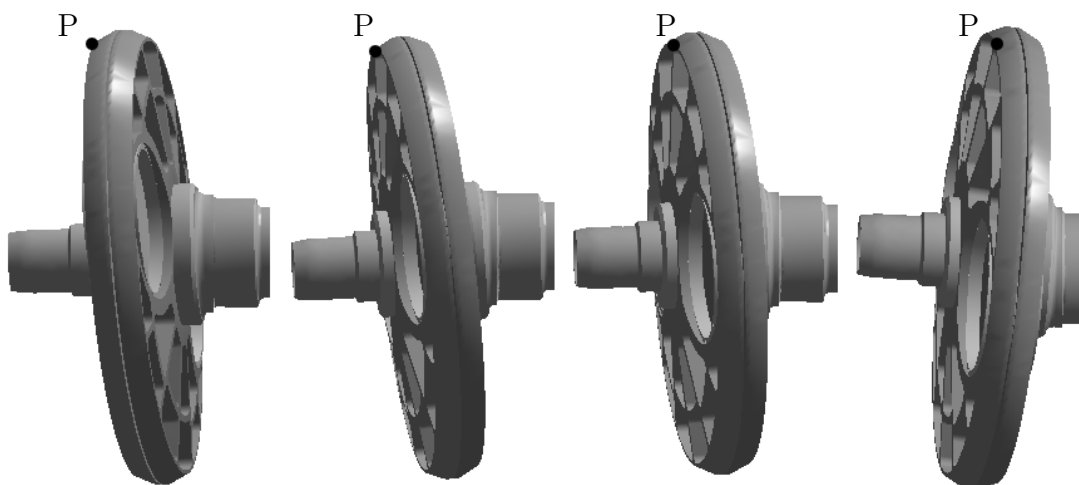


Figure 4.30: Harmonic response analysis, mode of motion at 34 Hz [134]

imbalance after balancing the rotor, is used as the excitation force. The highest amplitude is found at 34 Hz together with a change in phase angle of 180° . The shift in phase angle is the criterion for an eigenfrequency. The mode of motion is exemplarily shown in Fig. 4.30. Furthermore, the investigations indicate that both disks are oscillating in phase with an amplitude of similar order. Since the amplitude at this frequency is extremely low, the results are deemed to be acceptable and the mechanical design is not changed any more. However, it is concluded that the frequency of 34 Hz should be avoided, when the test rig is in operation. The frequency spectrum close to the eigenfrequency should be driven through, as fast as possible. This criterion can easily be implemented into the test rig control software. Moreover, the measurement data of the acceleration sensors for monitoring the behaviour of the bearings (Fig. 4.41) indicate a slight increase in amplitude of the rotor vibrations at a rotational speed of roughly 2000 min^{-1} . Thereby, the vibrations are also audible during operation. For this reason, the results obtained from the harmonic response analysis are in good agreement with the measurements.

4.4.7 Rotor balancing

The manufacturing tolerances are indicators for the maximal resulting imbalance of the mounted rotor. A worst-case scenario occurs, if the manufacturing tolerances accumulate to the highest possible imbalance. However, it must be ensured that there is enough volume in two parallel shifted axial planes, where rotor mass can be removed during rotor balancing. At first, the shaft is balanced alone. Therefore, rotor mass is simply removed by drilling holes in two different planes, which are highlighted as shaft plane 1 and 2 in Fig. 4.31. After that the rotor is balanced with one disk and afterwards with two disks. It is very important to avoid mechanical rotor vibrations for a successful measurement of the velocity distribution between the disks of the Tesla rotor. The two disks and the shaft can be assembled in four different combinations. Before balancing the rotor, all possible combinations are tested on the balancing machine, in order to find the lowest imbalance at that moment. The best configuration leads to lowest mass removal and therefore to lowest structural weakening. From [143] it is known that the residual imbalance can be greater the higher the mass of the rotor. Furthermore, the load of a bearing is approximately constant for the product of the centre of mass displacement of the rotor from the axis of rotation and the angular velocity, which denotes the quality level Q . The permitted residual imbalance I is defined to 10 gmm. The total rotating mass m is approximately 10 kg. The residual eccentricity of the centre of rotor mass is therefore 1 μm . The maximum angular velocity ω is 1047 rad/s (or 10000 min^{-1}). This leads to the quality level of

$$Q = \frac{I}{m} \cdot \omega = 1, \quad (4.3)$$

which is about one quality class higher, than what is typically used for gas turbines or hard disk drives. The mass can be removed in the planes 1 and 2, in order to reach the desired residual imbalance (Fig. 4.31).

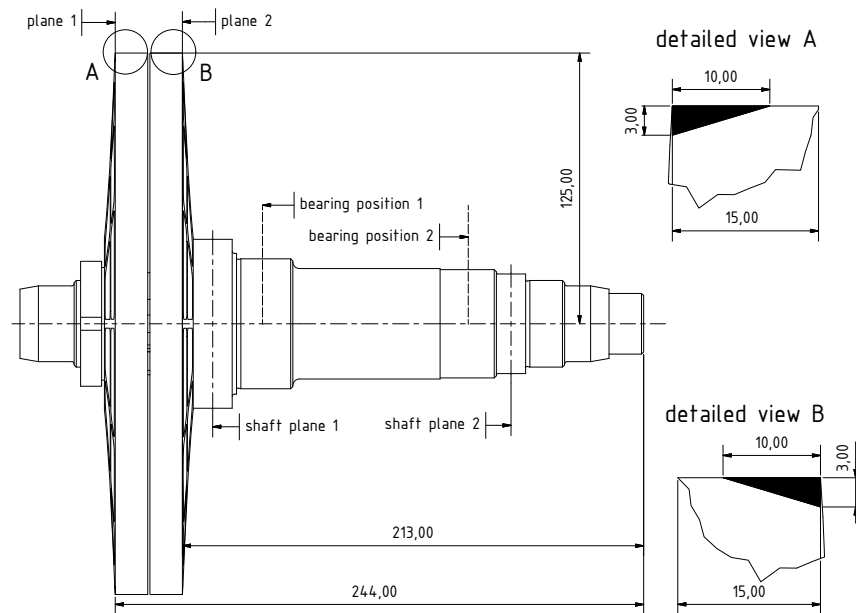


Figure 4.31: Drawing for balancing the rotor

4.5 Test rig design

The housing for rotor, guide vanes, and plenum is manufactured from one CNC turned part with a diameter of 880 mm. An illustration of the test rig can be found in Fig. 4.32. This is indeed more cost-efficient, compared to welding or cast constructions. It offers the most flexible and modular design for exchanging guide vanes or even the rotor for future applications. The casing cover is equipped with O-rings and a PTFE radial shaft seal ring, which closes the housing. Furthermore, it contains a static glass window to provide the optical access to the measuring volume. The casing cover is also made from a single CNC turned part and features enough space for placing the laser and both cameras. It is removable for assembly and cleaning the bull's eyes of the rotor. Furthermore, it can be lifted by a crane. The entire system is pressure resistant up to 10 bar. The design calculation of the casing cover is performed by means of FEM. The corresponding screws are designed according to [142]. To verify the pressure resistance, a leakage test is performed. The housing is pumped up to a pressure of 5 bar. In addition to that, the outlet is blocked by a tool made of steel, which enables the leakage flow through the radial shaft seal rings without rotor motion. The leakage flow is measured using the flow meter Bronkhorst EL-FLOW F-113AC for small mass flows below 20 g/s. No leakage mass flow could be detected for hours. For reasons of plausibility, the decrease in pressure is logged over time. Within 24 hours the pressure dropped from 5 bar to 4 bar. It is concluded that almost the entire mass flow from the inlet passes the gap between the disks and contributes to the generation of torque. Figure 4.33 shows the test rig with the main components in a lateral cut plane. The aerodynamic inflow is implemented by four inlets at the bottom of the annular plenum, which are equally distributed

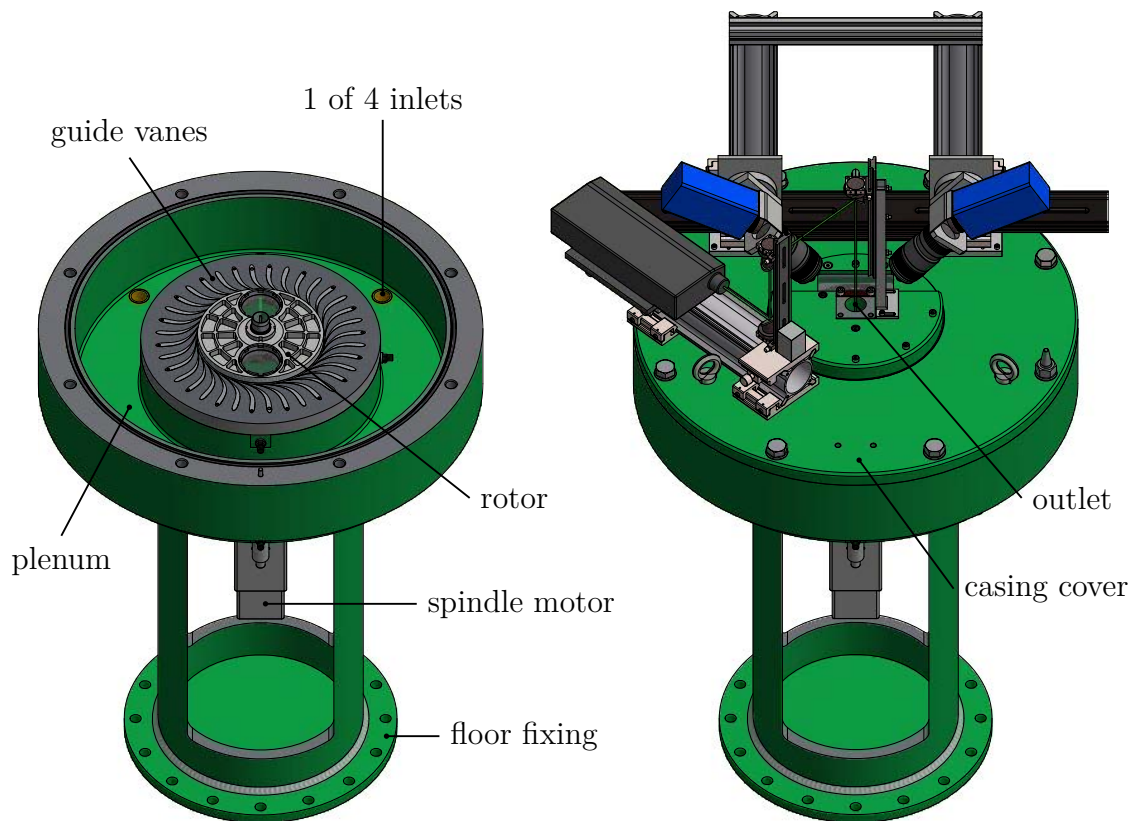


Figure 4.32: Test rig opened and closed view

around the circumference. From there, the compressed air enters the guide vanes in the radial direction. The guide vanes are designed by means of CFD. Details can be found in chapter 4.6. The stator consists of two parts, which are (axially) screwed together with 18 screws. The lower part of the guide vanes is re-milled. Merely the 36 profiles are remaining. Thereby, a flow passage with a height of 0.5 mm arises, which feeds the rotor generating a swirled inflow at an inlet angle of $V_1 = 0.3$. The flow leaves the rotor at the outlet near the centre of rotation at ambient pressure conditions. Furthermore, it contains DEHS tracer particles which could contaminate the lenses of the cameras. It is therefore deflected by a sheet metal. The working medium is removed from the lab using a suction device.

The rotor is located in the centre of the test rig. The assembly is carried out by inserting the pre-mounted rotor shaft without the disks from top to bottom. A bearing shell fixes the locating bearings. After that, the disks are mounted together using the desired spacer. In order to tighten the upper shaft nut, the rotor is temporarily fixed with an assembly tool. The rotor is connected to the spindle motor using a shaft coupling at the lower end. The motor itself is clamped to a flange. It features revolutionary speeds up to 14000 min^{-1} and is connected to a frequency converter. However, the revolutionary speed is limited to 10000 min^{-1} . The shaft is also sealed by a PTFE radial shaft seal ring. As the bearings are encapsulated and

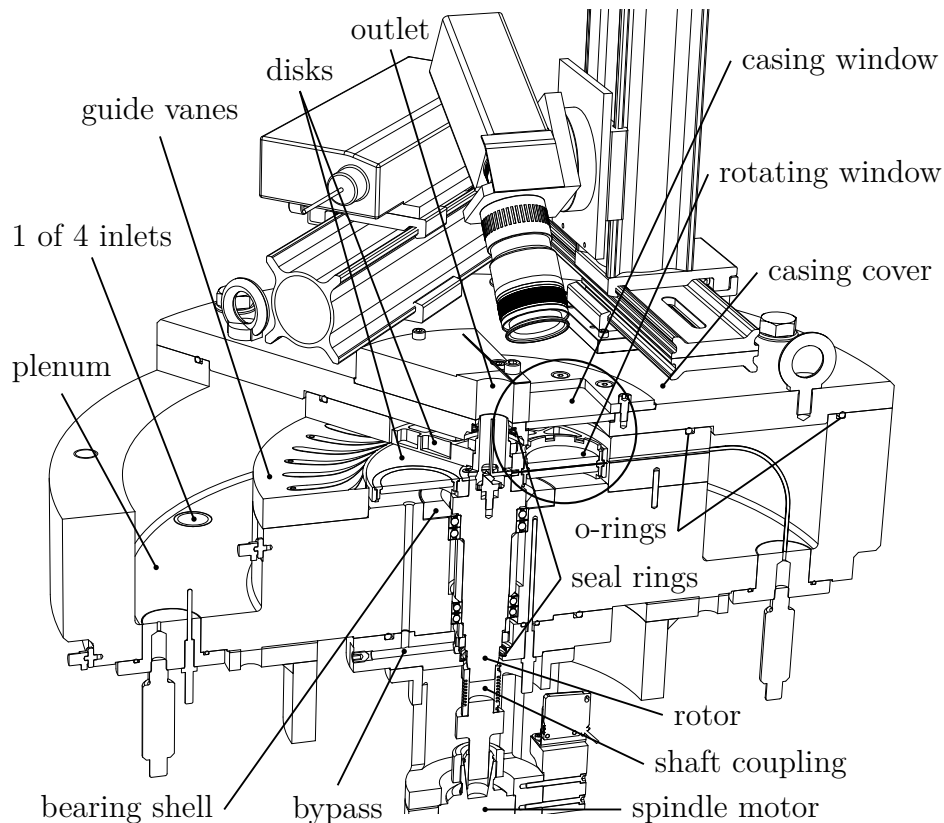


Figure 4.33: Intersected test rig with main components

life-time lubricated, it has to be ensured that the air is not leaving the rotor via the bearings. Therefore, a bypass providing less flow resistance is integrated into the housing. However, the housing is equipped with sensors. The measurement technique is described and illustrated in chapter 4.7.

The mass flow is delivered by a compressor, which usually supplies a small transonic wind tunnel. The system layout is illustrated in Fig. 4.34. The compressed air is filtered and is gathered from pressure accumulators. After measuring the total flow rate, the mass flow is divided into the main air supply and a bypass for the DEHS seeding generator. Both air flows are combined again in a 500 l pressure accumulator, which serves as a mixing chamber to generate a homogeneous distribution of the particles in the flow. Furthermore, the pressure accumulator divides the air into four equal mass flows for a homogeneous supply of the plenum in the test rig. Digital images of the test facility can be found in Appendix A.2.

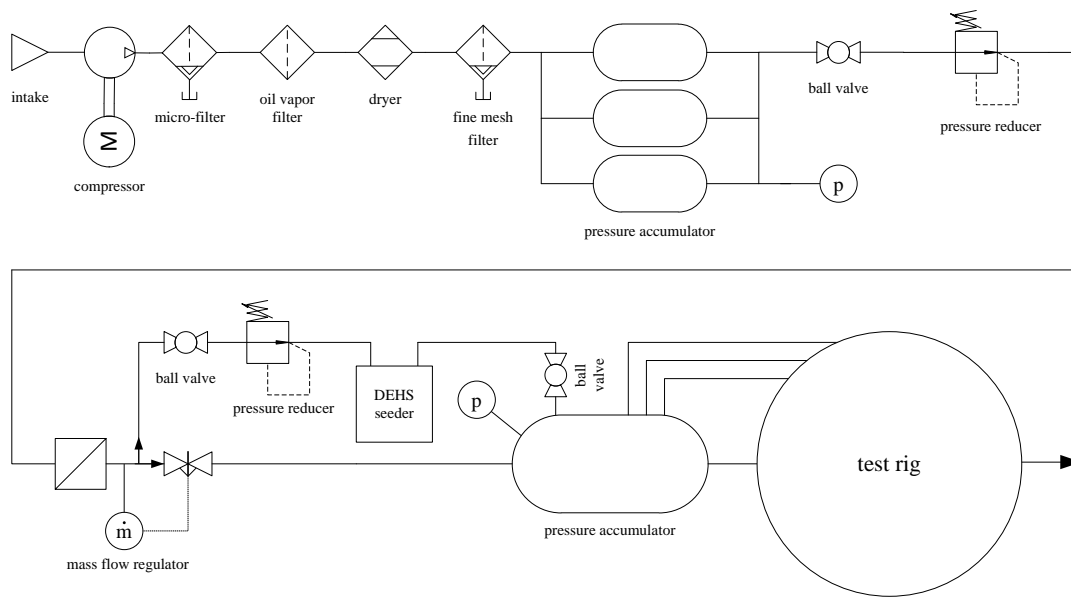


Figure 4.34: System layout of the test facility

4.6 CFD optimisation of test rig components

CFD was used as a tool for optimising the guide vanes and the rotor outlet. Even if laminar flow is expected for a range of parameters, the calculations were performed using turbulence models. The outlet region of the rotor contains an axial step (cf. Fig. 4.39), which is modelled and belongs to the flow domain. This step can originate turbulence and flow separation. The following CFD code and settings were used in this investigation:

- ANSYS CFX 14.0 and ICEM 14.0
- air, total energy, k - ω turbulence model
- local timescale with $CFL = 1$ to 20
- steady-state stage model with GGI interface
- one 90° section of the rotor and nine 10° sections of the stator domain (1:1 periodic interface)
- rotor, stator domains with 3 million cells in total
- inlet: $\dot{m} = 0.002$ to 0.02 kg/s
- outlet: $p_2 = 1$ bar
- residual convergence: $1 \cdot 10^{-5}$ RMS, $1 \cdot 10^{-3}$ MAX
- y^+ mesh adaption

- mesh independence study.

Further detailed information about the set-up of the grid can be found in chapter 3. The guide vanes were optimised by means of CFD for the desired inlet flow angle. The flow enters the guide vanes from the radial direction and ideally enters the rotor at the optimum inlet angle of $V_1 = 0.3$, described in chapter 2.7. The

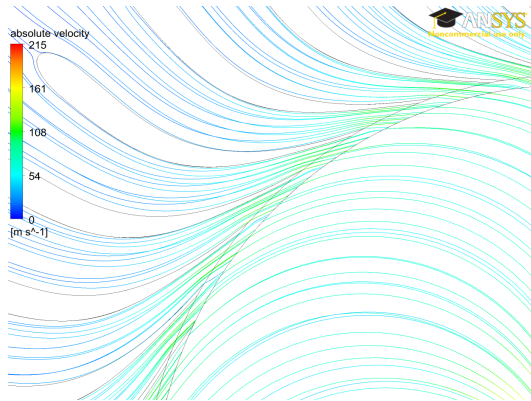


Figure 4.35: $n = 1000 \text{ min}^{-1}$, $V_1 = 0.34$

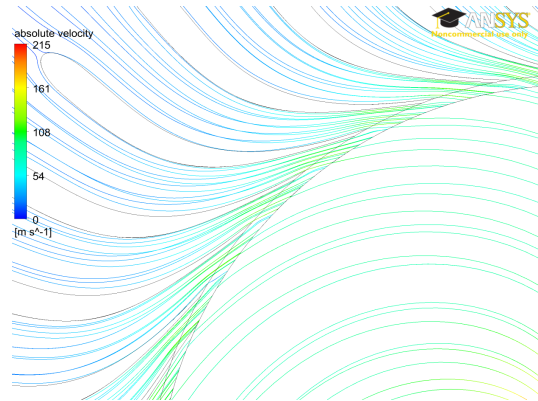


Figure 4.36: $n = 4000 \text{ min}^{-1}$, $V_1 = 0.33$

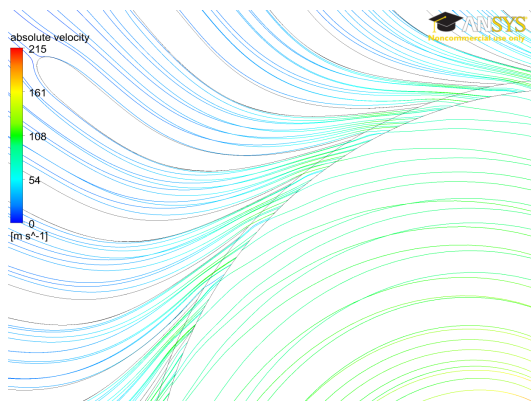


Figure 4.37: $n = 7000 \text{ min}^{-1}$, $V_1 = 0.32$

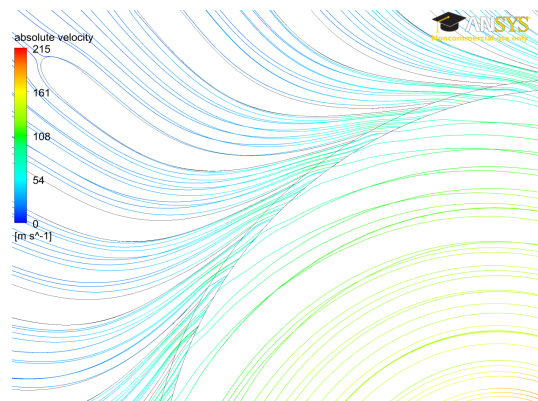


Figure 4.38: $n = 10000 \text{ min}^{-1}$, $V_1 = 0.29$

profiles were designed using 2D spline curves in a CAD system. The leading edge of the profiles, shown in Fig. 4.35 is elliptic. The axial gap in rotor and stator was set to 0.5 mm. Moreover, 36 blades are located around the circumference. The first CFD computations were used for the optimisation of the chord length, the number of blades, and the curvature of the profiles. The flow is attached to pressure and suction side of the guide vanes' profiles and avoids separations within the channels for a typical range of mass flows. As the guide vanes were chosen not to be adjustable, a compromise for the different rotational speeds was needed. While the rotational speed increases, the resulting inflow angles are slightly smaller. The rotational speed of the rotor was varied between 1000 and 10000 min^{-1} . At first, the resulting inlet angle differed from the geometrical exit angle of the guide vanes at the outer

radius of the disks. To find the best compromise for all rotational speeds, it was adapted iteratively. The theoretical optimal inflow angle, derived in chapter 2.7.2, was set to rotational speeds between 7000 and 10000 min^{-1} , where maximum performance is expected.

Disk spacing was established using spacers in the rotor outlet region near the centre of rotation. The flow leaves the rotor via a hollow shaft. The exchangeable spacer and the bars between the openings in the hollow shaft together form a profiled contour. The angle of the profile contour was adapted for the predominant exit swirl angle for different rotational speeds and for lowest flow separation. A good compromise was found for all possible rotational speeds. A streamline plot through the outlet section of the rotor is shown in Fig. 4.39.

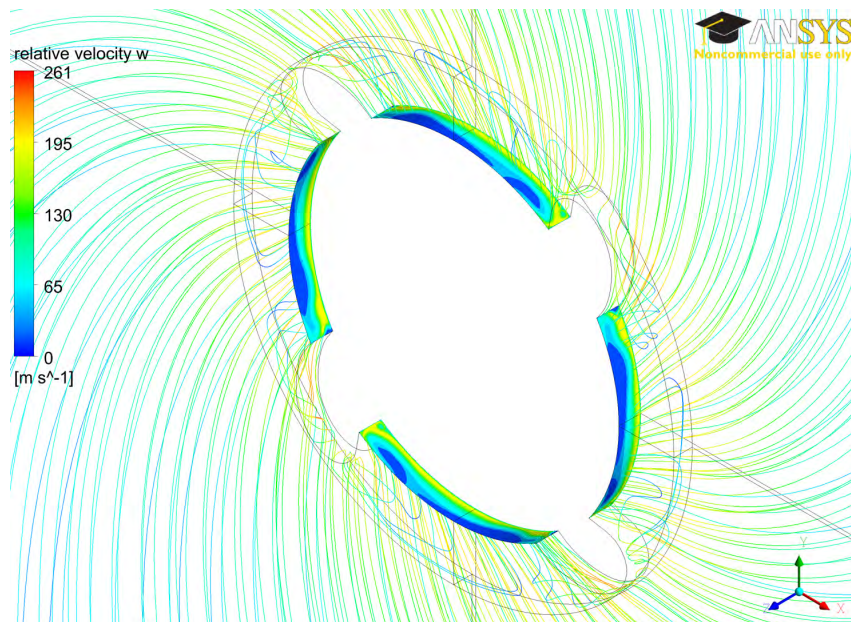


Figure 4.39: Relative streamline plot at the rotor outlet

4.7 Measurement techniques and control software

The flow rate and the rotational speed are the most important parameters during the measurements, which have to be kept constant. The setpoint of the rotational speed was chosen by sending a 0-10 V DC signal to the frequency converter. The rotational speed is additionally measured by the laser contrast sensor Baumer OZDM 16N1001. This signal is used for the feedback control of the revolution speed. The mass flow is measured and feedback controlled by the mass flow regulator Bronkhorst IN-FLOW F-106CI. It is connected to a process control valve, which sets the desired mass flow. The measuring section is illustrated in Fig. 4.40. Other

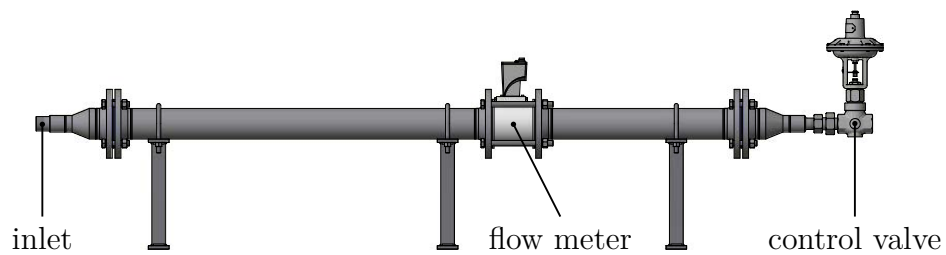


Figure 4.40: Measuring point of mass flow regulator

important measuring values are the plenum and the inlet pressure, as well as the plenum, and the ambient temperature. SETRA ASM1010 absolute pressure gauges with a measuring range of 0 to 10 bar are used.

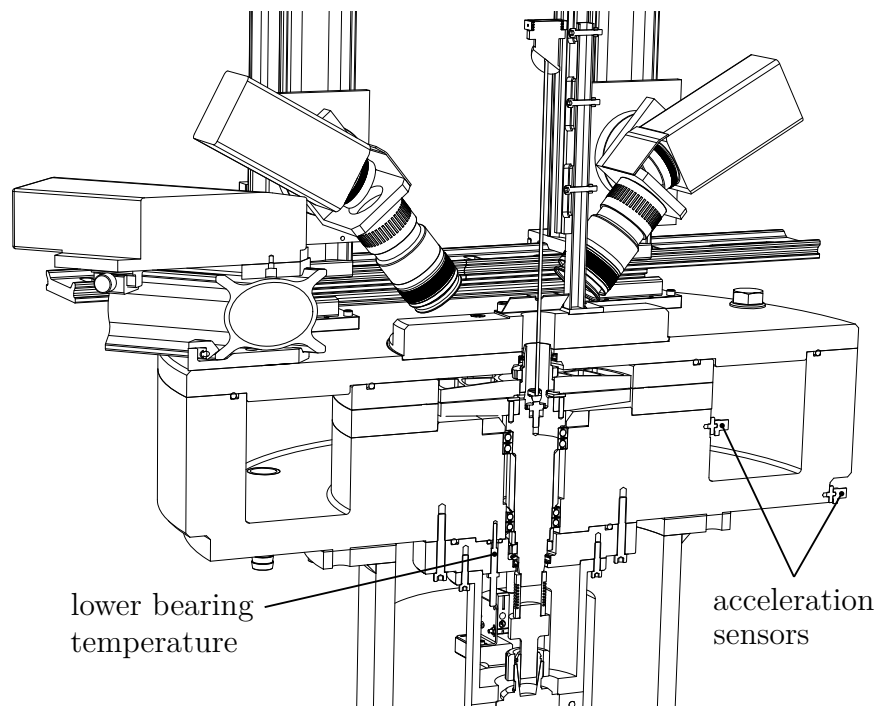


Figure 4.41: Test rig with measuring points part 1

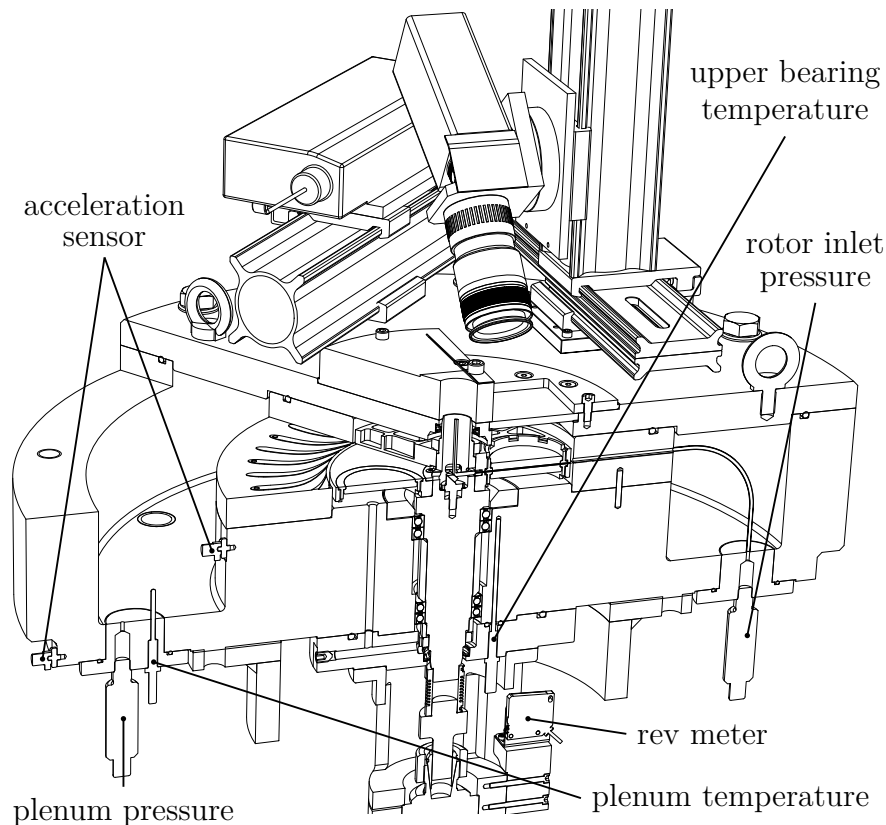


Figure 4.42: Test rig with measuring points part 2

The temperatures are measured with thermocouples type K. Safety monitoring is achieved by analysing the signals of two Kistler K-shear 8702B50 acceleration sensors of the radial vibrations on each bearing. They are arranged at a 90° angle to each other. Premature bearing damage can either be detected by this method, or by an increase in bearing temperatures. The measured quantities and their measuring points are illustrated in Figs. 4.41 and 4.42. The pressure gauges and the thermocouples were calibrated, using a calibration furnace. As the acceleration and the mass flow sensor were already calibrated, the manufacturer's certificates was used.

The test rig is controlled by a real-time cRIO system by National Instruments. The software was developed in the NI LabVIEW language. The measuring cards are plugged into the compact RIO chassis and are read by an internal FPGA. All sensor signals are acquired, digitalised, and transferred to the real-time engine with highest possible determinism. Then, the sensor data is transferred to the windows host computer, via direct memory access and local area network. The main routine of the measurement program is running on a windows host computer. The FPGA task is defined by using the hardware-in-the-loop technique. This is a method that is commonly used in the development of real-time embedded systems. It was also programmed in NI LabVIEW and finally loaded into the FPGA. These devices are pre-assembled integrated circuits with a variety of logic circuitry. Besides the deterministic data logging, the big advantage is that self-defined subroutines are

running on a hardware and can intervene within lowest latency periods. Even if the control software crashes, the FPGA can reliably acquire a quick system shutdown.

The compact RIO handles the feedback-control of the revolution speed. An laser rev meter determines the current readings. The PID controller, located on the FPGA, keeps the actuating variable constant. It is also used for the setpoint of the mass flow regulator, which is equipped with an independent PID routine. The mass flow regulator is selectively able to handle different process variables, like for example the plenum pressure. Besides the acquisition of the measured values, listed in Fig. 4.43, the FPGA runs a safety monitoring system including a security shutdown procedure.

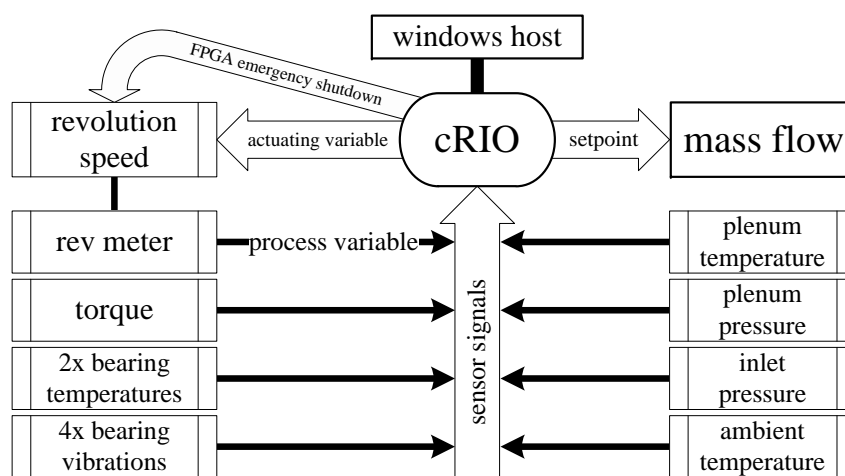


Figure 4.43: Sequence applied in the measurement and control software [134]

In case of emergency, the mass flow is immediately stopped and the rotor shuts down automatically. The reason for that can be a signal from a hardware-, or a software-panic-switch, the result of the online diagnosis of bearing failure computed from the acceleration sensors, or several predefined software parameters. These parameters denote limits for the maximum allowable revolutional speed or bearing temperature. In addition to that, the FPGA has a TTL trigger output for the PIV measuring system to trigger the cameras. The control software is able to shift the trigger signal and is therefore able to place the measuring volume into the optimal recording position. The main routine of the measurement and control software is illustrated in Fig. 4.43. The front panel is exemplarily shown in Fig. A.14 in Appendix A.2. Setpoints for the feedback controls, as well as the monitoring system, are located on the left side of the computer screen. The mass flow, the rotor speed, the data acquisition, and the data logging can be controlled in the middle section of the panel. The multifunctional panel on the right side either allows the detailed view of various measuring values or to adjust the program settings, if desired. There is, of course, the possibility to change and store the settings to file. In addition to that, several calibration routines of the sensors can be initiated. In order to prevent data loss on a system crash, the measurement file is updated at an interval of ten seconds.

5 PTV Set-up

This chapter describes the calibration technique, the experimental approach for the determination of the velocity profiles inside a Tesla turbine rotor, and the image post-processing carried out in this project.

5.1 Experimental Set-up

The test rig for the determination of the velocity profiles in the gap between the co-rotating disks of a Tesla rotor is described in chapter 4.5. A stereoscopic three-dimensional particle tracking velocimetry (3D-PTV) approach was used for the measurements of the flow inside the turbine. Therefore, the test rig is equipped with measurement components for 3D-PTV and with the newly developed non-intrusive calibration unit, shown in Fig. 5.1. For imaging, two PCO 2000 cameras are equipped

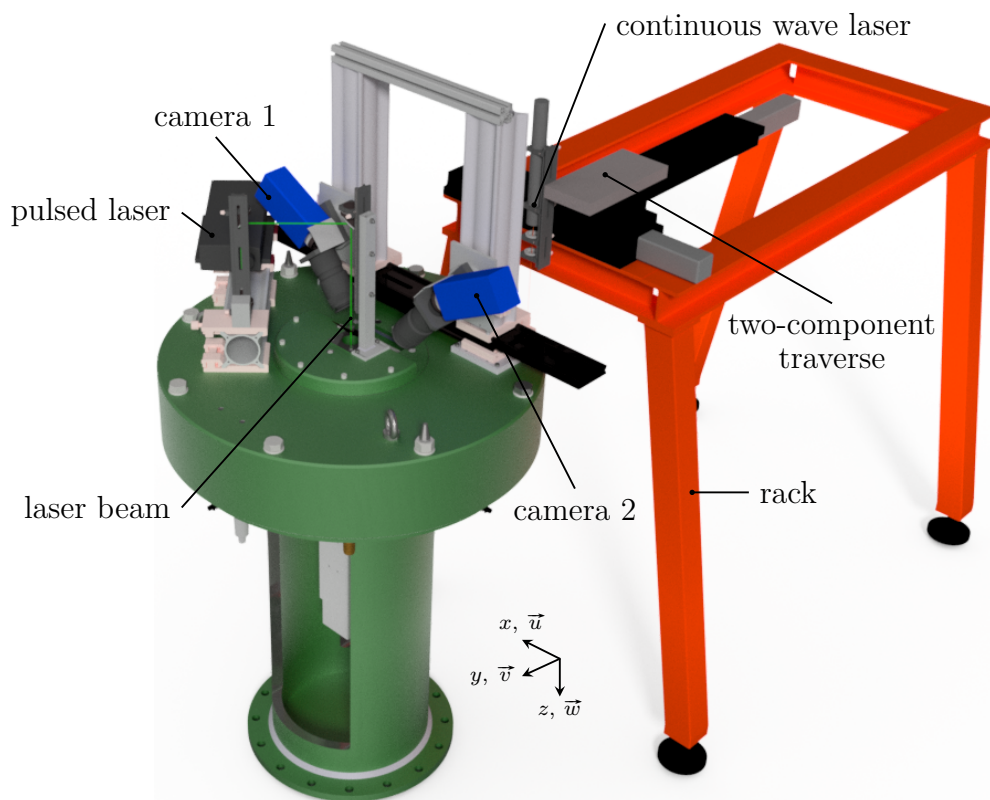


Figure 5.1: Turbine test rig with stereoscopic PTV set-up and calibration unit

with Scheimpflug tilt adapters and Nikkor lenses with a focal length of 60 mm, each combined with a two times magnifying teleconverter Kenko PRO 300. The CCD cameras feature a high dynamic range of 14 bit, a fast image recording with 160

MB/s, and a double shutter function for PIV measurements with a minimum inter-framing time of 180 ns. The cameras were triggered by an adjustable software TTL trigger, which is usually acquired by the test rig control software. More details can be found in chapter 5.6. The data transfer to the hard-disk drive of the computer was established with the camera link data interface.

To account for astigmatic aberrations caused by the angled view through the housing and rotor windows, illustrated in Fig. 5.2, the cameras and therefore the sensors were tilted according to the Scheimpflug condition. Changing the angle between image

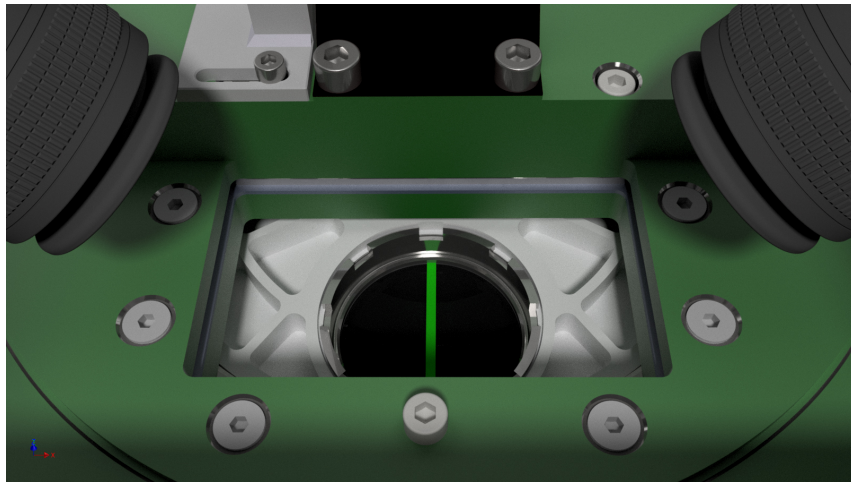


Figure 5.2: Optical access to the rotor

and lens plane influences the position of the plane of focus in three-dimensional space. However, the depth of focus is not enlarged, but the plane of focus is tilted, which ensures that the object of interest (DEHS particle) always remains in focus. Secondly, the aperture was set to $f_{\#} = 16$, resulting in a larger depth of focus to alleviate this problem. The reproduction scale in the centre of the image yields $11 \mu\text{m}/\text{pixel}$. The resulting magnification is $M = 0.67$. The measurements are carried out for the inter-disk spacing of 0.5 mm. Therefore, the size of the measuring volume is $12 \times 4 \times 0.5 \text{ mm}^3$.

It is illuminated through the rotor shaft by a double-pulsed New Wave Research Solo PIV III-15 Nd:YAG laser with a wavelength of 532 nm and a maximum intensity of 30 mJ. The pulse length is 3 ns and the repetition rate 15 Hz. The beam diameter is 4 mm, its divergence is less than 4 mrad. After the laser beam is deflected by three adjustable and coated mirrors, it enters the rotor via the hollow shaft at the centre of rotation (Fig. 5.3). The seeding in the measuring volume is illuminated by the beam, which is deflected by a fourth mirror. The mirror is smaller compared to the other three, because of the limited space inside the hollow shaft. Furthermore, it is not adjustable and fixed to the rotor (Fig. 4.27). In order to illuminate the entire gap, a divergent laser beam would have been desirable. Unfortunately, all attempts to place a combination of two lenses in order to create it, failed. The limited spatial access to the rotor and the small rotor dimensions required that the focal point was

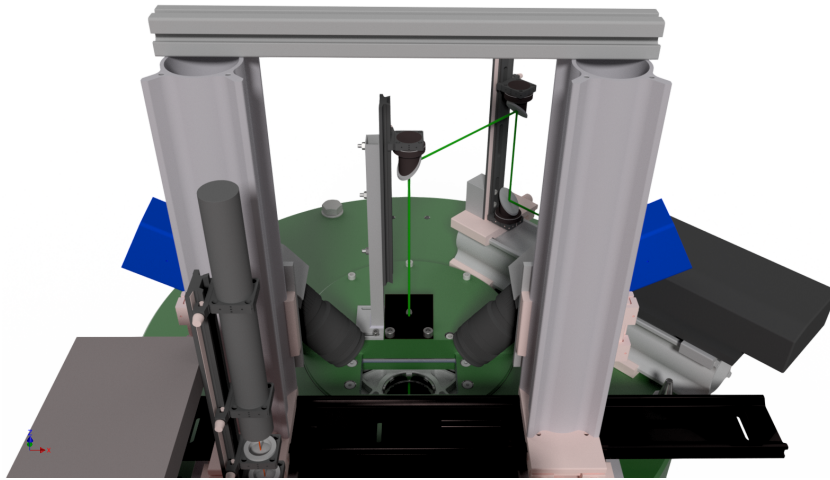


Figure 5.3: Trajectory of laser beam for the illumination of the measuring volume

near the rotating mirror. Therefore, the energy density of the laser beam can quickly be too high. The mirror was destroyed several times. There was no possibility to place a bigger and more resistant mirror inside the rotor.

The tracer particles are provided by a PIVTEC particle seeding generator PivPart12. It features up to twelve Laskin nozzles, which are adjustable in increments of four. Tracer particles with a diameter of $1\ \mu\text{m}$ on average can be generated. The seeder is pressure-resistant up to 14 bar and needs between 0.5 bar and 1 bar overpressure with respect to the maximum outlet pressure. The seeder is pressurised through a bypass of the main supply of compressed air, which is split after the mass flow measurement. An illustration of the system layout can be found in Fig. 4.34. For systematic and reproducible measurement results, the current pressure difference across the seeder is measured and visually displayed.

5.2 Stereoscopic 3D-PTV

Generally, tracking yields a better spatial resolution than cross-correlation approaches, as no spatial averaging is required, as outlined in [144]. Tomographic PIV, for instance, is not very suitable for the measurement of turbulent boundary layers flows, where strong velocity gradients near the wall are present, as shown by [145]. This double-frame stereoscopic 3D-PTV approach is suitable for measurements of the Tesla turbine rotor flow, where the measurement depth is small compared to the x and y dimensions of the measurement volume, when the seeding density is low and the optical access allows the use of two cameras only. For large measurement depths, the search area for the corresponding particle images on the other sensor is too large, yielding ambiguities. More cameras would be required to solve this problem. In 3D-PTV, the particle location determination is based on the triangulation of corresponding particle images from at least two views, as illustrated in Fig. 5.4.

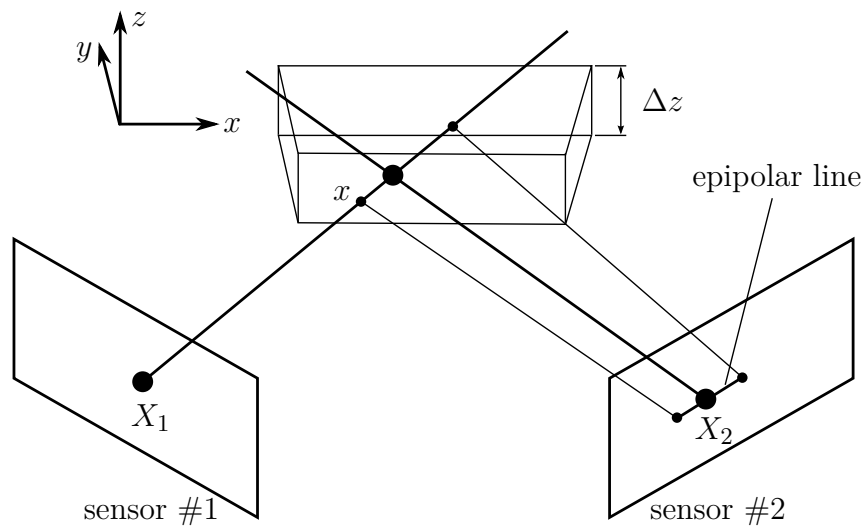


Figure 5.4: Triangulation principle

Epipolar geometry is employed to find these corresponding particle images on the other sensor. Thus, for a particle image on sensor #1, located at $\vec{X}_1 = (X_1, Y_1)$, the epipolar line on sensor #2 is calculated, where the length of this search area depends on the measurement depth Δz . Possible particle image matches are searched in the proximity of the epipolar line, while the maximum distance to the line is restricted, as illustrated by the search window in Fig. 5.5. However, with larger seeding densities an increasing number of possible particle image matches appear in the search area. Therefore, the seeding density is chosen such that the number of multiple matches is minimised. Once the spatial particle locations are estimated, the flow field is determined by means of double-frame particle tracking. In this Tesla turbine application, a fast and efficient nearest neighbour algorithm, described by

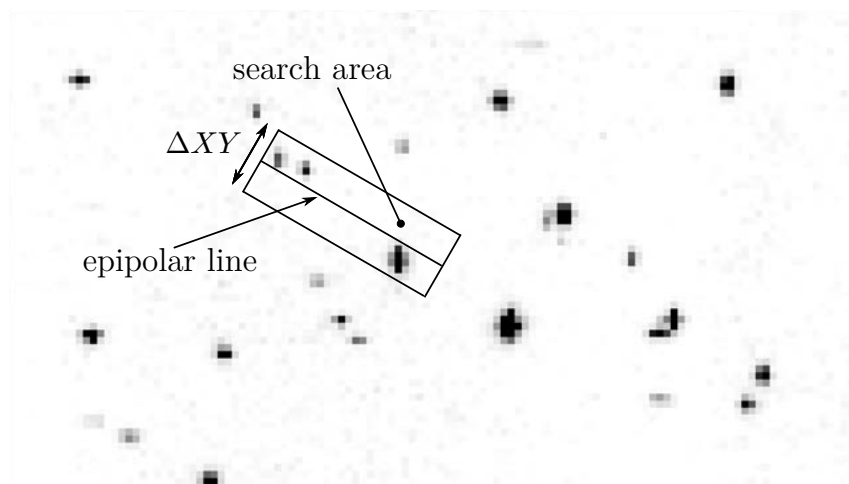


Figure 5.5: Sensor search area

[140], is employed.

5.3 Calibration and particle location determination

The calibration of the 3D-PTV system requires a set of calibration points, which can be derived from a calibration target with dots, grid intersections, or any other geometrical shape at known physical locations $\vec{x} = (x, y, z)$. After imaging the calibration target, the centre locations $\vec{X} = (X, Y)$ of these shapes are estimated for the two cameras, completing the required calibration information. From the calibration points the fundamental matrix F , as well as camera matrices, P_1 and P_2 of the stereoscopic imaging system can be calculated. These parameters are required to conduct the particle image matching, as well as the triangulation to determine the spatial particle location. This calibration is referred to the camera-pinhole model, introduced in [146]. As the spatial approach to the measurement volume is limited, a non-intrusive calibration approach, described in [147] is applied instead of using a regular calibration target. The calibration set-up and the non-intrusive calibration technique is described in chapters 5.4 and 5.5.

If vibrations and movement of the camera occur during measurements, this can be compensated for each recording individually by point correspondences derived from particles in the flow. This procedure is comparable to the self-calibration used in stereoscopic PIV, outlined in [148]. In this application, where the measurement depth lies in the range of the light sheet thickness, conducting a volumetric self-calibration does not yield any benefits.

Having determined the camera parameters in the calibration procedure, the particle locations can be determined. However, the recorded images first need to be pre-processed, before further steps can be applied. First, an average image of all recordings is subtracted from the individual images to eliminate the background reflections. This is followed by a subtraction of the local minimum intensities to better distinguish particle images from the background. Finally, the individual particle images are detected by means of an intensity threshold. After the particle image detection, the sub-pixel sensor coordinates are estimated by a least-squares approximation of a 2D Gaussian intensity distribution,

$$I(X, Y) = I_0 \cdot \exp \left[-8 \left(\frac{(X - X_0)^2}{d_{\tau X}^2} + \frac{(Y - Y_0)^2}{d_{\tau Y}^2} \right) \right], \quad (5.1)$$

where the coefficients X_0 and Y_0 denote the particle image sensor location, I_0 denotes the intensity at peak height, and $d_{\tau X}$ and $d_{\tau Y}$ denote the Gaussian peak width in the respective direction. The next step is the matching of the corresponding particle images on the two camera sensors using epipolar geometry, where the search area on the other sensor lies in the proximity of the epipolar line. When a uniquely matching particle image is found in the search area, the spatial particle location is triangulated by means of the optimal triangulation method, described in [149].

After the particle locations of the processed double-frame pictures are tracked with the nearest neighbour algorithm, outlined in [140], the displacement vectors are divided by the time delay Δt between both frames. The resulting velocity vectors are obtained in a three-dimensional Cartesian X, Y, Z frame of reference, due to the type of coordinate system of the calibration unit (chapter 5.4). However, cylindrical coordinate systems are usually desired in turbomachinery. Therefore it is necessary to transform the velocity vectors u_x, u_y, u_z into u, v, w . Details about the transformation can be found in Fig. A.71 in Appendix A.5.

5.4 Calibration Set-up

The calibration unit, which is illustrated in Figs. 5.1 and 5.3, consists of a continuous wave laser mounted onto a two-dimensional traverse system, which is placed on a rack. The traverse is composed of two linear slides. The Aerotech PRO 165 provides a traverse path of 300 mm in x -direction. The traverse path of the Aerotech PRO 115 is up to 400 mm in y -direction. The manufacturer specifies the positioning accuracy lower ± 0.01 mm. The HeNe-laser 25 is manufactured by Spindler & Hoyer. It emits red laser light at a wavelength of 632.8 nm and a typical power output of 1 mW. The beam diameter is 0.6 mm with a beam divergence of 1.3 mrad. Furthermore, the laser beam is focused to a diameter of approximately 0.1 mm by two spherical lenses. The calibration scheme that applies the above-described calibration unit, is introduced in chapter 5.5.

5.5 Non-intrusive calibration technique

For 3D-PTV measurement techniques, the calibration is carried out by imaging calibration points in at least two positions in depth within the measurement volume, as shown in the preliminary tests in chapter 4.2. Two-dimensional calibration targets are usually moved in the remaining direction in space. Three-dimensional targets with separated planes in depth are also applicable. However, it is difficult to place these targets within the flow domain of a Tesla rotor without major disassembly of the test rig, because of the restricted access to the measurement volume that limits the accuracy of the calibration. Moreover, moving optical equipment can make the calibration useless, due to the possible misalignment. In this case, it would be difficult to remove the lower disk of the rotor and to place the target exactly at the upper and at the lower wall for imaging. Ensuring the correct target positions would be difficult. In addition to that, the desired dimensions of a regular calibration target are very small. Targets of this size are not commercially available and therefore need to be printed out. This involves inaccuracies due to the limited resolution of standard laser printers. The non-intrusive calibration technique, which is developed here, overcomes this problem. It is also suitable for different fields of application, such as turbomachinery in general or cavity flows, where optical flow measurements are

challenging. Furthermore, the non-intrusive calibration scheme provides calibration functions not only for 3D-PTV. It is also applicable to tomographic PIV.

The calibration of a multi-camera measurement system requires calibration points, which have to be detectable on the sensors of all cameras. The corresponding points have to be matched uniquely without ambiguity. This leads to a set of coordinates on each sensor of the cameras. In order to obtain a successful mapping of the sensor locations to physical space, the physical coordinates have to be known. The calibration function, which is usually a third-order polynomial function, is computed from the sensor and physical coordinates.

This calibration scheme utilises the light reflections on the surface of the rotor's windows to determine the calibration points. A continuous wave laser beam is focused by two spherical lenses with a focal length of $f = -50\text{ mm}$ and $f = +50\text{ mm}$. Consequently, the beam is about 0.1 mm in diameter. The measuring volume is located between the two parallel bull's eyes in the disks of the rotor. A laser beam perpendicular to the glass windows creates four reflections on their surfaces. Only the two reflections between the windows are needed for the creation of the calibration points. The centre of the two reflections at the physical locations (x, y, z_0) and (x, y, z_1) denote the boundaries of the measurement volume. This is illustrated in Fig. 5.6. The distance between the windows is 0.5 mm . A displacement in depth is therefore

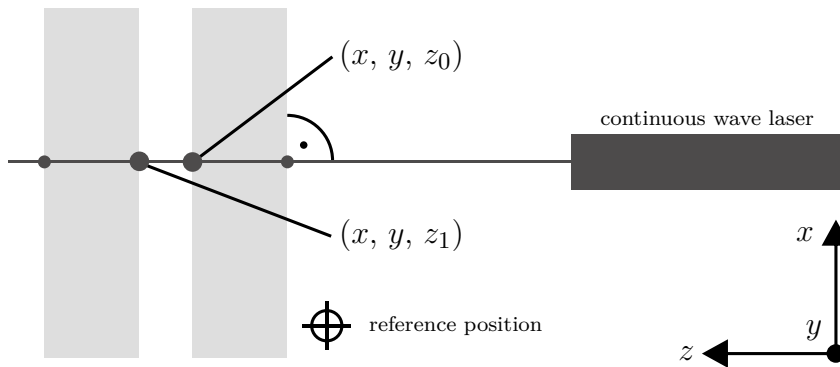


Figure 5.6: Calibration principle [147]

not needed. The laser itself is moved by a 2D traverse system within a positioning accuracy of less than $\pm 0.01\text{ mm}$. Figure 5.7 illustrates the traversable laser and the thereby created calibration target. Both cameras are imaging each position of the laser beam. This creates two 2D sets of calibration points. In total, 192 laser positions are approached with 24 rows in y -direction and eight columns in x -direction. The spacing between the positions are 0.5 mm in all three directions in space. The distance in z -direction can be adjusted by using different disk spacers. The distance between the rotor disks is ensured by an accurate distance measurement on a measuring table. For each position in the plane of the traverse, five images per camera are acquired at an exposure time of 1 s . The images are averaged and show an average variation of less than 0.1 pixel between the estimated centre locations of

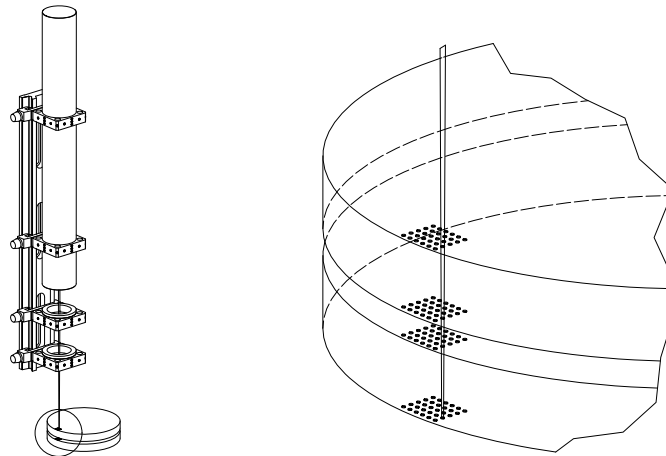


Figure 5.7: Traversable laser beam creating a non-intrusive calibration target [147]

the multiple images. To shorten the calibration time, only a single image would be sufficient concerning the spatial accuracy. The calibration time including imaging and translation of the laser using the single image approach is about 15 minutes. However, the quality of the reflections are mainly influenced by inhomogeneities and contamination of the rotating glass windows, but also by possible imperfections of the laser beam profile. These irregularities may be originated from the manufacturing process or by wear and tear during the operation. The centre locations of the reflections have to be fitted by a Gauss fit in two directions. Therefore, the mentioned imperfections can result in incorrect calibration functions. Slow rotations of the rotor alleviate this problem radically. The slightly moving reflections are then averaged over the exposure time. This leads to homogeneous intensity distributions of the light reflections that can be fitted accurately. Figure 5.8 exemplarily shows the greyscale image of the laser beam induced surface reflections from the point of view of a single camera. The intensity distribution of a single reflection in the lateral cut plane is shown in Fig. 5.9.

It is of special importance that the calibration only works properly, if all windows are clean. It is observed that especially the window of the housing has to be free of contamination. In this case, the laser beam is deflected and leads to deviations

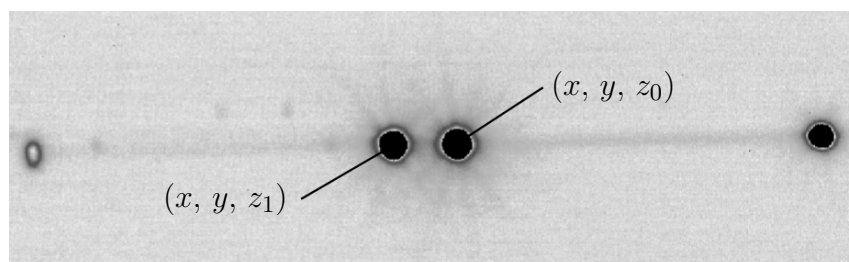


Figure 5.8: Greyscale image of light reflections of a single camera [147]

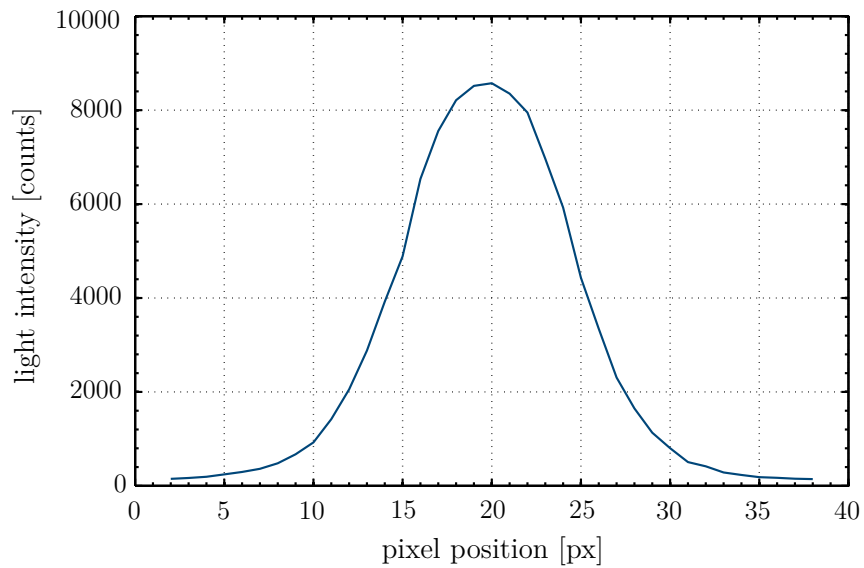


Figure 5.9: Intensity distribution of a reflection on a glass surface [147]

of the shape of the surface reflections. Therefore, the determination of the centre locations of the surface reflections is not always possible in this case and should be avoided.

Figure 5.10 illustrates the test rig during calibration. The beam of the Nd:YAG laser, which is used for the illumination of the tracer particles, is also shown in this figure.

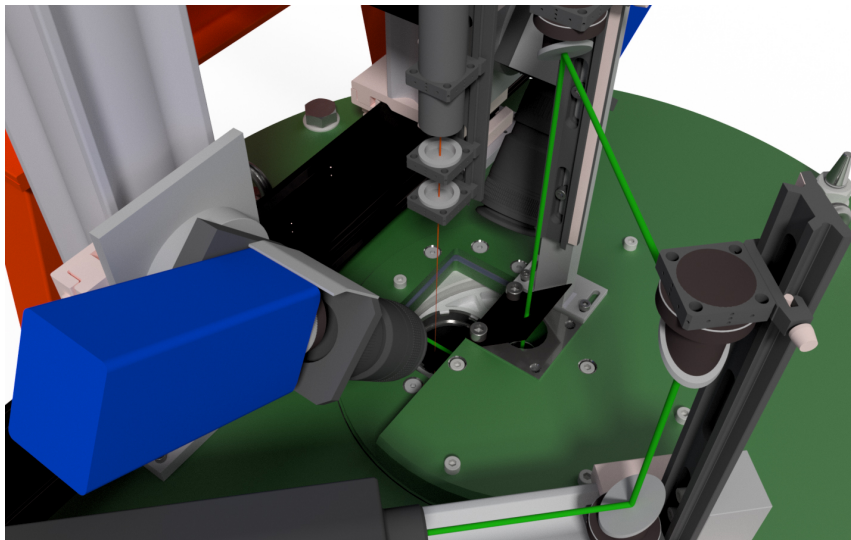


Figure 5.10: PTV set-up with non-intrusive calibration unit

5.6 Automation of the calibration scheme

The calibration process is fully automated. The traverse movement, as well as the image acquisition is controlled by a personal computer running the commercial software DaVis. Two other personal computers are involved in this procedure. The computer running the test rig software (cf. chapter 4.7) and the computer controlling the traverse movement. The test rig software controls the rotor speed via a LAN connection to the compact RIO. The compact RIO sends a TTL trigger signal to the DaVis computer. This signal is adjustable in phase. The DaVis software executes the image acquisition and sends the commands to move the traverse and the information regarding the desired laser positions to the traverse computer via a serial RS232 connection. The traverse computer runs a self-developed LabVIEW software to interpret the movement command regarding the desired laser positions. It also controls the traverse via a LAN connection. Furthermore, it also features a feedback channel, which informs the DaVis computer about the current states. Figure 5.11 illustrates the process operation of the automated non-intrusive calibration procedure.

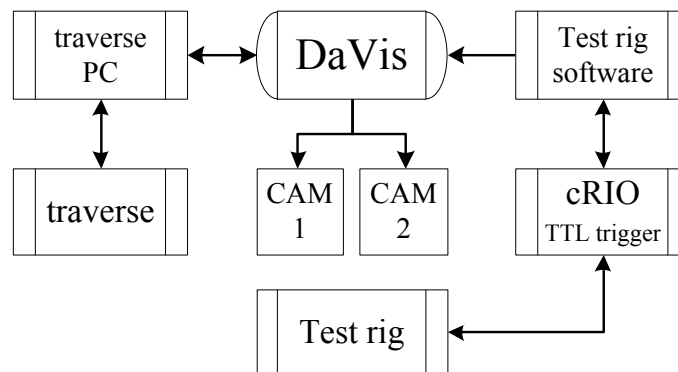


Figure 5.11: Automated calibration process

5.7 Post-processing of calibration data

Before the peaks of the light intensity of the reflections can be determined to obtain the sensor coordinates, image processing is performed. Undesired and indirect reflections that may occur are removed from the raw images using DaVis standard post processing. For all values below a threshold of several hundred counts, the light intensity is set to zero. After that, the calibration points are determined by means of a two-dimensional Gauss fit with sub-pixel accuracy. A MATLAB script is used to fulfil this task. The algorithm detects all light intensities found in the images above an adjustable threshold. A distance matrix of all reflections found on the sensors is calculated. After that, invalid reflections are pre-filtered by the expected diameter of the reflections within the measurement volume. Furthermore, the expected pixel distance between the inner reflections excludes outliers and the two surface re-

flections outside the measuring volume. The expected diameter, the expected pixel distance and their tolerances are adjustable. To ensure proper calibration data, images yielding undesired reflections and therefore wrongly more than two calibration points, are put on an alarm list for troubleshooting. These images are accessible and contain graphical information about the peaks found on the sensors. In this case, they are visually inspected by the experimenter. However, this happens rarely and is often caused by tracer seeding contamination of the glass windows. The physical coordinates and the pixel positions on each sensor are written to a text file for the particle tracking algorithm.

5.8 Quantification of the calibration error

The approach of the quantification of the calibration error is described here. The spatial coordinates of the calibration points are mapped back to their sensor coordinates using the calibration function. After that, the determined sensor coordinates are compared to the sensor coordinates from the calibration images, which denote the reference. The average absolute residuals on the sensor planes are shown in Tab. 5.1. Sensor #2 shows a slightly better performance. Also the sensor coordinates, ob-

residuals	sensor #1	sensor #2	unit
$\overline{R_{\Delta X}}$	0.207	0.157	px
$\overline{R_{\Delta Y}}$	0.186	0.166	px
$\overline{R_{\Delta XY}}$	0.278	0.229	px

Table 5.1: Average absolute residuals in sensor planes

tained from the calibration images are triangulated to spatial locations. Then, the triangulated physical locations are compared to the physical reference coordinates x , y , z known from the calibration. Table 5.2 shows the average absolute residuals in three-dimensional space. Based on the reproduction scale of 11 $\mu\text{m}/\text{pixel}$ in the cen-

residuals	in space	unit
$\overline{R_{\Delta x}}$	1.9	μm
$\overline{R_{\Delta y}}$	1.6	μm
$\overline{R_{\Delta z}}$	1.0	μm
$\overline{R_{\Delta xyz}}$	2.7	μm

Table 5.2: Average absolute spatial residuals

tre of the image and an area-averaged absolute residual of approximately 0.3 pixel, a deviation of about 3.3 μm in spatial coordinates is achieved. This is consistent with the average absolute spatial residuals in Tab. 5.2.

According to the manufacturer, the positioning accuracy of the traverse is ± 0.01 mm, which is about one magnitude lower compared to the determined residuals. Conse-

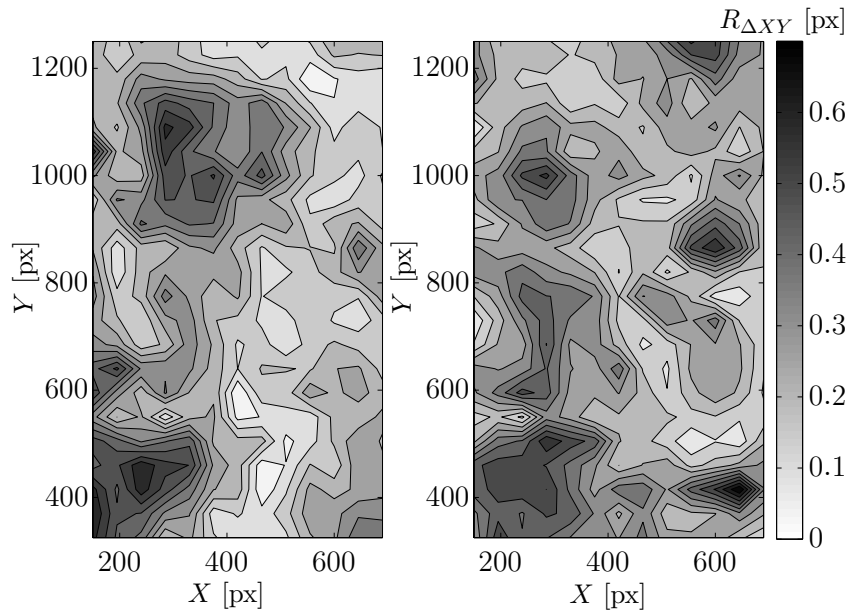


Figure 5.12: Residuals of calibration function of sensor #1 (left side: $z = 0.0$ mm, right side: $z = 0.5$ mm) [147]

quently, the residuals are plotted with respect to the corresponding locations on sensor #1 in Fig. 5.12. Apparently, there is no systematic deviation of the residuals, which could be referred to the positioning accuracy of the traverse. Specific locations with larger deviations are possibly caused by contamination or scratches on the glass windows. Highest residuals appear in roughly the same x - y -locations of both z -plane. Since the laser beam is perpendicular to both z -planes and has to pass the window of the housing first, the main imperfections probably occur either on the housing window or on the upper rotating window ($z = 0$ mm). This leads to the assumption that the positioning accuracy of the traverse is better than specified by the manufacturer.

6 Theoretical, numerical, and experimental results

This chapter analyses the accuracy limitations of the simplified, incompressible, laminar flow model, described in chapter 2.6. The theoretical solution of the rotor flow is compared to a laminar CFD. As no turbulence is modelled and the resolution of the flow is sufficiently high, the comparison can be regarded as a validation of the simplified, laminar flow model for a given geometry. Furthermore, the analytically derived laminar velocity profiles are compared to those obtained from CFD and 3D-PTV. The results from the turbulent particle imaging experiments are compared to turbulent CFD. Further details can be found in chapter 3. Moreover, the transition from laminar to turbulent flow is detected.

6.1 Comparison of incompressible, laminar theory with CFD

The governing equations of the incompressible, laminar flow model (Eqs. 2.11 to 2.13) are considerably simplified compared to the full set of Navier-Stokes-Equations (Eqs. 2.7 to 2.9). Therefore, the theoretical results are compared to those obtained from numerical simulations. The ANSYS CFX 16.1 solver is used in all simulations. Detailed information about physical and numerical modelling can be found in chapters 3.2.1 and 3.3.1. Equations 2.53 and 2.55 are used to evaluate the theoretical and the CFD results. Furthermore, they are normalised with their maximum occurring values, which are listed in Tab. A.10 in Appendix A.6.

For a better comparison of the velocity profiles, $F_{C,n}(R, Z)$ is introduced, where the profile $F_C(R, Z)$ is normalised by the division of its numerical integral

$$F_{C,n}(R, Z) = \frac{F_C(R, Z)}{\int_{-1}^1 F_C(R, Z) dZ}. \quad (6.1)$$

However, the radial velocity profile $G_C(R, Z)$ does not have to be normalised, as the continuity equation already requires

$$\int_{-1}^1 G_C(R, Z) dZ = 1. \quad (6.2)$$

6.1.1 Validation of the incompressible, laminar flow model

At first, performance map results of the test rig rotor geometry with different inter-disk spacings, which are obtained from theoretical modelling, are compared to CFD results (Fig. 6.1). The results agree excellently for small inlet angles V_1 . With increasing inlet angles however, the analytical results deviate more and more from the CFD data. The laminar incompressible flow model seems to overpredict shaft

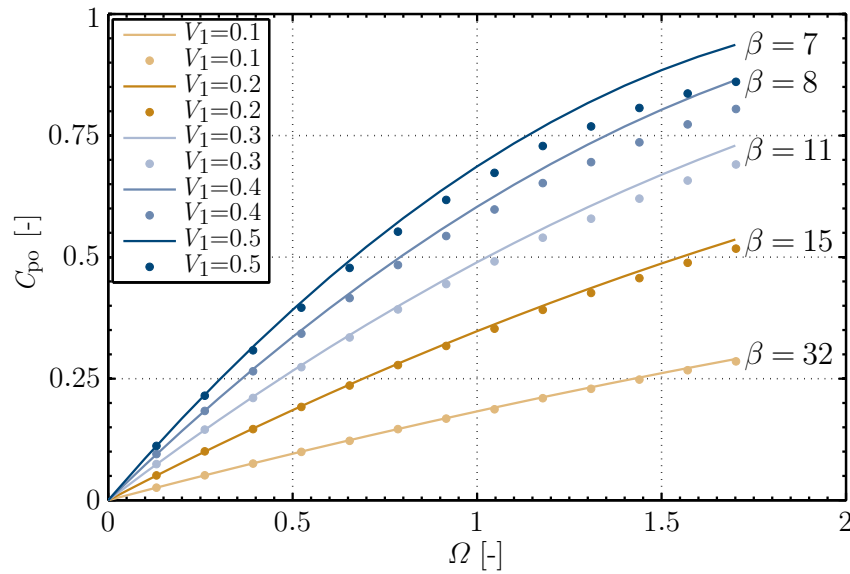


Figure 6.1: Comparison of analytical (solid lines) and numerical (dots) power maps

power. Same applies to the torque map (Fig. 6.2). The deviations between theory and laminar CFD concerning the isentropic efficiency are higher, compared to those of the performance and torque maps (Fig. 6.3). The isentropic efficiency is the ratio of shaft power and the total enthalpy difference between rotor inlet and outlet, multiplied by the mass flow. In other words, the isentropic efficiency depends on shaft power and the pressure drop across the rotor. Nevertheless, theoretical shaft power is overestimated and the associated theoretical pressure drop is slightly lower. Both

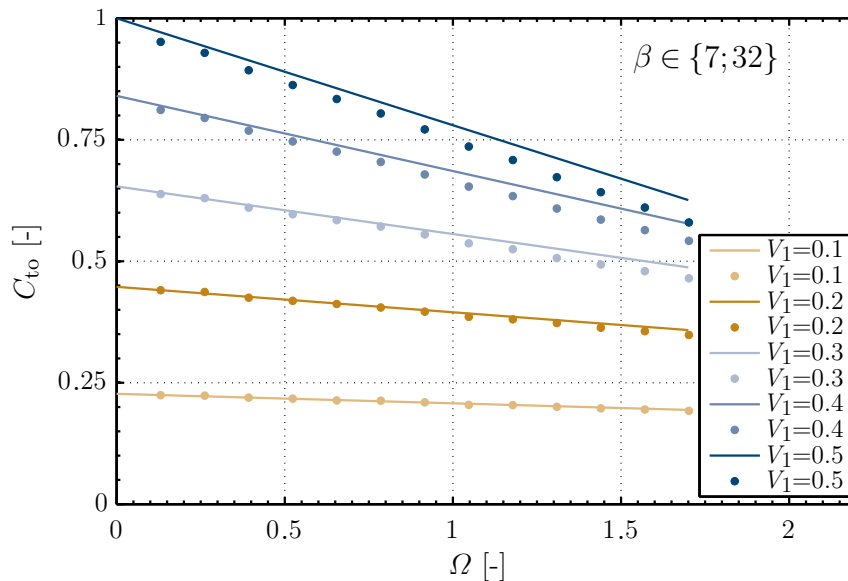


Figure 6.2: Comparison of analytical (solid lines) and numerical (dots) torque curves

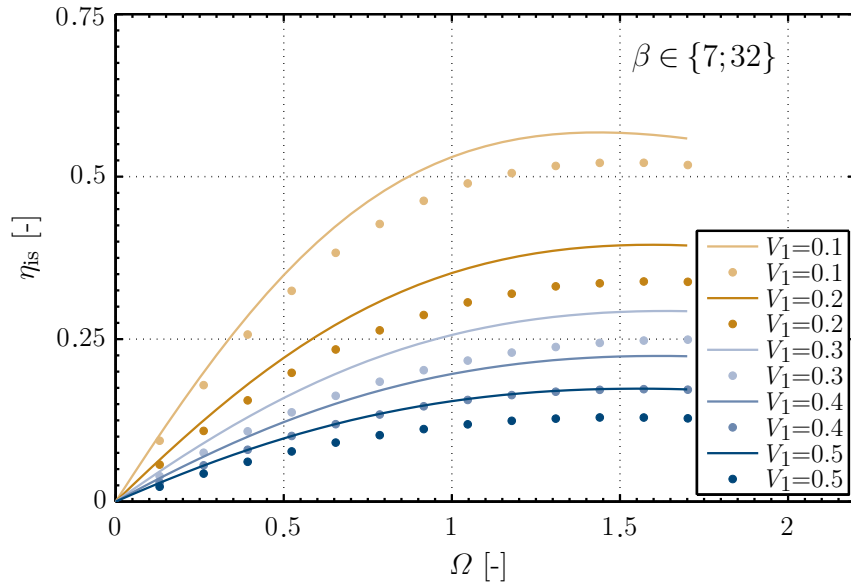


Figure 6.3: Comparison of analytical (solid lines) and numerical (dots) efficiency curves

errors are additive and lead to a much higher deviation in isentropic efficiency. More details about the comparison between laminar theory and CFD can be found in [11]. In contrast to the analytical flow model, the simulations imply that the velocity profiles at the inlet of the flow domain are ANSYS block-profile approximations. The flow model however assumes a parabolic velocity distribution and simply scales the velocity profiles with the mass flow. Moreover, they do not consider the inlet section, where the velocity profiles are not yet fully-developed. Furthermore it is unclear, if the parabolic velocity distribution is a physically correct assumption. According to the approximate solution from chapter 2.9, the profiles are rather fourth-order, than second-order polynomials in tangential direction. The radial velocity profile however, is quite well approximated by a parabolic velocity distribution. The development of the velocity profiles in the inlet section of the rotor are investigated in more detail using results from CFD. The profiles in radial and tangential direction are normalised according to Eqs. 6.1, 2.109, and 2.110. $F_{C,n}(Z)$ and $G_C(Z)$ are the fully-developed profiles obtained from CFD in Figs. 6.4 and 6.5. The shapes of the velocity profiles show a quick development across the rotor radius. As a consequence of that, inlet zone is therefore relatively short ($R > 0.98$).

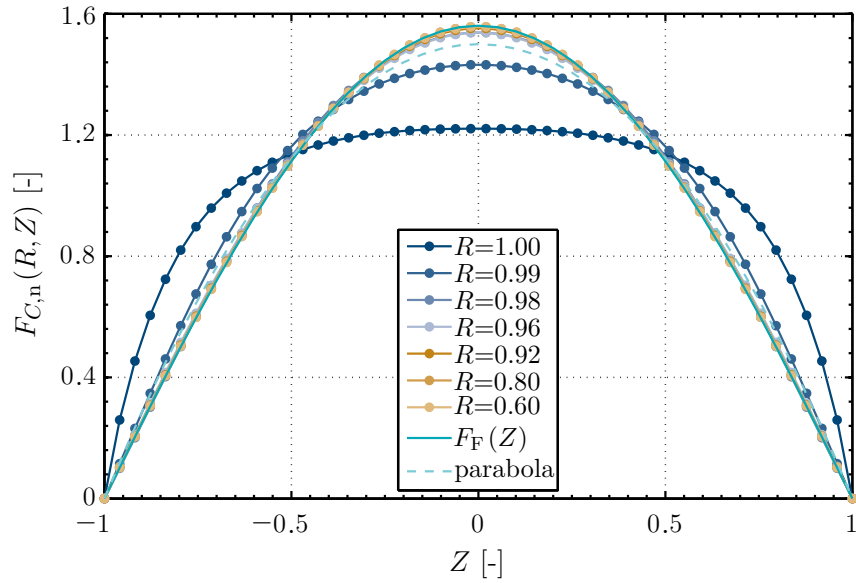


Figure 6.4: Development of tangential, relative CFD velocity profiles $F_{C,n}(R, Z)$ for $\Omega = 0.92$, $V_1 = 0.27$, $\beta = 11$, $Re_u = 630$ in comparison with the fully-developed analytical parabolic and $F_F(Z)$ the approximate profile for $A = 1.98$, $N = 1.48$

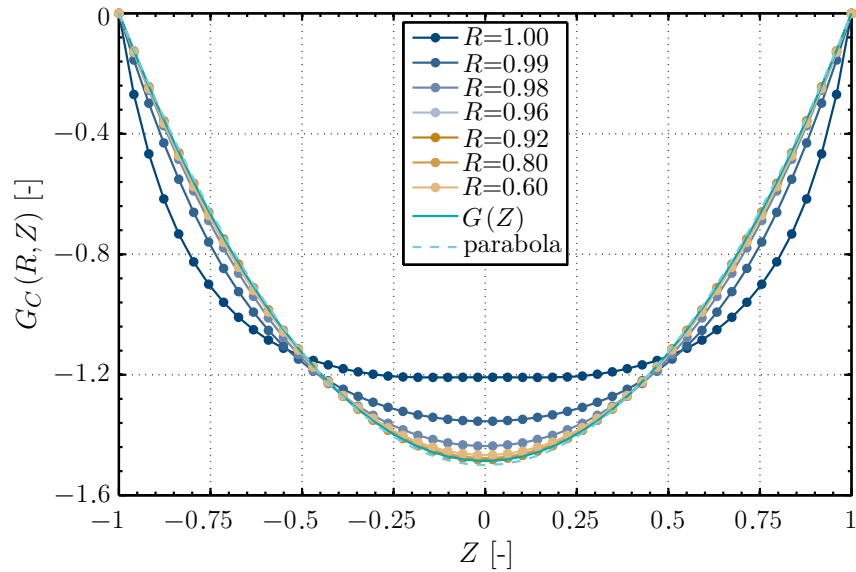


Figure 6.5: Development of radial CFD velocity profiles $G_C(R, Z)$ for $\Omega = 0.92$, $V_1 = 0.27$, $\beta = 11$, $Re_v = 170$ in comparison with the fully-developed analytical parabolic and $G(Z)$ the approximate profile for $A = 1.98$, $N = 1.48$

The fitting functions of the fully-developed profiles are

$$F_{C,n}(Z) = 4.194 \cdot Z^4 - 8.387 \cdot Z^3 - 0.9811 \cdot Z^2 + 5.175 \cdot Z - 0.001824 \quad (6.3)$$

and

$$G_C(Z) = 2.703 \cdot Z^4 - 5.405 \cdot Z^3 + 9.254 \cdot Z^2 - 6.551 \cdot Z + 0.001283. \quad (6.4)$$

6.1.2 Influences of the inlet profiles on turbine performance

In search of reasons for the deviation between CFD and theory, some essential issues have to be considered. The block-profile approximation at the rotor inlet is what probably happens in real Tesla turbines. The guide vanes or nozzles deliver the mass flow via an open jet across the radial gap between stator and rotor. Along this radial gap, the open jet starts to break up. Therefore, rather a block-profile, than a certain axial velocity distribution enters the rotor. In first approximation, the assumption of a parabolic velocity distribution appears to be a good estimate. Nevertheless, the fully-developed profiles from Figs. 6.4 and 6.5 represent the flow physics most likely. Applying these profiles to the theoretical solution, more accurate performance results will probably be obtained. It is assumed that the reason for the deviations in the results are originated by differences in the inflow condition. As a consequence, a second laminar, incompressible CFD without consideration of the development of velocity profiles in the rotor inlet section is performed. Instead of using parabolic inlet profiles, which would develop into a fourth-order polynomial shape, the fully-developed profiles $F_{C,n}(Z)$ and $G_C(Z)$ (Eqs. 6.3, 6.4) are used. In this case, the development of the profile shape is neglected. Figure 6.6 shows the performance maps for different inlet angles. Results from the theoretical flow model are compared to the CFD simulations with inlet and block-profiles. For small inlet angles, the agreement between all three results is excellent. Nevertheless, there is still a deviation between the results of the $F_{C,n}(Z)$, $G_C(Z)$ profiles and the results of the flow model assuming parabolic profiles. The deviations are about fifty percent lower. However, they additionally depend on the parameters V_1 , β , and Ω . Same applies to the torque map, due to the fundamental physical relation between both quantities. Therefore, the difference between the theoretical solution and the CFD

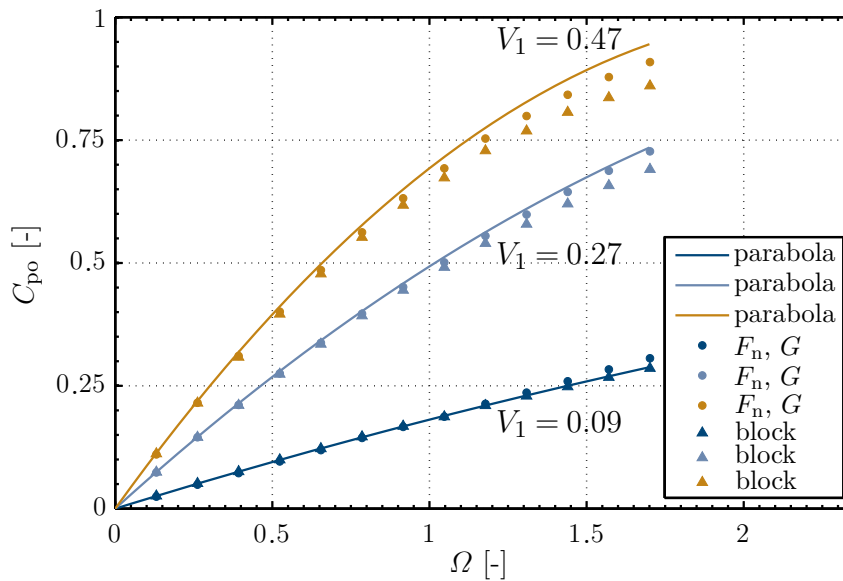


Figure 6.6: Comparison of numerical and analytical power maps

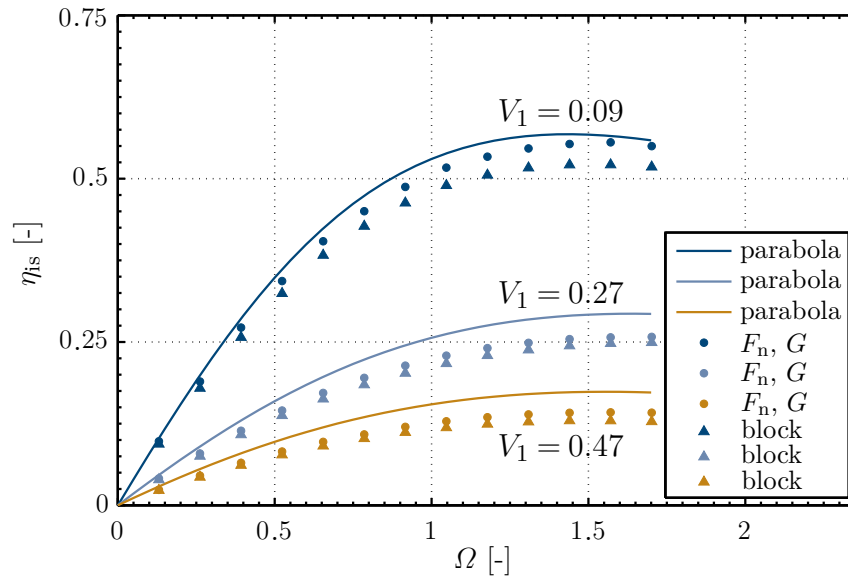


Figure 6.7: Comparison of numerical and analytical efficiency maps

can not fully be attributed to the inflow effect. Nevertheless, even if the inlet zone is relatively short, this is happening in real friction turbines and obviously lowers shaft power and torque. The efficiency results of the simulations with consideration of the new inlet profiles (Fig. 6.7) agree much better with the results obtained from theory. However, the deviations in efficiency are generally higher, as it is a superposition of pressure drop and shaft power, where both physical values are containing deviations. A closer look onto the radial development of the torque coefficient (Fig. 6.8) reveals

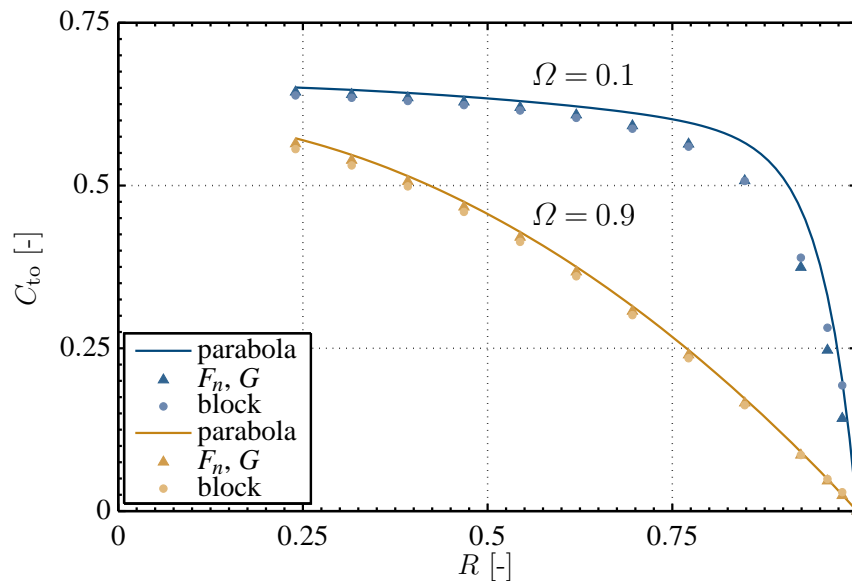


Figure 6.8: Development of torque across the radius

that the block-profile generates more torque at higher radius ratios. In addition to that, 90% of the torque is produced within approximately the first ten percent of the radius at the outer radius of the disks ($R = 1.0$) under certain operating conditions. However, the increased torque can be explained by the higher wall shear stress in tangential direction of the flow, which is originated by the profile development at the inlet section of the rotor. However, the increased wall shear stress leads to a higher pressure drop. As the outlet pressure is kept constant in all simulations, the inlet pressure increases. This contributes to a higher tangential outlet velocity (Fig. 6.9). Torque and shaft power are computed according to Eqs. 2.48 and 2.49. Higher outlet velocities u_2 lead to lower torques and lower shaft power.

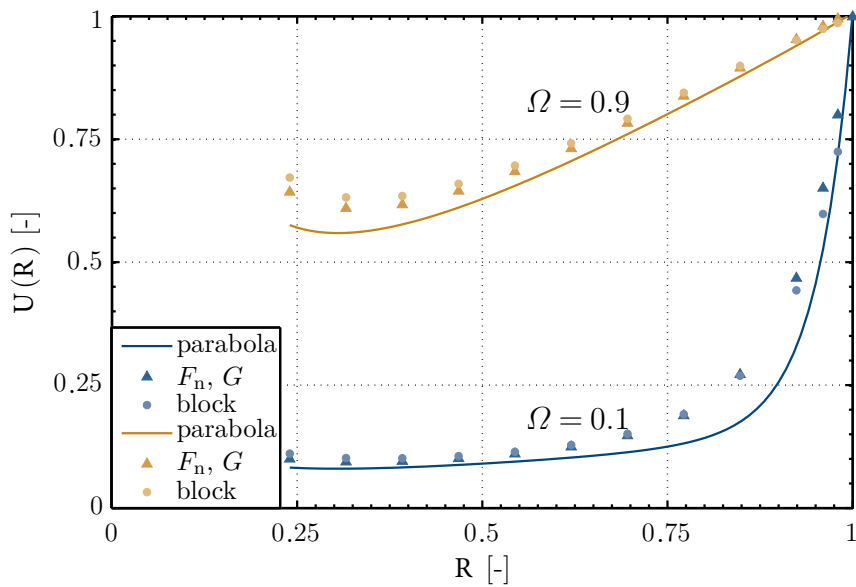


Figure 6.9: Tangential, absolute bulk velocity comparison

In summary, it can be concluded that the inflow effect is a partial explanation of the small differences between analytical flow model and laminar CFD. The remaining differences are dependent on the dimensionless parameter values. The equations of the incompressible, laminar theory neglect several mathematical terms in the full set of Navier-Stokes-Equations. In addition to that, the parabolic velocity distribution does not fully represent the laminar velocity field. However, for small inlet angles, the agreement is very promising, especially since Tesla turbines deliver optimum efficiencies under these inlet conditions.

6.2 Error propagation of particle image measurement data

The absolute measurement error of a single displacement vector can be decomposed into a group of systematic e_{sys} and residual errors e_{res}

$$e_{\text{vec}} = e_{\text{sys}} + e_{\text{res}}, \quad (6.5)$$

as described in [150]. Depending on the measurement task, systematic errors can be removed or at least reduced. However, the residual errors remain as a measurement uncertainty. These errors, however, often cannot fully be separated from the residual errors. Therefore, the following expression is chosen for the representation of the total measurement error for the field of displacement vectors in a measuring volume

$$e_{\text{field}} = e_{\text{bias}} + e_{\text{rms}}. \quad (6.6)$$

It consists of a bias and a random error, which is also called measurement uncertainty.

6.2.1 Systematic error

Systematic errors certainly arise in the measurement data carried out here. Some of the systematic errors can be corrected. According to [150], the others remain in the measurement data set. This type of error is comprised of rotor deformation and errors from the calibration method, which are included in the calibration function.

The wall positions and therefore the gap width are quite accurately known from the PTV measurements. They are determined by the clearance between the most distant displacement vector locations. The non-intrusive calibration method and also the PTV measurements are performed with a stagnant rotor. Consequently, it becomes apparent that the rotor disks deform under rotation. The outer rim of both disks have the tendency to move upwards, while the gap width remains almost entirely constant. Obviously, the inner part of the pair of disks is less shifted and deformed, as already expected from the FEM-simulations. The rotor displacement is systematically corrected in the measurement data by shifting the unscaled into the centre between the disks. The FEM-simulations in chapter 4.4.5 indicate that the gap closes slightly under rotation. This cannot be confirmed unambiguously from the PTV data recordings. Figure 6.10 shows the deformation of the disks at the outer radial measurement position for different operating conditions. Obviously, the gap is enlarged with increasing mass flow. Furthermore, it also enlarges with rising rotational speed. The maximum deformation enhances the distance between the walls by 5.2%. It is small compared to total gap width of 0.5 mm between the rotor walls. However, the inter-gap distance for the highest flow rate and the highest rotational speed seems to be an outlier. It is very likely that the disks actually have the highest deformation under these operational conditions. Due to the upward shift of the rotor at the outer radius of the disks, the beam of the

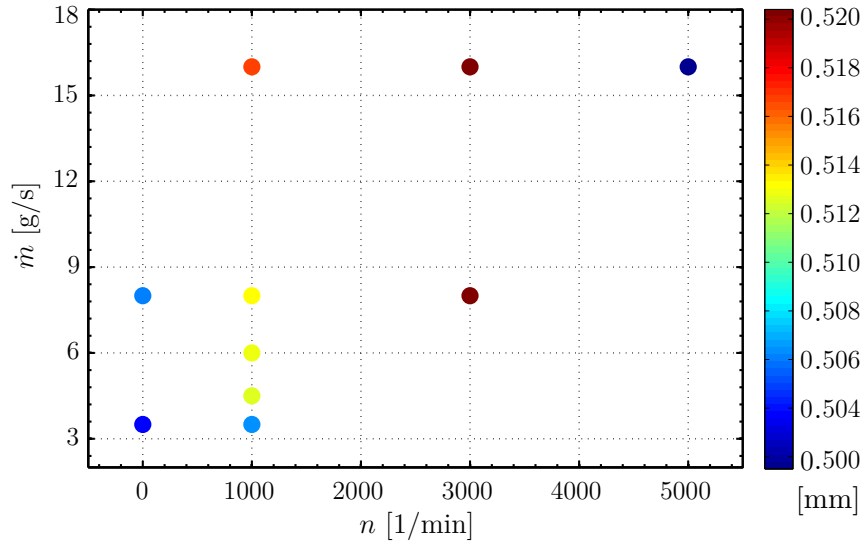


Figure 6.10: Deformation of the gap width between the disks at the outer radius

laser coming from the centre of rotation is only able to illuminate the measurement volume indirectly through reflections. Therefore, the light intensity of the particles' scatter is significantly reduced, compared to the inner radial measurement volume. In this case it cannot be ensured that the entire gap is illuminated, as the laser beam is not diverging significantly within the short distances inside the rotor. However, establishing a suitable illumination of the measurement volume is a challenging and time-consuming task in this configuration. Nevertheless, the determination of the wall positions is more precise at the inner radial measurement volume, because the illumination at the flow boundaries is more intense. Unfortunately, the deviations in the distance between the disks cannot be systematically corrected.

The test rig and both cameras, which are directly mounted to the turbine housing are vibrating in dependency of the operational conditions. The vibrations rise with increasing rotational speeds and are corrected for each measuring point.

Another systematic error is hidden in the calibration function. The non-intrusive calibration method is described in [147]. It requires that the constant-wave laser is perpendicularly aligned to the glass windows of stator and rotor, as accurately as possible. Nevertheless, tiny misalignments always remain, which lead to smallest beam deflections and finally to a systematic error. Furthermore, the variations in the light intensity of the reflections at the flow boundaries at different calibration points are observed. These deviations can be caused by little scratches on the glass surfaces, inhomogeneities from the manufacturing process, and contamination of the windows. They finally lead to incorrect Gauss-fits of the algorithm for the determination of the centre of the non-intrusive calibration points. Altogether, 192 laser positions are approached, yielding 24 rows, and eight columns in two axial planes. However, calibration data containing sparse outliers, lead to the fact that they are usually averaged out in the calibration function. Unfortunately, the systematic errors, which

are hidden in the calibration function, cannot be corrected.

A good indicator for the estimation of the remaining systematic errors' dimension, is the magnitude of the average displacement vector $\overline{\Delta z}$ in axial direction of all particle images. Although, periodic flow fluctuations occur inside the measurement volume, the average displacement in z -direction should ideally be $0 \mu\text{m}$ (or $\overline{w} = 0 \text{ m/s}$). The average displacement of all particles $\overline{\Delta z}$ at the highest circumferential disk velocity at the inner radial position ($r = 48 \text{ mm}$) is $0.06 \mu\text{m}$. However, it is approximately doubled at the outer radial position ($r = 110 \text{ mm}$). Furthermore, it can be demonstrated that the average displacement of the particles $\overline{\Delta z}$ is a function of the rotational speed of the rotor (Fig. 6.11). It rises with increasing rotational speeds. Moreover, the displacement is larger at the outer radial position, where the rotor deformation is more intense. Measurements with a stagnant rotor, however, show that the average displacement of both radial positions is virtually equal. As a result, Fig. 6.11 provides considerable evidence that the increase in average particle displacement

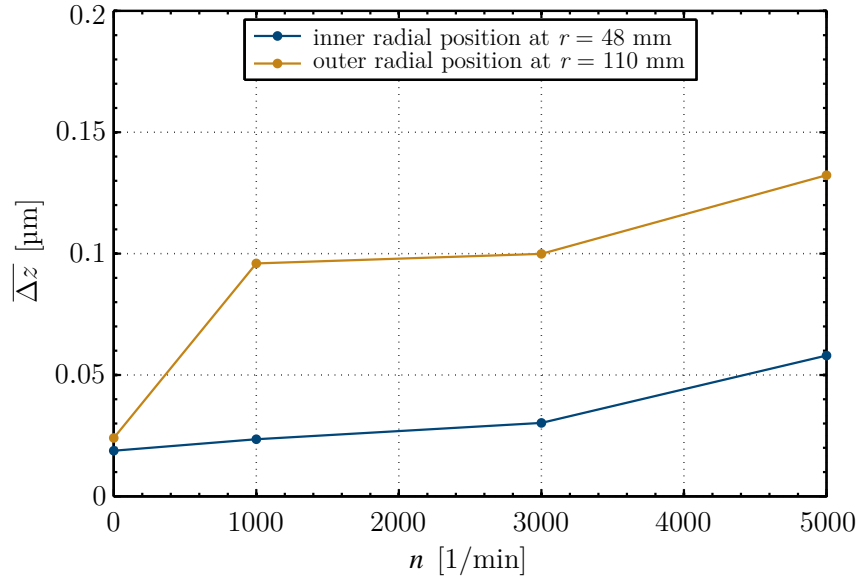


Figure 6.11: Particle displacement $\overline{\Delta z}$ averaged for each operational point as a function of the rotational speed n

$\overline{\Delta z}$ is caused by rotation, deformation, and rotor vibration. The maximum particle displacement Δz at the outer radial position is utilised for the estimation of the bias error. The maximum displacement of $\Delta z = 0.13 \mu\text{m}$ at the highest rotational speed can be converted to the particle image displacement on the sensor, using the reproduction scale of $11 \mu\text{m}/\text{pixel}$. With an average particle image displacement of 10 pixel in the main flow direction at the centre of the image, the bias error of the entire field of displacement vectors can be estimated, yielding

$$e_{\text{bias}} = \frac{0.012 \text{ pixel}}{10 \text{ pixel}} = 0.1 \%. \quad (6.7)$$

In summary, it can be said that this is a strong indication for an extremely small

bias error of the average field of displacement vectors. Hence, it is considered to be negligible. However, the bias error cannot be completely determined or corrected.

6.2.2 Residual error

All measured velocity profiles show fluctuations in radial, tangential, and axial direction. They are presumably originated by phenomena of fluid mechanics, such as periodic vortices between rotor and stator. However, there are local measurement inaccuracies, which need further discussion. The stereoscopic PTV set-up on the test rig has a camera angle of approximately 90° and leads to the following order of directional accuracies. Highest spatial accuracy is found in radial direction. The accuracy in tangential direction is slightly lower. The out-of-plane component in axial direction shows the lowest spatial accuracy.

It is observable for all measuring points that the standard deviation $\sigma_{\Delta z}$ of all displacement vectors near the rotor walls is about $2\ \mu\text{m}$ for laminar and turbulent flows. In case of turbulent flow, the standard deviation $\sigma_{\Delta z}$ rises clearly in the centre between the disks and indicates the presence of turbulent fluctuations. Furthermore, the value of the standard deviation $\sigma_{\Delta z}$ at the walls is a measure for the residual error of a single displacement vector, as it is almost entirely constant for all measurements carried out. To account for the 95.4% confidence interval, twice the standard deviation of all displacement vectors $2\sigma_{\Delta z}=4\ \mu\text{m}$ is assumed to be the random measurement error, respectively the measurement uncertainty e_{rms} . Together with a reproduction scale of $11\ \mu\text{m}/\text{pixel}$, the maximum random displacement is 0.36 pixel. With an average particle displacement of 10 pixel between the double-frames at the image centre in the main flow direction, the maximum residual error of a single displacement vector in radial and tangential direction is estimated to be

$$e_{\text{res}} = e_{\text{res,rad}} = \frac{0.36\ \text{pixel}}{10\ \text{pixel}} = 3.6\ \%. \quad (6.8)$$

The tangential velocity component is examined in the relative frame of reference throughout this thesis. During the measurements, the circumferential disk velocity is kept constant, as much as possible. Due to control deviation of the rotors' revolutional speed, the wall velocity is subjected to an additional random error. The fluctuation of the circumferential disk velocity is computed using the equation

$$\omega \cdot r_{o,i} = \frac{\pi}{30} \cdot (\bar{n} \pm \Delta n) \cdot (r_{o,i} \pm \Delta r), \quad (6.9)$$

with $\Delta n = \pm 2\sigma_n$, $\Delta r_o = \pm 0.2\ \text{mm}$, and $\Delta r_i = \pm 0.1\ \text{mm}$. The additional residual error in tangential direction, averaged for all revolutional speeds, is therefore

$$e_{\text{res},\omega} = 2.0\ \%. \quad (6.10)$$

As a consequence, the total residual error in tangential direction is estimated to be

$$e_{\text{res,tan}} = \sqrt{e_{\text{res}}^2 + e_{\text{res},\omega}^2} = 4.1\ \%. \quad (6.11)$$

The increase in spatial uncertainty at the walls, originated by rotation indicates that the tangential velocity component contains a larger error, compared to the velocity component in radial direction. The velocity fluctuations observed in the PTV data are higher in tangential direction and are therefore in good agreement with the appraisal of the residual error $e_{\text{res,tan}}$ of a single displacement vector. Due to the relatively strong velocity gradient in radial and tangential flow direction, the velocity profiles are determined in very small radial positions, using the binning technique. The addressed residual errors refer to a single displacement vector. With the exception of the first PTV measurement value near the wall, the measurement uncertainty of the field of particle images is almost averaged out with an increasing number of double-frame images and assigned displacement vectors per bin. It can be computed by dividing the error by the square of the number of displacement vectors per bin. The bias error of the field of displacement vectors is therefore negligible. Therefore, it is required to ensure that each bin contains enough displacement vectors, which are preferably distributed homogeneously across the inter-disk spacing.

The closer the particle position is at the wall, the higher is the probability of mismatches of particle images, which create physically wrong displacement vectors. As already mentioned in [144], the very first data point at the wall is biased when using PTV in post processing. This is caused by the uncertainty in the estimation of the particle image position. Particles with smallest distances to the wall and with smallest velocities, may be associated with the wall position, as outlined in [144]. Usually, no particles can be found below the wall surface, when using non-transparent walls. However, applying PTV on the measurement data of the flow field inside the Tesla rotor containing transparent walls, leads to the fact that it is very likely that tiny cavities or inhomogeneities inside the wall may be illuminated and therefore associated with the wall position. In this application, the uncertainty near the wall is higher, than in usual measurement environments.

6.3 Experimental, numerical, and theoretical results

Flow fields at different operating conditions are measured using volume illumination with a particle tracking approach. The rotational speeds vary between 1000 and 5000 min^{-1} . Mass flows from 3.5 to 16 g/s are examined. The shape of the velocity profiles have a substantial influence on the process of energy conversion in Tesla turbines. They are therefore in focus during the investigations. All measurements are carried out using the 0.5 mm disk-spacing. Flow fields are obtained at different radial positions. An outer and inner radial position is chosen for the visualisation of the results. The outer position is at the radius of (0.8800 ± 0.0024) or (110.0 ± 0.2) mm in dimensioned data. The inner position is set to the radius of (0.3840 ± 0.0016) , respectively (48.0 ± 0.1) mm. The disk radius is 125 mm. Only selected cases are presented in this chapter. The complete set of measurement, simulation, and theoretical data can be found in Appendix A.3.

6.3.1 Laminar flow

Figures 6.12 and 6.13 exemplarily show the tangential and radial velocity profiles across the inter-disk spacing at the outer radial position. The mass flow is set to 3.5 g/s. The rotational speed is 1000 min^{-1} in this case. Obviously, the flow regime is laminar. The profile shapes of the laminar CFD and those obtained from the approximate analytical solutions (AFP and AGP) agree reasonably well. In addition to that, both solutions are in good agreement with the PTV results. The velocity profiles are normalised, using the median of all experimentally determined velocity vectors, which are located $\pm 2.5\%$ around the centre of the gap between the disks.

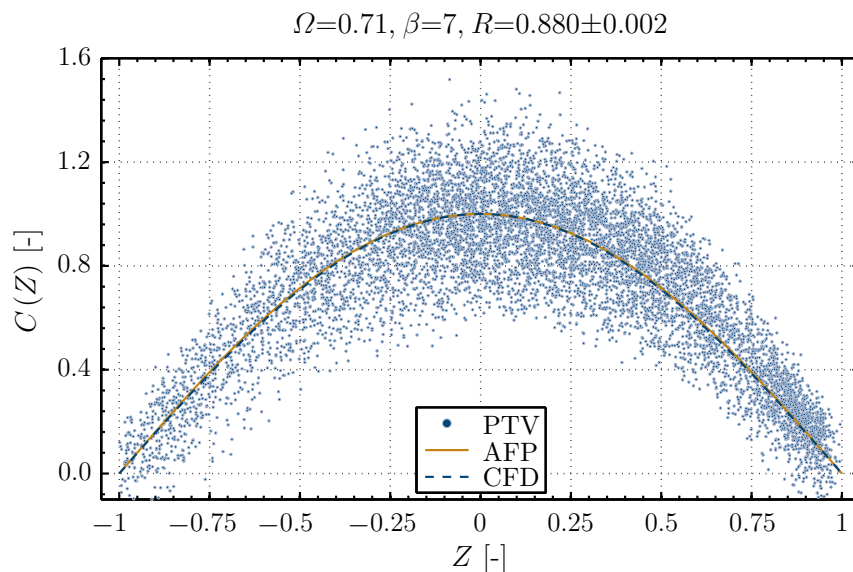


Figure 6.12: Tangential, laminar velocity profile at the outer radius

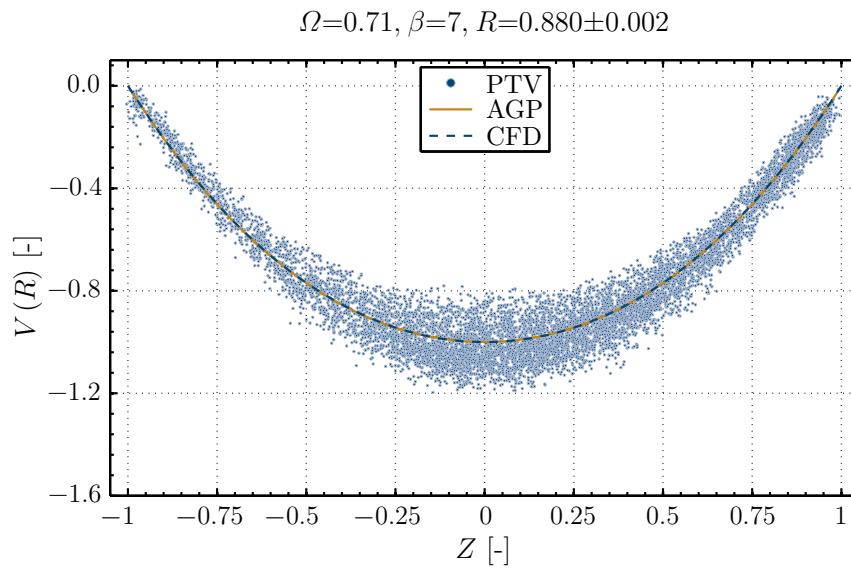


Figure 6.13: Radial, laminar velocity profile at the outer radius

The median values are listed in Tabs. A.7, A.8, and A.9 of Appendix A.3. The associated tangential and radial profiles at the inner radial position are shown in Figs. 6.14 and 6.15. The predicted tangential profiles from the laminar CFD and from the approximate analytical solution AFP are in very good agreement with the PTV results. However, there is a deviation between the shapes of the velocity profiles in radial direction. Although, the laminar CFD and the theoretical profile AGP show identical results, the recorded PTV profile indicates a stronger inclination of the velocity gradient at the wall. As the laminar CFD and the theoretical solution are modelled assuming ideal outflow and are in excellent agreement, one possible ex-

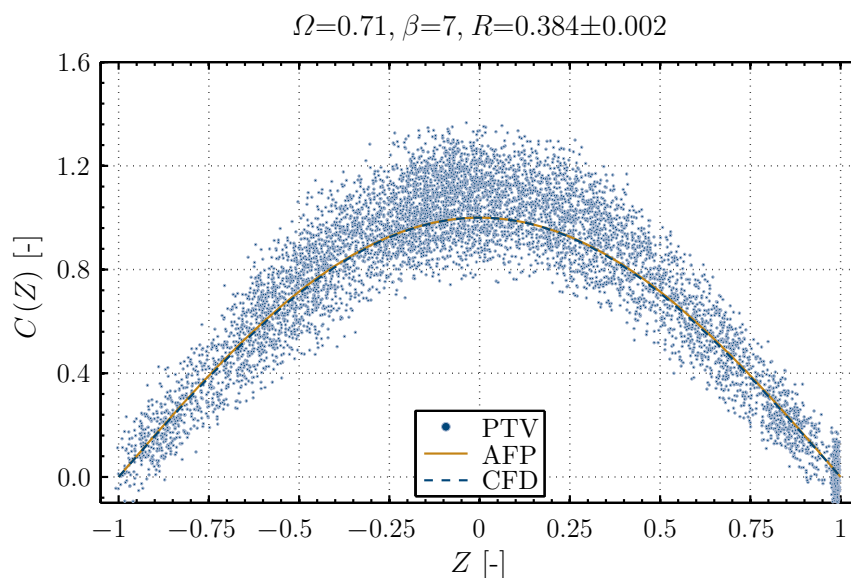


Figure 6.14: Tangential, laminar velocity profile at the inner radius

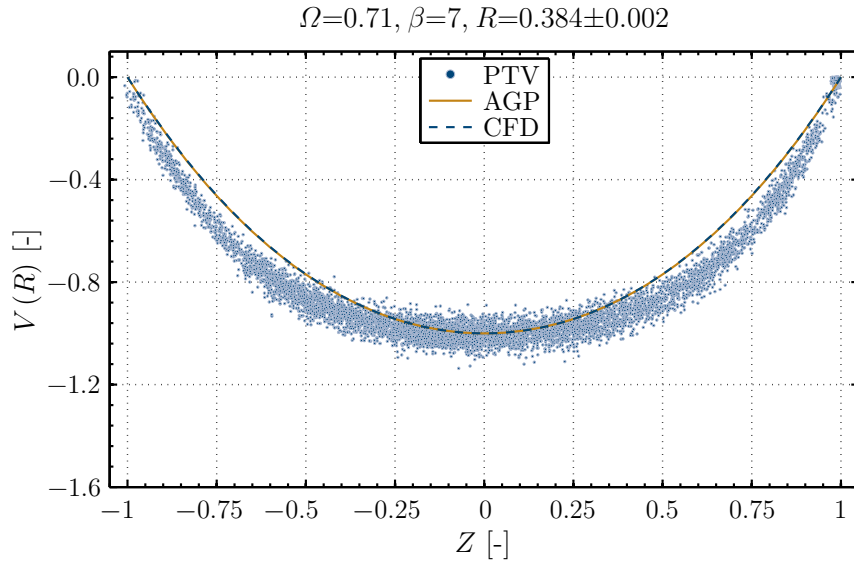


Figure 6.15: Radial, laminar velocity profile at the inner radius

planation might be a retroactive effect of the outlet geometry onto the rotor flow upstream. Independent of the predominant flow regime inside the rotor, the plots of the PTV measurement results (tracks) are generally more dense and more homogeneously distributed across the gap at the inner radial position. The illumination is also significantly better at the inner radius. This is due to the fact that the pulsed laser is coupled into the rotor with a non-adjustable deflection mirror at the centre of rotation. Unfortunately, it is impossible to use lenses in order to create a divergent beam for an illumination of the entire axial rotor gap. This is caused by the limited spatial access to the measurement volume. The longer the path from the rotor-fixed deflection mirror to the measurement volume, the worse is the illumination. The particles at the outer radial position are partially indirectly illuminated by reflections. Hence, the signal-to-noise ratio is lower. Therefore, the tracer particles scatter less light at the outer radial position.

However, all measurement results also clearly show velocity oscillations in both direction. In general, the fluctuations are higher in the tangential direction. Furthermore, the amplitude of the velocity variations decrease from the outer to the inner radius. More details about the velocity oscillations can be found in chapter 6.3.3.

6.3.2 Turbulent flow

Turbulent flow behaviour can be observed beginning at a mass flow rate of 4.5 g/s. Figures 6.16 and 6.17 exemplarily show the turbulent, tangential, and radial velocity distribution along the rotor gap at the outer radial position for the operational conditions 1000 min^{-1} and 16.0 g/s. PTV measurement data is compared to turbulent CFD, using the standard SST turbulence model. The turbulent profiles at the inner

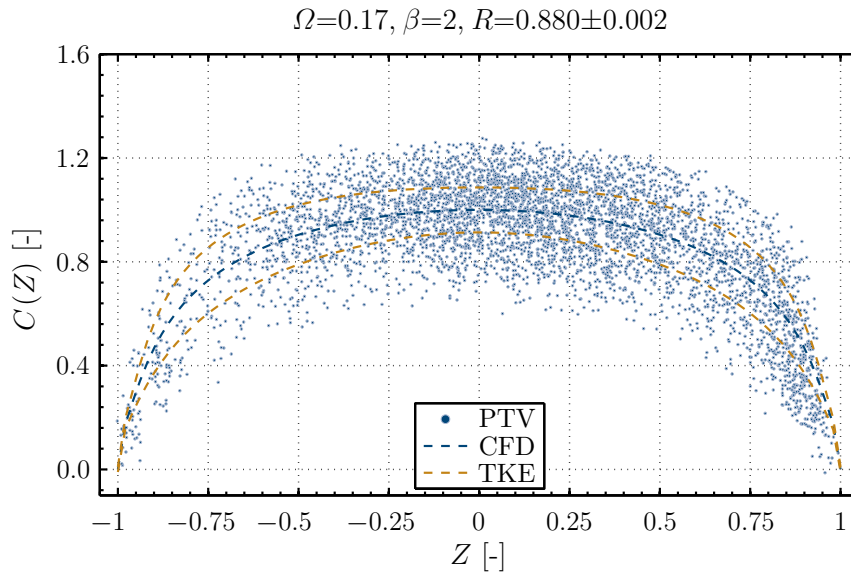


Figure 6.16: Tangential, turbulent velocity profile at the outer radius

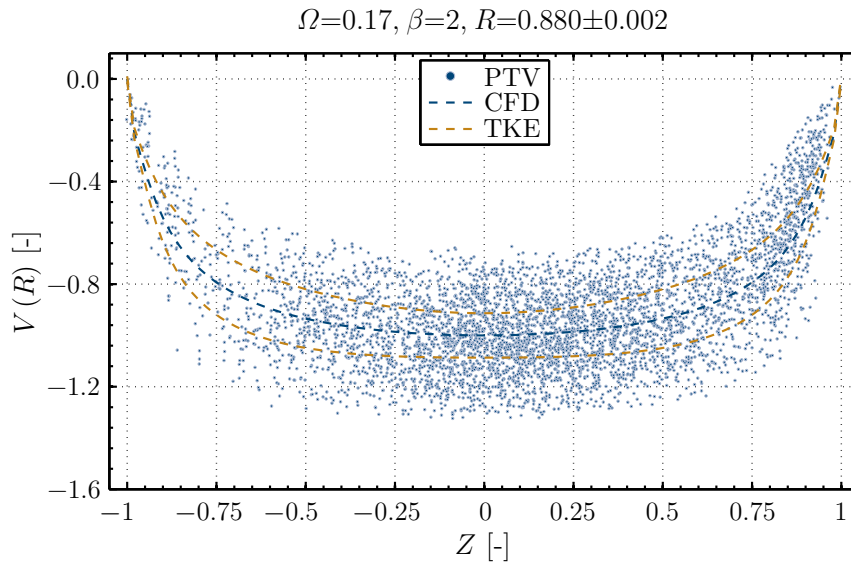


Figure 6.17: Radial, turbulent velocity profile at the outer radius

radial position are shown in the Figs. 6.18 and 6.19. The turbulent velocity profiles are superimposed by velocity oscillations and cannot be separated from each other. In order to estimate the magnitude of the turbulent fluctuations, the plots contain the velocity profile TKE showing the normalised turbulent velocity fluctuations $\overline{U'^2}$ and $\overline{V'^2}$. They are computed from the turbulent kinetic energy k of the CFD data under the assumption of isotropic turbulence ($\overline{u'^2} = \overline{v'^2} = \overline{w'^2} = 2/3 \cdot k$). The results from turbulent CFD simulations and PTV measurements correspond well in this specific case. The profile shapes at the outer radial position show best matches. They differ most for the radial velocity profile at the inner radial position (Fig. 6.19). The

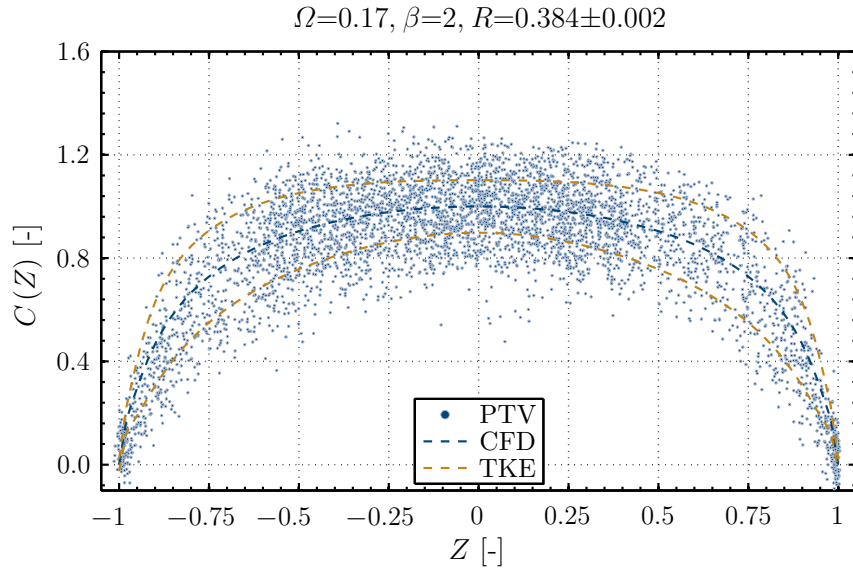


Figure 6.18: Tangential, turbulent velocity profile at the inner radius

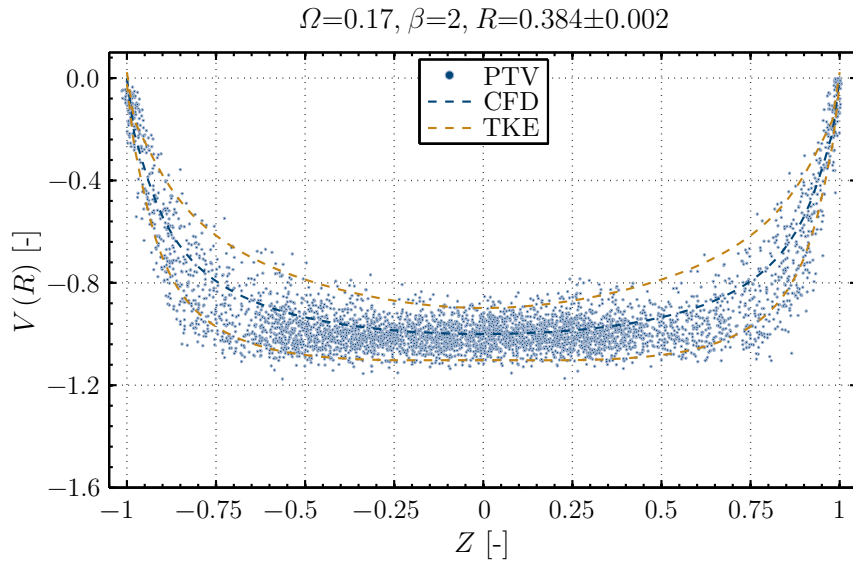


Figure 6.19: Radial, turbulent velocity profile at the inner radius

spread of the fluctuations in both directions is comparable with those of the outer radial position in this operational point. However, in most of the turbulent cases, the velocity variations are partially higher in the tangential direction. The range of velocity variations decreases with the flow direction from the outer to the inner radius, just like observed in the laminar cases. Nevertheless, the comparison indicates that the standard SST turbulence model does not fully represent the flow field inside a Tesla turbine rotor, which is crucial for the correct prediction of the performance maps. A calibration of the turbulence model constants to the measurement data should help to improve the accuracy of the turbulent CFD results in the future.

6.3.3 Flow oscillations

All measured velocity profiles continuously show velocity fluctuations. Predominantly, the oscillations are higher in the tangential direction and decrease from the outer to the inner radius. Obviously, the amplitudes of the oscillations additionally increase with rising rotational speed and mass flow rate. The observable velocity oscillations are superimposed by turbulent fluctuations. However, it is not possible to separate them from each other, as the repetition rate of the laser is too low to resolve the different frequencies (sampling error). In addition to that, they cannot be estimated from the turbulent CFD results, because two equation models like the standard SST model simulate Reynolds stresses instead of turbulent velocity fluctuation values.

In [151] a theoretical prediction of the phenomenon using the equations of unsteady motion of an incompressible viscous fluid was presented. It was shown that even for tiny amplitudes of pressure oscillations, the amplitude of the oscillations of the relative velocity at resonance is able to reach values comparable with the mean velocity of the flow. The initial suspicion was that the pressure oscillations were generated by the mass flow regulator. High frequency-resolved Kulite measurement probes are therefore used to detect the pressure oscillations in the plenum. The limited spatial access to the rotor inlet prevented desirable Kulite measurements in the area of the rotor and the stator. It is very likely that vortices are generated in the gap between rotor and stator. The PTV measurements show that the oscillations generally decay further downstream. This fact is a strong indication that the velocity fluctuations occur at the rotor inlet region. Transient CFD results of a simplified, two-dimensional stator-rotor geometry offer deeper insights into this flow phenomenon. However, the simulation neglects rotation. The velocity is set to values for laminar flow conditions. The non-perfect axial alignment between rotor and stator might be a suitable explanation for the oscillations.

Therefore, two cases are modelled:

- rotor and stator walls aligned in axial direction
- rotor and stator walls with axial displacement of 20% of the gap width.

The results indicate that the open jet in the radial gap between rotor and stator breaks up in both cases. Thereby, it hits the outer rim of the disks and creates vortices. The flow enters the rotor, due to the pressure difference between rotor inlet and outlet. The results of this two-dimensional case show velocity oscillations in both directions. Figure 6.20 exemplarily shows the velocity distribution of the two-dimensional, transient CFD with an axial displacement between stator and rotor. The axial alignment of rotor and stator certainly influences the frequency and the amplitude of the velocity oscillations in the main flow direction, but is not crucial for the fluctuations in general. However, the configuration with aligned walls of rotor and stator creates velocity fluctuations in the direction of flow propagation of

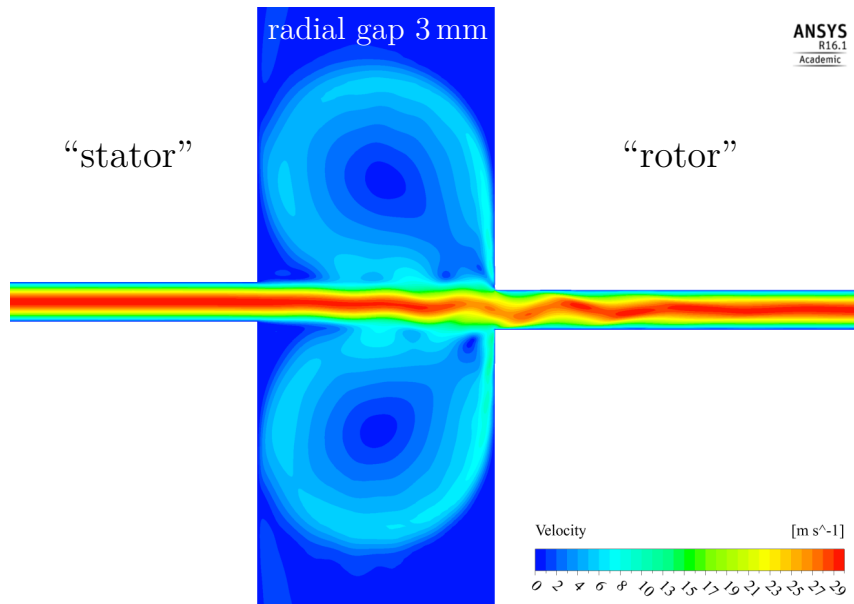


Figure 6.20: Transient, laminar flow through the non-aligned, 2D, simplified stator-rotor domain at the time step $\Delta t = 0.001$ s ($2s=0.5$ mm; $\bar{u}_1=20$ m/s; $\bar{p}_2=1$ bar)

approximately 12% of the bulk flow at frequencies of about 15 kHz. The non-aligned configuration approximately doubles the occurring frequencies of the aligned set-up, while the velocity amplitude is halved. More details about this transient flow investigation can be found in Appendix A.4. However, Figs. 6.21 and 6.22 show the radial velocity profiles with and without rotation for different mass flow rates. In both cases, the velocity profiles involve macroscopic fluctuations in the same order of magnitude. The tangential profiles without rotating walls show a similar behaviour and can additionally be found in Figs. A.16 to A.19 in Appendix A.3. Furthermore, the tangential and the radial profiles show increasing fluctuations with increasing flow rate, as well as increasing rotational speed of the rotor (see Appendix A.3).

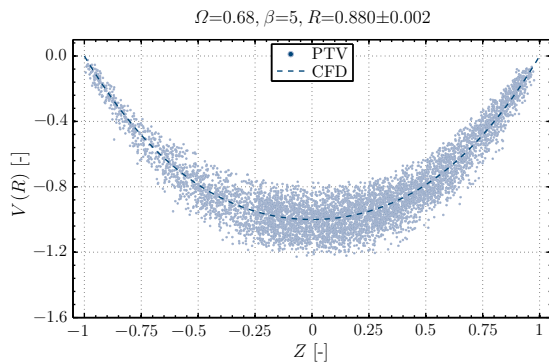


Figure 6.21: Radial velocity profile under rotation ($n = 1000$ min $^{-1}$)

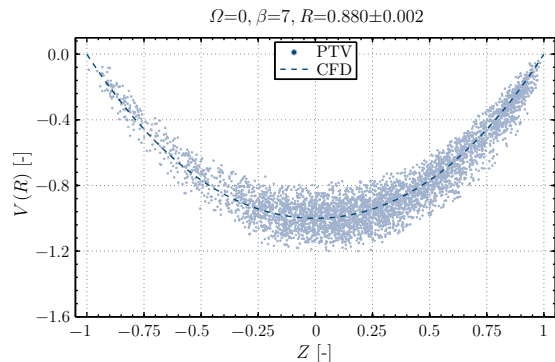


Figure 6.22: Radial velocity profile without rotation ($n = 0$ min $^{-1}$)

All fluctuations decay further downstream. This strongly indicates that the velocity fluctuations can probably not be attributed to the consequences of rotation, but rather to effects happening at the rotor inlet. Nevertheless, certain influences onto the fluctuating flow field are possible.

It is very likely that the geometry between stator and rotor leads to the velocity fluctuations inside the rotor. Therefore, it is proposed to optimise the geometry of the stator outlet and the rotor inlet in the future. Possible approaches towards implementation are: Lowering the radial gap between stator and rotor or chamfering the outer rim of the disks. In a next step, a transient rotor-stator CFD of the entire turbine would be desirable. However, the tangential velocity profiles are subjected to a minor additional uncertainty, due to variations in the circumferential disk velocity originated by the revolutionary speed regulator. The error propagation of the variations in circumferential disk velocity is further discussed in chapter 6.2.2.

6.3.4 Classification of flow regimes

The PTV measurement results show fluctuations of the velocity profiles in radial and tangential direction. Therefore, it can be difficult to judge, whether the flow regime is laminar or turbulent. Figures 6.23 and 6.24 show the standard deviation $\sigma_{\Delta z}$ of the particle displacement vectors $\vec{\Delta z}$ in axial direction along the inter-disk spacing for laminar and turbulent flow fields. The distribution of the standard deviation $\sigma_{\Delta z}$ across the gap is subjected to a random error. The mean value of the standard deviation $\sigma_{\Delta z}$ for all axial positions of the laminar case in Fig. 6.23 is about 1.7 to 2.0 μm . It is therefore relatively constant across the gap width. In case

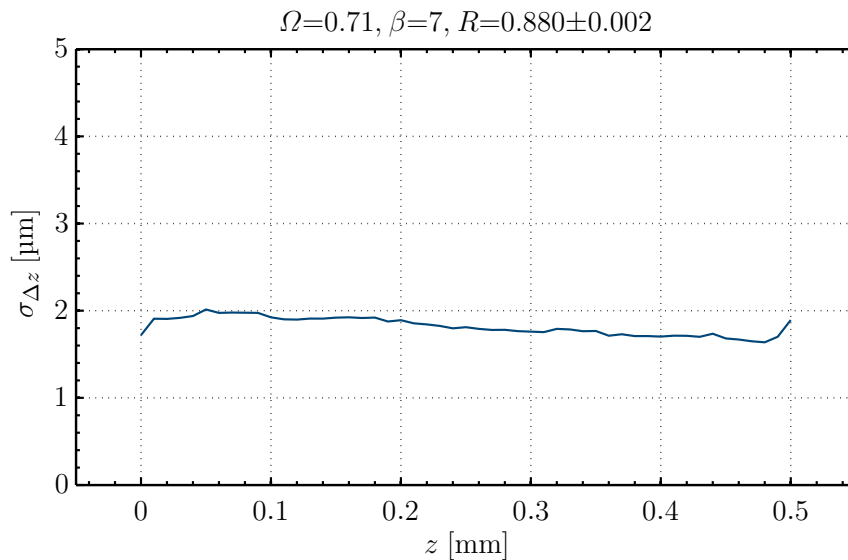


Figure 6.23: Standard deviation $\sigma_{\Delta z}$ of the particle displacement Δz in z -direction along the inter-disk spacing at the outer radius (laminar flow)

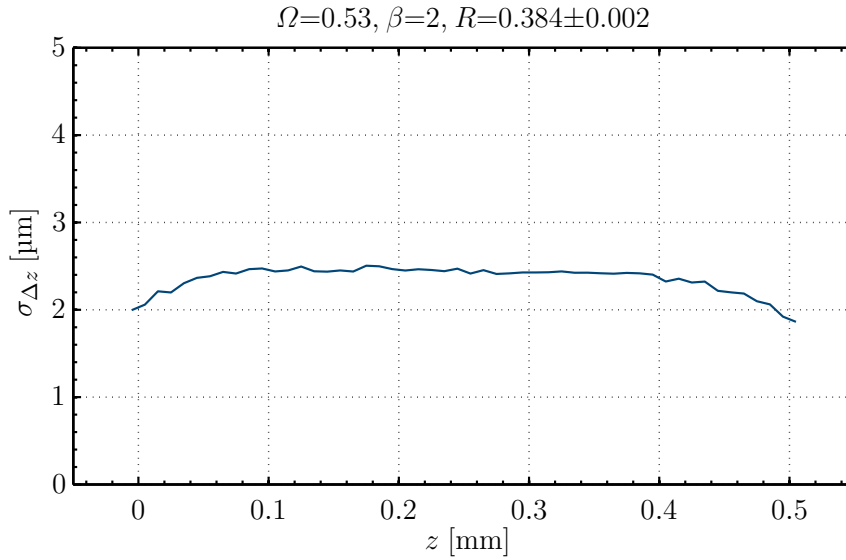


Figure 6.24: Standard deviation $\sigma_{\Delta z}$ of the particle displacement Δz in z -direction along the inter-disk spacing at the inner radius (turbulent flow)

of turbulent flow (Fig. 6.24) the standard deviation $\sigma_{\Delta z}$ of the particle displacement Δz in axial direction is higher in the middle section between the disks. Near the walls, the mentioned fluctuations $\sigma_{\Delta z}$ fall to the mean value of the laminar cases to approximately $2.0 \mu\text{m}$. The statistical description of the velocity oscillations normal to the wall show the typical and physical behaviour of turbulent flows. Observing the captured flow fields from Figs. A.15 to A.68 in Appendix A.3 leads to the assumption that this method seems to be a suitable indicator to classify the type of flow regime. The mean value of the standard deviation $\sigma_{\Delta z}$ of the axial particle displacement Δz is also about $2 \mu\text{m}$ in the laminar cases without rotational speed. It is therefore a strong indication that the fluctuations are probably not originated by vibrations due to rotation. The distribution of the standard deviation $\sigma_{\Delta z}$ of the particle image displacement Δz across the inter-disk spacing for the cases without rotation and different mass flow rates can be found in Figs. A.17 and A.20.

6.3.5 Transition to turbulence

Observing the transition to turbulence of highly resolved velocity profiles inside rotors of Tesla turbines is desired since the time of the investigations of [12, 25, 45, 97, 113].

However, during the PTV flow field measurements, it was possible to detect and record the laminar-turbulent transition of the flow inside the rotor. The flow regime is laminar for a small range of operating conditions. In other words, the transition happens at a relatively low mass flow rate for the inter-disk spacing of 0.5 mm and β -values slightly below ten. At a rotational speed of only 1000 min^{-1} , a mass flow rate of 4.5 g/s , a tangential Reynolds number of 310, a radial Reynolds number of 157, and

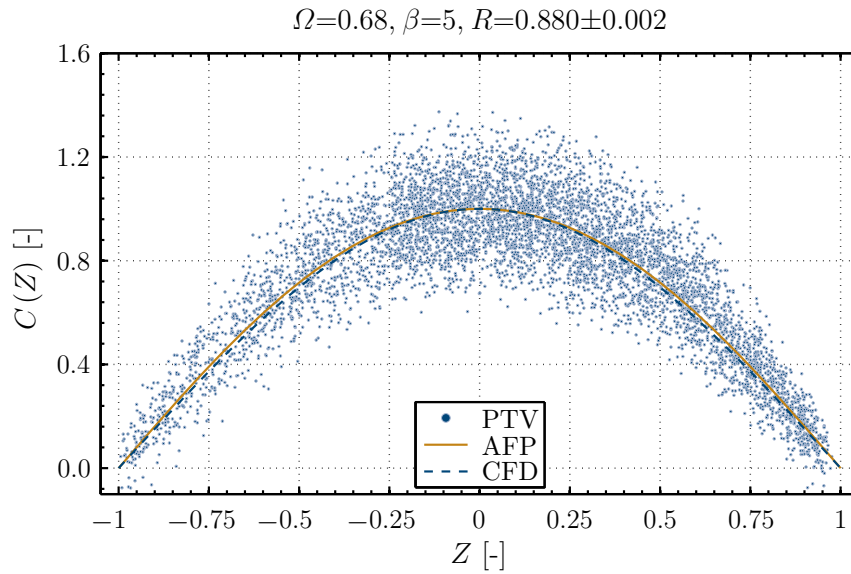


Figure 6.25: Tangential, laminar velocity profile at the outer radius

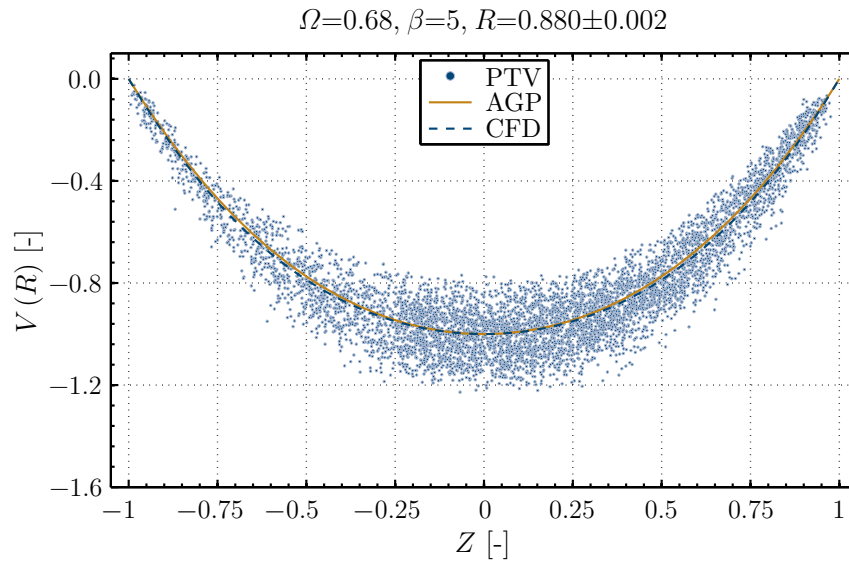


Figure 6.26: Radial, laminar velocity profile at the outer radius

a resulting Reynolds number of 347, a transitional flow regime can be observed at the radius $R = 0.384$. Figures 6.25 and 6.26 show the velocity distribution across the gap between the disks at the outer radial measurement position. The tangential and the radial velocity PTV profiles at the outer radial position are in good agreement with the corresponding profiles, which are obtained from theory (AFP, AGP) and laminar CFD. According to chapter 6.3.4 and the chart of the standard deviation $\sigma_{\Delta z}$ of the particle displacement Δz in z -direction along the gap (Fig. 6.27), the flow regime is still laminar. It is assumed that the laminar flow regime might be maintained for higher absolute velocities of the flow, if the inter-disk spacing is further reduced. As a consequence, higher values of β would be achievable. However, for turbine

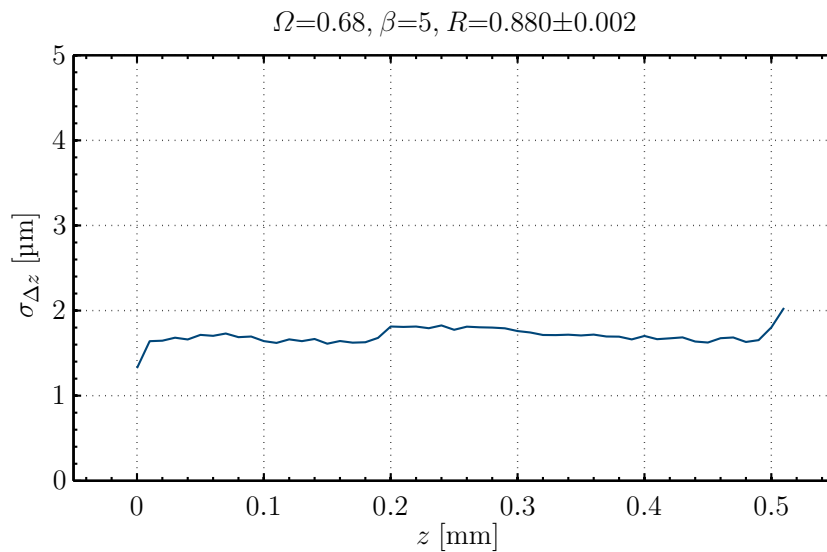


Figure 6.27: Standard deviation $\sigma_{\Delta z}$ of the particle displacement Δz in z -direction along the inter-disk spacing at the outer radius

applications more gaps would be needed, if the available mass flow was assumed to be constant.

Now, the measurements of the velocity profiles at the inner radial position are in focus. The tangential velocity profile in Fig. 6.28 is rather laminar like. Despite the variations between the three tangential relative velocity profiles, the velocity distribution can still be approximated with the analytical AFP- and the laminar CFD-profile. However, the flat shape of a turbulent velocity profile is more obvious

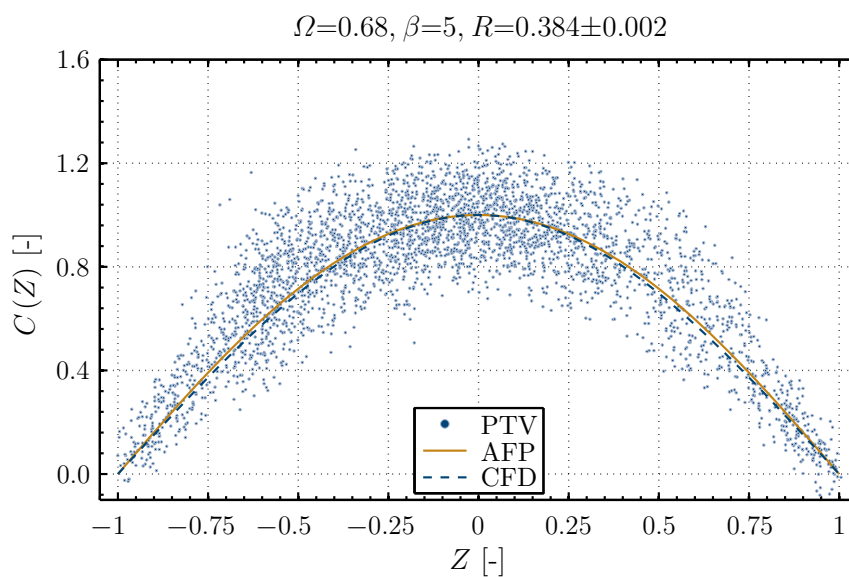


Figure 6.28: Transitional, tangential velocity profile at the inner radius

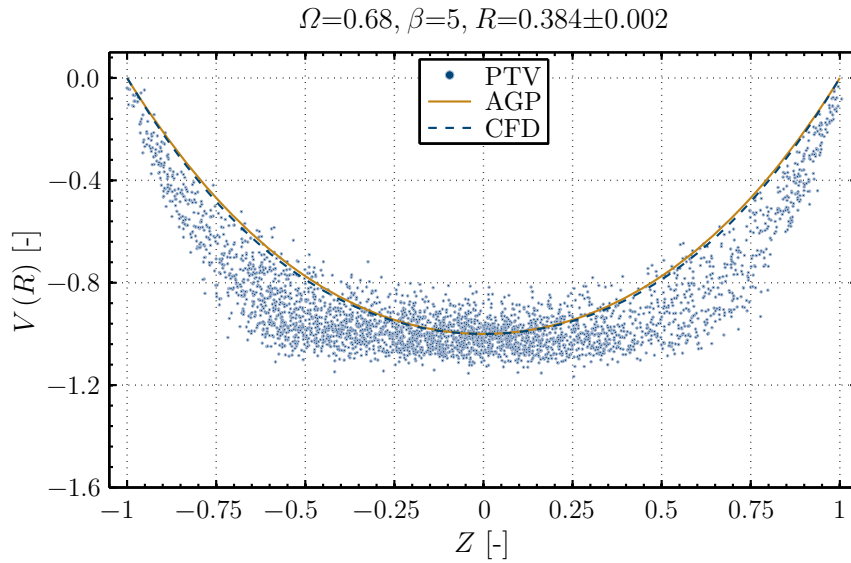


Figure 6.29: Transitional, radial velocity profile at the inner radius

in the radial direction, shown in Fig. 6.29. The standard deviation $\sigma_{\Delta z}$ of the particle displacement Δz along the z -direction (Fig. 6.30) shows increased values at the centre of the disks. It is therefore assumed that the flow regime is transitional, respectively turbulent, although, the AGP- and the laminar CFD-profile are in good agreement with each other, they differ from the radial velocity profile, which is obtained by means of PTV (Fig. 6.29). However, the turbulent flow behaviour first becomes apparent in the radial velocity direction at the inner radial measurement position.

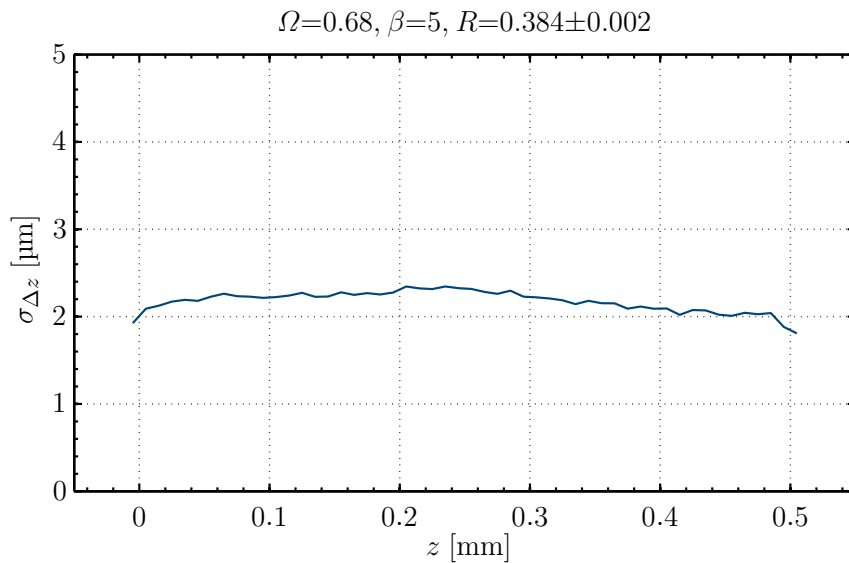


Figure 6.30: Standard deviation $\sigma_{\Delta z}$ of the particle displacement Δz in z -direction along the inter-disk spacing at the inner radius

6.3.6 Velocity profile shape

The shape of the laminar and turbulent velocity distribution along the narrow inter-disk spacing between two co-rotating disks was extensively discussed during the last century. Nowadays, the optical measurement technique is highly sophisticated and enables the possibility to provide insights into fields of application where measurements were extremely difficult to obtain in the past. The evaluation of the PTV measurements carried out in this thesis are useful for the validation of the theoretical and simulation results.

Laminar and turbulent flow fields, as well as velocity profiles indicating the laminar-turbulent transition, are recorded. A method for the classification of the flow regime is presented. Furthermore, flow oscillations are observed and discussed. All experimentally determined velocity profiles are exemplarily compared to the theoretical and the CFD results in the chapters 6.3.1 to 6.3.5. However, more sets of data are provided in the Appendix A.3 and are needed to be discussed.

The laminar PTV velocity profiles inside the stagnant rotor are in very good agreement with the results from the laminar CFD (see Figs. A.15, A.16). The AFP and the AGP profiles are not presented, due to the arising division by zero in Eq. 2.116. The transitional velocity profiles in Figs. A.18 and A.19 can still be approximated using laminar CFD. The radial profiles almost show identical shapes. Apparently, there is a clear divergence between the tangential profiles. This and the fact that Fig. A.20 shows slightly increased values of the standard deviation $\sigma_{\Delta z}$ of the particle image displacement Δz in the centre of the disks, indicate that the flow field is transitional. It is recommended to utilise transitional turbulence models for future investigations of such a flow field.

Although, laminar flow fields quickly become transitional and then fully turbulent in this moving Tesla rotor configuration, it is nevertheless useful to provide a validated method to model the velocity profiles analytically or using laminar CFD. Moreover, a further reduction of the gap width $2s$ and the dimensionless disk spacing ratio σ is still possible in future applications, which may maintain the laminar flow field at higher mass flow rates. The Figs. A.21, A.22, and the Figs. A.24, A.25 show a fully laminar velocity distribution across the gap in the tangential and the radial direction at the outer and the inner radial measurement volume. The operational conditions were $n = 1000 \text{ min}^{-1}$, $\Omega \approx 0.7$, $\dot{m} = 3.5 \text{ g/s}$, $\beta = 7$, and $V_1 \approx 0.3$. The laminar CFD, the AFP, and the AGP profiles are in very good agreement with the PTV profiles. Only the shape of the radial PTV profile in Fig. A.25 differs from the analytical and laminar CFD profiles, as already discussed in chapter 6.3.1.

Figures A.27 and A.28 provide information about the laminar velocity profiles at the outer radial measurement position for the operational conditions $n = 1000 \text{ min}^{-1}$, $\Omega \approx 0.7$, $\dot{m} = 4.5 \text{ g/s}$, $\beta = 5$, and $V_1 \approx 0.3$. All three profiles show smallest deviations from each other. The plots in the Figs. A.30 and A.31 indicate that the flow field becomes transitional further downstream. The shape of the three tangential velocity profiles in Fig. A.30 are still in good agreement. However, the radial PTV velocity

profile in Fig. A.31 rather shows a transitional velocity distribution along the inter-disk spacing. This and the estimation of the turbulent fluctuations normal to the rotating walls, which are described in chapter 6.3.4, indicate that the incompressible, laminar approximate solution can no longer be applied. Furthermore, transitional turbulence models should be used under these conditions in future investigations. However, the radial, theoretical AGP and laminar CFD profiles agree well.

A similar transition of laminar flow fields from the outer to the inner radial measurement volume can be observed in the Figs. A.33, A.34 and the Figs. A.36, A.37. The operational conditions were $n = 1000 \text{ min}^{-1}$, $\Omega \approx 0.4$, $\dot{m} = 6 \text{ g/s}$, $\beta = 4$, and $V_1 \approx 0.3$. The laminar CFD profiles are in very good agreement with PTV profiles at the outer radial measurement position. As the flow field becomes transitional at the inner radius, the laminar CFD clearly varies from the measurement results. Furthermore, the AFP and the AGP profile show visible deviations from the laminar CFD and the PTV profiles. Nevertheless, the deviations are smaller between the tangential profiles. One possible explanation is that the analytical approximate solution of the Navier-Stokes-Equations is only valid for $\Omega \rightarrow 1$. In this case the parameter $N = 3.6$ contributes to the deviations, which was already predicted in Fig. 2.36. Instead of solving Eq. 2.121 and using the five boundary conditions, which are defined in Eqs. 2.119 and 2.120, the AFP and the AGP profile may also be obtained by solving the Navier-Stokes-Equations numerically, if needed. This should provide the correct AFP and AGP profiles. However, this is not shown here. Furthermore, the inlet angle V_1 remains unknown, as it is not measured using the PTV method. It cannot be excluded that the inlet angle used in the experiments is effectively different from the one, which is applied in the laminar CFD set-up.

The Figs. A.39 to A.43 show the theoretical, the numerical, and the PTV velocity profiles under the operational conditions $n = 1000 \text{ min}^{-1}$, $\Omega \approx 0.3$, $\dot{m} = 8 \text{ g/s}$, $\beta = 3$, and $V_1 \approx 0.3$. The velocity profiles at the outer radial measurement volume already seem to have a transitional shape. Downstream, at the inner radial position (Figs. A.42, A.43), they are apparently fully turbulent. Exactly, like mentioned before, the AFP and the AGP profiles deviate visibly from the velocity profiles of the measurement data. The deviations are higher compared to the flow fields in the Figs. A.33 to A.37. This is in good agreement with the fact that the value of the dimensionless angular velocity Ω is small. In addition to that the value of the parameter $N = 4.6$ is even higher than in the case before.

The turbulent velocity profiles are plotted in the Figs. A.45 to A.67. The measurements are carried out for different rotational speeds between $n = 1000$ and 5000 min^{-1} and for different mass flow rates between $\dot{m} = 8$ and 16 g/s . More information about the dimensionless machine parameters and other physical quantities of the velocity profiles can be found in the Tabs. A.4 to A.9 of Appendix A.3. The analytical velocity profiles are only valid for incompressible, laminar flows and are therefore not shown in the plots of the fully turbulent flow fields. However, the turbulent CFD results using the standard SST turbulence model agree reasonably well with the shapes of the PTV velocity profiles. Systematic deviations between

CFD and PTV results are found in the radial velocity profiles at the inner radial measurement volume (see Figs. A.49, A.55, A.61, and A.67 for details). As this also systematically happens at this location for laminar flows, it is very likely that this is caused by a retroactive effect of the outlet geometry of the Tesla rotor onto the flow upstream. However, the highest deviations between the shapes of the velocity profiles are found at high rotational speeds with highest mass flow rates at the outer radial measurement volume. The plots are shown in Figs. A.51, A.57, and A.63. It is obvious that the gap is not entirely illuminated in all three measurements, which is probably caused by rotor shift and rotor deformation. Parts of the measurement volume at the flow boundaries are therefore only illuminated indirectly. Additionally, it seems that the gap slightly closes under rotation near $Z = 1$ in all three figures. This leads to a marginal increase in velocity, due to the continuity equation and therefore differs from the CFD set-up. Altogether, the comparisons between the simulation and the measurement results demonstrate that the SST turbulence model is not able to describe all flow features of an accelerated, squeezed flow under rotation in small gaps.

6.3.7 Velocity magnitude

So far only the shapes of the velocity profiles are analysed. However, the velocity magnitudes are also available from the PTV measurements, from the CFD, and at least for the incompressible, laminar cases from the theoretical investigations. Depending on the operational points, the circumferential speed of the co-rotating disks at the outer radius $r_1 = 125\text{ mm}$ varies between zero and 65 m/s . Figures 6.31 to 6.34 show the tangential absolute and the relative velocity profiles for different operating conditions.

For $n = 1000\text{ min}^{-1}$, $\dot{m} = 3.5\text{ g/s}$, and the radial position at $r = (110 \pm 0.2)\text{ mm}$, the tangential absolute velocity yields a value of $\bar{u}(r) = 14.4\text{ m/s}$ in average and $u_{\text{max}}(r) = 17.4\text{ m/s}$ in maximum. Relative to the disks, these values reduce to $\bar{c}(r) = 2.9\text{ m/s}$ and $c_{\text{max}}(r) = 5.9\text{ m/s}$. The mean value of the radial velocity component is $\bar{v}(r) = 8.8\text{ m/s}$ with a velocity maximum of $v(r) = 14.4\text{ m/s}$ in the centre of the disks. The Mach number of $Ma = 0.05$, which is built with the absolute velocity obtained from PTV, indicates that the flow can be treated as incompressible. Despite smallest deviations, the magnitudes of the AFP, the AGP, and both laminar, incompressible CFD velocity profiles are in good agreement. The velocity fluctuations are of the same order of magnitude in the tangential and the radial direction.

At a rotational speed of $n = 5000\text{ min}^{-1}$, a mass flow rate of $\dot{m} = 16\text{ g/s}$, and a radial position at $r = (110 \pm 0.2)\text{ mm}$, the tangential absolute velocity shows an average value of $\bar{u}(r) = 68.2\text{ m/s}$ with a peak velocity of $u_{\text{max}}(r) = 78.2\text{ m/s}$. The tangential velocity, which is relative to the disks yields $\bar{c}(r) = 10.6\text{ m/s}$ and $c_{\text{max}}(r) = 20.6\text{ m/s}$ in maximum. The mean value of the radial velocity component is $\bar{v}(r) = 26.7\text{ m/s}$. The maximum velocity of $v(r) = 37.5\text{ m/s}$ in the centre of the disks. The Mach number of $Ma = 0.2$, built with the absolute PTV velocity, indicates that the compressible

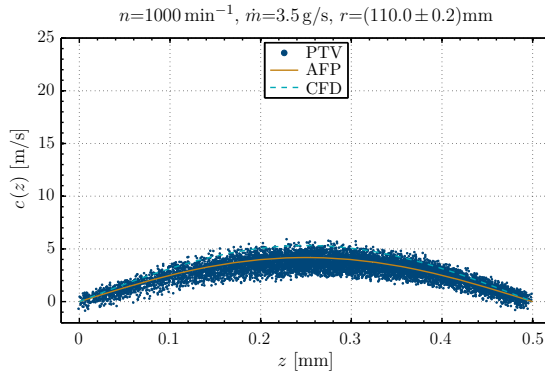


Figure 6.31: Tangential, relative velocity profile at $n = 1000 \text{ min}^{-1}$

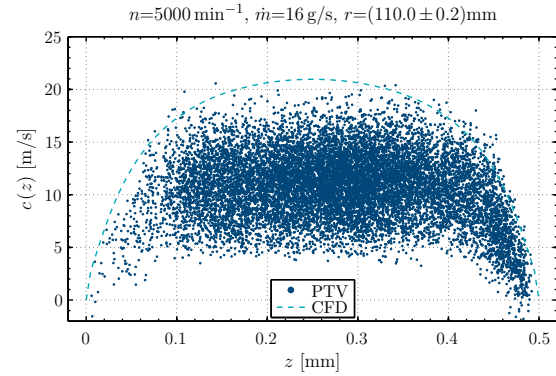


Figure 6.32: Tangential, relative velocity profile at $n = 5000 \text{ min}^{-1}$

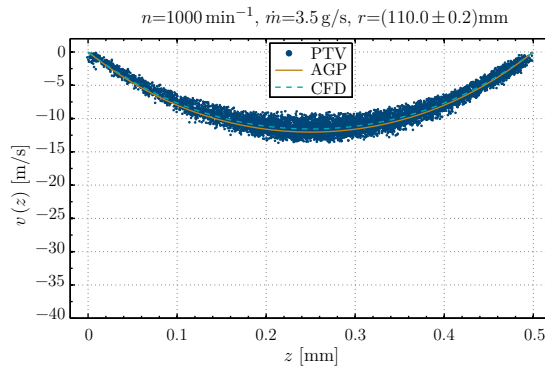


Figure 6.33: Radial, velocity profile at $n = 1000 \text{ min}^{-1}$

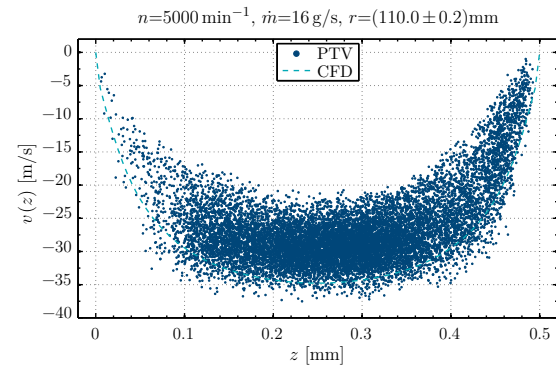


Figure 6.34: Radial, velocity profile at $n = 5000 \text{ min}^{-1}$

effects are still small. However, the comparison of the velocity magnitudes between PTV and turbulent CFD indicates that the CFD is somewhat overpredicting the velocities. With reference to chapter 6.3.8, there is considerable evidence that there are small leakages in the long path between mass flow regulator and measurement volume, which slightly reduces the mass flow rate inside the experimental rotor. One possible explanation might be that the values of the flow rate used in the numerical simulations are taken from the recordings of the precise mass flow gauge and effectively leads to a higher mass flow rate inside the CFD turbine. Furthermore, it is plausible that the effective mass flow differs more from the values of the flow gauge for higher absolute values of the flow rate, because then leakage has a stronger effect. In addition to that, it is very likely that the inlet angle V_1 is slightly different within the experiments, than previously assumed. Nevertheless, all couples of numerically and experimentally obtained velocity profiles are of the same order of magnitude. The shape of the velocity profiles can still be assessed quite accurately.

6.3.8 Conservation of mass in Tesla turbines

Usually, the mass flow \dot{m} through Tesla turbines is computed according to Eq. 2.47, when applying the theoretical flow models, as described in chapter 2. The radial velocity profile $v_1(z)$ at the rotor inlet r_1 and hence the radial bulk velocity v_1 are normal to the lateral surface A_1 . Together with the density of the fluid, they determine the mass flow rate of such devices. In general, the mass flow rate \dot{m} of a Tesla rotor can be calculated at any radius r of the disks using the radial velocity profile $v(r)$, the corresponding lateral control surface A , and the fluid density ρ . There is no doubt that conservation laws are valid. However, the measurement data enable the possibility for an experimental proof of the continuity equation for the laminar cases. Furthermore, this evaluation provides evidence for the plausibility of the measurement results. Figure 6.35 shows the radial, laminar velocity profiles of the operational point $n = 1000 \text{ min}^{-1}$ and $\dot{m} = 3.5 \text{ g/s}$ at two different radial po-

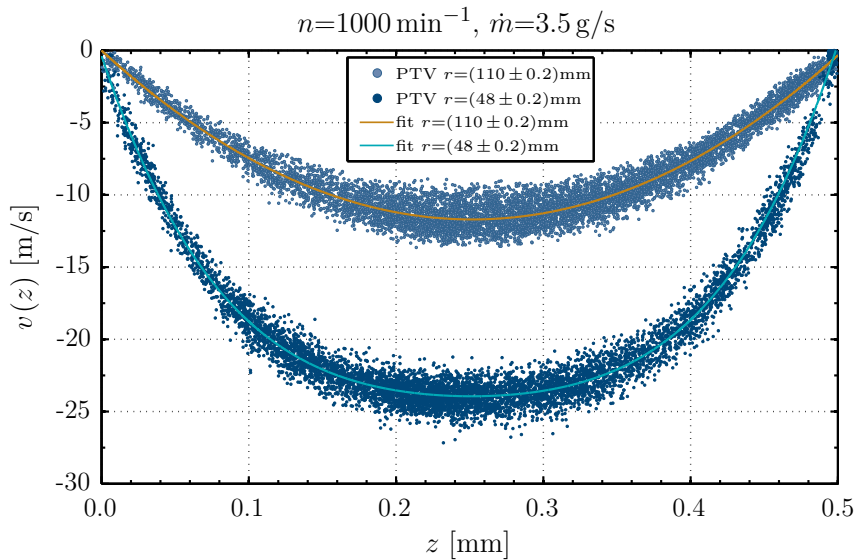


Figure 6.35: Laminar, radial velocity profiles with second and fourth-order polynomial curve fits at different radial positions for one operational point

sitions. Therefore, the PTV profile at the radius $r=(110 \pm 0.2)\text{mm}$ is fitted with a second-order polynomial and a coefficient of determination of 0.94. The radial profile at the position $r=(48 \pm 0.2)\text{mm}$ deviates clearly from the parabolic velocity distribution and is therefore fitted using a fourth-order polynomial and a coefficient of determination of 0.98. Both radial velocity profiles are plotted in a normalised view in the Figs. A.22 and A.25 of Appendix A.3. It is particularly noticeable that the shape of the radial PTV profile in Fig. A.25 deviates visibly from the AGP and laminar CFD profile, while the others fall together. However, the shapes of PTV, AGP, and laminar CFD profile at the outer radius $r=(110 \pm 0.2)\text{mm}$ almost match completely (see Fig. A.22). The mass flow is computed at both radial positions with

the corresponding lateral surfaces using

$$\dot{m} = \rho \cdot \underbrace{\frac{1}{2s} \cdot \int_0^{2s} v(z) dz}_{\bar{v}(r)} \cdot \underbrace{2\pi r(2s)}_A. \quad (6.12)$$

The fluid density is assumed to be constant for the incompressible flow conditions with $Ma_r < 0.75$. The function of the curve fits are numerically integrated using the trapezoidal rule with an appropriate axial resolution. The mass flow is 3.21 g/s at the outer radial position and 3.19 g/s at the inner radius. Altogether a deviation of 0.7% arises, which is deemed to be acceptable. However, the mass flow also differs slightly from the recordings of the mass flow regulator, which shows a value of (3.43 ± 0.08) g/s (see Tabs. A.5, A.6 in Appendix A.3). It is very likely that the variations between the results of the PTV and the mass flow regulator measurements are caused by leakages between the measuring points. On closer inspection of the system layout in Fig. 4.34, it becomes apparent that the mass flow is divided and merged several times between the widely separated measurement points. Each screw connection involves small leakages, which are summed up to an average difference of 0.23 g/s in mass flow rate. The differences in the results between the measurement methods are small and indicate that the PTV measurements worked properly and are plausible.

7 Conclusions and future research

The scope of this work is to study and determine the velocity distribution between the disks of a Tesla rotor by theoretical, numerical, and experimental methods. At first, an extensive literature review of research about the development and the scientific investigations of Tesla turbines during the last century is performed and summarised. A closed-form analytical solution for the radial and tangential momentum equations of the simplified, incompressible, laminar model, derived by Beans [45, 47], is provided. Furthermore, typing errors in the governing equations of Beans [47] are corrected. Then, the model is extensively evaluated and leads to the description of the design criteria of high performance and highly efficient Tesla turbine rotors. Moreover, the governing equations are extended and adapted for compressible flow conditions.

The model is shown to agree well with the results of the incompressible model and the laminar CFD for small Mach numbers. The encountered influences of the compressibility are plausible. The laminar CFD results indicate that the assumption of parabolic velocity profiles between the co-rotating disks are valid in radial direction. Nevertheless, they show deviations in the tangential direction, which are crucial for turbine performance. Therefore, an approximate solution of the velocity profile shapes for laminar, incompressible flows is developed. The velocity profiles agree well with those obtained by laminar CFD.

In addition to that, a flexible test rig for the investigation of the flow field inside a rotor of a Tesla turbine is designed, simulated by means of FEM and CFD, and finally built. The complex measurement and control software is created in NI LabVIEW and features advanced FPGA and real-time programming. PTV measurements of the radial and tangential velocity distribution across the inter-disk spacing are in focus in this thesis. A particular highlight is the application of a stereo-PIV set-up in combination with PTV measurement and evaluation techniques in this unusual field of turbomachinery. However, several restrictions arise.

As regular calibration targets cannot be placed inside the measurement volume of the rotor, due to the limited spatial access, new non-intrusive calibration methods using reflections on the flow boundaries of a traversable continuous wave laser are developed. The control software running on the PIV measurement computer is therefore linked to the traverse control and the test rig measurement and control software in a sophisticated manner. The calibration routine works fully automatically. Post-processing of calibration and measurement data is entirely carried out in MATLAB.

Finally, the theoretical and numerical velocity profiles are compared to those obtained from the PTV measurements. The novel scientific achievement is that the shape of the velocity profiles at different operating conditions is determined for the first time. Furthermore, the transition from laminar to turbulent flow behaviour is

observed. In addition to that, the theoretical prediction of possible oscillations in Tesla rotors, developed by Chesnokov [151] is proven experimentally. The reasons for those phenomena are discussed in chapter 6.3.3. Finally, error propagation is examined more thoroughly.

Future studies could focus firstly on CFD simulations and the comparison to existing measurement data. As the transition to turbulence happens relatively quickly inside the rotor, investigations using different turbulence models should be performed. The standard SST model certainly does not always predict the correct velocity profiles. In addition to that, the model constants of selected turbulence models should be calibrated with experimental data. Furthermore, LES is quite a popular simulation technique for studying turbulent flows and should therefore be applied on the rotor of a Tesla turbine. This method allows to explicitly solve for large eddies and implicitly account for small eddies using a sub-grid-scale model.

Another important field of research is the stator-rotor interface in CFD simulations. The different stator-rotor interface models should systematically be examined in a first step. Complex transient CFD simulations should definitively be performed. Nozzles and guide vanes with different angles of attack should be considered.

The origin of the flow oscillations discovered in this thesis, should be investigated more thoroughly. It is very likely that the size of the radial gap between rotor and stator is the key issue to prevent or at least alleviate the radial and tangential flow fluctuations. However, a transient CFD of the entire turbine focusing on the inlet region of the rotor is still lacking. This aspect should be clarified before the stator is exchanged for an experimental verification in the future. These fluctuations are an important topic, because turbine performance is certainly affected. Especially the inlet angle of the rotor is a parameter with strong influence on performance and efficiency. The analysis of the flow oscillations on the inlet angle would certainly be a valuable work.

Due to the relatively early laminar-turbulent transition, it would be very interesting, if the laminar flow could be kept stable for higher flow velocities and rotational speeds by a further reduction of the inter-disk spacing. This would increase β and the length of the streamlines through the rotor. Therefore, it is desirable to carry on with extended PTV measurements. However, a smaller gap width could trigger an aggravation of the measurement volume illumination at the outer radius of the disks. Performing those measurements is – without doubt – a challenging task.

Nevertheless, further flow experiments inside the Tesla rotor should be performed at different angles of attack. One possible solution to adjust this angle, might be the use of movable blocks. The movable block principle, described by Leuckel [152] is often applied in a swirl generator for premixing fuel and air. Moreover, it is important to mention that flow experiments with increased rotational speeds and mass flows are just as important as studies with different inlet angles.

Furthermore, studies of multi-gap rotors for performance investigations are desirable.

A Appendix

A.1 Theoretical investigations

configuration	r_1	r_2	$2s$	\dot{m}	p_1	T_1	V_1
units	[mm]	[mm]	[mm]	[g/s]	[bar]	[K]	[–]
A	125	30	0.5	15.5	1.3	293.15	0.3
B	125	30	0.5	5.5	1.1	293.15	0.3

Table A.1: Rotor configurations for compressible, laminar flow validations using CFD (see chapter 2.8.3 for details)

A.2 Test rig

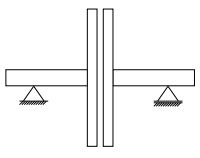
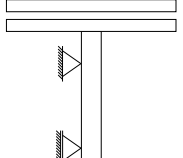
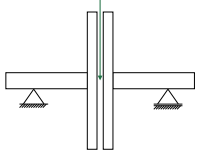
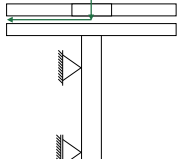
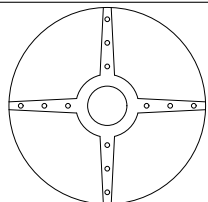
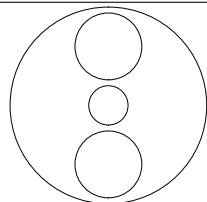
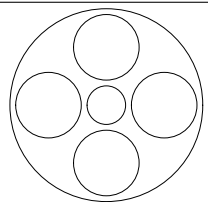
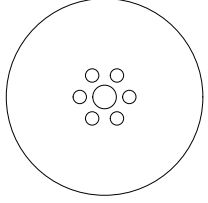
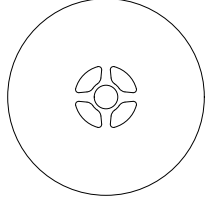
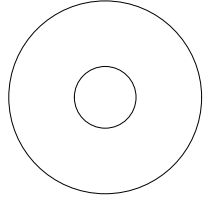
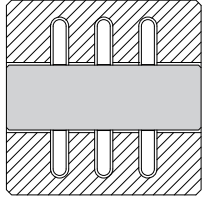
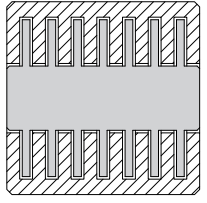
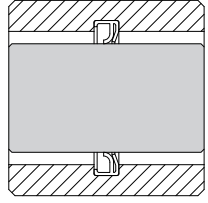
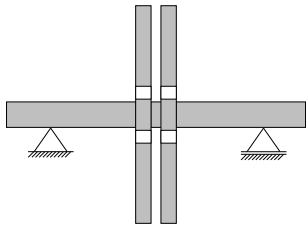
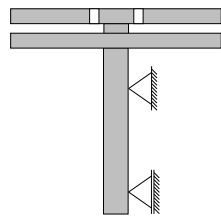
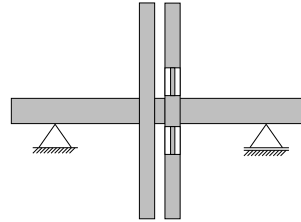
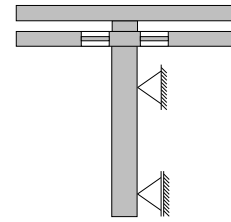
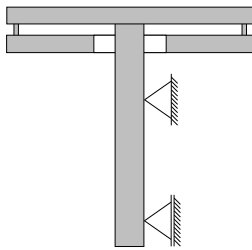
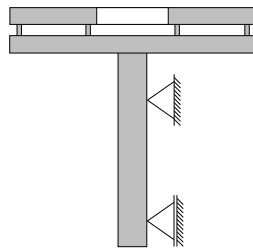
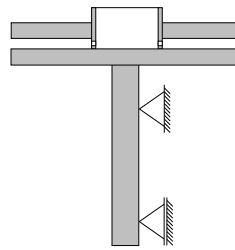
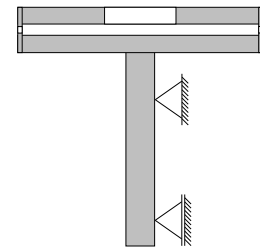
designation	A	B	C	D
bearing concept			-	-
illumination			-	-
optical access				-
disk outlet				-
disk spacing	shaft	spacers	hollow shaft	shaft, spacers
shaft sealing	radial	axial	-	-
sealing design				-

Table A.2: Morphological box for subtasks and partial solutions

Figure A.1:
Concept 1Figure A.2:
Concept 2Figure A.3:
Concept 3Figure A.4:
Concept 4Figure A.5:
Concept 5Figure A.6:
Concept 6Figure A.7:
Concept 7Figure A.8:
Concept 8

concepts	1		2		3		4		5		6		7		8	
bearing	A	5	B	10	A	5	B	10	B	10	B	10	B	10	B	10
illumination	A	5	A	5	A	5	A	5	B	10	B	10	B	10	B	10
optical access	B	10	B	10	B	10										
disk outlet	A	3	A	3	B	5	B	5	C	10	C	10	C	10	C	10
disk spacing	B	10	B	10	B	10	B	10	D	5	A	3	C	8	A	3
sealing	A	3	A	3	A	3	A	3	B	10	B	10	B	10	B	10
sealing design	C	10	C	10	C	10										
rating	46		51		48		53		60		63		68		63	
rank	7		5		6		4		3		2		1		2	

Table A.3: Concept assessment of possible mechanical designs

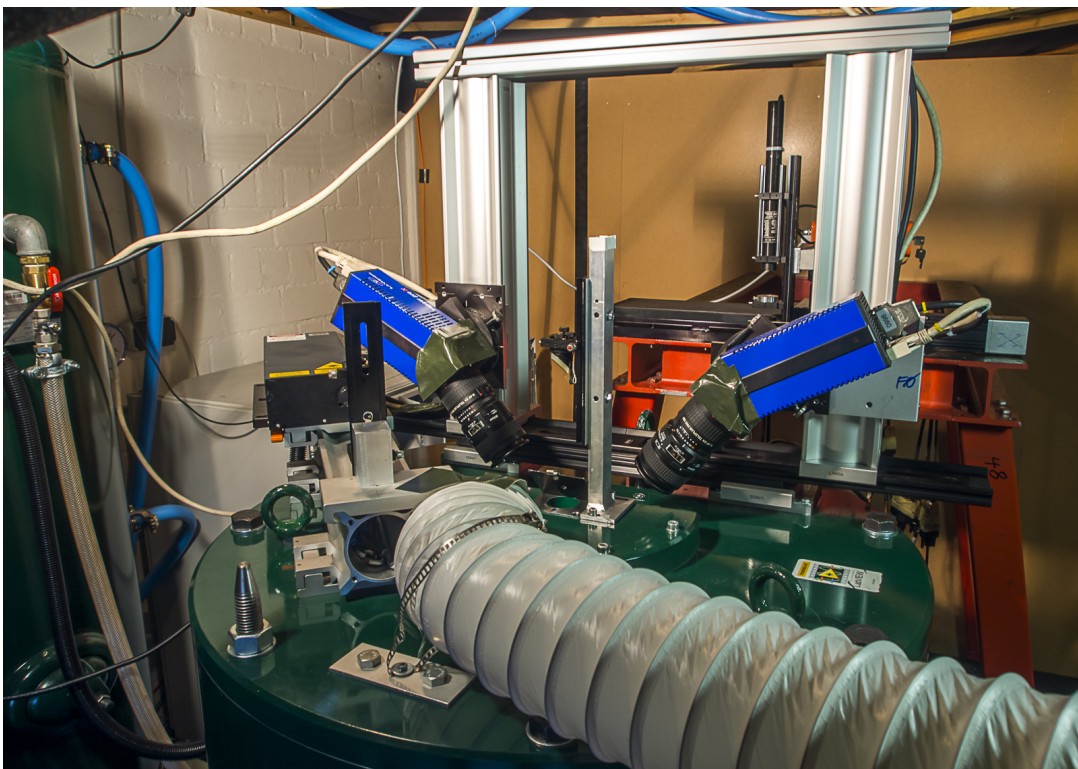


Figure A.9: Image of the test rig

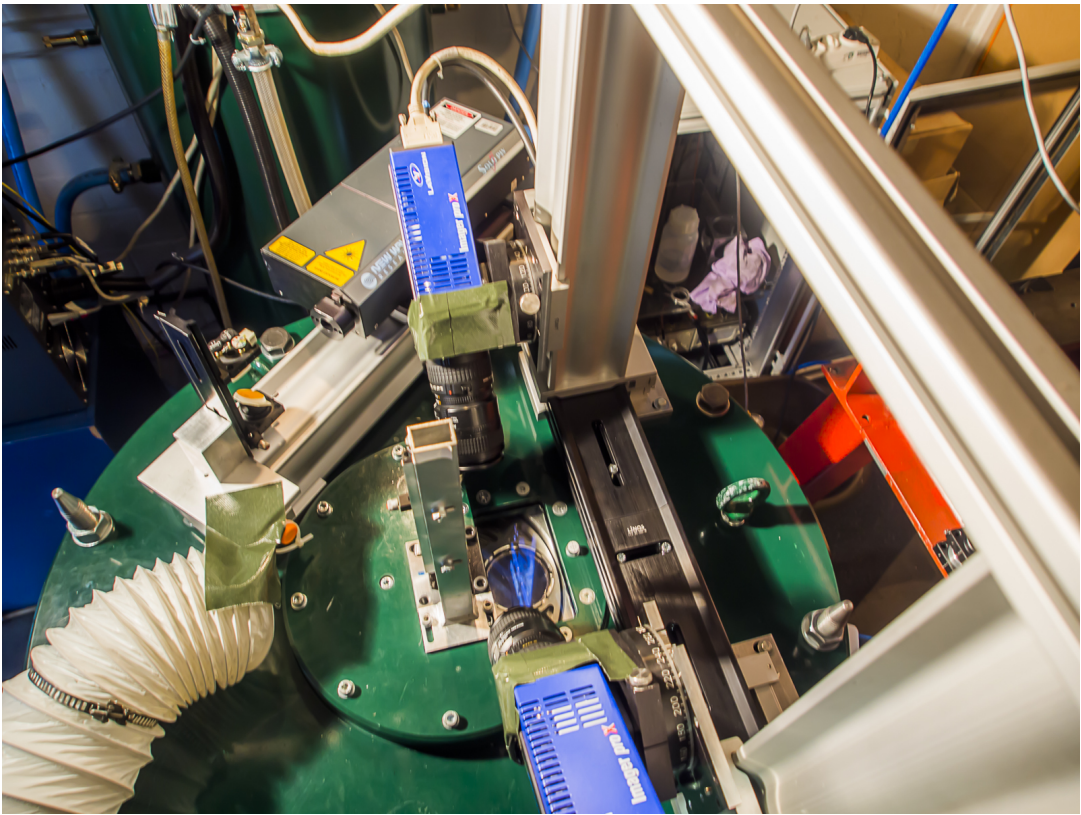


Figure A.10: Top view of the test rig

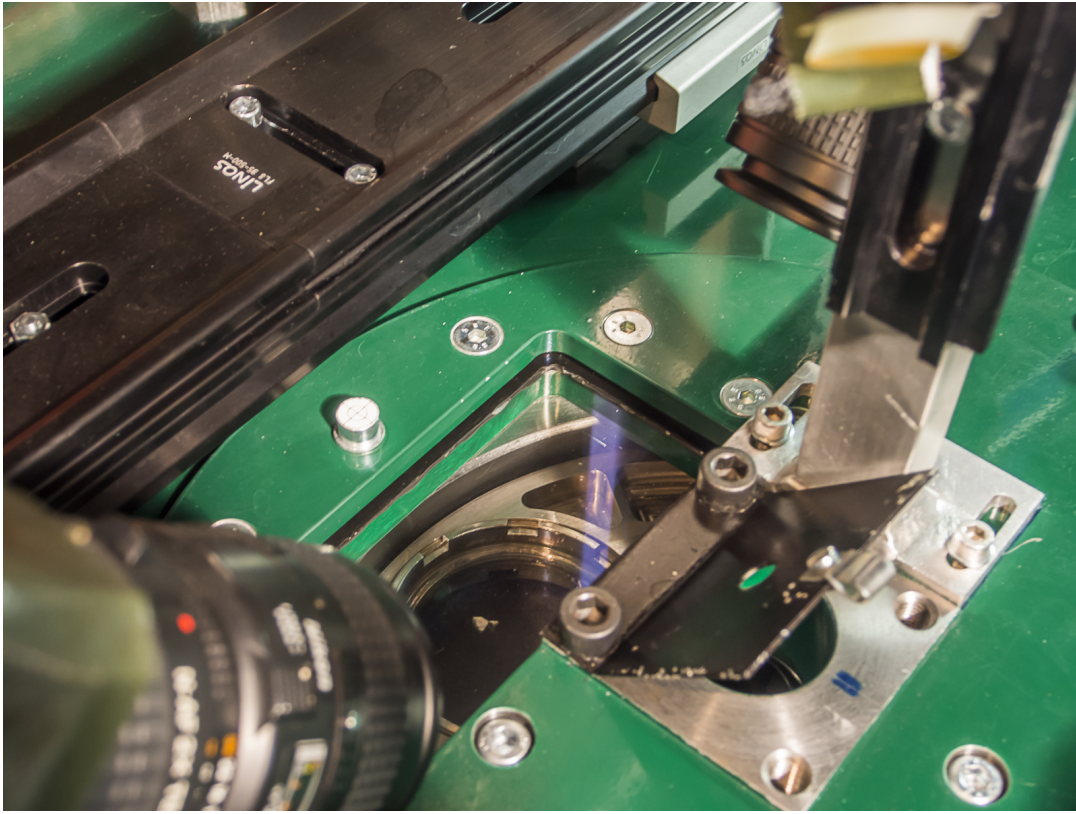


Figure A.11: Optical access to the measurement volume

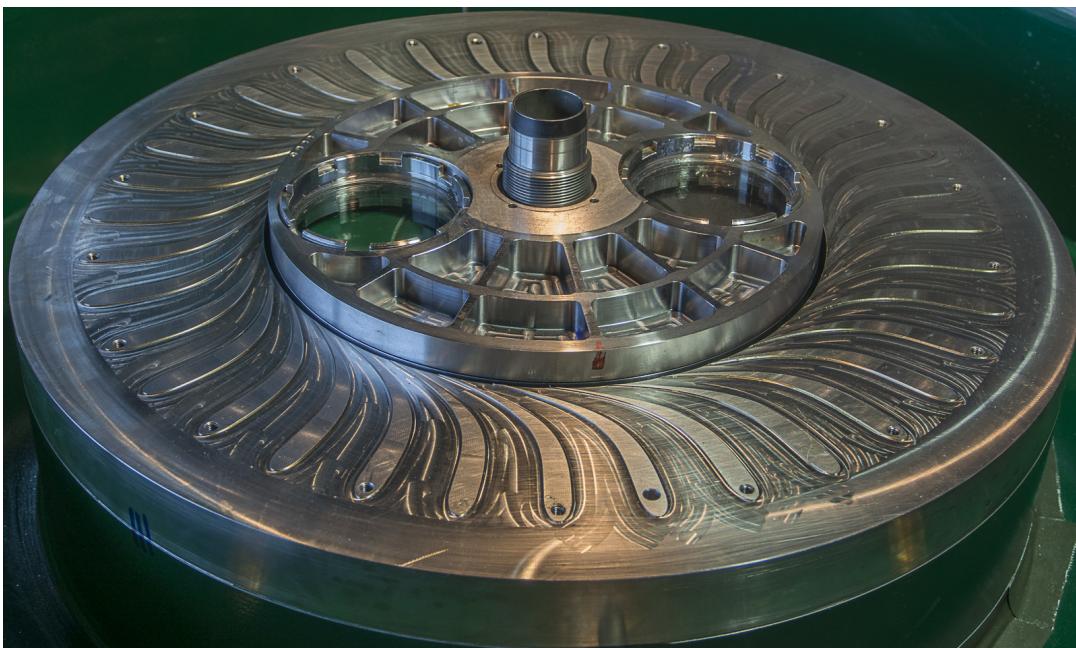


Figure A.12: Rotor and guide vanes

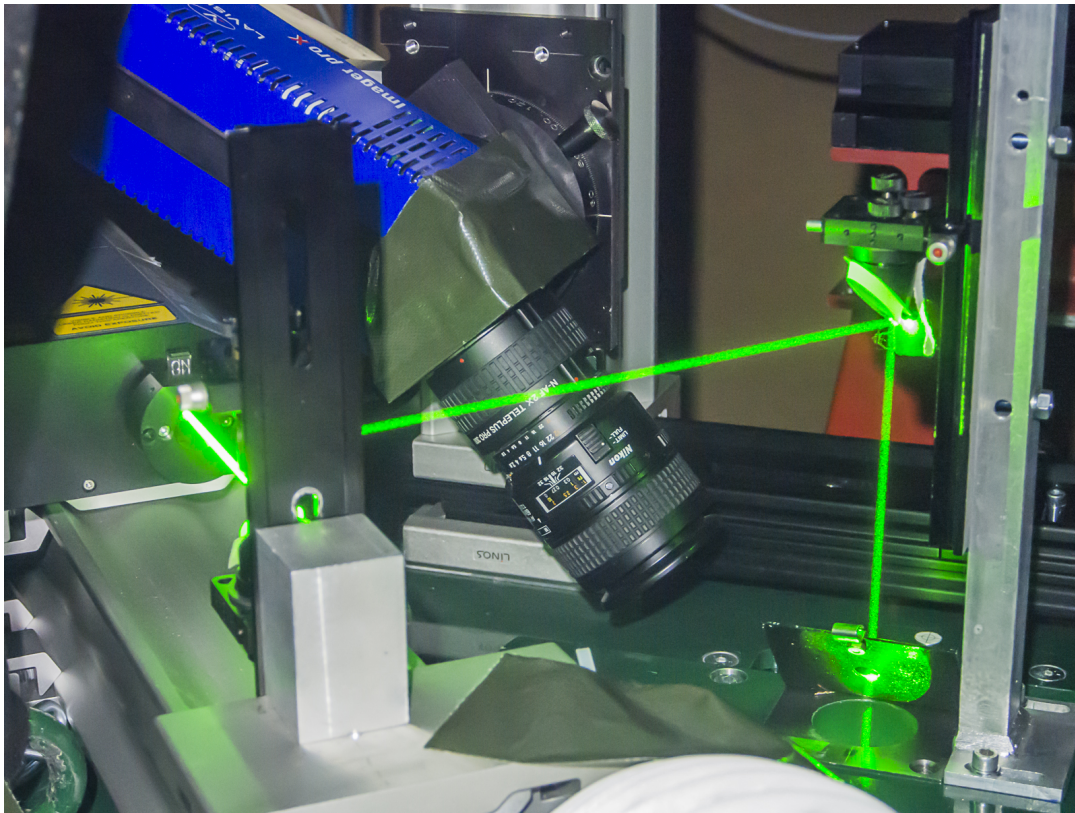


Figure A.13: PIV laser in operation

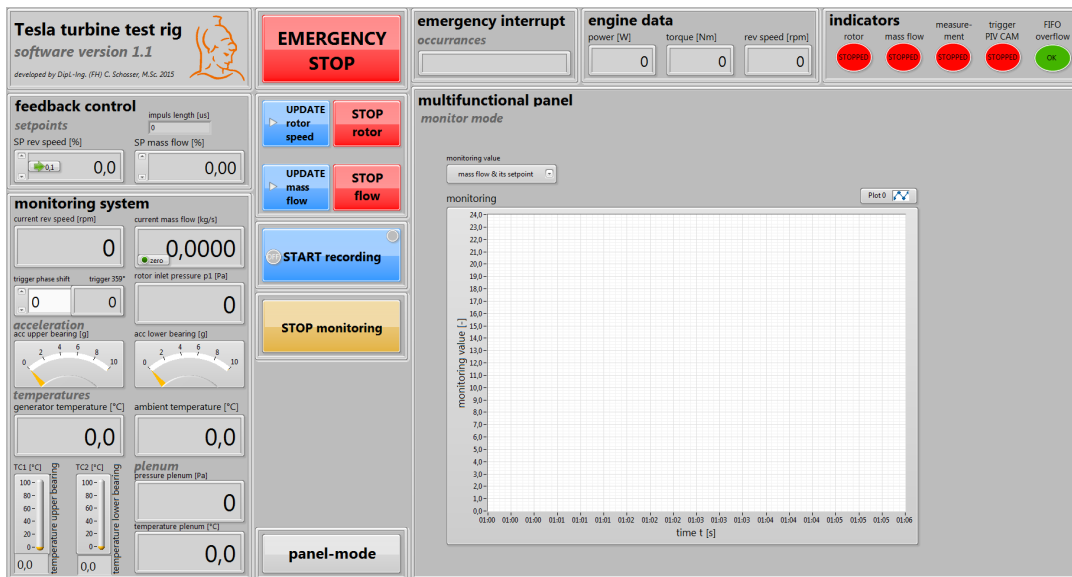


Figure A.14: LabVIEW front panel

A.3 PTV measurement data

The entire set of measurement data obtained from particle imaging is shown in this chapter. The settings of the PTV measurements are listed in Tab. A.4. Further information about the measuring points is provided in the Tabs. A.5, A.6, A.7, A.8 and A.9.

setpoints		time delay between illumination pulses	
rev speed	mass flow	at outer radius	at inner radius
[1/min]	[g/s]	[μ s]	[μ s]
0	3.5	4.1	-
0	8.0	2.2	-
1000	3.5	5.8	4.0
1000	4.5	4.7	3.3
1000	6.0	4.3	2.6
1000	8.0	3.7	2.2
1000	16.0	2.1	1.5
3000	8.0	2.4	1.75
3000	16.0	1.75	1.25
5000	16.0	1.6	1.1

Table A.4: Additional information about PTV measurements part 1

n	σ_n	\dot{m}	$\sigma_{\dot{m}}$	p_a	σ_{p_a}	T_a	σ_{T_a}
[1/min]	[1/min]	[g/s]	[g/s]	[Pa]	[Pa]	[$^{\circ}$ C]	[$^{\circ}$ C]
0.0	0.0	3.43	0.05	95100	48	21.60	0.05
0.0	0.0	8.10	0.07	95122	53	21.64	0.05
1000.0	0.8	3.42	0.08	95243	216	21.84	0.05
1000.1	0.6	4.61	0.03	95221	113	21.88	0.04
1000.1	0.7	6.00	0.05	95225	198	21.90	0.01
999.9	0.6	8.09	0.04	95202	201	21.96	0.05
1000.3	0.5	16.04	0.06	95178	199	21.99	0.02
2999.6	0.6	8.10	0.04	95151	190	22.03	0.05
3000.4	0.9	16.04	0.06	95152	186	22.01	0.03
4999.9	0.8	16.06	0.09	95144	123	21.81	0.08

Table A.5: Additional information about PTV measurements part 2

n	σ_n	\dot{m}	$\sigma_{\dot{m}}$	p_{pl}	$\sigma_{p_{pl}}$	T_{pl}	$\sigma_{T_{pl}}$	p_1	σ_{p_1}
[1/min]	[1/min]	[g/s]	[g/s]	[Pa]	[Pa]	[°C]	[°C]	[Pa]	[Pa]
0.0	0.0	3.43	0.05	98 129	49	22.84	0.05	97 542	52
0.0	0.0	8.10	0.07	105 639	411	22.88	0.05	101 309	225
1000.0	0.8	3.42	0.08	98 759	264	22.91	0.02	98 116	259
1000.1	0.6	4.61	0.03	100 496	265	22.90	0.03	99 063	263
1000.1	0.7	6.00	0.05	102 955	288	22.91	0.04	100 447	276
999.9	0.6	8.09	0.04	107 437	268	22.96	0.05	103 029	266
1000.3	0.5	16.04	0.06	130 290	583	23.02	0.10	117 247	433
2999.6	0.6	8.10	0.04	111 143	279	22.78	0.10	106 921	247
3000.4	0.9	16.04	0.06	136 653	222	22.90	0.02	124 319	219
4999.9	0.8	16.06	0.09	143 110	858	23.15	0.16	131 732	625

Table A.6: Additional information about PTV measurements part 3

Fig.	n	\dot{m}	r_{\min}	r_{\max}	\tilde{c}	\tilde{v}
-	[1/min]	[g/s]	[mm]	[mm]	[m/s]	[m/s]
A.15	0	3.5	109.8	110.2	7.4	0.0
A.16	0	3.5	109.8	110.2	0.0	12.1
A.18	0	8.0	109.8	110.2	20.2	0.0
A.19	0	8.0	109.8	110.2	0.0	22.9
A.21	1000	3.5	109.8	110.2	3.9	0.0
A.22	1000	3.5	109.8	110.2	0.0	11.4
A.24	1000	3.5	47.8	48.2	10.7	0.0
A.25	1000	3.5	47.8	48.2	0.0	23.9
A.27	1000	4.5	109.8	110.2	7.9	0.0
A.28	1000	4.5	109.8	110.2	0.0	14.3
A.30	1000	4.5	47.8	48.2	13.4	0
A.31	1000	4.5	47.8	48.2	0.0	28.8
A.33	1000	6.0	109.8	110.2	11.9	0.0
A.34	1000	6.0	109.8	110.2	0.0	18.1
A.36	1000	6.0	47.8	48.2	16.5	0.0
A.37	1000	6.0	47.8	48.2	0.0	34.4
A.39	1000	8.0	109.8	110.2	18.1	0.0
A.40	1000	8.0	109.8	110.2	0.0	22.6
A.42	1000	8.0	47.8	48.2	22.6	0.0
A.43	1000	8.0	47.8	48.2	0.0	44.2
A.45	1000	16.0	109.8	110.2	33.0	0.0
A.46	1000	16.0	109.8	110.2	0.0	33.8
A.48	1000	16.0	47.8	48.2	37.1	0.0
A.49	1000	16.0	47.8	48.2	0.0	73.1
A.51	3000	8.0	109.7	110.3	6.1	0.0
A.52	3000	8.0	109.7	110.3	0.0	19.9
A.54	3000	8.0	47.8	48.2	38.0	0.0
A.55	3000	8.0	47.8	48.2	0.0	40.3
A.57	3000	16.0	109.7	110.3	23.2	0.0
A.58	3000	16.0	109.7	110.3	0.0	32.0
A.60	3000	16.0	47.8	48.2	54.8	0.0
A.61	3000	16.0	47.8	48.2	0.0	69.5
A.63	5000	16.0	109.7	110.3	11.0	0.0
A.64	5000	16.0	109.7	110.3	0.0	29.2
A.66	5000	16.0	47.8	48.2	71.0	0.0
A.67	5000	16.0	47.8	48.2	0.0	61.1

Table A.7: Additional information about PTV measurements part 4

Fig.	Ω	R_{\min}	R_{\max}	V_1	β
-	[-]	[-]	[-]	[-]	[-]
A.15	0.00	0.8784	0.8816	0.38	6.9
A.16	0.00	0.8784	0.8816	0.38	6.9
A.18	0.00	0.8784	0.8816	0.36	2.8
A.19	0.00	0.8784	0.8816	0.36	2.8
A.21	0.71	0.8784	0.8816	0.37	6.9
A.22	0.71	0.8784	0.8816	0.37	6.9
A.24	0.71	0.3824	0.3856	0.37	6.9
A.25	0.71	0.3824	0.3856	0.37	6.9
A.27	0.68	0.8784	0.8816	0.51	4.8
A.28	0.68	0.8784	0.8816	0.51	4.8
A.30	0.68	0.3824	0.3856	0.51	4.8
A.31	0.68	0.3824	0.3856	0.51	4.8
A.33	0.36	0.8784	0.8816	0.35	3.7
A.34	0.36	0.8784	0.8816	0.35	3.7
A.36	0.36	0.3824	0.3856	0.35	3.7
A.37	0.36	0.3824	0.3856	0.35	3.7
A.39	0.28	0.8784	0.8816	0.36	2.8
A.40	0.28	0.8784	0.8816	0.36	2.8
A.42	0.28	0.3824	0.3856	0.36	2.8
A.43	0.28	0.3824	0.3856	0.36	2.8
A.45	0.17	0.8784	0.8816	0.35	1.8
A.46	0.17	0.8784	0.8816	0.35	1.8
A.48	0.17	0.3824	0.3856	0.35	1.8
A.49	0.17	0.3824	0.3856	0.35	1.8
A.51	0.89	0.8776	0.8824	0.35	3.0
A.52	0.89	0.8776	0.8824	0.35	3.0
A.54	0.89	0.3824	0.3856	0.35	3.0
A.55	0.89	0.3824	0.3856	0.35	3.0
A.57	0.53	0.8776	0.8824	0.34	1.8
A.58	0.53	0.8776	0.8824	0.34	1.8
A.60	0.53	0.3824	0.3856	0.34	1.8
A.61	0.53	0.3824	0.3856	0.34	1.8
A.63	0.92	0.8776	0.8824	0.34	1.9
A.64	0.92	0.8776	0.8824	0.34	1.9
A.66	0.92	0.3824	0.3856	0.34	1.9
A.67	0.92	0.3824	0.3856	0.34	1.9

Table A.8: Additional information about PTV measurements part 5

Fig.	Re_u	Re_v	Re	α_ν	P_{Ph}	Ta	A	N
-	[-]	[-]	[-]	[-]	[-]	[-]	[-]	[-]
A.15	287	109	307	0.9	0.0	0.0	1.8	-
A.16	287	109	307	0.9	0.0	0.0	1.8	-
A.18	737	267	784	2.1	0.0	0.0	0.7	-
A.19	737	267	784	2.1	0.0	0.0	0.7	-
A.21	296	109	315	0.9	0.7	0.4	1.7	1.8
A.22	296	109	315	0.9	0.7	0.4	1.7	1.8
A.24	296	109	315	0.9	0.7	0.4	1.7	1.8
A.25	296	109	315	0.9	0.7	0.4	1.7	1.8
A.27	310	157	347	1.3	0.7	0.4	1.6	1.9
A.28	310	157	347	1.3	0.7	0.4	1.6	1.9
A.30	310	157	347	1.3	0.7	0.4	1.6	1.9
A.31	310	157	347	1.3	0.7	0.4	1.6	1.9
A.33	581	205	616	1.6	0.7	0.4	0.9	3.6
A.34	581	205	616	1.6	0.7	0.4	0.9	3.6
A.36	581	205	616	1.6	0.7	0.4	0.9	3.6
A.37	581	205	616	1.6	0.7	0.4	0.9	3.6
A.39	744	267	790	2.1	0.7	0.4	0.7	4.6
A.40	744	267	790	2.1	0.7	0.4	0.7	4.6
A.42	744	267	790	2.1	0.7	0.4	0.7	4.6
A.43	744	267	790	2.1	0.7	0.4	0.7	4.6
A.45	1215	423	1287	3.4	0.7	0.4	0.4	7.5
A.46	1215	423	1287	3.4	0.7	0.4	0.4	7.5
A.48	1215	423	1287	3.4	0.7	0.4	0.4	7.5
A.49	1215	423	1287	3.4	0.7	0.4	0.4	7.5
A.51	709	249	134	2.0	1.1	1.3	0.7	2.5
A.52	709	249	134	2.0	1.1	1.3	0.7	2.5
A.54	709	249	134	2.0	1.1	1.3	0.7	2.5
A.55	709	249	134	2.0	1.1	1.3	0.7	2.5
A.57	1188	407	134	3.3	1.1	1.3	0.4	4.2
A.58	1188	407	134	3.3	1.1	1.3	0.4	4.2
A.60	1188	407	134	3.3	1.1	1.3	0.4	4.2
A.61	1188	407	134	3.3	1.1	1.3	0.4	4.2
A.63	1150	387	134	3.1	1.5	2.1	0.4	3.2
A.64	1150	387	134	3.1	1.5	2.1	0.4	3.2
A.66	1150	387	134	3.1	1.5	2.1	0.4	3.2
A.67	1150	387	134	3.1	1.5	2.1	0.4	3.2

Table A.9: Additional information about PTV measurements part 6

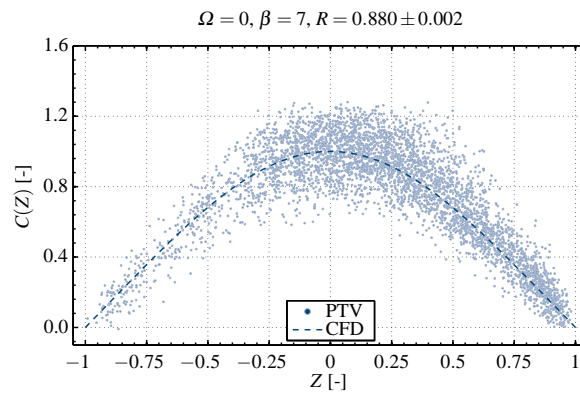


Figure A.15: Laminar, tangential velocity profile without rotation at the outer radius

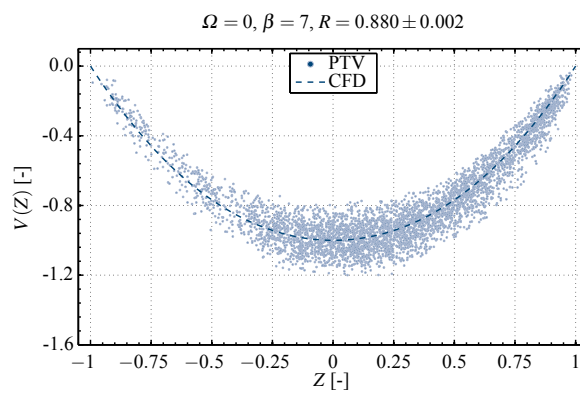


Figure A.16: Laminar, radial velocity profile without rotation at the outer radius

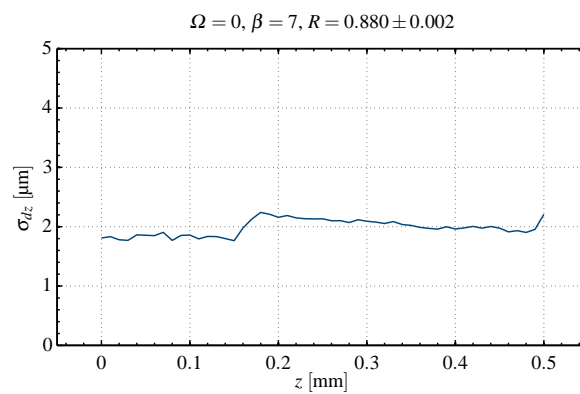


Figure A.17: Standard deviation $\sigma_{\Delta z}$ of the particle displacement Δz in z -direction along the inter-disk spacing without rotation at the outer radius

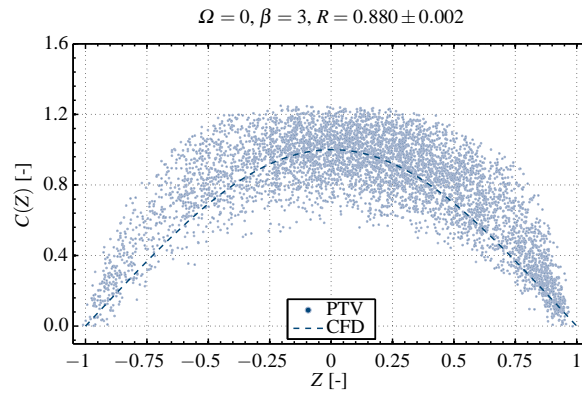


Figure A.18: Transitional, tangential velocity profile without rotation at the outer radius

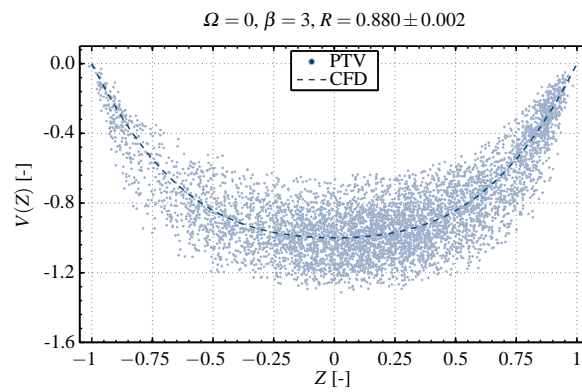


Figure A.19: Transitional, radial velocity profile without rotation at the outer radius

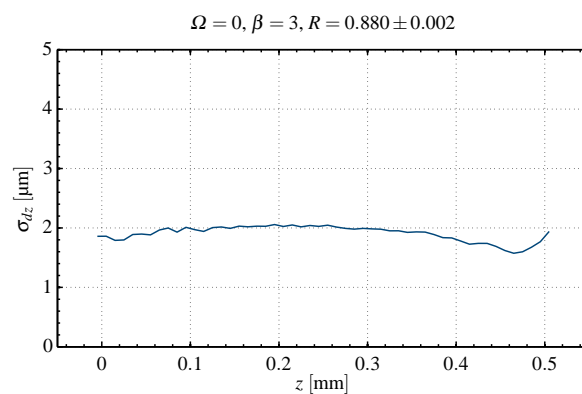


Figure A.20: Standard deviation $\sigma_{\Delta z}$ of the particle displacement Δz in z -direction along the inter-disk spacing without rotation at the outer radius

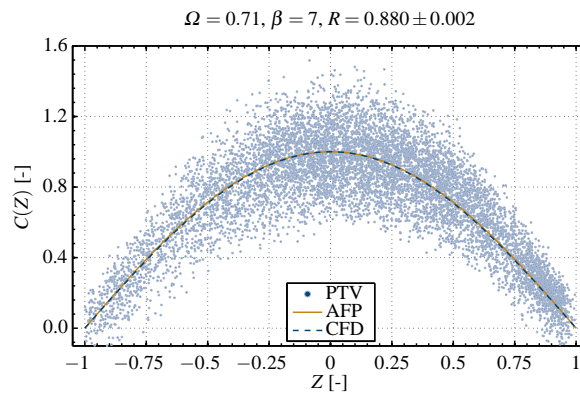


Figure A.21: Laminar, tangential velocity profile at the outer radius

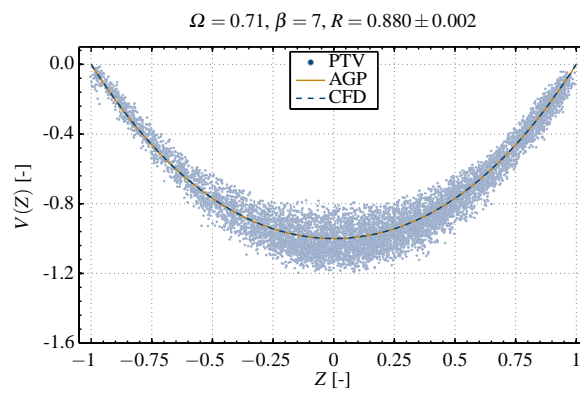


Figure A.22: Laminar, radial velocity profile at the outer radius

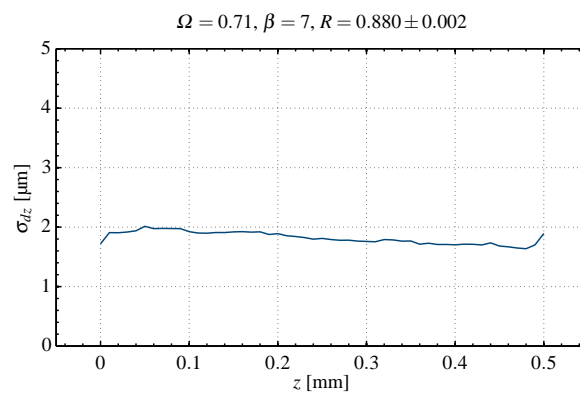


Figure A.23: Standard deviation $\sigma_{\Delta z}$ of the particle displacement Δz in z -direction along the inter-disk spacing at the outer radius

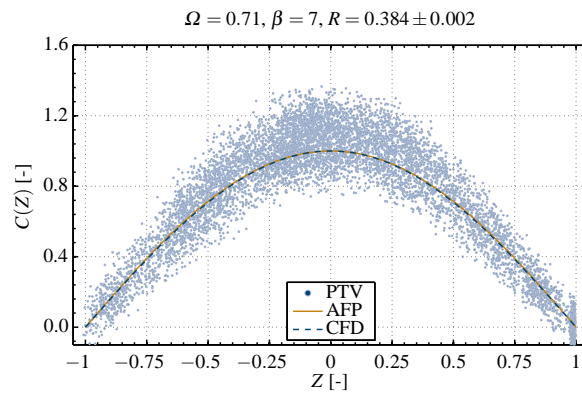


Figure A.24: Laminar, tangential velocity profile at the outer radius

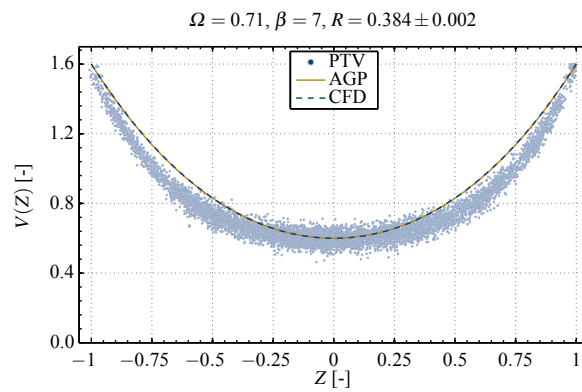
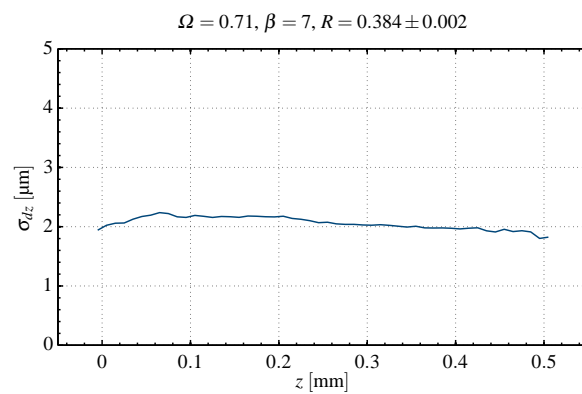


Figure A.25: Laminar, radial velocity profile at the outer radius

Figure A.26: Standard deviation $\sigma_{\Delta z}$ of the particle displacement Δz in z -direction along the inter-disk spacing at the outer radius

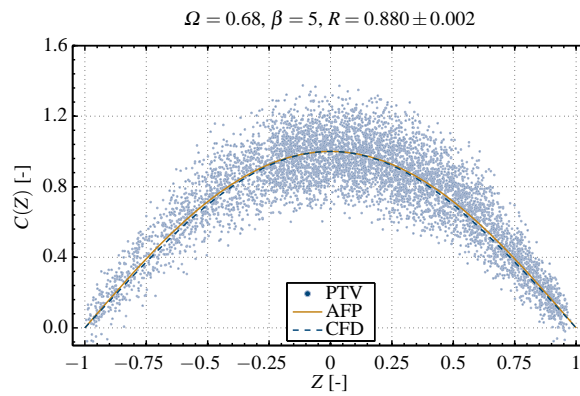


Figure A.27: Laminar, tangential velocity profile at the outer radius

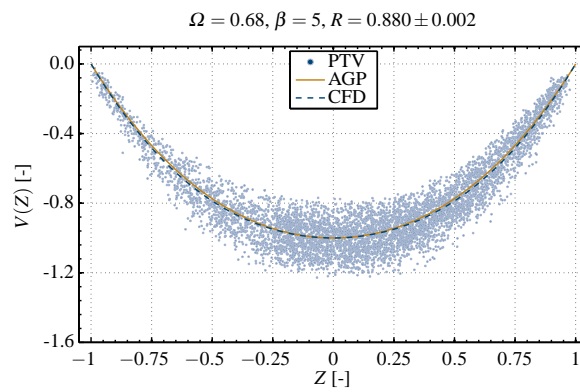


Figure A.28: Laminar, radial velocity profile at the outer radius

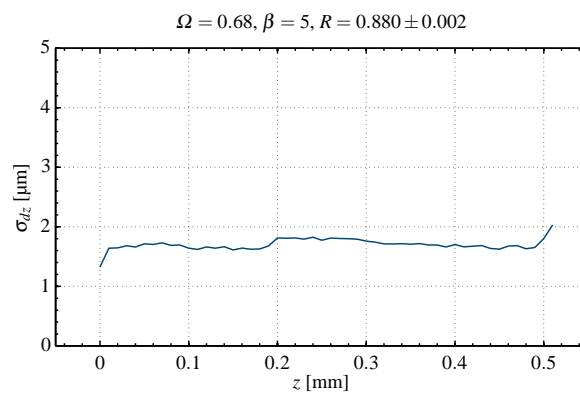


Figure A.29: Standard deviation $\sigma_{\Delta z}$ of the particle displacement Δz in z -direction along the inter-disk spacing at the outer radius

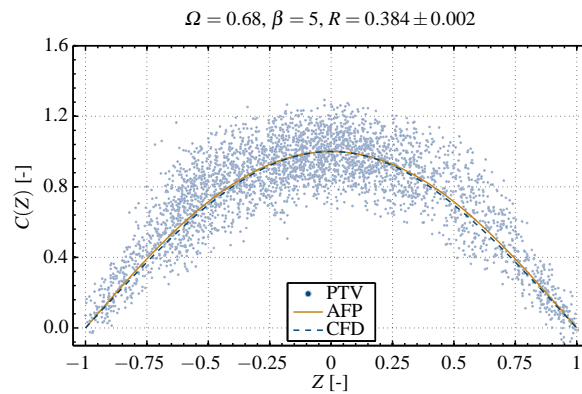


Figure A.30: Transitional, tangential velocity profile at the inner radius

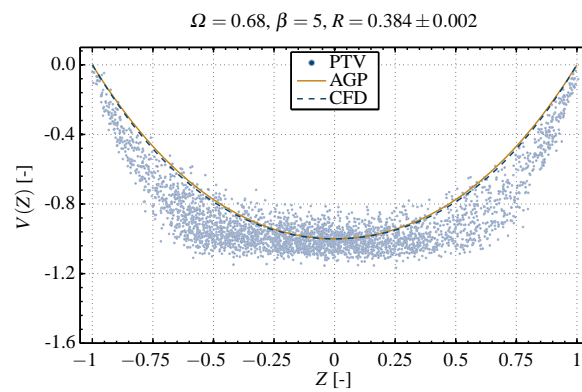
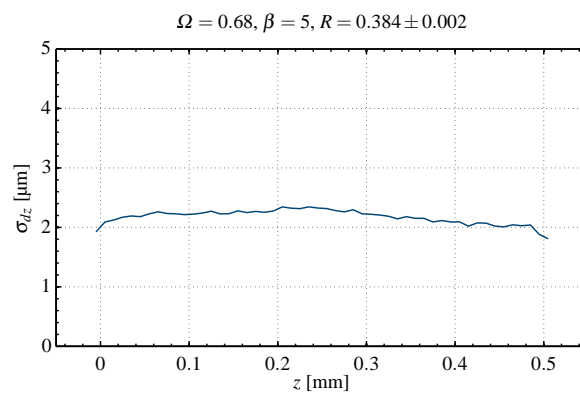


Figure A.31: Transitional, radial velocity profile at the inner radius

Figure A.32: Standard deviation $\sigma_{\Delta z}$ of the particle displacement Δz in z -direction along the inter-disk spacing at the inner radius

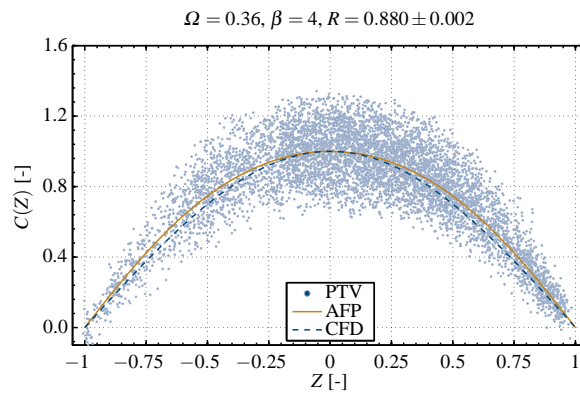


Figure A.33: Laminar, tangential velocity profile at the outer radius

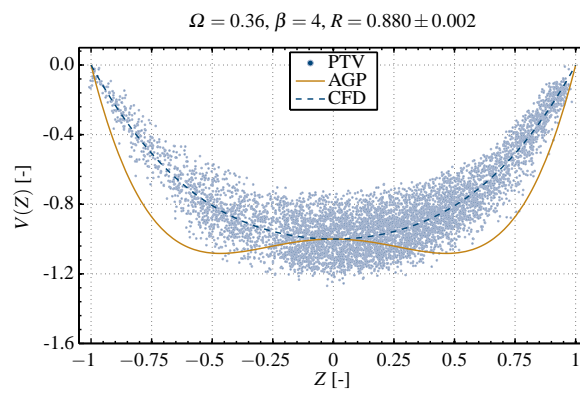


Figure A.34: Laminar, radial velocity profile at the outer radius

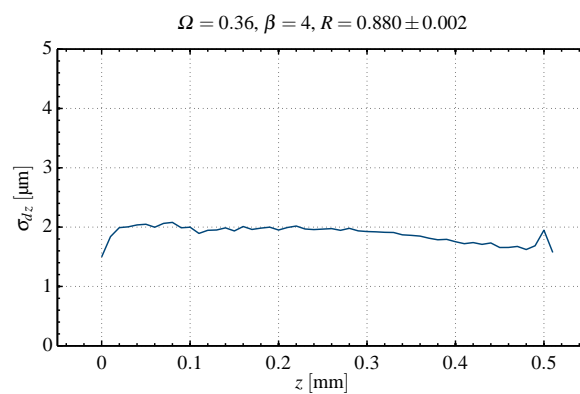


Figure A.35: Standard deviation $\sigma_{\Delta z}$ of the particle displacement Δz in z -direction along the inter-disk spacing at the outer radius

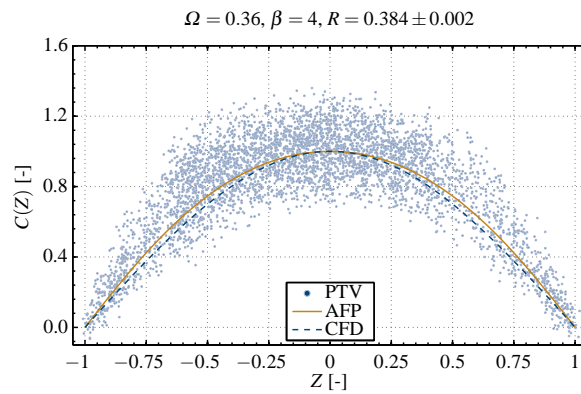


Figure A.36: Transitional, tangential velocity profile at the inner radius

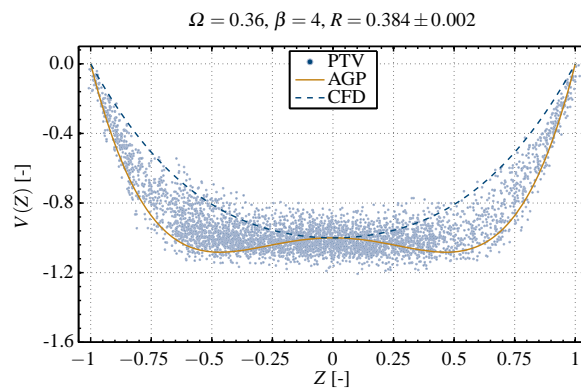
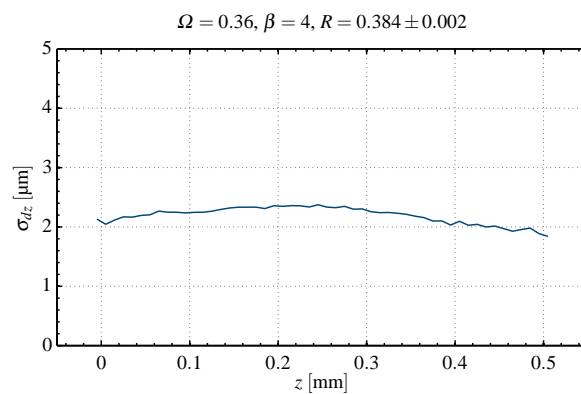


Figure A.37: Transitional, radial velocity profile at the inner radius

Figure A.38: Standard deviation $\sigma_{\Delta z}$ of the particle displacement Δz in z -direction along the inter-disk spacing at the inner radius

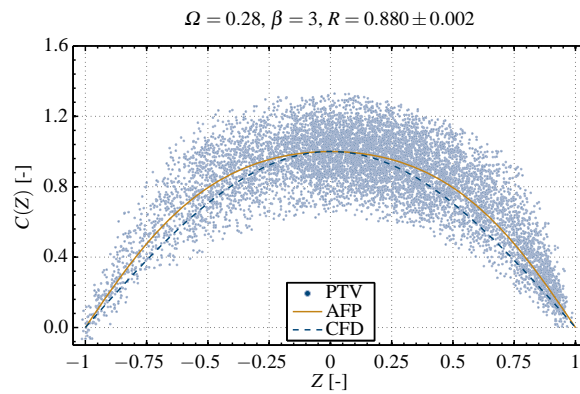


Figure A.39: Transitional, tangential velocity profile at the outer radius

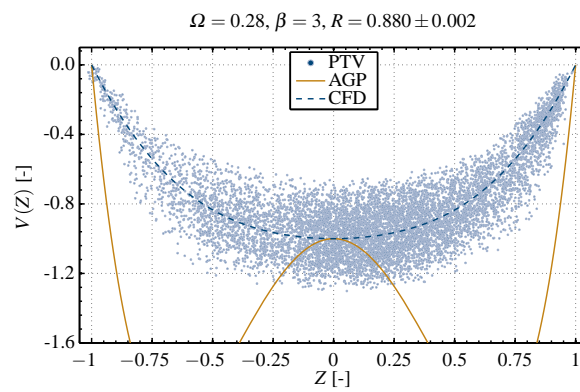


Figure A.40: Transitional, radial velocity profile at the outer radius

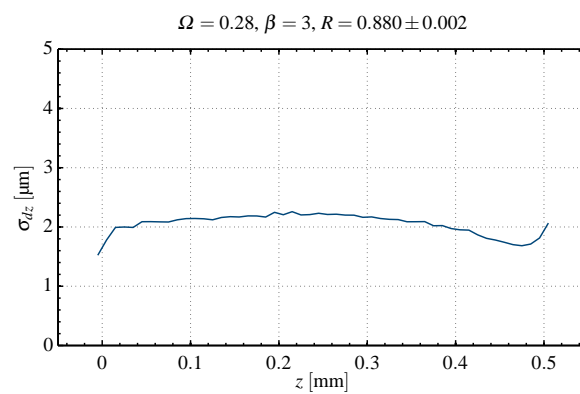


Figure A.41: Standard deviation $\sigma_{\Delta z}$ of the particle displacement Δz in z -direction along the inter-disk spacing at the outer radius

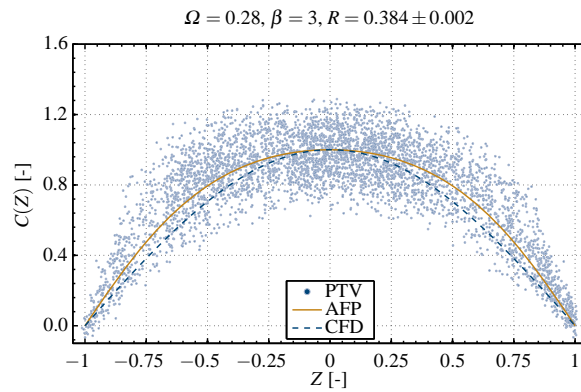


Figure A.42: Transitional, tangential velocity profile at the inner radius

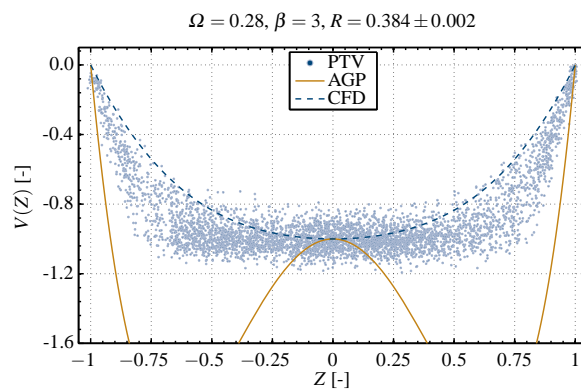
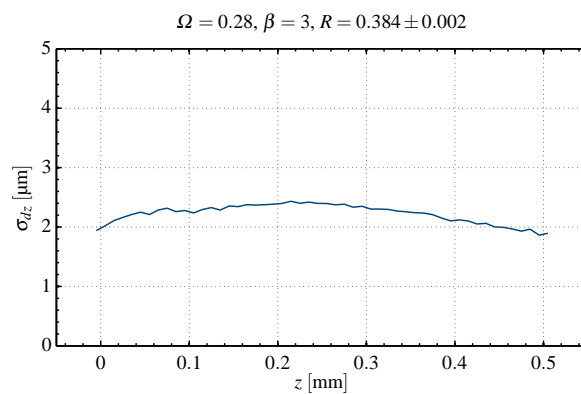


Figure A.43: Transitional, radial velocity profile at the inner radius

Figure A.44: Standard deviation $\sigma_{\Delta z}$ of the particle displacement Δz in z -direction along the inter-disk spacing at the inner radius

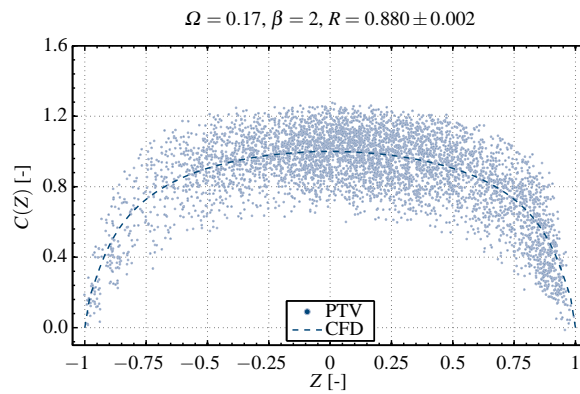


Figure A.45: Turbulent, tangential velocity profile at the outer radius

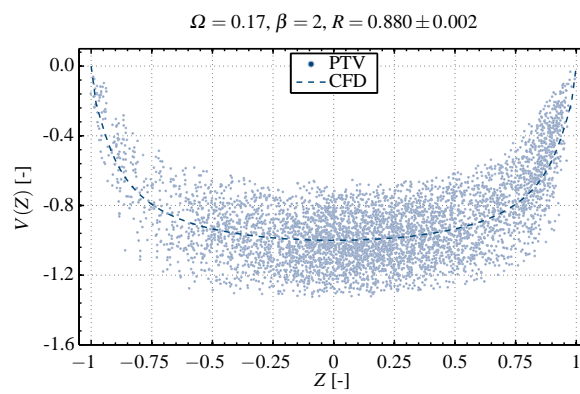


Figure A.46: Turbulent, radial velocity profile at the outer radius

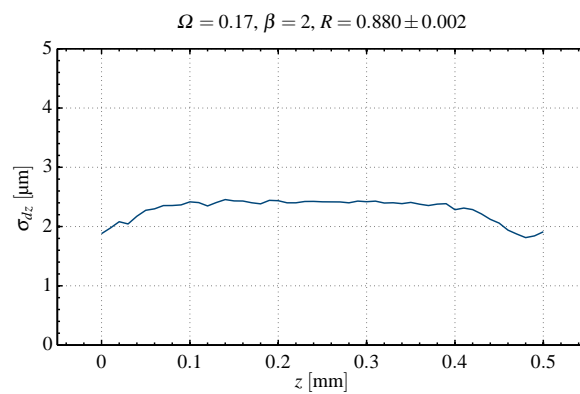


Figure A.47: Standard deviation $\sigma_{\Delta z}$ of the particle displacement Δz in z -direction along the inter-disk spacing at the outer radius

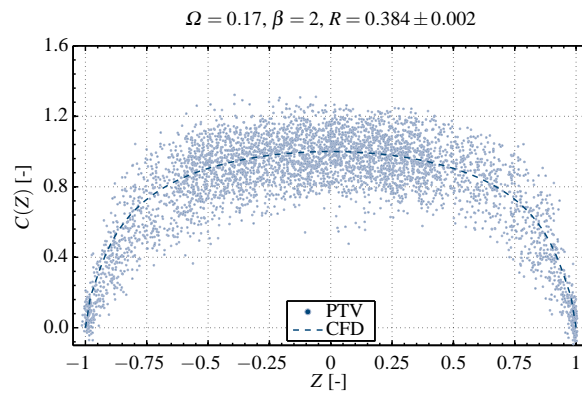


Figure A.48: Turbulent, tangential velocity profile at the inner radius

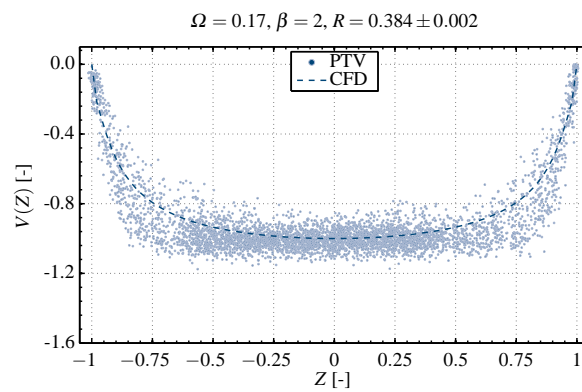
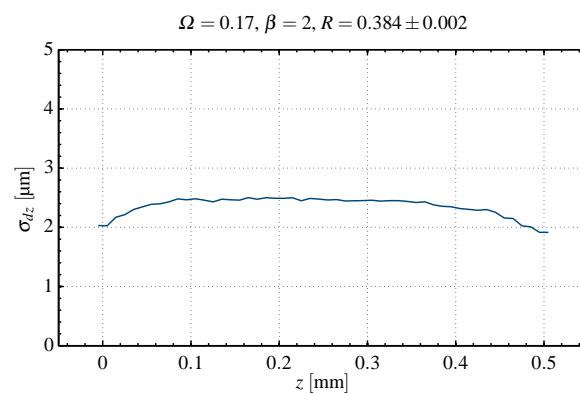


Figure A.49: Turbulent, radial velocity profile at the inner radius

Figure A.50: Standard deviation $\sigma_{\Delta z}$ of the particle displacement Δz in z -direction along the inter-disk spacing at the inner radius

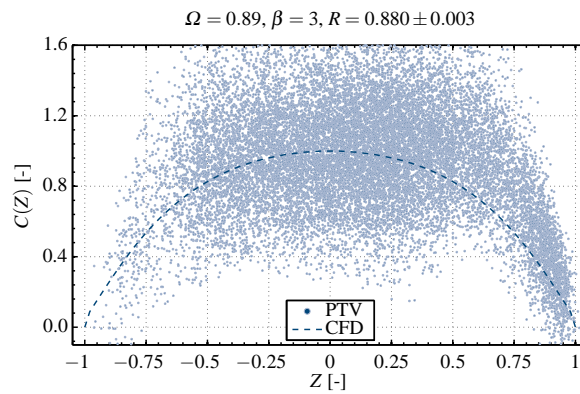


Figure A.51: Turbulent, tangential velocity profile at the outer radius

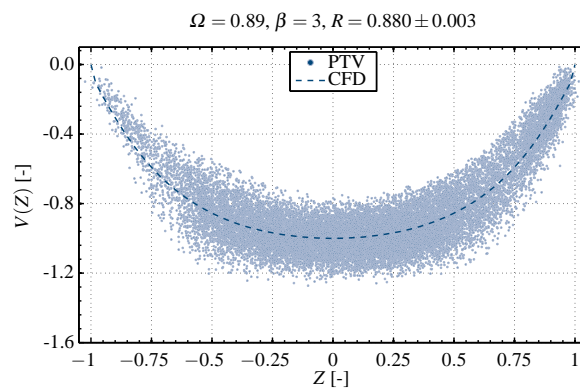


Figure A.52: Turbulent, radial velocity profile at the outer radius

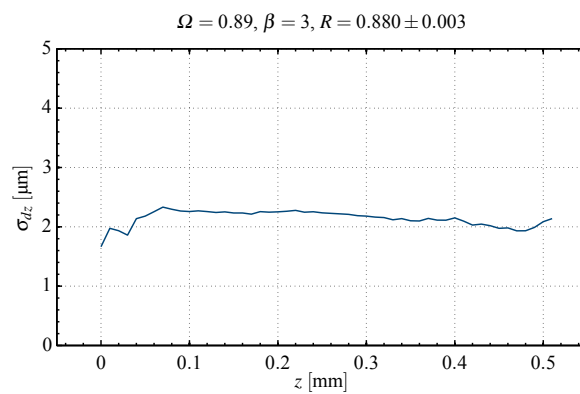


Figure A.53: Standard deviation $\sigma_{\Delta z}$ of the particle displacement Δz in z -direction along the inter-disk spacing at the outer radius

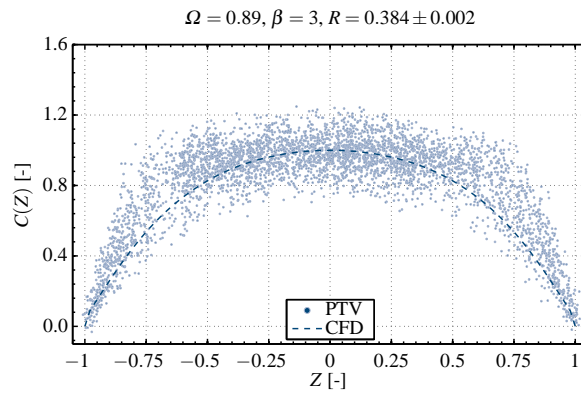


Figure A.54: Turbulent, tangential velocity profile at the inner radius

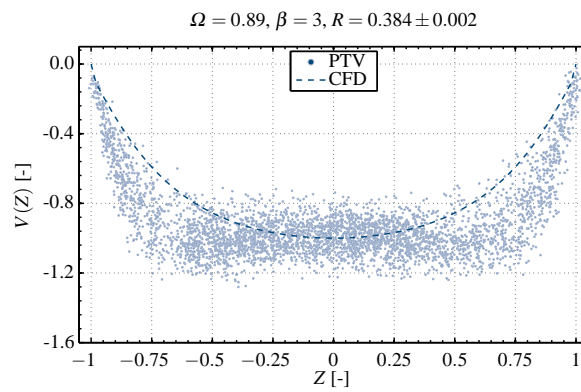
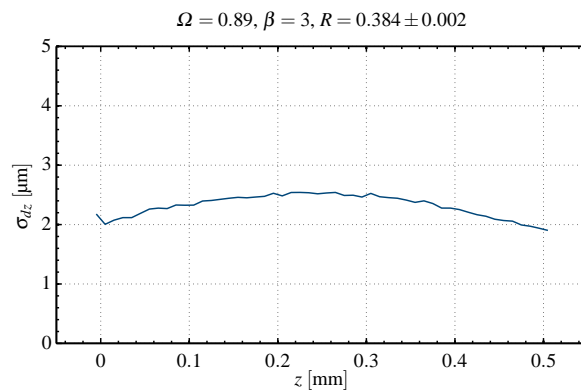


Figure A.55: Turbulent, radial velocity profile at the inner radius

Figure A.56: Standard deviation $\sigma_{\Delta z}$ of the particle displacement Δz in z -direction along the inter-disk spacing at the inner radius

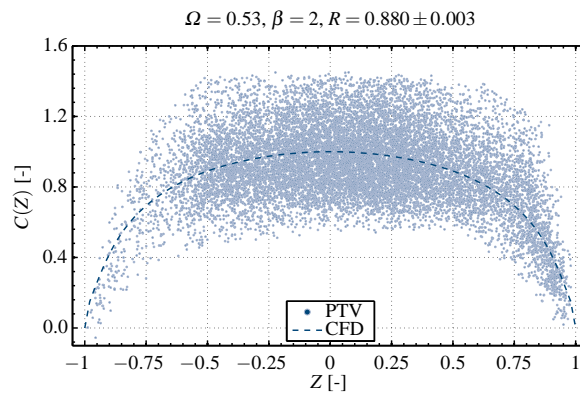


Figure A.57: Turbulent, tangential velocity profile at the outer radius

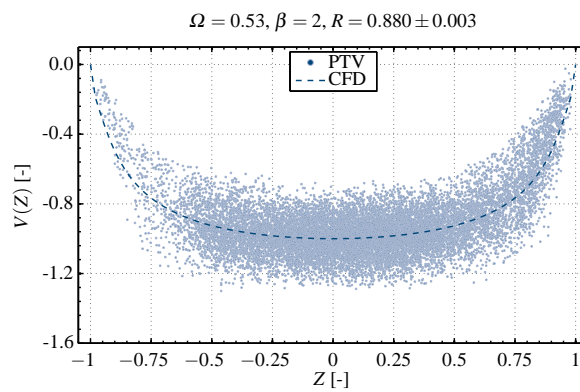


Figure A.58: Turbulent, radial velocity profile at the outer radius

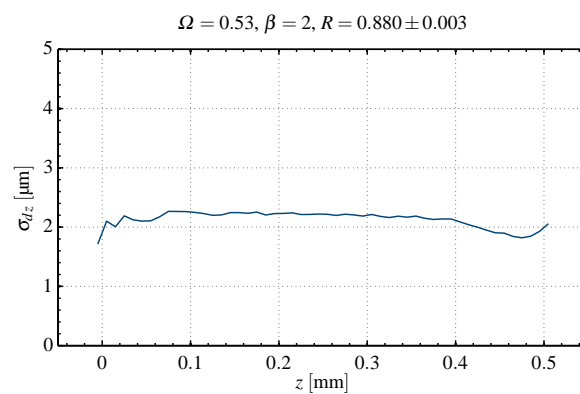


Figure A.59: Standard deviation $\sigma_{\Delta z}$ of the particle displacement Δz in z -direction along the inter-disk spacing at the outer radius

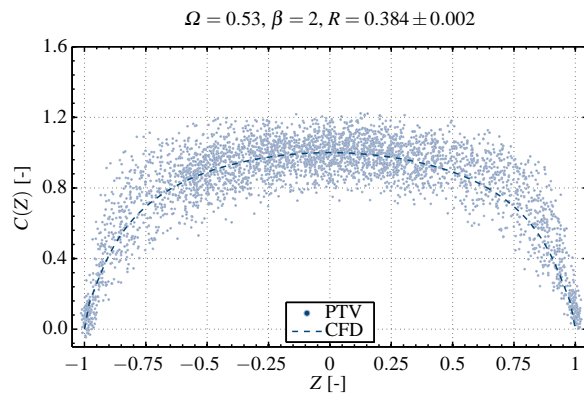


Figure A.60: Turbulent, tangential velocity profile at the inner radius

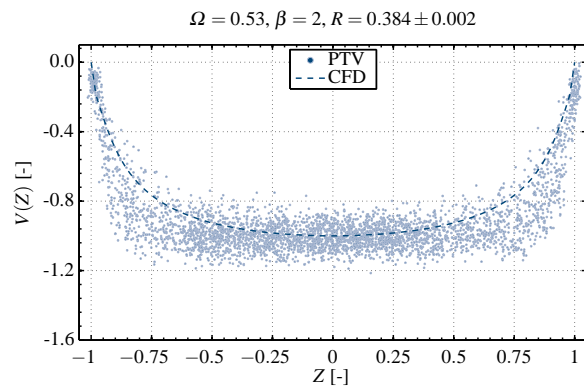
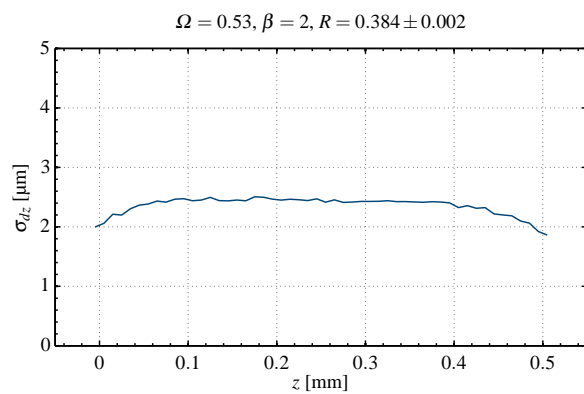


Figure A.61: Turbulent, radial velocity profile at the inner radius

Figure A.62: Standard deviation $\sigma_{\Delta z}$ of the particle displacement Δz in z -direction along the inter-disk spacing at the inner radius

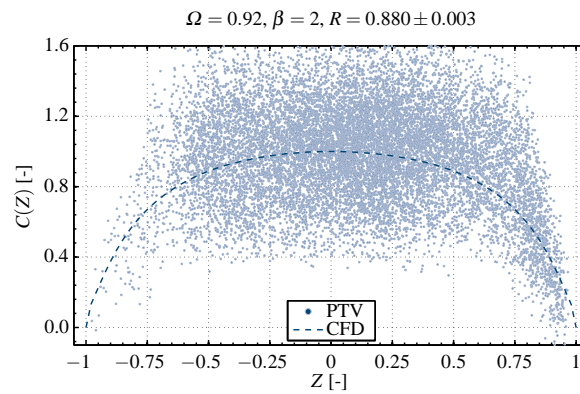


Figure A.63: Turbulent, tangential velocity profile at the outer radius

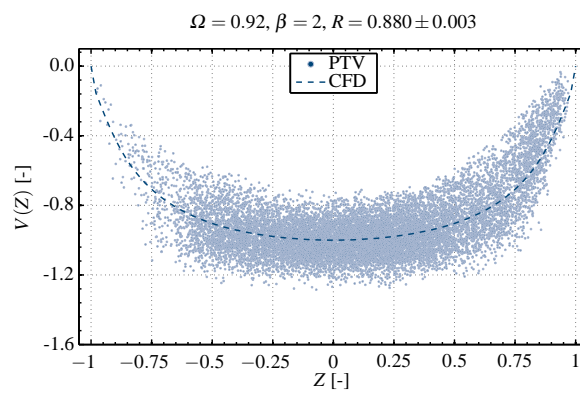


Figure A.64: Turbulent, radial velocity profile at the outer radius

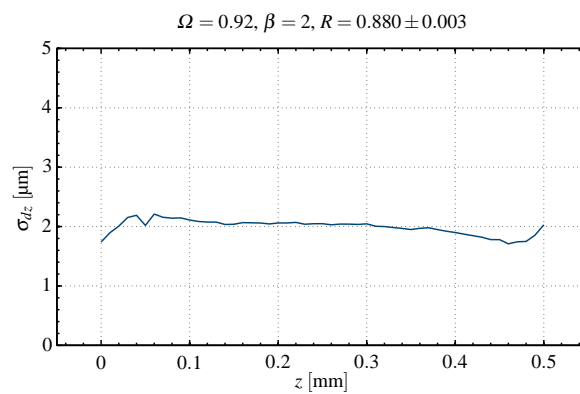


Figure A.65: Standard deviation $\sigma_{\Delta z}$ of the particle displacement Δz in z -direction along the inter-disk spacing at the outer radius

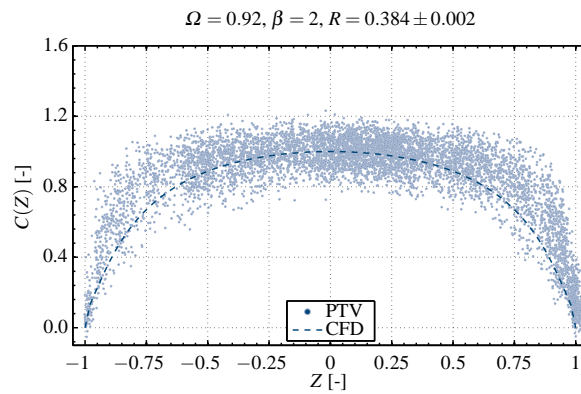


Figure A.66: Turbulent, tangential velocity profile at the inner radius

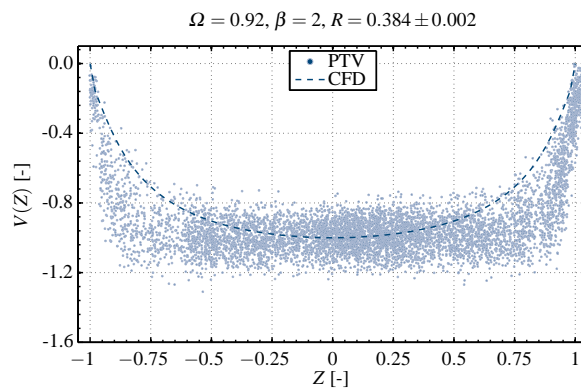
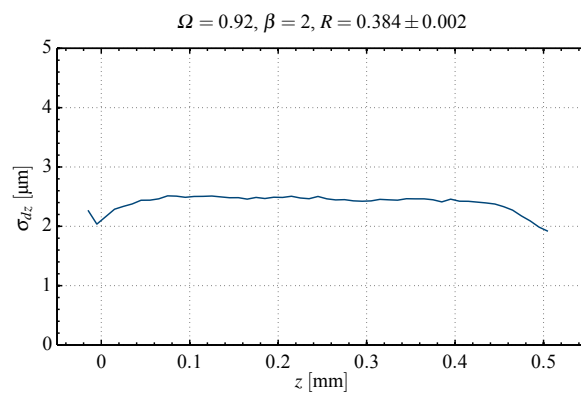


Figure A.67: Turbulent, radial velocity profile at the inner radius

Figure A.68: Standard deviation $\sigma_{\Delta z}$ of the particle displacement Δz in z -direction along the inter-disk spacing at the inner radius

A.4 Two-dimensional transient CFD

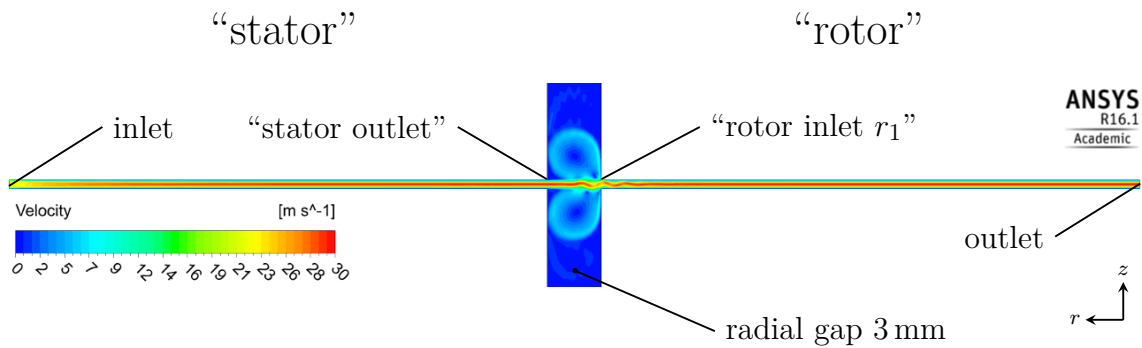


Figure A.69: Transient, laminar flow through a simplified 2D domain; stator and rotor axially aligned ($\Delta t = 0.001$ s; $2s = 0.5$ mm; $\bar{u}_1 = 20$ m/s; $\bar{p}_2 = 1$ bar)

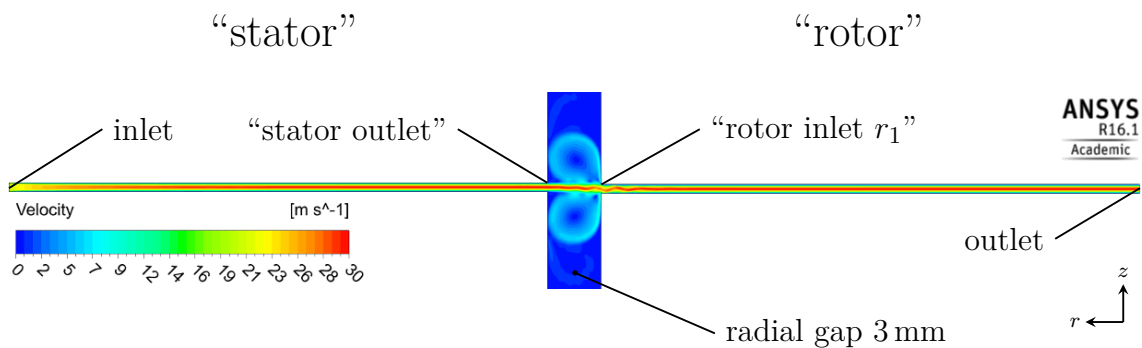


Figure A.70: Transient, laminar flow through a simplified 2D domain; stator and rotor with 20% axial offset ($\Delta t = 0.001$ s; $2s = 0.5$ mm; $\bar{u}_1 = 20$ m/s; $\bar{p}_2 = 1$ bar)

A.5 Post processing of measurement data

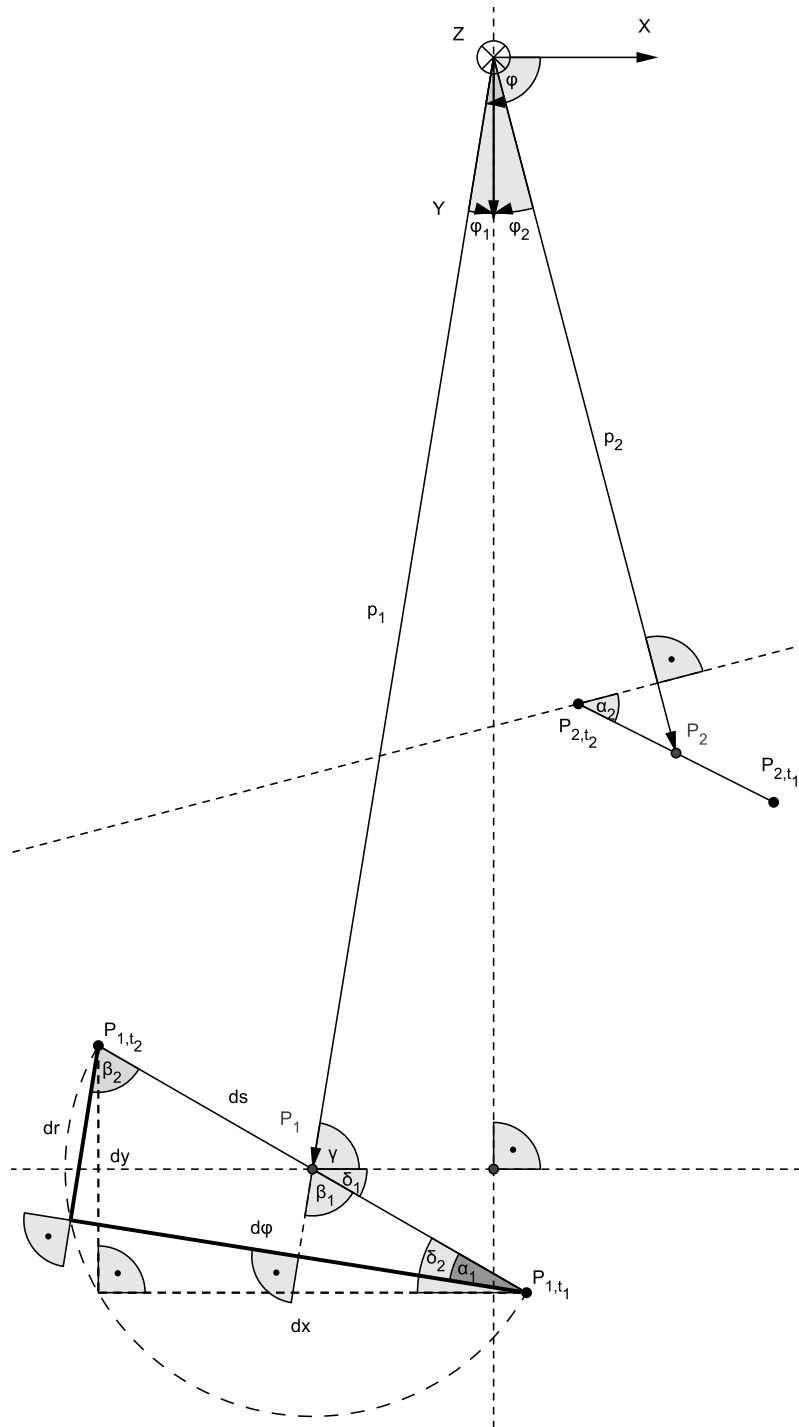


Figure A.71: Coordinate transformation from Cartesian into cylindrical coordinates

A.6 CFD investigations

M_{\max}	P_{\max}	u_1
[Nm]	[W]	[m/s]
0.96	88.1	100

Table A.10: Physical quantities used for normalisation of laminar CFD

Bibliography

- [1] International Energy Agency (IEA). Struktur der Stromerzeugung weltweit nach Energieträger 2012, 2015. URL <http://de.statista.com/statistik/daten/studie/164193/umfrage/stromproduktion-weltweit-nach-energietraeger-im-jahr-2009/>. retrieved on 21/07/2015.
- [2] N. Tesla. Turbine. US Patent 1,061,206, May 6 1913. URL <http://www.google.com/patents/US1061206>.
- [3] A. Kölling, R. Lisker, U. Hellwig, and F. Wildenauer. Friction expander for the generation of electricity (fege). *International Conference on Renewable Energies and Power Quality (ICREPQ'15)*, 2015.
- [4] R. Steidel and H. Weiss. Performance test of a bladeless turbine for geothermal applications. Technical Report Report No. UCID-17068, California Univ., Livermore (USA). Lawrence Livermore Lab., 1976.
- [5] C. R. Truman, W. Rice, and D. F. Jankowski. Laminar throughflow of varying-quality steam between co-rotating disks. *Journal of Fluids Engineering*, 100(2): 194–200, 1978.
- [6] V. D. Romanin. *Theory and Performance of Tesla Turbines*. PhD thesis, University of California, Berkeley, 2012.
- [7] S. U. M. Khan, I. M. Maqsood, E. Ali, J. Sahah, and M. Javed. Proposed applications with implementation techniques of the upcoming renewable energy resource, the Tesla Turbine. In *Journal of Physics: Conference Series*, volume 439. IOP Publishing, 2013. doi: 10.1088/1742-6596/439/1/012040.
- [8] V. Krishnan. *Design and Fabrication of cm-scale Tesla Turbines*. PhD thesis, University of California at Berkeley, 2015.
- [9] G.-A. Euteneuer and M. Piesche. Betriebsverhalten einer Reibungsturbine bei turbulentem Stromfeld und viskosem, inkompressiblem Medium im Spaltelement. *Forschung im Ingenieurwesen*, 44(3):79–84, 1978.
- [10] Q. Deng, W. Qi, and Z. Feng. Improvement of a theoretical analysis method for Tesla Turbines. In *ASME Turbo Expo 2013: Turbine Technical Conference and Exposition*, pages V06CT40A012–V06CT40A012. American Society of Mechanical Engineers, 2013.
- [11] C. Schosser and M. Pfitzner. A numerical study of the three-dimensional incompressible rotor airflow within a Tesla Turbine. *Proceedings of Conference on Modelling Fluid Flow CMFF'15, Budapest, Hungary*, 2015.
- [12] W. Rice. Tesla Turbomachinery. In *Conference Proceedings of the IV International Tesla Symposium, Serbian Academy of Sciences and Arts, Belgrade, Yugoslavia*, 1991.

- [13] W. Rice. Tesla Turbomachinery. *Mechanical Engineering - New York and Basel*, Marcel Dekker, pages 861–874, 2003.
- [14] W. Rice. Handbook of Turbomachinery: Tesla Turbomachinery. *Jr. Earl Logan, Ramendra Roy*, 2005.
- [15] S. Sengupta and A. Guha. A theory of Tesla disc Turbines. *Proceedings of the Institution of Mechanical Engineers, Part A: Journal of Power and Energy*, 226(5): 650–663, 2012.
- [16] R. Deam, B. Mace, R. Collins, and E. Lemma. On scaling down turbines to millimeter size. *Journal of Engineering for Gas Turbines and Power*, 130(5): 052301, 2008. URL <http://gasturbinespower.asmedigitalcollection.asme.org/article.aspx?articleid=1426795>.
- [17] V. D. Romanin and V. P. Carey. An integral perturbation model of flow and momentum transport in rotating microchannels with smooth or microstructured wall surfaces. *Physics of Fluids (1994-present)*, 23(8):082003, 2011.
- [18] V. G. Krishnan, Z. Iqbal, and M. M. Maharbiz. A micro Tesla Turbine for power generation from low pressure heads and evaporation driven flows. In *Solid-State Sensors, Actuators and Microsystems Conference (TRANSDUCERS), 2011 16th International*, pages 1851–1854. IEEE, 2011.
- [19] V. D. Romanin, V. G. Krishnan, V. P. Carey, and M. M. Maharbiz. Experimental and analytical study of sub-watt scale Tesla Turbine performance. In *ASME 2012 International Mechanical Engineering Congress and Exposition*, pages 1005–1014. American Society of Mechanical Engineers, 2012. URL <http://proceedings.asmedigitalcollection.asme.org/proceeding.aspx?articleid=1751200>.
- [20] V. G. Krishnan, V. Romanin, V. P. Carey, and M. Maharbiz. Design and scaling of microscale Tesla Turbines. *Journal of Micromechanics and Microengineering*, 23(12):125001, 2013.
- [21] A. Guha and S. Sengupta. Similitude and scaling laws for the rotating flow between concentric discs. *Proceedings of the Institution of Mechanical Engineers, Part A: Journal of Power and Energy*, 228(4):429–439, 2014.
- [22] P. Lampart, K. Kosowski, M. Piwowarski, and Ł Jędrzejewski. Design analysis of Tesla micro-Turbine operating on a low-boiling medium. *Polish Maritime Research*, 16(Special):28–33, 2009.
- [23] T. C. Martin. *The inventions, researches and writings of Nikola Tesla*. Health Research Books, 1997.
- [24] N. Tesla. Fluid propulsion, May 6 1913. US Patent 1,061,142.
- [25] A. F. R. Ladino. Numerical simulation of the flow field in a friction-type turbine (Tesla Turbine). Diploma thesis, Technical University of Vienna. Technical report, Institute of Thermal Powerplants, Vienna University of Technology, 2004.

-
- [26] unknown author. Tesla's new method of and apparatus for fluid propulsion. *Electrical Rev.*, pages 515–517, 1911.
- [27] unknown author. The Tesla Turbine. *Electrical Rev.*, page 637, 1911.
- [28] unknown author. Blade-less turbines. *Engineering*, 92:637, 1911.
- [29] unknown author. The Tesla steam Turbine. *Eng. News*, 66:448–449, 1911.
- [30] unknown author. The Tesla steam Turbine. *Sci. Am.*, pages 296–297, 1911.
- [31] E. Merigeault. Les Turbines à Frottements ou Turbines Tesla. *Rev. Mecan.*, pages 534–544, 1914.
- [32] D. Nendl. Reibungsturbine. *VDI-Berichte*, 193:287–293, 1973.
- [33] E. Lemma, R. T. Deam, D. Toncich, and R. Collins. Characterisation of a small viscous flow turbine. *Experimental Thermal and Fluid Science*, 33(1):96–105, 2008.
- [34] K. Okamoto, T. Hidema, D. Onozato, and S. Teramoto. Numerical investigation of internal flow dynamics for Tesla Turbine design. In *ISABE Conference 2013*, 2013.
- [35] P. Lampart and Ł. Jędrzejewski. Investigations of aerodynamics of Tesla blade-less microturbines. *Journal of Theoretical and Applied Mechanics*, 49:477–499, 2011.
- [36] A. Guha and S. Sengupta. The fluid dynamics of work transfer in the non-uniform viscous rotating flow within a Tesla disc turbomachine. *Physics of Fluids*, 26(3):033601, 2014.
- [37] R. K. Warner. The design, construction, and testing of a Tesla Turbine. Master's thesis, University of Maryland, 1949.
- [38] H. B. Schroeder. An investigation of viscosity force in air by means of a viscosity turbine. *BAE Thesis, Rensselaer Polytechnic Institute*, 1950.
- [39] J. H. Armstrong. An investigation of the performance of a modified Tesla Turbine. Master's thesis, Georgia Institute of Technology, 1952.
- [40] T. Vannérus. Rotierende Scheiben für Luftvorwärmer mit Gebläsewirkung. *Allgemeine Wärmetechnik*, 6:257–262, 1955.
- [41] S. K. P. Young. The investigation and analysis of the Tesla Turbine. Master's thesis, University of Illinois at Urbana-Champaign, 1957.
- [42] E. M. Gol'din. Hydrodynamic flow between separator plates. *Izv. Akad. Nauk SSSR, Otd. Tekh. Nauk*, 7:80–88, 1957.
- [43] G. A. Tirskaa. Nonstationary flow with heat transfer in a viscous, incompressible fluid between two revolving discs accompanied by fluid influx. In *Soviet Physics Doklady*, volume 119, pages 226–228, 1958.
- [44] E. L. Gruber. An investigation of a turbine with a multiple disk rotor. Master's thesis, Department of Mechanical Engineering, Arizona State University, 1960.

- [45] E. W. Beans. *Performance characteristics of a friction disc turbine*. PhD thesis, Pennsylvania State University, 1961.
- [46] W. Rice. An analytical and experimental investigation of multiple-disk turbines. *Journal for Engineering for Power*, 87(1):29–36, 1965. URL <http://gasturbinespower.asmedigitalcollection.asme.org/pdfaccess.ashx?ResourceID=4441869&PDFSource=13>.
- [47] E. W. Beans. Investigation into the performance characteristics of a friction turbine. *Journal of Spacecraft and Rockets*, 3(1):131–134, 1966. URL <http://arc.aiaa.org/doi/pdf/10.2514/3.28398>.
- [48] R. C. North. *An Investigation of the Tesla Turbine*. PhD thesis, University of Maryland, 1969.
- [49] J.-L. Peube. Sur l'écoulement radial permanent d'un fluide visqueux incompressible entre deux plans parallèles fixes. *Journal de Mécanique*, 2(4):377–395, 1963.
- [50] F. Kreith and J.-L. Peube. Écoulement entre deux disques parallèles en rotation. *Comptes rendus Hebdomadaires des Seances de l'academié des sciences*, 260(20):5184, 1965.
- [51] J.-L. Peube and F. Kreith. Écoulement permanent d'un fluide visqueux incompressible entre deux disques parallèles en rotation. *Journal de Mécanique*, 5(2):261, 1966.
- [52] L. Matsch and W. Rice. An asymptotic solution for laminar flow of an incompressible fluid between rotating disks. *Journal of Applied Mechanics*, 35(1):155–159, 1968.
- [53] M. C. Breiter and K. Pohlhausen. Laminar flow between two parallel rotating disks. Technical Report Report No. ARL 62-318, Aeronautical Research Laboratories, Wright-Patterson AFB, Ohio, 1962. URL <http://oai.dtic.mil/oai/oai?verb=getRecord&metadataPrefix=html&identifier=AD0275562>.
- [54] K. E. Boyd and W. Rice. Laminar inward flow of an incompressible fluid between rotating disks, with full peripheral admission. *Journal of Applied Mechanics*, 35(2):229–237, 1968.
- [55] S. Hasinger and L. Kehrt. Investigation of a shear-force pump. *Journal for Engineering for Power*, 85(3):201–206, 1963. URL <http://gasturbinespower.asmedigitalcollection.asme.org/article.aspx?articleid=1416450>.
- [56] E. M. Gol'din. Flow stability between separator plates. *Fluid Dynamics*, 1(2):104–106, 1966.
- [57] A. V. Gorin and M. I. Shilyaev. Laminar flow between rotating disks. *Fluid Dynamics*, 11(2):219–224, 1976.
- [58] I. V. Lyskovtsov. Separation of fluids in centrifugal apparatuses. *Mashinostroenie, Moscow*, 1968.
- [59] N. A. Slezkin and S. M. Targ. Generalization of Reynolds' equation. *Doklady Akademii Nauk SSSR*, 54(3), 1946.

- [60] V. I. Misyura. Laminar flow of an incompressible liquid between two rotating discs. *Fluid Dynamics*, 7(5):860–864, 1972.
- [61] E. Bakke. *Theoretical and Experimental Investigation of the Flow Phenomena Between Two Co-Rotating Parallel Disks with Source Flow*. PhD thesis, University of Colorado, 1965.
- [62] L. Matsch and W. Rice. Potential flow between two parallel circular disks with partial admission. *Journal of Applied Mechanics*, 34(1):239–240, 1967. URL <http://appliedmechanics.asmedigitalcollection.asme.org/article.aspx?articleid=1398128>.
- [63] B. E. Boyack and W. Rice. Integral method for flow between corotating disks. *Journal of Fluids Engineering*, 93(3):350–354, 1971.
- [64] R. Adams and W. Rice. Experimental investigation of the flow between corotating disks. *Journal of Applied Mechanics*, 37(3):844–849, 1970.
- [65] M. E. Crawford. A composite solution method for analytical design and optimization studies of a multiple-disk pump. Master’s thesis, Arizona State University, 1972.
- [66] M. J. Lawn and W. Rice. Calculated design data for the multiple-disk turbine using incompressible fluid. Technical report, Report No. ERC-R-73004, Engineering Research Center, Arizona State University, 1973.
- [67] M. J. Lawn and W. Rice. Calculated design data for the multiple-disk turbine using incompressible fluid. *Journal of Fluids Engineering*, 96(3):252–258, 1974.
- [68] J. W. Daily and R. E. Nece. Chamber dimension effects on induced flow and frictional resistance of enclosed rotating disks. *Journal of Fluids Engineering*, 82(1):217–230, 1960.
- [69] C. E. Basset. An integral solution for compressible flow through disc turbines. In *10th Intersociety energy conversion and engineering conference, Newark, DE*, August 1975.
- [70] P. W. Garrison, D. W. Harvey, and I. Catton. Laminar compressible flow between rotating disks. *ASME Journal of Fluids Engineering*, 98(3):382–388, 1976.
- [71] C. R. Truman, W. Rice, and D. F. Jankowski. Laminar throughflow of a fluid containing particles between co-rotating disks. *Journal of Fluids Engineering*, 101(1):87–92, 1979.
- [72] M. Piesche. Berechnung der kompressiblen, laminaren Unterschallströmung in einer Tesla Turbine. *Strömungsmechanik und Strömungsmaschinen, Universität Karlsruhe*, 28:25–31, 1980.
- [73] P. Harwood. Further investigations into Tesla turbomachinery. In *SID*, volume 3046768, page 75, 2008.

- [74] P. I. San'kov and E. M. Smirnov. Asymptotic solution of the Navier-Stokes equations for radial fluid flow in the gap between two rotating disks. *Journal of Applied Mechanics and Technical Physics*, 24(1):8–12, 1983.
- [75] V. I. Misyura. Experimental investigation of the flow of an incompressible fluid between two rotating disks. *Izv. Vyssh. Uchebn. Zaved., Energet.*, 5, 1977.
- [76] G. Lonsdale and J. E. Walsh. Acceleration of the pressure correction method for a rotating Navier-Stokes problem. *International Journal for numerical methods in Fluids*, 8(6):671–686, 1988.
- [77] S. V. Patankar and D. B. Spalding. A calculation procedure for heat, mass and momentum transfer in three-dimensional parabolic flows. *International Journal of Heat and Mass Transfer*, 15(10):1787–1806, 1972.
- [78] J. Allen. Examining the Tesla Turbine. Master's thesis, University of Dayton, OH, 1989. URL <http://arc.aiaa.org/doi/pdf/10.2514/6.1989-838>.
- [79] V. P. Carey. Assessment of tesla turbine performance for small scale rankine combined heat and power systems. *Journal of Engineering for Gas Turbines and Power*, 132(12):122301, 2010. URL <http://gasturbinespower.asmedigitalcollection.asme.org/article.aspx?articleid=1429091>.
- [80] H. S. Couto, J. B. F. Duarte, and D. Bastos-Netto. The Tesla Turbine revisited. In *8th Asia-Pacific International Symposium on Combustion and Energy Utilization*, 2006.
- [81] R. Puzyrewski and K. Tesch. 1D model calibration based on 3D calculations for Tesla Turbine. *TASK Quarterly: Scientific bulletin of Academic Computer Centre in Gdansk*, 14(3):237–248, 2010.
- [82] V. P. Carey. Computational/theoretical modeling of flow physics and transport in disk rotor drag turbine expanders for green energy conversion technologies. In *ASME 2010 International Mechanical Engineering Congress and Exposition*, pages 31–38. ASME, 2010. URL <http://proceedings.asmedigitalcollection.asme.org/proceeding.aspx?articleid=1616936>.
- [83] B. P. Ho-Yan. Tesla Turbine for pico hydro applications. *Guelph Engineering Journal*, 4:1–8, 2011.
- [84] A. Guha and S. Sengupta. The fluid dynamics of the rotating flow in a Tesla disc turbine. *European Journal of Mechanics-B/Fluids*, 37:112–123, 2013.
- [85] W. Rice, D. F. Jankowski, and C. R. Truman. Bulk-parameter analysis for two-phase throughflow between parallel co-rotating disks. In *Heat Transfer and Fluid Mechanics Institute, Meeting, 25th, Davis, California*, pages 77–91, 1976.
- [86] V. M. Kapinos. Heat transfer during the flow of a stream from the center to the periphery between two rotating disks. *International Chemical Engineering*, 5:461–466, 1965.

- [87] K. O. Felsch and M. Piesche. Zum Betriebsverhalten einer Reibungsturbine und deren Einsatz als Wärmeaustauscher. *Strömungsmechanik und Strömungsmaschinen*, 27, 1979.
- [88] K. O. Felsch and M. Piesche. Ein Beitrag zur Berechnung der Strömung in einer Tesla-Turbine bei temperaturabhängiger Zähigkeit des Fördermediums. *Ingenieur-Archiv*, 50(2):121–129, 1981.
- [89] F. Kreith. Transfert de chaleur et de mass dans un écoulement radial entre disques parallèles fixes, en tournant à la même vitesse. *Journal of Heat and Mass Transfer*, 9:265–282, 1966.
- [90] M. Piesche. *Strömung und Wärmeübergang in einem inkompressiblen, viskosen Medium zwischen parallelen, synchron rotierenden Scheiben mit radialem Durchfluß*. PhD thesis, Universität Karlsruhe, 1978.
- [91] R. Wollkind and R. C. DiPrima. Effect of a coriolis force on the stability of plane Poiseuille flow. *Physics of Fluids (1958-1988)*, 16(12):2045–2051, 1973.
- [92] J. E. Flaherty and R. C. DiPrima. Effect of a coriolis force on the stability of plane poiseuille flow. *Physics of Fluids (1958-1988)*, 21(5):718–726, 1978.
- [93] A. Gusev and F. H. Bark. Stability of rotation-modified plane poiseuille flow. *Physics of Fluids (1958-1988)*, 23(11):2171–2177, 1980.
- [94] D. F. Jankowski and D. R. Squire. Energy stability limit for rotation-modified plane poiseuille flow. *Physics of Fluids (1958-1988)*, 20(12):2149–2150, 1977.
- [95] L. L. Pater. *Transition of inward flow between closely-spaced parallel co-rotating disks*. PhD thesis, Arizona State University, 1973.
- [96] E. W. Crowther. An experimental investigation of outward flow of an incompressible newtonian fluid between closely spaced parallel co-rotating disks. Master's thesis, Arizona State University, 1973.
- [97] L. L. Pater, E. Crowther, and W. Rice. Flow regime definition for flow between corotating disks. *Journal of Fluids Engineering*, 96(1):29–34, 1974.
- [98] V. M. Chesnokov. Oscillations of a viscous fluid in a thin layer between coaxial rotating disks. *Akademiia Nauk SSSR Izvestiia Mekhanika Zhidkosti i Gaza*, 20: 166–169, 1984.
- [99] A. B. Leaman. The design, construction and investigation of a Tesla Turbine. Master's thesis, University of Maryland, 1950.
- [100] A. B. Davydov and A. N. Sherstyuk. Experimental research on a disc microturbine. *Russian Engineering Journal*, 60(8):19–22, 1980.
- [101] G. Hoya and A. Guha. The design of a test rig and study of the performance and efficiency of a Tesla disc turbine. *Proceedings of the Institution of Mechanical Engineers, Part A: Journal of Power and Energy*, 223(4):451–465, 2009.

- [102] V. Romanin, V. P. Carey, and Z. Norwood. Strategies for performance enhancement of Tesla Turbines for combined heat and power applications. In *ASME 2010 4th International Conference on Energy Sustainability*, pages 57–64. American Society of Mechanical Engineers, 2010. URL <http://proceedings.asmedigitalcollection.asme.org/proceeding.aspx?articleid=1607440>.
- [103] H. P. Borate and N. D. Misal. An effect of surface finish and spacing between discs on the performance of disc turbine. *International Journal of Applied Research in Mechanical Engineering*, 2:25–30, 2012.
- [104] M. U. S. Khan, E. Ali, M. I. Maqsood, and H. Nawaz. Modern improved and effective design of boundary layer turbine for robust control and efficient production of green energy. In *Journal of Physics: Conference Series*, volume 439. IOP Publishing, 2013. doi: 10.1088/1742-6596/439/1/012043.
- [105] D. Zhao, C. Ji, C. Teo, and S. Li. Performance of small-scale bladeless electromagnetic energy harvesters driven by water or air. *Energy*, 74:99–108, 2014.
- [106] A. Guha and B. Smiley. Experiment and analysis for an improved design of the inlet and nozzle in Tesla disc turbines. *Proceedings of the Institution of Mechanical Engineers, Part A: Journal of Power and Energy*, 224(2):261–277, 2010.
- [107] F. Kreith, E. Doughman, and H. Kozlowski. Mass and heat transfer from an enclosed rotating disk with and without source flow. *Journal of Heat Transfer*, 85(2):153–162, 1963.
- [108] M. Köhler. *Die Strömung durch das Spaltelement einer Reibungspumpe*. PhD thesis, Karlsruhe, 1969.
- [109] M. Köhler. Die Strömung zwischen zwei parallelen, rotierenden Scheiben. *Acta Mechanica*, 12(1-2):33–51, 1971.
- [110] M. DeSantis, L. Galowin, and E. Rakowsky. Discussion: "An asymptotic solution for laminar flow of an incompressible fluid between rotating disks" (Matsch, L., and Rice, W., 1968, ASME J. Appl. Mech., 35, pp. 155–159). *Journal of Applied Mechanics*, 37(3):887–887, 1970.
- [111] E. Bakke, J. F. Kreider, and F. Kreith. Turbulent source flow between parallel stationary and co-rotating disks. *Journal of Fluid Mechanics*, 58(02):209–231, 1973.
- [112] D. Nendl. Three-dimensional laminar instabilities at flat walls. In *Gesellschaft Angewandte Mathematik und Mechanik Workshop Paris France*, volume 56, page 211, 1976.
- [113] D. Nendl. *Eine theoretische Betrachtung der Reibungsturbomaschinen von Nikola Tesla*. PhD thesis, Rheinisch-Westphälische Technische Hochschule Aachen, 1966.
- [114] D. Nendl. Eine theoretische Betrachtung der Tesla-Reibungspumpe. *VDI-Forschungsheft*, 527:29–36, 1968.
- [115] M. Fiebig. Über die Bewegung in Strömungskreiseln. *Deutsche Versuchsanstalt für Luft- und Raumfahrt*, 655, 1967.

- [116] W. Rice. Computed results, incompressible flow in a multiple-disk turbine. Technical report, Engineering Science Department, Arizona State University, 1973.
- [117] P.-S. Wu. Evaluation of analytical models for multiple disk pump rotor calculations. Master's thesis, Department of Mechanical and Aerospace Engineering, Arizona State University, 1986.
- [118] S. Mochizuki and W.-J. Yang. Self-sustained radial oscillating flows between parallel disks. *Journal of Fluid Mechanics*, 154:377–397, 1985.
- [119] M. Zhou, C. P. Garner, and M. Reeves. Numerical modelling and particle image velocimetry measurement of the laminar flow field induced by an enclosed rotating disc. *International journal for numerical methods in fluids*, 22(4):283–296, 1996.
- [120] Y. Nakata, J. Y. Murthy, and D. E. Metzger. Computation of laminar flow and heat transfer over an enclosed rotating disk with and without jet impingement. *Journal of Turbomachinery*, 114(4):881–890, 1992.
- [121] K. Hirata, M. Furue, N. Sugawara, and J. Funaki. An experimental study of three-dimensional vortical structures between co-rotating disks. In *Journal of Physics: Conference Series*, volume 14, pages 213–219. IOP Publishing, 2005.
- [122] Y. S. Tsai, Y. M. Chang, Y. J. Chang, and Y. M. Chen. Phase-resolved PIV measurements of the flow between a pair of co-rotating disks in a cylindrical enclosure. *Journal of Fluids and Structures*, 23(2):191–206, 2007.
- [123] E. Laroche and Y. Ribaud. An analysis of the internal aerodynamic losses produced in the laminar and centrifugal flow between two parallel co-rotating disks. In *Proc. 3rd European Conference on Turbomachinery-Fluid Dynamics and Thermodynamics, IMechE Event Publications, London, Paper*, number C557 in 001, 1999.
- [124] Y. Ribaud. Disk flow energy transmitters. In *5th ISAIF symposium, Gdansk, Poland*, 2001.
- [125] N. Huybrechts, O. Berten, and E. Lenclud. Numerical study of a Tesla Turbine. *7th Belgian National Congress on Theoretical and Applied Mechanics, Ghent, Belgium*, 2003.
- [126] C. Singleton. The investigation and analysis of Nikola Tesla's blade-less turbine. In *Queensland University of Technology*, 2000.
- [127] A. F. R. Ladino. Numerical simulation of the flow field in a friction-type turbine (Tesla Turbine). Technical report, Institute of Thermal Powerplants, Vienna University of Technology, 2004.
- [128] T. W. Choon, A. A. Rahman, F. S. Jer, and L. E. Aik. Optimization of Tesla Turbine using computational fluid dynamics approach. In *Industrial Electronics and Applications (ISIEA), 2011 IEEE Symposium on*, pages 477–480. IEEE, 2011.
- [129] M. S. Siddiqui, H. Ahmed, and S. Ahmed. Numerical simulation of a compressed air driven Tesla Turbine. In *ASME 2014 Power Conference*, pages V002T09A009–V002T09A009. ASME, 2014.

- [130] R. Lakshman and A. Francis. Fabrication and design analysis of blade-less turbine operating on a low boiling medium. *International Conference on Advanced Trends in Engineering and Technology*, 2014.
- [131] R. J. Pandey, S. Pudasaini, S. Dhakal, R. B. Uprety, and H. P. Neopane. Design and computational analysis of 1 kw Tesla Turbine. *International Journal of Scientific and research Publication*, 4:1–5, 2014.
- [132] L. I. Anderson and W. Rice. *Tesla Turbine references*. Breckenridge, Twenty First Century Books, 2001.
- [133] Heinz Schade, Ewald Kunz, Frank Kameier, and Christian Oliver Paschereit. *Strömungslehre*. Walter de Gruyter, 2013.
- [134] C. Schosser, S. Lecheler, and M. Pfitzner. A test rig for the investigation of the performance and flow field of Tesla friction turbines, gt2014-25399. *Proceedings of ASME Turbo Expo 2014, Düsseldorf, Germany*, 2014.
- [135] Stefan Lecheler. *Numerische Strömungsberechnung: Schneller Einstieg durch anschauliche Beispiele mit ANSYS 15.0*. Springer-Verlag, 2014.
- [136] ANSYS. ANSYS CFX-Solver Theory Guide 15, 2015.
- [137] C. Schosser, R. Hain, C. Cierpka, S. Lecheler, C. J. Kähler, and M. Pfitzner. Determination of velocity profiles in small gaps between parallel flat plates by means of tomographic PIV. *21. Fachtagung, Lasermethoden in der Strömungsmesstechnik, Munich, Germany*, 2013.
- [138] R. W. Hanks and H. C. Ruo. Laminar-turbulent transition in ducts of rectangular cross section. *Industrial & Engineering Chemistry Fundamentals*, 5(4):558–561, 1966.
- [139] H. Schlichting and K. Gersten. *Grenzschicht-Theorie*. Springer-Verlag Berlin Heidelberg, 10th edition, 2006.
- [140] C. Cierpka and C. J. Kähler. Particle imaging techniques for volumetric three-component (3D3C) velocity measurements in microfluidics. *Journal of Visualization*, 15(1):1–31, 2012.
- [141] H. Dubbel, W. Beitz, and K.-H. Kuttner. *Handbook of Mechanical Engineering*. Springer-Verlag, 1994.
- [142] H. Wittel, D. Muhs, D. Jannasch, and J. Voßiek. *Roloff/Matek Maschinenelemente. Vieweg+Teubner*, 2009.
- [143] Robert Gasch, Rainer Nordmann, and Herbert Pfitzner. *Rotordynamik*. Springer-Verlag, 2006.
- [144] C. J. Kähler, S. Scharnowski, and C. Cierpka. On the uncertainty of digital PIV and PTV near walls. *Experiments in Fluids*, 52(6):1641–1656, 2012.

-
- [145] C. Atkinson, S. Coudert, J.-M. Foucaut, M. Stanislas, and J. Soria. The accuracy of tomographic particle image velocimetry for measurements of a turbulent boundary layer. *Experiments in Fluids*, 50(4):1031–1056, 2011.
- [146] R. Y. Tsai. A versatile camera calibration technique for high-accuracy 3D machine vision metrology using off-the-shelf TV cameras and lenses. *IEEE Journal of Robotics and Automation*, 3(4):323–344, 1987.
- [147] C. Schosser, T. Fuchs, R. Hain, and C. J. Kähler. Non-intrusive calibration for three-dimensional particle imaging. *Experiments in Fluids*, 57:69, 2016. doi: 10.1007/s00348-016-2167-z.
- [148] B. Wieneke. Stereo-PIV using self-calibration on particle images. *Experiments in Fluids*, 39(2):267–280, 2005.
- [149] R. I. Hartley and P. Sturm. Triangulation. *Computer vision and image understanding*, 68(2):146–157, 1997.
- [150] M. Raffel, C. Willert, S. Wereley, and J. Kompenhans. *Particle Image Velocimetry: A practical guide*. Springer, 2013.
- [151] V. M. Chesnokov. Oscillations of a viscous fluid in a thin layer between two coaxial disks rotating together. *Fluid Dynamics*, 19(1):146–149, 1984.
- [152] W. Leuckel. Swirl intensities, swirl types and energy losses of different swirl generating devices. *Flame Research Foundation Report-G*, 2, 1967.